Photocatalytic Water Splitting by Utilising Oxide Semiconductor Materials

(Henry) Hung-Chun Lai

Department of Chemistry and St Anne's College

A thesis submitted to the for the degree of

Doctor of Philosophy

University of Oxford

May 2012

Supervisor: Professor Peter P. Edwards FRS

ABSTRACT

Photocatalytic Water Splitting by Utilising Oxide Semiconductor Materials

(Henry) Hung-Chun Lai

Submitted for the degree of Doctor of Philosophy

St Anne's College, Oxford Trinity 2012

This thesis reports the study of metal oxide semiconductors for the application of photoelectrochemical water splitting with a particular emphasis on both anion and cation-doped zinc oxides. A study of the mechanisms of visible light absorption in both anion and cation-doped ZnO semiconductors, the potentials of metal oxide materials modified by impurities as one of the ideal photocatalysts in harvesting solar light has been explored. X-ray photoelectron spectroscopy (XPS) and UV-Vis spectroscopes have been performed to establish the electronic structures of anion and cation-doped ZnO. Aluminium impurities in ZnO thin films reveal the relationship between the bandgap broadening and the so-called Burstein Moss effect. Both cadmium and sulphur dopants were incorporated in ZnO either as powders by the solid state synthesis or as thin films by spray pyrolysis technique. Cadmium and sulphur dopants demonstrate effective electronic bandgap reduction and an increasing absorption of visible light. Furthermore, the incorporation of cadmium and sulphur in ZnO were prepared as photoanodes and evaluated in a custom-built photoelectrochemical workstation for the measurement of photon energy conversion efficiencies.

ABSTRACT

Photocatalytic Water Splitting by Utilizing Oxide Semiconductor Materials

Henry Hung-Chun Lai

Submitted for the degree of Doctor of Philosophy

St Anne's College, Oxford Trinity 2012

Extended Abstract

The *Introduction* surveys recent developments in photocatalytic water splitting reaction and outlines the scope of the current research effort. The introduction also presents a review of the underlying materials chemistry and physics of the undoped, anionic and cationic doping in ZnO materials, which is the main focus of this thesis.

Chapter 2 describes the methods of synthesis and characterisation techniques. The principles, instrumentation used, and data analysis of the key techniques are demonstrated, along with providing the detailed experimental conditions for preparing powders and thin films.

In *Chapter 3*, essential parameters for growing high quality ZnO thin films, such as the thermodynamic driving force and the misfit between the substrate and film were investigated. ZnO films demonstrated a highly orientation in the *c* axis of crystallites at high deposition temperature due to the atomic arrangement on the terminated plane. The Burstein-Moss (BM) effect determined the energy shift in the bandgap of Al-doped ZnO (AZO) thin films. The strain-induced bandgap shift in AZO films was ruled out because the magnitudes of strain between AZO films are almost equal. Epitaxial growth of ZnO thin films were carried out successfully by the spray pyrolysis method. The vital conditions for growing a ZnO epilayer

were a substrate with small lattice mismatch (e.g. single crystal $Al_2O_3(0001)$) and a substrate deposition temperature at 500˚C.

Chapter 4 focused on the effect of Cd impurity on the electronic structures, electrical transport and optical properties in ZnO. It revealed that the conduction and valence bands shift simultaneously when Cd was incorporated in ZnO. The valence band offset was caused by the rehybridisation of Cd 4d and Zn 3d orbitals while the conduction band offset was a result of the perturbation by underlying Cd 5s impurity states. The electron accumulation and downward band bending were observed on the surface of $Cd_xZn_{1-x}O$ powders but thin films.

Chapter 5 illustrated the influence of S doping in ZnO on the grain size and electronic structure. In contrast to $Cd_xZn_{1-x}O$, adding S only changed the ZnO valence band. This was because high lying S 3p states compared to O 2p states in the valence band, which leads to an upward shift in the valence band maximum.

A photoelectrochemistry workstation with a three-electrode cell was established to test the undoped ZnO, $Cd_xZn_{1-x}O$, and $ZnO_{1-x}S_x$ photoelectrodes and those results were presented in *Chapter 6*. Under illumination, the bandgap reduction as well as the heterojunction structure in $Cd_xZn_{1-x}O$ photoelectrodes increased visible light harvesting. The $Cd_{0.065}Zn_{0.935}O$ sample was enhanced by 240% in the photocurrent density at +0.8 V and increased by 220% in the photon-to-hydrogen efficiency when compared to the undoped ZnO photoanode.

With regard to $ZnO_{1-x}S_x$ photoanodes, the photocurrent density and the photon-to-hydrogen efficiency in the x = 0.004 sample increased by 260% and 330% compared to the undoped ZnO. However, as the S content increases, the photocurrent density and efficiency decreased. Film crystallite determined the photocurrent generation and the energy conversion efficiency instead of bandgap in $ZnO_{1-x}S_x$ photoanodes. It is believed that crystallinity is responsible for the recombination rate of electrons and holes. The x = 0.028 photoelectrode

has the highest level of grain boundaries as a result of the smallest grain size. Therefore, photogenerated electrons and holes were inefficiently separated, leading to the lowest energy conversion efficiency.

ACKNOWLEDGES

Firstly, I would like to express my deepest gratitude to my doctorate supervisor, Professor Peter P. Edwards for giving me a chance to conduct research in this big PPE family. I also appreciate your strong support, encouragement and guidance over the past three years, without which I would not have been able to produce this thesis.

Secondly, I would thank all the people who I have worked with to help me to get the results for this thesis. My warm appreciation to Dr. Vladimir L. Kuznetsov, for a lot of advice, together with the infinite patience and kindness you have invariably shown me. I express my deep gratitude for your great help on reviewing of my every manuscripts as well as this thesis.

I own my special thank to Professor Russell G. Egdell, for so many useful discussions. Your suggestions always make me stunned and enrich my manuscript, thesis and knowledge. Thank you for all the input. I would also thank Dr. Danny Law and Dr. Graham Beamson for their help with the Scienta XPS. Dr. Robert Jacobs for teaching me to use the XPS and AFM facilities and doing the refinements of optical properties

I would like to thank Dr Hongliang Zhang, one of my best friends at Oxford, for the endless help, discussions and sharing life experiences. I must thank all the people in PPE group, including Andrew, Philippe, Liang, Katie and Josh to make me cheerful, without you my research life would be very boring.

Finally, I heartfelt thank to my parents, brothers and my girl friends, Eugenie, who have shown me their total love and support (spiritual and financial). This work is for you.

(Henry) Hung-Chun Lai

May 2012

PUBLICATIONS

1. *Electronic structure of ternary $Cd_xZn_{1-x}O$ ($0 \leq x \leq 0.075$) alloys
   Lai, H. H.-C., Kuznetsov V., Egdell R. G. and Edwards P. P.,
   Appl. Phys. Lett., **100**, 072906 (2012).

2. *Electron carrier induced bandgap shifting in Al-doped ZnO thin films
   Lai, H. H.-C., Basheer T., Kuznetsov V., Pepper M., and Edwards P. P.,
   J. Appl. Phys. (2012), Accepted.

3. *Band gap narrowing in the epitaxial growth of $ZnO_{1-x}S_x$ thin films prepared by spray pyrolysis
   Lai, H. H.-C., Zhang, K. H. L., Lazarov, V., Egdell, R.G. and Edwards P. P.,
   Phys. Chem. Chem. Phys, (2012), In preparation.

4. Domain matching epitaxial growth of In_2O_3 thin films on αlpha-Al_2O_3(0001)
   Zhang, K. H. L., Lazarov, V., Galindo, P., Oropeza, F., Payne, D., **Lai, H. H.-C**.,
   Egdell, R. G.,
   Cryst. Growth Des., **12**, 1000-1007 (2012)

5. Unusual visible-light-responsive photoactivity of AgBr-BiOBr heterojunction photocatalysts
   Kong L., Jiang Z., **Lai, H. H.-C**., Jones M. O., Xiao T., Edwards P.P.,
   J. Catal., (2012), Submitted.

6. Influence of temperature on the epitaxial growth of In_2O_3 thin films on Y-ZrO2(111),
   Zhang K. H. L., Lazarov V. K., **Lai H. H.-C**., and Egdell R. G.,
   J. Cryst. Growth , **318**, 345-350 (2011).

*These papers report work from this thesis

TABLE OF CONTENTS

CHAPTER 1

INTRODUCTION

1.1 Overview

Harvesting solar energy by utilizing semiconductor materials to convert inert molecular (e.g. H_2O) to solar fuels (e.g. H_2) is recognised as a promising way to replace the use of fossil fuels because the sunlight is a renewable, sustainable and substantial energy source. Seeking durable, efficient, low cost and non-toxic semiconductor materials that can convert solar energy into solar hydrogen and electricity is the one of the most important challenges. In 1972 Fujishima and Honda[1] reported that a xenon lamp illumination of a n-type titanium dioxide (TiO_2) semiconductor generated a photocurrent that could split water. Since then a wide variety of semiconductors has been explored to date. Among these semiconductors, metal oxides, such as TiO_2, zinc oxide (ZnO) and iron oxide (Fe_2O_3), are thought to offer the potential for the photoactive based applications due to the advantages of aqueous stability, anti-corrosion and abundancy.[2-5]

1.2 A Review of the General Properties of Zinc Oxide

ZnO is the one of the group of II-VI semiconductor materials. The general properties of ZnO are summarized in Table 1.1. Thin films of ZnO have been widely used as a transparent conducting oxide (TCO), UV light emitter, high-output

nanogenerator and self-powered devices.[6-8] The later two applications, relaying on the coupling of piezoelectric and semiconducting properties of ZnO, harvest energy by converting mechanical energy into electrical power. ZnO has a wide and direct bandgap of 3.3 eV at 300 K. Although the bandgap value and electronic band positions for ZnO are similar to TiO_2, electronic mobility in ZnO is over two orders of magnitude higher than that in TiO_2.[9, 10] The direct bandgap at the Γ point in the bixbyite indium oxide (In_2O_3) is about 3.6 eV.[11] Owing to In_2O_3 structure with metal cations in sites with locally centrosymmetric coordination, the hybridisation of O 2p with In 4d states may be away from the zone centre, leading to an indirect band gap of 2.6 eV.[12] In contrast to In_2O_3, ZnO only exhibits a direct bandgap. Furthermore, only ZnO exhibits piezoelectricity (i.e. the generation of electricity when a mechanical treatment is enforced) due to its polarity. As for the optoelectronic applications, gallium nitride (GaN) is commonly used in the applications of white, green and blue-UV light emitting devices. The bandgap in GaN is direct and at around 3.4 eV. ZnO has benefits over GaN to optoelectronics due to larger exciton binding energy (60 meV for ZnO versus 26 meV for GaN at 300 K), availability of large bulk single crystals which can be prepared using various techniques, and amendment to wet chemical etching.[13, 14] Chemical etching is known as a crucial step for device design and fabrication.

Unfortunately, the wide bandgap of ZnO has a poor spectral response to visible light and makes it difficult to be used in the visible-based applications, such as photovoltaic and photoelectrochemical water splitting. The irradiation intensity of UV light in the whole solar spectrum is less that 5%. Narrowing the ZnO bandgap to allow ZnO harvesting visible light appears to be a effective approach to enhance the light-capturing performance.

Impurity substitution has been demonstrated to modify the ZnO bandgap effectively. For example, bandgap engineering has been achieved by alloying ZnO with MgO or CdO.[15, 16] The substitution of Mg for Zn enlarges the bandgap of ZnO, whereas incorporating Cd in ZnO decreases its bandgap. The doping process itself also modifies the electrical transport, magnetic properties and optical transparency of ZnO arisen from the modifications of crystal and electronic structures. The details of ZnO properties and impurities doping effect will be introduced in the following sections.

Table 1.1 Properties of wurtzite ZnO[13]

Properties	**Values**
Lattice parameter at 300 K: a_0 c_0 a_0/c_0 Cell volume	 0.3250 nm 0.5207 nm 1.602 (1.633 for ideal hexagonal structure) 0.047 nm^3
Density	5.606 g/cm^3
Melting point	1975˚C
Thermal conductivity	0.6, 1-1.2 W/m·K
Static dielectric constant	8.656
Refractive index	2.008
Electronic bandgap	3.3 eV (direct)
Intrinsic carrier concentration	< 10^6 /cm^3
Exciton binding energy	60 meV
Electron effective mass	0.26
Electron Hall mobility at 300 K for *n*-type conductivity	200 cm^2/Vs
Hole effective mass	0.59

1.3 *Crystal Structure of Zinc Oxide*

Similar to the most II^b-VI binary compound semiconductors, the crystal structures adopted by ZnO are wurtzite (hexagonal), zinc blende (cubic), and rocksalt (cubic).[14] However, different to other II^b-VI semiconductors existing both in cubic zinc blende and hexagonal wurtzite structures, the thermodynamically stable structure for ZnO at ambient conditions is wurtzite. The zinc blende structure for ZnO is only grown epitaxially on a suitable substrate with cubic structure. It is even harder to obtain the rocksalt structure of ZnO, which can be only synthesized at relatively high pressure.[14]

Figure 1.1 shows a crystal structure for the hexagonal wurtzite ZnO with lattice parameters a = 3.25 Å and c = 5.21 Å.[17] The space group is $P6_3mc$ or C_{6v}.[4] The unit cell contains two formula units of ZnO and the coordination number is 4 (i.e each O^{2-} anion is surrounded by four Zn^{2+} cations at the corner of a tetrahedron, and *vice versa*). The tetrahedral coordination is a typical of sp^3 covalent bonding but shows polarity due to the lack of inversion symmetry. In Figure 1.2, the compounds at the top corner imply entirely covalent bonding, such as diamond, Si, and Ge. On the other side, the compounds at the bottom reveal completely ionic bonding, for example alkali halides. Likewise, the compounds in the middle are formed with partial covalent and partial ionic characters. Tetrahedral coordinated ZnO resided in the centre of solid states physics diagram (Figure 1.2) and exhibits a fraction of ionic bonding leading to the fact that the conduction band minimum (CBM) is mainly constructed from Zn 4s and the valence band maximum (VBM) is formed from O 2p.[14]

Surfaces of real crystals never adopt the bulk-truncated structures shown in Figure 1.1 The atoms on the surface will construct or relax (i.e. the inward or outward movement of atoms) in order to minimize the surface energy that is defined as the excess energy on the surface than in the bulk. There are four phase terminations for the low-index ZnO surface, namely $(10\bar{1}0)$, $(11\bar{2}0)$, (0001), and $(000\bar{1})$. The $(10\bar{1}0)$ and $(11\bar{2}0)$ are nonpolar planes due to equal numbers of Zn and O atoms. By contrast, the (0001) and $(000\bar{1})$ are polar planes, corresponding to Zn and O terminated surfaces of the polar $\{0001\}$ direction, respectively. In XRD patterns, the greatest peak in a ZnO film is (0002), growing along $[0001]$ direction, whereas $(10\bar{1}0)$ is the most preferential peak in powdered ZnO. The (0002) phase grows as the highest preferential orientation in ZnO thin films because the basal (0001) and $(000\bar{1})$ surfaces can rearrange the charges to minimize the surface energy, whereas the $(10\bar{1}0)$ and $(11\bar{2}0)$ phases do not occur lateral surface reconstruction. The charge rearrangement on the surface can be achieved by follows: (1) creation of a metallic surface by introducing surface states; (2) removal of surface atoms; and (3) charged impurities at the surface, such as hydroxyl or hydroxide species. In contrast, powdered ZnO exhibits the preferential orientation in $(10\bar{1}0)$ instead of (0002), where (0002) is a less stable phase because the planes along *c*-axis creates a diverging electrostatic potential due to the alternating charge of atomic planes in polar direction (i.e. one plane has entire Zn^{2+} ions and the next one plane is O^{2-}).[18]

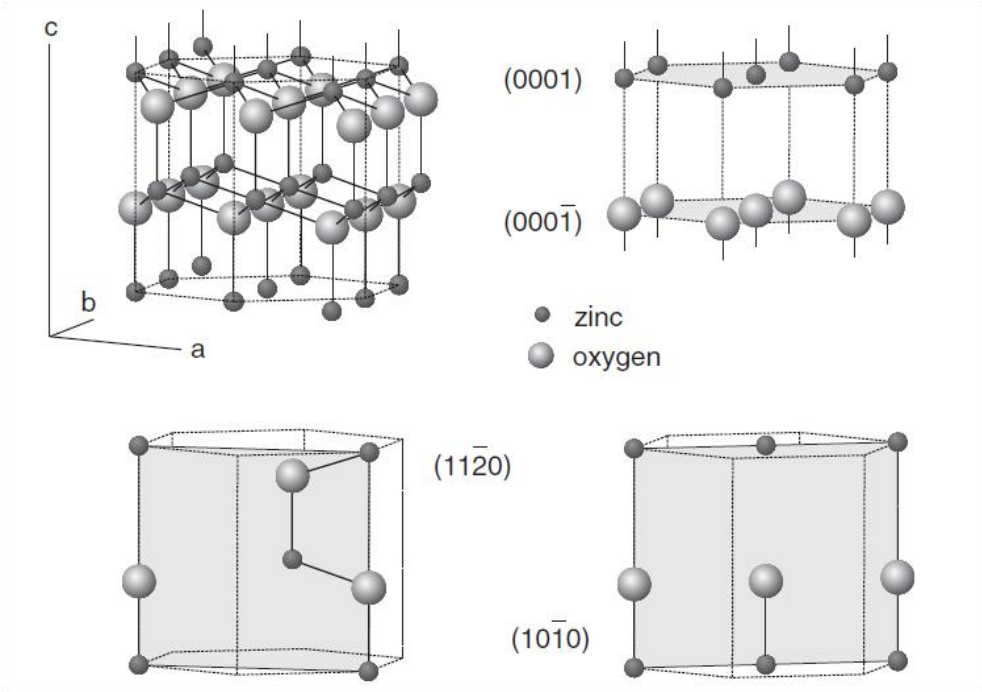

Figure 1.1 Crystallographic structure of ZnO and its basic surfaces.[18]

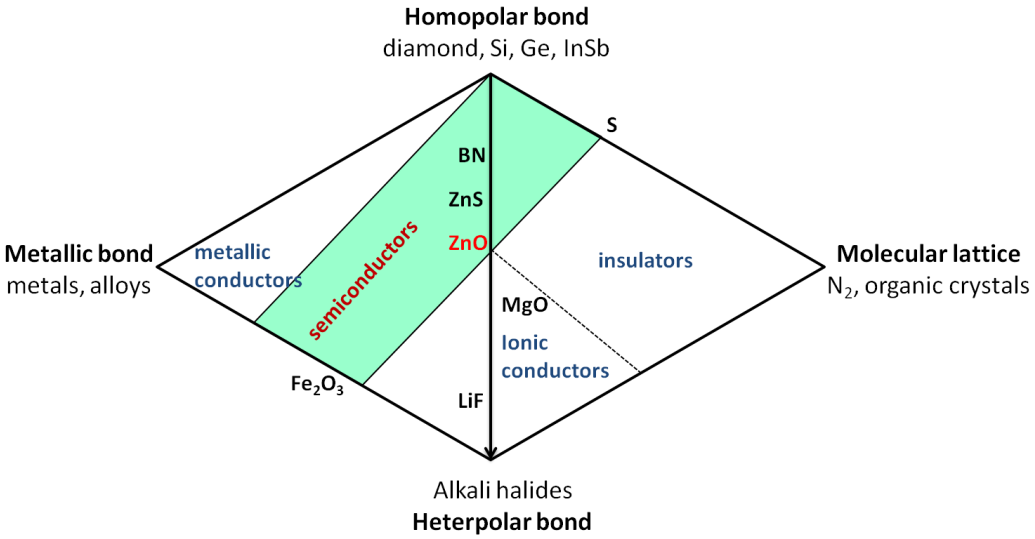

Figure 1.2 A solid state physics diagram displays a variety types of chemical bondings for solids and their electronic properties.[19]

1.4 The Electronic Structure of Metal Oxide

1.4.1 The Ionic Model of Metal Oxide Solids

The simplest way to understand the electronic band structure of solids is to take a local view in terms of the *ionic model* that describes the properties of individual ions, which is assumed to have integral charges given by the oxidation states of the different elements present. The ionic model is a simple but useful theory to understand the structures and properties of solids. Figure 1.3 illustrates the steps required to form an electronic bandgap using ion model arguments. For the isolated ions in a gas phase, the gaseous O^{2-} energy level is on the top since it is less stable than M^{n+} level, Figure 1.3 (a). The *Madelung potential* stabilises the O^{2-} level while destabilising the level of metal ions by arranging the gaseous ions into a long-range lattice, Figure 1.3 (b). After that, polarization takes place and reduces the bandgap when moving charges around in a lattice. The magnitude of polarization is given[20]

$$\Delta E_{pol} = \frac{-q^2}{8\pi\varepsilon_0 R}(1-1/\varepsilon_r) \tag{1.1}$$

where q is the charge, R is the effective radius, ε_r is the relative dielectric constant, and ε_0 is the dielectric constant under vacuum. A typical value calculated for one unit of electrical charge in an oxide is approximately 2 eV, Figure 1.3 (c). Finally, the overlap between ions forms the O 2p and M ns bandwidths and decreases the bandgap further, Figure 1.3 (d).

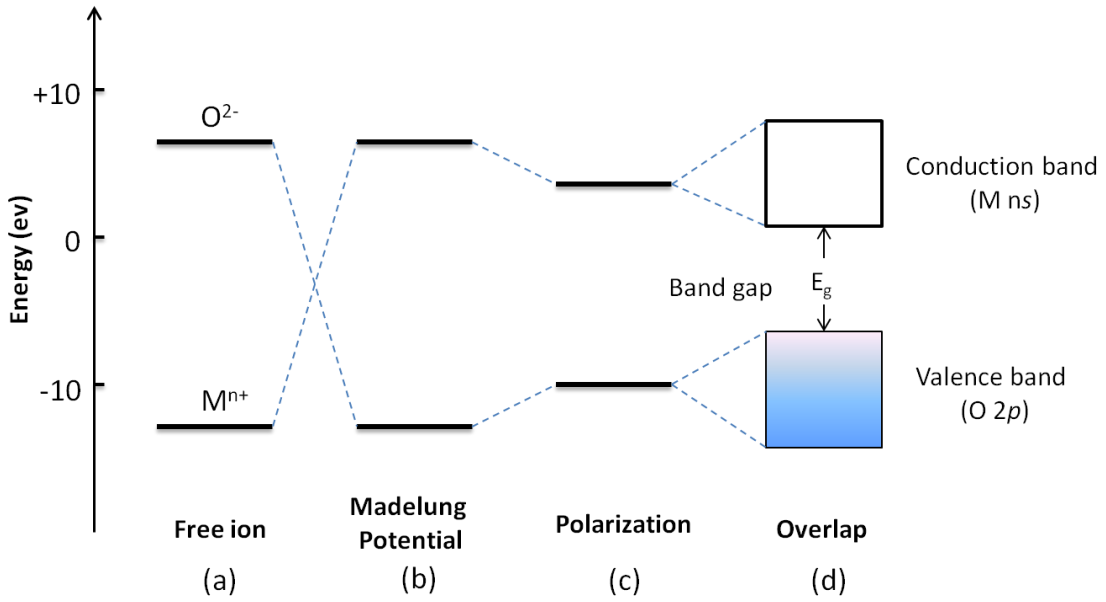

Figure 1.3 Ionic model interpretation of the bandgap in metal oxide. The orbital energies of the filled oxygen 2*p* and the empty metal n*s* levels are shown.[20]

Molecular orbital (MO) theory via the linear combination of atomic orbital (LCAO) approximation is the most commonly used model to understand the overlap model with limited atoms, which is shown as,[20]

$$\psi = \sum_i c_i \varphi_i \tag{1.2}$$

where Ψ is molecular orbital, c_i is the coefficient, and φ_i is the basis of valence atomic orbital. In partially ionic systems, molecular orbitals can be viewed as the simplest perturbations of atomic orbitals due to their overlap interactions. A real electronic band structure is very complicated and experimental techniques can be used to image the band structure. A traditional method to approach a real case is using band theory to sketch the band structure diagram in one dimensional at the beginning. In MO theory, the electronic orbitals are formed in the chain by making LCAO basis function. Therefore, the periodic and symmetry crystal orbital can be expressed as,[20]

$$\psi_k = \sum_n e^{ikna} \varphi_n \quad (1.3)$$

where φ_n is an atomic orbital located in the unit cell number n in the lattice, a is the lattice spacing between unit cells, and k is the quantum number for crystal orbital, also known as the wavevector. Equation 1.3 shows that each ψ_k represents one basis AO per unit cell, giving one band in an ionic structure. These orbitals will form bonding and antibonding when mixed. Figure 1.4 demonstrates the level of two basis states of transition metal (M) 3d and O 2p overlapping in the band structure diagram of metal oxide as the function of k. The *first Brillouin zone* is defined in a range of wavevector, $-\pi/a < k \leq \pi/a$. Pure M 3d and O 2p states at k = 0 have no net interaction. Moving to Brillouin zone edge as the k changes in the range from 0 to π/a, the band energies are forced apart by forming bonding and antibonding as the consequent of overlapping. Thus, a general trend seen for many oxides is that the O 2p orbital disperses downwards and metal based states disperse upwards with increasing wavevector. Note that this model simplifies in two AOs in one dimension. In a real crystal orbital, covalency and band dispersion are very important. The effect of covalent hybridization rises up the energy of metal states as well as lowers down the O 2p energy level. In addition to overlapping between M nd and O 2p orbitals, the low-lying O 2s, M ns and M np orbitals at higher energy have a great influence on the crystal orbital. The interactions between AOs with the variation of k lead to the dispersion in band structure. As a consequent of these considerations, the lowest bandgap should be direct and occurs at the zone centre.

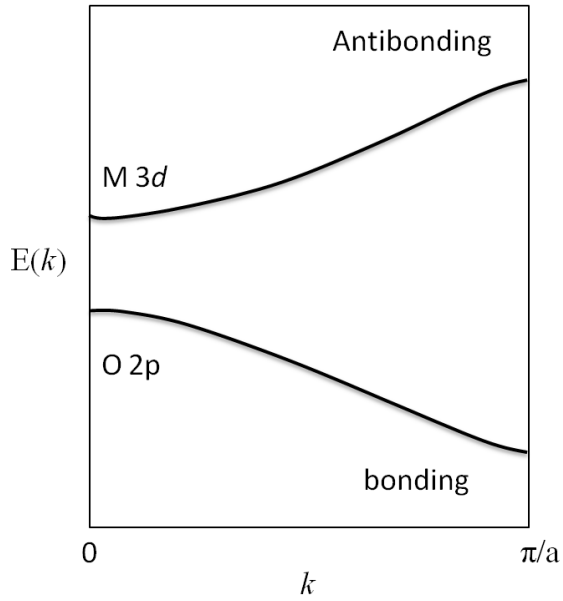

Figure 1.4 Band structure diagram in one dimension is formed by overlapping the basis atomic orbitals of M 3*d* and O 2*p*.

1.4.2 Electronic Structure of Zinc Oxide

ZnO is an example of a direct bandgap semiconductor with the both of upmost valence and the lowest conduction band at $\Gamma = 0$ in the Brillouin zone. The conduction band minimum (CBM), also known as lowest unoccupied molecular orbital (LUMO), consists of the empty 4s orbitals of Zn^{2+} in view of ionic bonding or the antibonding sp^3 hybridised states in terms of covalent bonding. Figure 1.5 shows a schematic drawing of the electronic structure of ZnO. The CBM has Γ_1 symmetry and Γ_7 symmetry. On the other hand, the valence band maximum (VBM), also called highest occupied molecular orbital (HOMO), is composed of filled O 2p orbitals. The threefold degeneracy in the valence band (VB) is levelled up due to the interactions of spin-orbital splitting and noncentrosymmetric crystal fields. These splits are A (Γ_7), B (Γ_9), and C (Γ_9) at 0 meV, 4.9 meV, and 48.6 meV at helium (He) liquid temperature

with respect to VBM, respectively. The order of splitting levels is still debated and remains an open question.[19, 21]

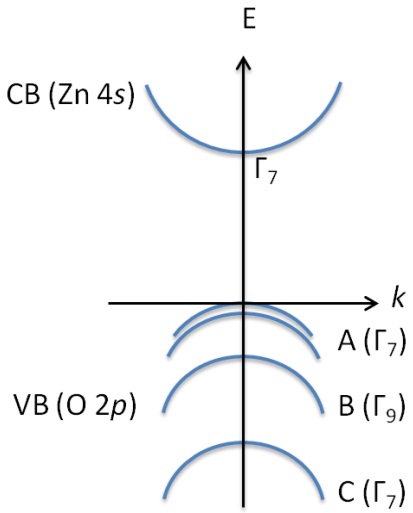

Figure 1.5 The electronic band structure of ZnO. Both of CBM and VBM are located at Γ-point. A, B and C represent three splitting excition states in the valence band.[19]

For II^b-VI semiconductors, the d states which lie below O 2p states is very important to the valence band. The p-d states repulsion is known to be able to (1) lower the bandgap, (2) reduce VB offset, (3) decrease cohesive energy, (4) increase the equilibrium lattice parameters, (5) reduce the spin-orbital splitting, (6) alter the sign of the crystal-field splitting, and (7) modify the charge distribution of various II^b-VI alloys.[22]

In addition, anion p orbitals also affect the level of VBM in II^b-VI semiconductors. In the LCAO approximation, the VBM of a tetrahedrally bonded semiconductor is derived from anion p orbitals and its energy is given by

$$E_{VB} = \frac{(E_p^a + E_p^c)}{2} - \left\{ \left[\frac{(E_p^a + E_p^c)}{2} \right]^2 + \left[\frac{1.28\hbar^2}{m_e d^2} \right]^2 \right\}^{1/2} \qquad (1.4)$$

where E_p^a and E_p^c are the p orbital energy of anion and cation, m_e is the electron mass, and d is the interatomic spacing. Equation 1.4 indicates that a larger binding energy of anion p orbital gives a lower energy of VB. Zn chalcogenide alloys (ZnX, X = S, Se, Te) is a good example to demonstrate the VB offsets. In Figure 1.6 the binding energy of the p orbitals increases from Te (9.54 eV), Se (10.68 eV), S (11.6 eV) to O (16.72 eV),[23] and thereby the resulting bandgap offset rises from ZnS (0.80 eV), ZnSe (1.32 eV) to ZnTe (2.16 eV).[24]

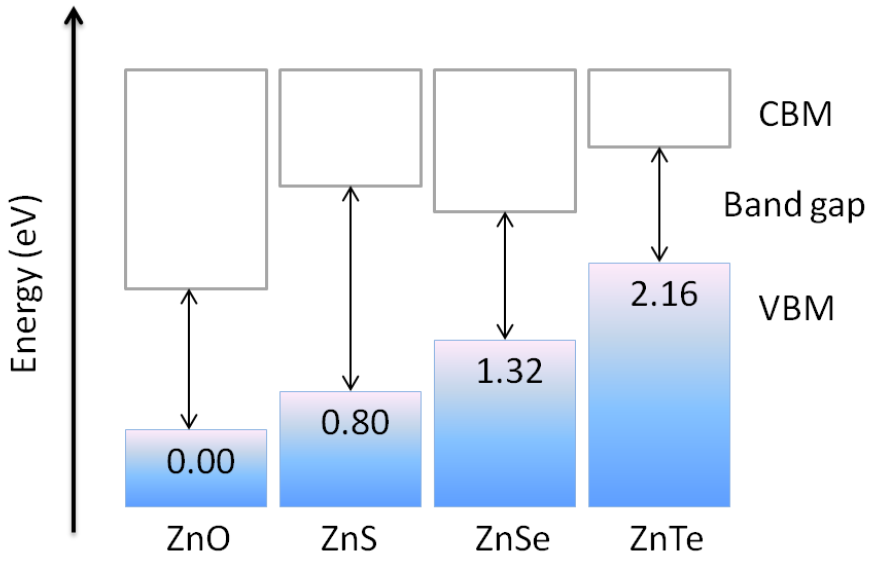

Figure 1.6 The band offsets between ZnX (X = S, Se, Te) compounds according to the density functional theory calculations.[24]

1.5 Electrical Transport in Metal Oxides

1.5.1 Conduction Electrons in Solids

Electrical transport for n-type oxide semiconductors is highly related to the properties of conduction electrons. The *velocity* of an electron travelling in one dimension in a particular band is defined as the slope of E(k) curve in Figure 1.4 as

$$v = \hbar^{-1} \frac{dE}{dk} \tag{1.5}$$

where ħ is the Planck constant and k is the wavevector. A real model in three-dimension is expressed as

$$v = \hbar^{-1} \Delta_k E \equiv \hbar^{-1} \left(\frac{\partial E}{\partial k_x}, \frac{\partial E}{\partial k_y}, \frac{\partial E}{\partial k_z} \right) \tag{1.6}$$

Equation 1.5 and equation 1.6 reflect that the electrical conductivity for a metal or a semiconductor prefers a wider band since the derivative of E(k) is large. Another essential quantity related to electronic transport is *effective mass* (m*), which can be simply represented as

$$m^* = \frac{\hbar^2}{d^2E/dk^2} \tag{1.7}$$

Equation 1.7 is used in one dimension or even in three-dimension if the bands are isotropic. As such, when considering the equation 1.5 and equation 1.7, it implies that light and highly mobile electron needs wide bands (i.e. dE is large). On the other hand, heavy electrons in narrow band sometimes lose the metallic character because

they are more easily scattered by impurities and are also easily trapped by defects and lattice polarizations.

In practice, electron mass can be predicted by *Free-electron theory*. One formula related to the effective mass in the theory is conductivity, which gives

$$\sigma = ne^2\tau/m^* \tag{1.8}$$

where σ is the electrical conductivity, n is the electron density, and τ is the average carrier life time. Another approach to obtain electron effective mass is through *Drude model* shown in equation 1.9.

$$\varepsilon(\omega) = \varepsilon(\infty)\left[1 - \frac{\omega_p^2}{\omega^2 + (i\omega/\tau)}\right] \tag{1.9}$$

where ε(∞) is the high-frequency dielectric constant resulting from the polarisability of electrons other than those in conduction band, the magnitude of ε(∞) can be gained from optical measurements. ω is the angular frequency, and ω_p is the plasma frequency, given by

$$\omega_p^2 = \frac{ne^2}{\varepsilon_0\varepsilon(\infty)m^*} \tag{1.10}$$

where ε_0 is the vacuum permittivity. As a result of calculation via equations 1.9 and equation 1.10, effective mass is obtained.

1.5.2 Electrical Properties in Zinc Oxide

Tracing back the history of ZnO transport measurements, Somerville was the first who performed the resistivity measurements of cylindrical ZnO rods up to temperatures of 1200˚C in 1912.[18] A large bandgap for ZnO has the advantages associated with the higher breakdown voltages, the ability to sustain large electric fields, a lower noise generation, and the tolerable operations at high temperature or high power. The highly conducting ZnO crystals are generally associated with nonstoichiometry, also known as intrinsic doping – either oxygen vacancies or zinc interstitials. Throughout either experimental conditions during preparation or treatments after the growth have been shown to change transport properties effectively. For instance, Wagner and Schottky[25] in 1930 demonstrated that the carrier concentration and electrical conductivity strongly depended on the oxygen content of the crystals which could be changed by annealing them at different oxygen partial pressures. Fritsch[26] published temperature dependent electrical measurements on ZnO single crystal, polycrystalline powder and polycrystalline plates. The resistivity for single crystal and polycrystalline ZnO samples both increased by two orders of magnitude when annealing them at 900^{o}C under oxygen atmosphere (Figure 1.7). All samples showed typical semiconductor behaviour – conductivity enhances as temperature increases. All measurements were classified into three groups for (1) as-grown polycrystalline samples, (2) polycrystalline plates annealed in oxygen, and (3) single crystals annealed in oxygen, with activation energies of 7-17 meV (group 1), 60-80 meV (group 2), and 200-400 meV (group 3). Singe crystals with annealing treatments in oxygen exhibited the lowest conductivity and largest activation energy. Although oxygen vacancies has been regarded as the main source for conductivity in

ZnO, some researchers have argued that zinc interstitials are more probable due to the smaller radius of Zn^{2+} (74 pm) than O^{2-} (138 pm).[27]

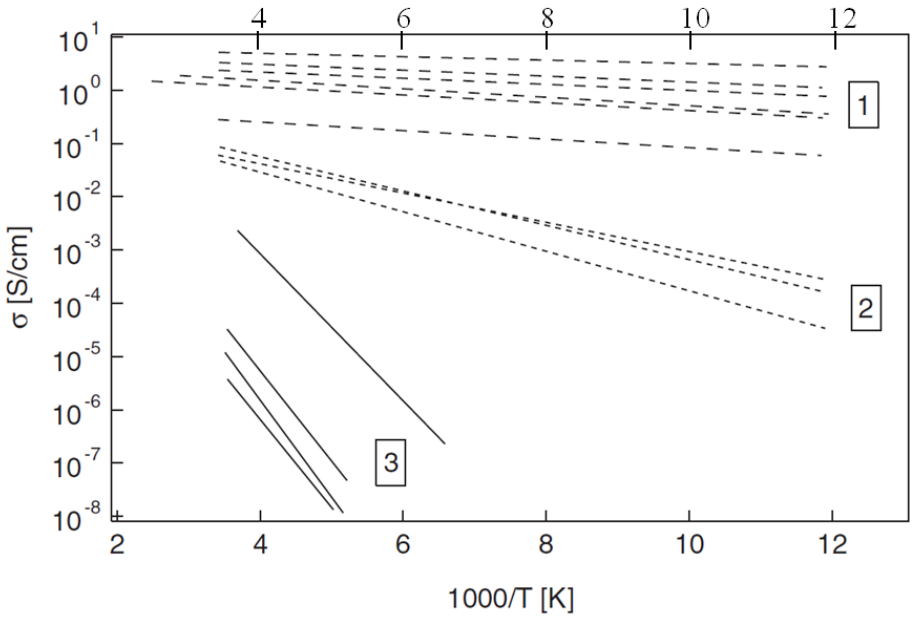

Figure 1.7 Temperature dependent conductivity measurements for (1) as-grown polycrystalline samples, (2) annealed polycrystalline plates in oxygen, and (3) annealed single crystals in oxygen.[26]

Hahn studied the electrical properties of ZnO and indicated that the excess Zn atoms gives rise to two donor levels: a "low temperature" level slightly below the conduction band (0.017-0.045 eV in the donor concentration range of 1.6×10^{16} - 9.0×10^{17} cm^{-3}) and a "high temperature" level above the valence band.[28] The possibility to give the levels are: (a) isolated and paired interstitial Zn atoms, (b) interstitial Zn atoms and Zn^{+} ions, (c) interstitial Zn atoms in the bulk of the grains and near or at the grain boundaries, (d) foreign impurities and interstitial Zn atoms.[28] Through the conductivity and Hall effect measurements over a temperature range from 54-300 K, Harrison proposed a D-centre model with oxygen vacancies.[29] He found two D-centre levels at about 0.02 eV and about 1.4 eV below the conduction band edge obtained

from the low temperature and high temperature measurements, respectively. The upper level is nearly unoccupied, whereas the lower one is completely filled. Harrison also pointed out that a very low-lying oxygen vacancy containing two electrons below the two D-centre levels and the electrons of the excess zinc are divided between the lower D-centre level and the level of oxygen vacancies.

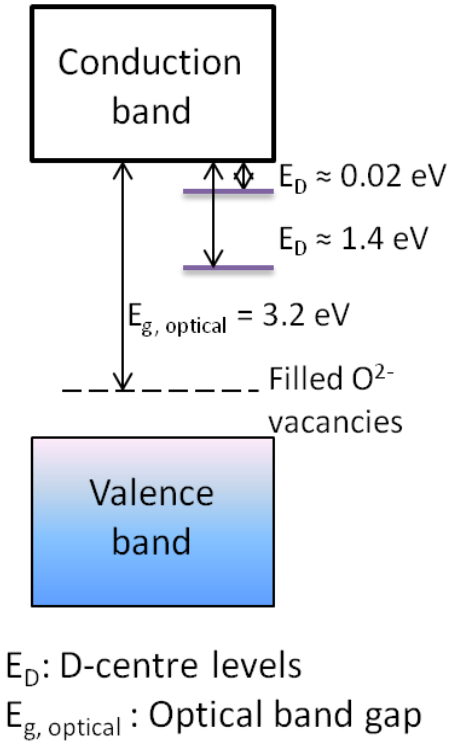

Figure 1.8 A schematic diagram for the D-centre model with excess oxygen vacancies. E_D is the ionisation energy for an electron from the D-centre levels to the conduction band.[29]

Carrier scattering in the lattice also contributes to the electrical transport properties. The major scattering mechanisms are:[14]

(1) Ionized impurity scattering: the free carriers are deflected by the defects-induced long-range Coulomb potential of the charge centres.

(2) Dislocation scattering: electron traps will dominate along dislocation line if the density of dislocations is high. The trapping centres become negatively charged

and a space-charge region is form as a result of capturing electrons. Therefore, electrons suffer scattering when travelling across the dislocation region.

(3) Acoustic-phonon scattering: The changes in the strain-induced band edges deformation potential associated with acoustic phonons, where the scattering rate increases with the wavevectors of the phonons.

(4) Piezoelectric scattering: this scattering is attributed to the electric fields that are generated by the strain associated with phonons in a crystal with no inversion symmetry.

(5) Polar longitudinal optical (LO)-phonon scattering: this is caused by the interaction of a moving charge with an electric filed induced by electric polarization associated with lattice vibration due to the ionic nature of the bonding in a polar semiconductor. For a polar and ionic semiconductor, electric polarization associated with lattice vibration creates an electric field. The interaction of the moving chargers with an electric field is called polar LO - phonon scattering.

Hall effect measurement is a useful technique to examine the carriers scattering mechanisms by measuring the transport properties at various temperatures. Figure 1.9 demonstrates a plot of mobility as a function of temperature for bulk ZnO at the electric field perpendicular to *c*-axis. The Hall mobility at 6-8 K is relative low due to the carrier freeze-out effect. Follow by increasing the temperature to the range of 10-14 K, the mobility increases because of the combination of the hopping process and mixed band conduction. Then, the mobility reaches the maximum at 2000 cm^2/Vs at 50 K, and reverses at higher temperature caused by the acoustic scattering, optic phonon via the deformation potential coupling or piezoelectric field interaction, giving values of 200-400 cm^2/Vs. Additionally, the mobility for epilayers and thin films is usually lower than bulk structure due to scattering at surface/interface

roughness or grain boundaries, valuing around or below 100 cm^2/Vs at room temperature.[30]

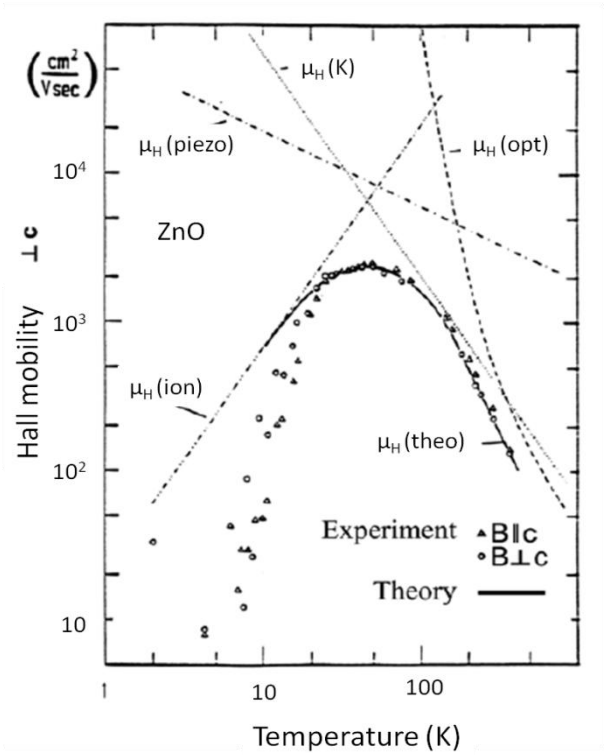

Figure 1.9 Experimental and theoretical Hall motilities as a function of temperature in bulk ZnO.[31]

Although native point defects like oxygen vacancies or zinc interstitials are generally accepted as the reasons for the conductivity in undoped ZnO, another argument has been claimed that the conductivity results from hydrogen acting as shallow donor.[32, 33] Hydrogen can diffuse into the lattice easily and forms a multi-centre bond with atoms, such as H-Si-H in silicon. In compound semiconductors, hydrogen bonds to the anions in a p-type semiconductor and to cations in a n-type semiconductor.[34] The interstitial hydrogen that bonds to oxygen in the ZnO acts as a shallow donor as evidenced in electron paramagnetic resonance (EPR) and density functional calculations.[35-37] Nevertheless, the interstitial hydrogen is not stable and

easy to diffuse out of the lattice, which cannot explain why the conductivity at relative high temperature is still stable for ZnO materials.

Janotti and Walle proposed that the conductivity in ZnO is due to hydrogen substitution.[32, 33] When one oxygen atom is removed from the lattice, four "dangling bonds" around Zn atoms will form. As shown in Figure 1.10, the dangling bonds form a symmetric electronic level (a_1) with a paired off of electrons in the bandgap of ZnO. Providing that a hydrogen atom lies at the centre of vacancy, a bonding state (H_0) will be generated in the deep valence band; meanwhile an antibonding state will be produced in the conduction band of ZnO. Two of the three electrons (a_1 and H 1s) occupy H_0 and the rest one fills the highest unoccupied state near the conduction band. A transferable electron to the conduction band minimum (CBM) at room temperature is expected to response the conductivity.[33] Substitional hydrogen is more stable due to occurrence of orbital's hybridisation, which is likely to explain the stable conductivity in n-type ZnO at relative high temperature.

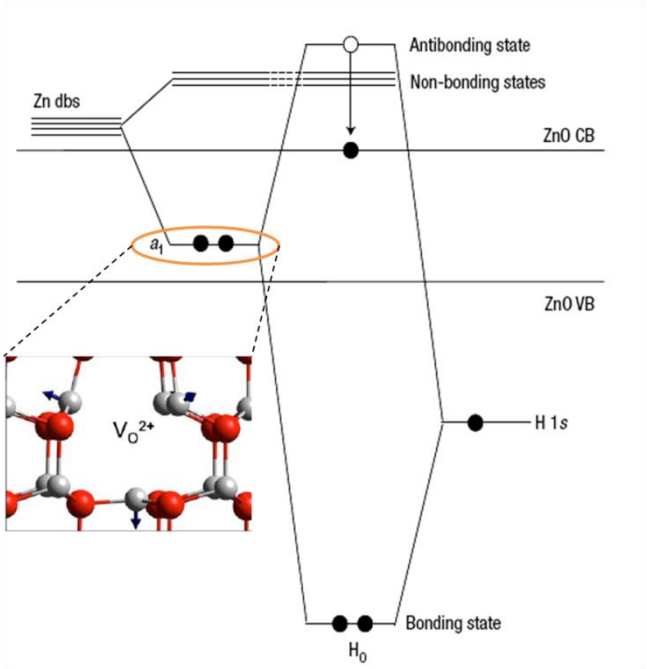

Figure 1.10 Oxygen deficiency induced two-electron a_1 state in ZnO, where Zn 4s couples with H 1*s* atomic orbital forms a new molecular orbital for H-doped ZnO. The interaction of a_1 (ZnO) and 1*s* (H) produces a bonding state (H_0) in deep valence band and an antibonding state in conduction band.[33]

1.6 Optical Properties of Zinc Oxide

The optical absorption process in a direct-gap semiconductor is the electronic transition across valence and conduction bands at the same point in Brillouin zone.[19] In a two-particle model, it describes an electron in conduction band and a hole in the valence band by absorbing photons with sufficient energy above the bandgap. The separated electron and hole lead to an attractive Coulomb potential which gives rise to a series of exciton states with the quantum number n_B =1, 2, 3,… within the gap (Figure 1.11).[38] Excitons are usually characterised by the average distance between electron and hole, that is, the excitonic Bohr radius (a_B). The exciton binding energy

(E_x^b) and excitonic Bohr radius in ZnO are 60 meV and 1.8 nm, respectively. In fact, the absorption spectrum at low temperature due to exciton states and the ionisation continuum produces a series of relatively sharp absorption bands for the exciton states with n_B =1, 2, 3,…etc. In contrast, the scattering between phonons is significant at higher temperatures and the resulting homogeneous broadening becomes serious. This broadening leads to an exponential tail of the absorption in the spectrum. With increasing temperature, the tail extends more and more to lower energy, which is known the *Urbach-Martienssen* theory.[19] Optical properties are highly related to the optical phonons and plasmons in heavily doping ZnO samples. Plasmons are the quantum of plasma oscillation. Phonons are the quantum mechanical description of a special type of vibration motion, in which a lattice uniformly oscillates at the same frequency.[18] Optical phonons studied by Raman and IR techniques can provide the information on lattice strain and the incorporations of impurity atoms. The phonon features can be used to investigate the quality of crystallinity, for example a broadening mode tells a lower crystalline quality due to increasing atomic scattering.

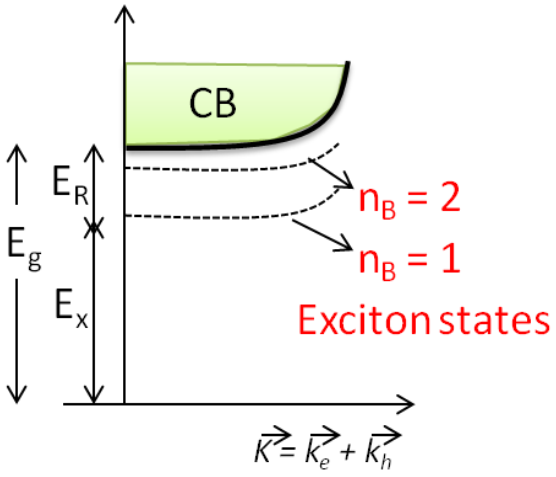

Figure 1.11 Schematic drawing for the coulomb interaction induced exciton states. E_g and E_x are the bandgap energy and exciton binding energy, respectively.[19]

ZnO has wurtzite symmetry with a point group of C_{6v} and 4 atoms in one unit cell, resulting in 12 phonon branches – 9 optical and 3 acoustic. Optical phonons for wurtzite ZnO at the Γ point of Brillouin zone can be classified as following irreducible representations: $\Gamma_{opt} = A_1 + E_1 + 2E_2 + 2B_1$, where A_1 and E_1 are polar modes, active in infrared (IR) and Raman, while E_2 is nonpolar mode and Raman active only.[14, 39] B_1 is a silent mode in Raman and IR. The vibration patterns in unit cell are shown in Figure 1.12. Furthermore, A_1 and E_1 split into two phonons, transverse optical (TO) and longitudinal optical (LO) with different frequencies due to the macroscopic electric fields associated with the LO phonons. The Raman vibration modes for ZnO will be discussed in more detail in chapter 4.2.2.

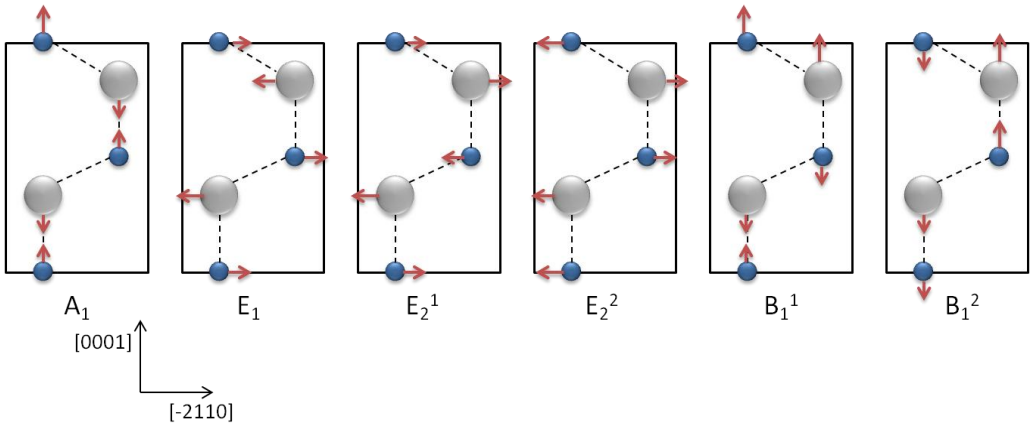

Figure 1.12 Displacement vectors for the 6 optical modes in wurtzite ZnO structure.[40] The atoms in A_1 and E_1 move parallel and perpendicular to *c*-axis modes, respectively.

1.7 Impurities Substitution in Zinc Oxide

One of great advantages for ZnO is the possibility to tune optoelectronic properties by a doping with impurity atoms to satisfy a variety of applications.

Extrinsic defects have great influence on fundamental properties. For instance, optical bowing phenomenon in the bandgap was achieved by doping ZnO with group VI elements. The column IA and column V atoms in the Periodic Table are the candidates for preparing p-type ZnO semiconductors, although the re-production of p-type ZnO still remains questionable. The transport properties of ZnO can be improved by incorporating group III or VII atoms, which are an important discovery in the transparent conducing oxides field. ZnO bandgap engineering was demonstrated by alloying with Magnesium or Cadmium oxides. Table 1.2 summarises a list of donor, acceptor and magnetic impurities doping into ZnO. In the following sections, I will review the recent developments in anionic and cationic doping ZnO.

Table 1.2 Donor, acceptor and magnetic impurities in ZnO.[14, 24, 32, 41-43]

	Impurity dopants
Donor impurity (n-type ZnO)	IIIA (Al, Ga, and In) VIA (O, S, Se and Te) VIIA (F)
Acceptor impurity (p-type ZnO)	IA (Li, Na, and K), IB (Cu, Ag and Au) VA (N, P, As and Sb)
Magnetic impurity (DMS)	Mn, Fe, Co and Ni

1.7.1 Anionic Impurities Doped Zinc Oxide

Group V (nitrogen, phosphorus, arsenic, and antimony) atoms which substitute O ions in ZnO lattice have the potentials as dopants to produce p-type ZnO. It is very challenging in preparing p-type ZnO because the solubility of impure atoms/ions in the host structure is rather low, or because the shallow acceptors may be compensated with low-energy intrinsic defects, unwanted impurity complexes or defects. Taking solubility as the example, the expected impurity concentration is 5-10% (i.e. 4×10^{21} cm^{-3}), but the measured hole concentration in p-type ZnO is much lower around 10^{16} - 10^{17} cm^{-3}. This example indicates that not all the induced impurities form shallow acceptors but some of them turn to precipitates or donor defects in host lattice.[41]

Only nitrogen is likely to produce a shallow acceptor level in ZnO and the other elements in Group V (P, As, and Sb) are all deep acceptors.[42] N has the advantages of similar atomic size to oxygen and the close energy of valence 2p states between nitrogen and oxygen. Varies types of nitrogen sources, including N_2, NO, N_2O, NH_3, and Zn_3N_2 have been used to prepare p-type ZnO with a variety of techniques.[44, 45] The N_2 molecule is too large to diffuse into ZnO lattice. Only nitrogen atoms or ions are able to diffuse into ZnO lattice. However, the preparation of p-type ZnO with N as impurity source is not reliable since the measurements of electrical transport and optical properties are not reproducible.[32, 46]

The doping mechanism for the other elements in Group V (P, As, and Sb) to synthesize p-type ZnO is more complicated. The substitution of P, As and Sb for O sites produces deep acceptors.[42] Moreover, some studies reported that P, As or Sb atoms may replace Zn and form complexes with two zinc vacancies due to a large size mismatch compared to oxygen, but the formation energies of these complexes are

very high and they unlikely to be formed.[47] In addition to previous concern, p-type ZnO formed by doping with P or As still lacks the stability of p-type conductivity or the information on crystal quality.[44, 45, 48] As a result, p-type ZnO semiconductors made of Group V atoms have to overcome the problems of solubility, stability and reproducibility.

Zinc chalcogenide (O, S, Se, Te) mixing-anion alloys exhibits systematic changes in the electronic band structure, optical properties and crystal structure due to the size and electronegativity mismatches. If the electronegativity of isovalent impurity is larger than that of the host anion (e.g. O + ZnTe → $ZnTe_{1-x}O_x$) the induced impurity levels will lie near conduction band minimum (CBM). On the other hand, if the electronegativity of isovalent impurity is smaller than that of the host atom (Te + ZnO → $ZnO_{1-x}Te_x$) the resulting impurity levels will be close to the valence band maximum (VBM). Thus, we can tune the offsets of valence or conduction bands by controlling the concentration ratio of anions. As the consequence of rehybridisation between isovalent anions, their bandgap energies as a function of anion substitution concentration display a bowing curve, which is called the bandgap bowing effect, and is given by

$$E_g = x \cdot E_{g(ZnA)} + (1-x) \cdot E_{g(ZnB)} - bx(1-x) \qquad (1.11)$$

where E_g is the alloy's bandgap, $E_{g\,(ZnA)}$ or $E_{g\,(ZnB)}$ is the bandgap energy for the zinc chalcogenide semiconductor, and *b* is the bowing coefficient. Figure 1.13 demonstrates the predicted bowing curves for oxygen doping in ZnA and CdA (A = S, Se and Te) semiconductors.[24]

Group VII elements act as shallow donor as having one more electron than oxygen. Due to the low formation energy and the ionization energy of 80 meV, fluorine is easily incorporated into ZnO. The electrical resistivity for $ZnO_{1-x}F_x$ films reaches 5×10^{-4} Ω·cm at moderate doping. The carrier mobility reaches about 45 cm^2/Vs and electron density can increase to 3×10^{20} cm^{-3}.[43, 49]

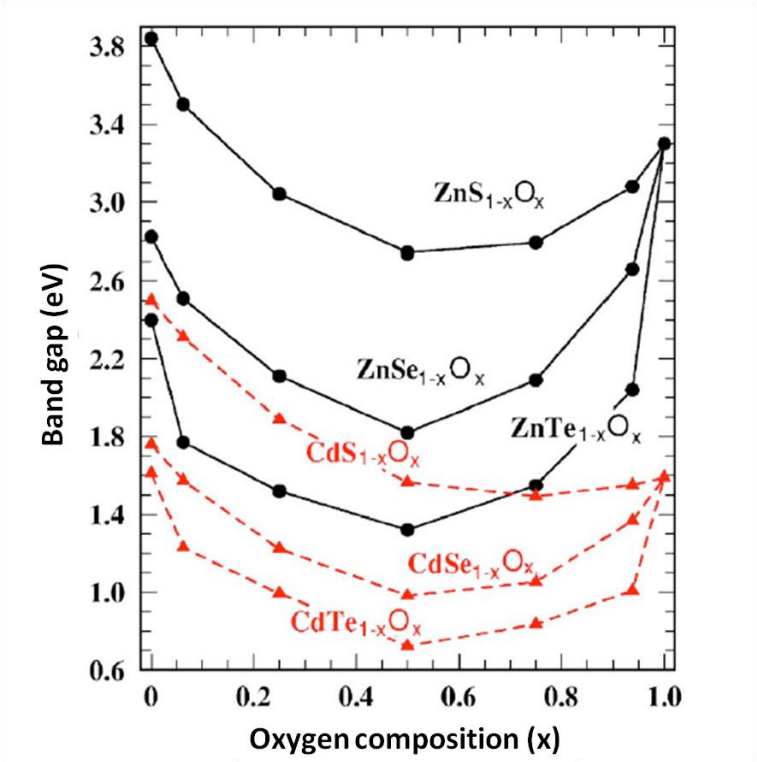

Figure 1.13 The predicted bandgaps as the functions of oxygen content (x) for isovalent oxygen doping in ZnA and CdA (A = S, Se and Te) semiconductors.[24]

1.7.2 Cationic Impurities Doped Zinc Oxide

Group IA (Li, Na, K) and IB (Cu, Ag, Au) elements are also the candidates for producing p-type ZnO. Group IA atoms are either deep acceptors or interstitial donors which compensate p-type conductivity.[42] Group IB elements are all deep acceptors used to reduce the carrier concentration in n-type ZnO by acting as compensating

centres. However, this group does not contribute to p-type conductivity.[50] The first record reporting the preparation of p-type ZnO was published back to 1950s by Lander using lithium as a dopant.[51] Lander proposed that Li can be either a donor as Li reduced ZnO to form LiO^- or an acceptor if Li replaces a zinc site in ZnO lattice. However, in his work p-type conductivity could not be measured with Li doping presumably due to the compensation in equilibrium of Li^+ and Li^-. Many papers have mentioned the p-type conductivity by incorporating Li atoms, however, similar to the problem of N-doped ZnO, the reproducibility of these results remain an issue.

Highly conducting metal-doped ZnO samples were discovered in 1950 by alloying with Al, Ga and In.[52] Al-doped ZnO (AZO) is seen as material having the potential to substitute indium tin oxide (ITO) due to the lower cost of ZnO based materials for applications of transparent conducting oxides (TCOs).[53, 54] It is known that Al, Ga and In ions are shallow donors in ZnO, enabling the production of conducting materials with carrier concentration above 10^{20} cm^{-3}.[55] A wide range of techniques have been used to fabricate Al-doped ZnO (AZO) films, including magnetron sputtering,[56] molecular beam epitaxy,[57] sol-gel,[58] and spray pyrolysis.[59, 60]

The mechanism for AZO of increasing the performance of transport properties is demonstrated in Figure 1.14. Figure 1.14 (a) displays the undoped ZnO with a large bandgap (E_{go}) crossing from VBM derived from O 2p to CBM made of metal ns orbitals. The promising electronic conduction in AZO is due to free or itinerant electrons induced by substitution of Al for Zn in the host lattice as well as carriers derived from oxygen vacancies. In terms of electronic band structure for carrier concentrations above the Mott critical density, n_c, (occurring typically at a moderate Al concentration, ca. 3-4 mol % Al, the free electrons are able to occupy the ZnO

(host) conduction band and a subsequent widening the bandgap is observed, known as the Burstein Moss (BM) effect (Figure 1.14(b)).[61] At higher doping concentration, an electronic bandgap shrinkage occurs typically attributed to many-body (many-electron) effects.[61] Therefore, in highly doping AZO films, the observed optical bandgap is expected to be the combination of BM shift and bandgap shrinkage.

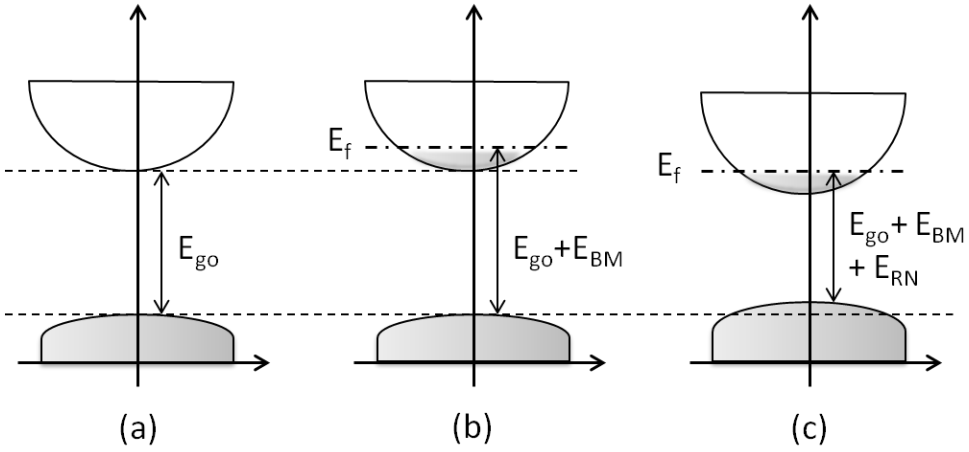

Figure 1.14 The schematic electronic structures for **(a)** oxide semiconductors with large bandgap (E_{go}) between valence band maximum (VBM) derived from O 2*p* and conduction band minimum (CBM) made of metal n*s*. **(b)** Degenerated doping induces electrons to block the bottom of conduction and therefore the Fermi level is shifted into conduction band. The increased bandgap energy is named Burstein-Moss shift energy, E_{BM}. **(c)** Bandgap renormalisation occurs at highly doping concentration due to many-body effect.[61]

Zinc oxide based dilute magnetic semiconductors (DMSs) have attracted significant attention because the spin-based magnetic phenomena have been widely applied to the basis of hard drive in information storage devices. Mn^{2+} is the major doping element involving DMS materials. The $3d^5$ orbitals of Mn^{2+} exhibits the largest magnetic moment and can diffuse into ZnO without changing the host crystallographic quality if the DMS.[14] Fe, Co and Ni-doped ZnO have been approved

to have ferromagnetic characters. However, those ferromagnetism become weaker as the hole concentrations increase.[62]

Bandgap engineering that is a very crucial step for the modern optoelectronic devices builds up carrier/quantum confinement[63], or quantum wells[64] in the heterojunction semiconductors, such as high electron mobility transistors (HEMTs) and light emitting diodes (LEDs).[32] Similar to GaN mixing with AlN and InN, alloying CdO or MgO with ZnO can accomplish the bandgap engineering (i.e. MgO enlarges the ZnO bandgap, whereas CdO narrows the ZnO bandgap). The difference between (Al, In) GaN and (Mg, Cd) ZnO based ternary alloys is that the nitrides compounds are all wurtzite structure, but MgO and CdO have rocksalt crystal structure different to wurtzite ZnO. Thus, low solid solubility of MgO or CdO in ZnO leads to phase segregation at very limited doping concentration. Figure 1.15 shows the lattice constant *a* as a function of bandgap in conjunction with impurity concentrations of Mg/Cd in ZnO and Al/In in GaN, respectively. (Mg, Cd) ZnO has a greater lattice match and a maximum barrier height of 0.09 eV in the wurtzite structure over (Al, In) GaN. Alloying In (or Al) into GaN expands (or compresses) the lattice and increase strain significantly in the lattice. It is known that the dislocation resulting from the strain can reduce the internal quantum efficiency of optoelectronic devices. In contrast to nitride families, the lattice constants for CdZnO and MgZnO both increase monotonically with increasing alloy concentration, resulting in perfectly lattice-match multi-quantum wells with high internal quantum efficiency.[15, 65] More discussions about structural and optical properties in the Cd-doped ZnO alloys will be given in chapter 4.

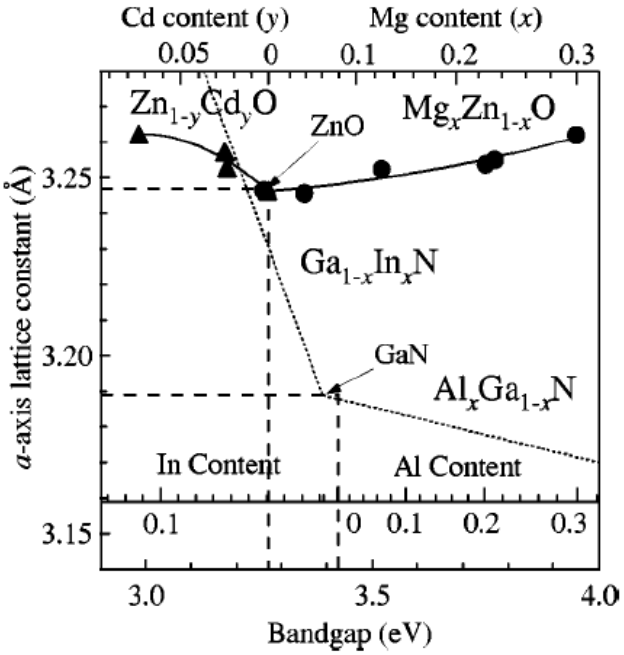

Figure 1.15 The *a* lattice constant is plotted as the function of bandgap at room temperature and impurity concentrations of Mg/Cd for ZnO (solid line) and Al/In for GaN (dash line), respectively.[15]

1.8 Photoelectrochemical Cell (PEC)

1.8.1 Recent Developments in Photoelectrochemical Cell

Solar hydrogen production through the photocatalytic splitting of water sensitised by semiconductor materials is attractive because of abundant solar resource and zero carbon emission during the whole process, which has been regarded as a sustainable, clean and renewable method to develop a low-carbon energy economy. The development of semiconducting materials has undergone a considerable attention since Honda and Fujishima reported that photocurrent was generated by utilising TiO_2 as photoanode in 1972.[1] The principle of operation of photoelectrochemical cell

(PEC) for splitting of water into hydrogen and oxygen is illustrated in Figure 1.16. An n-type semiconductor is utilised as a photoanode to harvest solar energy to generate electrons (e^-) and holes (h^+) simultaneously. Electrons are excited from valence band to conduction band in the photoanode, travel to cathode via external circuit, and reduce protons (H^+) to produce H_2. Meanwhile, holes oxidise water to form O_2 on the anode side. A good semiconductor material that can drive this reaction efficiently should satisfy the following requirements:

(1) Its bandgap must be approximately 2.0 eV, including 1.23 eV for water decomposition and ~ 0.8 eV for the sum of overpotential and Ohmic drop losses.[66]

(2) The band position of valence band should be lower (more positive) than oxygen evolution potential as well as the position of conduction band should be higher (more negative) than hydrogen evolution potential.

(3) Electrons and holes must be separated effectively (i.e. the inhibition in the recombination of electrons and holes). Lastly, electrodes must be stable and resistant to photocorrosion in aqueous electrolytes.

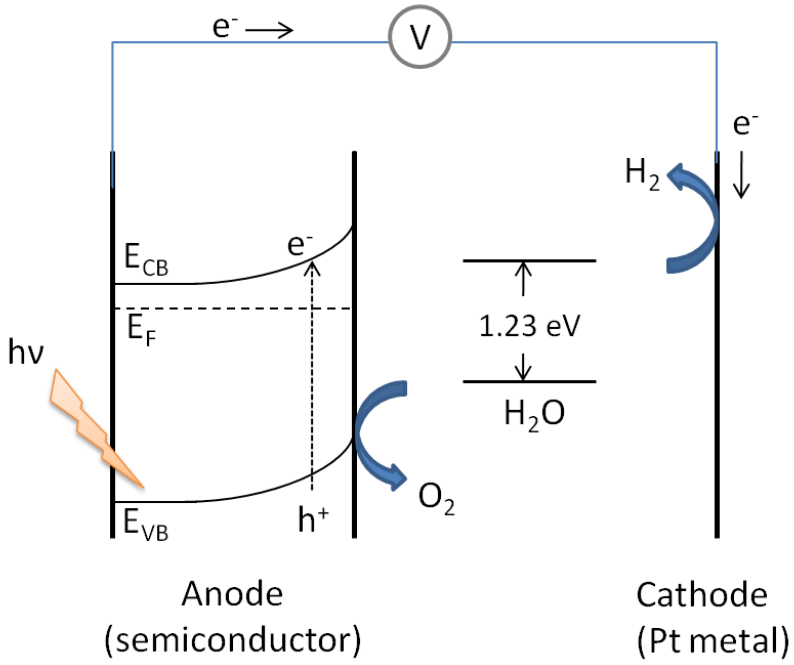

Figure 1.16 A schematic diagram showing a photoelectrochemical cell using n-type semiconductor as its anode to split water into H_2 and O_2.

Figure 1.17 displays the conduction and valence band positions related to normal hydrogen electrode (NHE) at the pH = 1 electrolyte for semiconductors. Among these semiconductors, oxide materials are relatively stable in aqueous solution. Some oxides, such as ZnO and TiO_2, the bandgaps and band positions fulfil the requirements to decompose water molecules upon illumination. However, oxide semiconductors usually exhibit a relatively low solar energy conversion efficiency due to their large bandgap (E_g > 3.0 eV). The photon intensity of UV region in solar spectrum is less than 5%. It is very crucial for oxide semiconductors to increase their ability to absorb visible light.

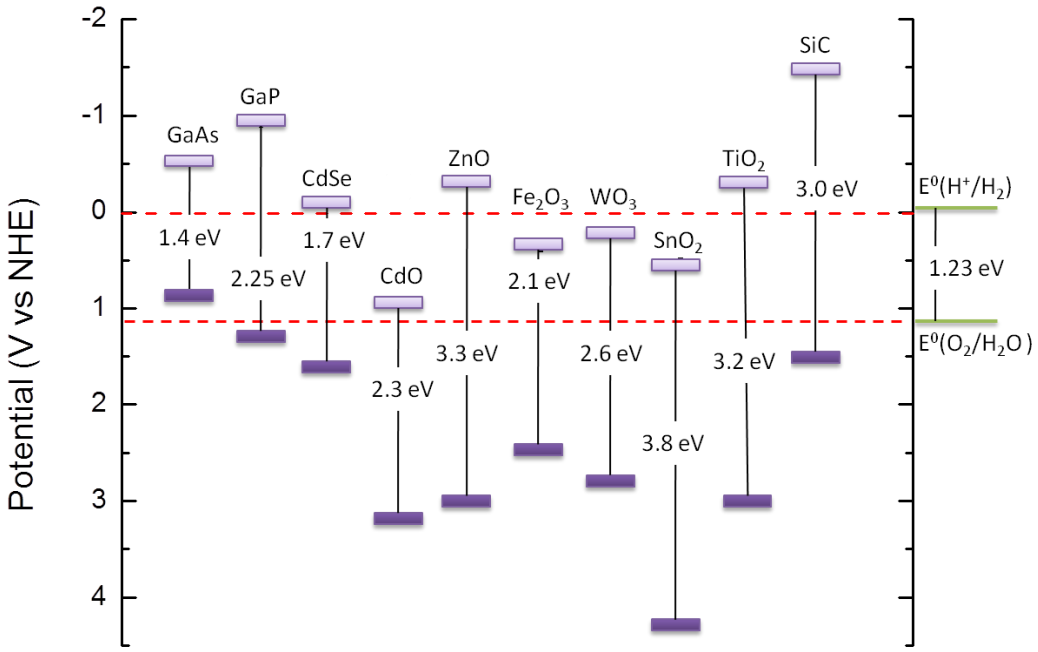

Figure 1.17 Conduction (light purple) and valence (dark purple) band positions for semiconductors in contact with aqueous solution at pH = 1.[3]

1.8.2 The Interface of N-Type Semiconductor Electrode and Electrolyte

As described in chapter 1.7.1, charge transfer occurs in the interface of electrode and electrolyte. Of primary importance in the development of photoelectrochemical water splitting is to understand the energy levels between semiconductor electrode and electrolyte.[67] An energy level diagram for an n-type semiconductor electrode and electrolyte is shown in Figure 1.18 (a). For an n-type semiconductor, the CB edge is drawn in the upper level whereas the VB is presented in the lower level. The Fermi level is the energy at which the probability of an electronic state being occupied is 0.5. With regard to electrolyte, the energy level is described as separate Gaussian distributions because solvent molecular exchange between the coordination sphere of the redox-active species and the bulk electrolyte is

a dynamic process. As the result of electrons transporting from Red to Ox species (i.e. $Ox + e^- \rightarrow Red$), the energy states of Red and Ox in the solutions are referred to the occupied and unoccupied states, respectively. The redox Fermi level (E_{red}) is again the energy at which the probability of a state being occupied by an electron is 0.5.[68]

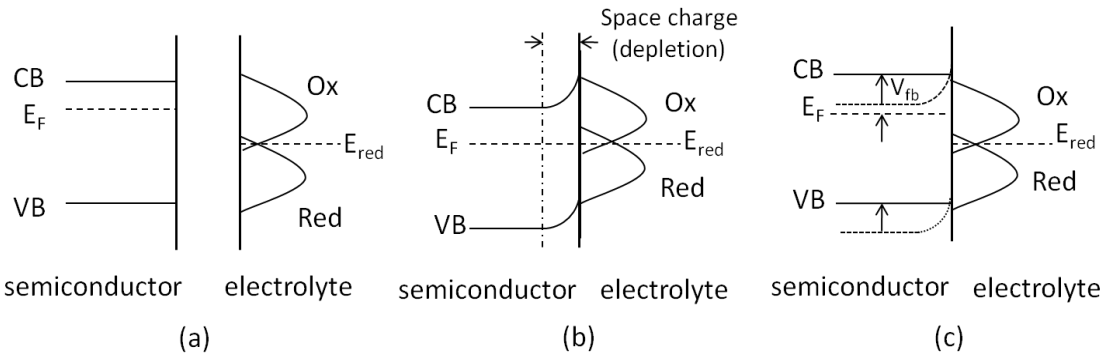

Figure 1.18 **(a)** Energetic band position for n-type semiconductor electrode and electrolyte solution before contact. **(b)** An equilibrium state presented at the interface between solid and solution phases through the charge transfer. Positive depletion region and upward band bending are then accompanied in the near surface of semiconductor by charge transfer. **(c)** The flat-band potential (V_{fb}) is the certain potential where no charge transfer and no band banding occurs.

Figure 1.18 (b) shows an electronic equilibrium between solid and solution phases when in contact, where two Fermi levels have the same electrochemical potential. In order to achieve equilibrium, electrons transfer from the semiconductor to electrolyte as the Fermi level in the n-type semiconductor is higher than that in the electrolyte. Consequently, there is a positive charge associated with the space charge region (depletion region), leading to an upward band bending in the near surface region of semiconductor. As long as the band edges are upwards, the holes travel to the interface and the electrons move to the interior of the semiconductor. Holes are high energy species that can extract electrons from the electrolyte, which explains that

the n-type semiconductor acts as a photoanode. Furthermore, in the case of metallic electrode, changing the applied potential shifts the E_F, CB and VB edges in the bulk (i.e. away from depletion region), but those band edges in the interface are not shifted. For instance, scan to negative potential will raise the Fermi level, CB and VB levels in the interior of semiconductor. Hence, the magnitude and direction of band bending vary with the applied potential. When the applied potential reaches the condition of no net charge transfer between two phases and no band bending, at which the potential is called *flatband potential*, V_{fb}, Figure 1.18 (c). The flat-band potential is a useful quantity in photoelectrochemistry because it facilitates to determine the energetic position of the valence and conduction band edges of a given semiconductor material. In aqueous solution the flatband potential of the most oxide materials shifts about 0.059 V when pH is changed by one unit.[3]

1.8.3 Solar to Chemical Conversion Efficiency

Assuming that there is no corrosion reaction at photoelectrodes and all the current generated that travels through external circuit to cathode for water splitting, the overall *solar-to-hydrogen conversion efficiency (η)* of PEC can be conducted as[69, 70]

$$\eta(\%) = \frac{j(1.23 - V_{app})}{P_{in}} \times 100\% \qquad (1.12)$$

where j is the externally measured photocurrent density (mA/cm^2), V_{app} is the applied potential, and P_{in} is the incident density in mW/cm^2. The redox potential given here by 1.23 V is based on the Gibbs free energy of formation for 1 mole of water at room temperature (H_2O = 237.14 KJ/mol).[71] The determination of P_{in} requires knowledge of

the air mass coefficient (AM) which defines the direct optical path length through the Earth's atmosphere, expressed as a ratio relative to the path length vertically upward (i.e. at the zenith).[72] For AM 1.5, which alters simulator's output to match terrestrial solar spectrum occurring when the sun's position vector has rotated 48.3 degrees away from its perpendicular position, P_{in} is equal 970 W/cm^2.[71] To measure the true solar to hydrogen production efficiency (i.e. illuminated by sunlight), photocurrent density can be recorded under a short-circuit condition of V_{app} = 0 V.

Another common expression for PEC efficiency is *incident photon-to-current-conversion efficiency (IPCE)*, which is usually used to determine the efficiency at the specific wavelength. The equation is given by

$$IPCE(\%) = \frac{j(1.23 - V_{app})}{P_{in}} \times 100\% \qquad (1.13)$$

where j is the externally measured photocurrent density (mA/cm^2), λ is the specific wavelength of incident light, and P_{in} is the incident light density in mW/cm^2.

1.9 The Aims of This Thesis

To seek an ideal material satisfying the demands of photocatalytic water splitting is very challenging. Metal oxide semiconductors have the potentials to be used as the catalysts to decompose water into hydrogen and oxygen by utilising solar energy. Unfortunately, owing to the wide bandgap, electron-hole recombination or insatiability, oxide semiconductors cannot convert solar light into electricity or solar hydrogen in an efficient way.

Zinc oxide (ZnO) is the one of promising metal oxide materials for the use in photoelectrochemical cell. The aims of this thesis are as following: (1) Increasing the light harvesting and enhancing the solar energy conversion efficiency by reducing the ZnO electronic bandgap. (2) Achieving the bandgap narrowing and improving the electronic transport properties by doping impurities into ZnO. (3) Performing PEC measurements to test the photon conversion efficiency of the prepared undoped ZnO and impurities-doped ZnO photoanodes. (4) Characterising the physical and chemical properties, such as electronic band structure, optical properties, crystal structure, surface character, and electronic transport properties for the prepared impurities-doped zinc oxide thin films and powders.

1.10 References

1. A. Fujishima and K. Honda, Nature **238**, 37 (1972).
2. F. E. Osterloh, Chemistry of Materials **20**, 35 (2008).
3. M. Gratzel, Nature **414**, 338 (2001).
4. X. B. Chen, S. H. Shen, L. J. Guo and S. S. Mao, Chemical Reviews **110**, 6503 (2010).
5. F. Le Formal, M. Gratzel and K. Sivula, Advanced Functional Materials **20**, 1099 (2010).
6. C. Klingshirn, Physica Status Solidi B-Basic Solid State Physics **244**, 3027 (2007).
7. Z. L. Wang, G. A. Zhu, R. S. Yang and S. H. Wang, Nano Letters **10**, 3151 (2010).
8. S. Xu, Y. Qin, C. Xu, Y. G. Wei, R. S. Yang and Z. L. Wang, Nature Nanotechnology **5**, 366 (2010).
9. D. C. Look, D. C. Reynolds, J. R. Sizelove, R. L. Jones, C. W. Litton, G. Cantwell and W. C. Harsch, Solid State Communications **105**, 399 (1998).
10. J. Nowotny, M. K. Nowotny and T. Bak, Journal of Physical Chemistry B **110**, 16270 (2006).
11. P. Erhart, A. Klein, R. G. Egdell and K. Albe, Physical Review B **75** (2007).
12. C. McGuinness, C. B. Stagarescu, P. J. Ryan, J. E. Downes, D. Fu, K. E. Smith and R. G. Egdell, Physical Review B **68**, 165104 (2003).
13. S. J. Pearton, D. P. Norton, K. Ip, Y. W. Heo and T. Steiner, Journal of Vacuum Science & Technology B **22**, 932 (2004).
14. U. Ozgur, Y. I. Alivov, C. Liu, A. Teke, M. A. Reshchikov, S. Dogan, V. Avrutin, S. J. Cho and H. Morkoc, Journal of Applied Physics **98**, 41301 (2005).
15. T. Makino, Y. Segawa, M. Kawasaki, A. Ohtomo, R. Shiroki, K. Tamura, T. Yasuda and H. Koinuma, Applied Physics Letters **78**, 1237 (2001).
16. S. Sadofev, S. Blumstengel, J. Cui, J. Puls, S. Rogaschewski, P. Schafer and F. Henneberger, Applied Physics Letters **89**, 201907 (2006).
17. W. L. Bragg, Philosophical Magazine **39**, 647 (1920).
18. K. Ellmer, A. Klein and B. Rech, edited by R. Hull, J. Parisi, R. Osgood and H. Warlimont (Springer, New York, 2008), pp. 443.
19. C. Klingshirn, Chemphyschem **8**, 782 (2007).
20. P. A. Cox, (Oxford press, Oxford, 1995).
21. J. J. Hopfield and D. G. Thomas, Physical Review Letters **15**, 22 (1965).
22. S. H. Wei and A. Zunger, Physical Review B **37**, 8958 (1988).
23. W. A. Harrison, (Daver Publications, New York, 1989).

24. C. Y. Moon, S. H. Wei, Y. Z. Zhu and G. D. Chen, Physical Review B **74**, 233202 (2006).
25. C. Wagner and W. Schottky, Z. Phys. Chem. B **11**, 163 (1930).
26. O. Fritsch, Ann. Phys. **5**, 375 (1935).
27. H. H. Von Baumbach and C. Wagner, Z. Phys. Chem. B **22**, 199 (1933).
28. E. E. Hahn, Journal of Applied Physics **22**, 855 (1951).
29. S. E. Harrison, Physical Review **93**, 52 (1954).
30. K. Ellmer, Journal of Physics D-Applied Physics **34**, 3097 (2001).
31. P. Wagner and R. Helbig, J. Phys. Chem. Solids **35**, 327 (1974).
32. A. Janotti and C. G. Van de Walle, Reports on Progress in Physics **72**, 126501 (2009).
33. A. Janotti and C. G. Van de Walle, Nature Materials **6**, 44 (2007).
34. C. G. Van de Walle and J. Neugebauer, Nature **423**, 626 (2003).
35. D. M. Hofmann, A. Hofstaetter, F. Leiter, H. J. Zhou, F. Henecker, B. K. Meyer, S. B. Orlinskii, J. Schmidt and P. G. Baranov, Physical Review Letters **88**, 45504 (2002).
36. S. F. J. Cox, E. A. Davis, S. P. Cottrell, P. J. C. King, J. S. Lord, J. M. Gil, H. V. Alberto, R. C. Vilao, J. P. Duarte, N. A. de Campos, A. Weidinger, R. L. Lichti and S. J. C. Irvine, Physical Review Letters **86**, 2601 (2001).
37. C. G. Van de Walle, Physical Review Letters **85**, 1012 (2000).
38. C. Klingshirn, J. Fallert, H. Zhou, J. Sartor, C. Thiele, F. Maier-Flaig, D. Schneider and H. Kalt, Physica Status Solidi B-Basic Solid State Physics **247**, 1424 (2010).
39. T. C. Damen, S. P. S. Porto and B. Tell, Physical Review **142**, 570 (1966).
40. E. Ruiz, S. Alvarez and P. Alemany, Physical Review B **49**, 7115 (1994).
41. B. Q. Cao, M. Lorenz, M. Brandt, H. von Wenckstern, J. Lenzner, G. Biehne and M. Grundmann, Physica Status Solidi-Rapid Research Letters **2**, 37 (2008).
42. C. H. Park, S. B. Zhang and S. H. Wei, Physical Review B **66** (2002).
43. S. B. Zhang, S. H. Wei and A. Zunger, Physical Review B **63** (2001).
44. K. K. Kim, H. S. Kim, D. K. Hwang, J. H. Lim and S. J. Park, Applied Physics Letters **83**, 63 (2003).
45. Y. R. Ryu, T. S. Lee and H. W. White, Applied Physics Letters **83**, 87 (2003).
46. E.-C. Lee, Y. S. Kim, Y. G. Jin and K. J. Chang, Physical Review B **64**, 085120 (2001).
47. S. Limpijumnong, S. B. Zhang, S. H. Wei and C. H. Park, Physical Review Letters **92** (2004).
48. T. Aoki, Y. Hatanaka and D. C. Look, Applied Physics Letters **76**, 3257 (2000).

49. H. F. Liang and R. G. Gordon, Journal of Materials Science **42**, 6388 (2007).
50. G. Muller, Physica Status Solidi B-Basic Research **76**, 525 (1976).
51. J. J. Lander, Journal of Physics and Chemistry of Solids **15**, 324 (1960).
52. K. Hauffe and K. Block, Z. Phys. Chem. B **196**, 438 (1950).
53. X. Jiang, F. L. Wong, M. K. Fung and S. T. Lee, Applied Physics Letters **83**, 1875 (2003).
54. S. H. Lee, S. H. Han, H. S. Jung, H. Shin, J. Lee, J. H. Noh, S. Lee, I. S. Cho, J. K. Lee, J. Kim and H. Shin, Journal of Physical Chemistry C **114**, 7185 (2010).
55. C. Klingshirn, Physica Status Solidi B-Basic Solid State Physics **244**, 3027 (2007).
56. B. C. Mohanty, Y. H. Jo, D. H. Yeon, I. J. Choi and Y. S. Cho, Applied Physics Letters **95**, 62103 (2009).
57. T. Makino, K. Tamura, C. H. Chia, Y. Segawa, M. Kawasaki, A. Ohtomo and H. Koinuma, Physica Status Solidi B-Basic Solid State Physics **229**, 853 (2002).
58. S. Mridha and D. Basak, Journal of Physics D-Applied Physics **40**, 6902 (2007).
59. M. Gabas, S. Gota, J. R. Ramos-Barrado, M. Sanchez, N. T. Barrett, J. Avila and M. Sacchi, Applied Physics Letters **86**, 42104 (2005).
60. Y. Caglar, S. Ilican, M. Caglar and F. Yakuphanoglu, Spectrochimica Acta Part a-Molecular and Biomolecular Spectroscopy **67**, 1113 (2007).
61. B. E. Sernelius, K. F. Berggren, Z. C. Jin, I. Hamberg and C. G. Granqvist, Physical Review B **37**, 10244 (1988).
62. K. Sato and H. Katayama-Yoshida, Semiconductor Science and Technology **17**, 367 (2002).
63. B. K. Meyer, A. Polity, B. Farangis, Y. He, D. Hasselkamp, T. Kramer and C. Wang, Applied Physics Letters **85**, 4929 (2004).
64. M. Brandt, H. von Wenckstern, M. Stolzel, H. Hochmuth, M. Lorenz and M. Grundmann, Semiconductor Science and Technology **26** (2011).
65. H. von Wenckstern, H. Schmidt, M. Brandt, A. Lajn, R. Pickenhain, M. Lorenz, M. Grundmann, D. M. Hofmann, A. Polity, B. K. Meyer, H. Saal, M. Binnewies, A. Borger, K. D. Becker, V. A. Tikhomirov and K. Jug, Progress in Solid State Chemistry **37**, 153 (2009).
66. B. D. Alexander, P. J. Kulesza, L. Rutkowska, R. Solarska and J. Augustynski, Journal of Materials Chemistry **18**, 2298 (2008).
67. K. Gelderman, L. Lee and S. W. Donne, Journal of Chemical Education **84**, 685 (2007).
68. H. Gerischer, Electrochimica Acta **35**, 1677 (1990).

69. M. G. Walter, E. L. Warren, J. R. McKone, S. W. Boettcher, Q. X. Mi, E. A. Santori and N. S. Lewis, Chemical Reviews **110**, 6446 (2010).
70. S. U. M. Khan, M. Al-Shahry and W. B. Ingler, Science **297**, 2243 (2002).
71. T. Bak, J. Nowotny, M. Rekas and C. C. Sorrell, International Journal of Hydrogen Energy **27**, 991 (2002).
72. F. Kasten and A. T. Young, Applied Optics **28**, 4735 (1989).

CHAPTER 2

EXPERIMENTAL TECHNIQUES

2.1 Atomic X-Ray Spectrometry

2.1.1 White Radiation and Characteristic Radiation

X-rays are produced by the deceleration of high energy electrons or by the electronic transitions of electrons in the inner orbital of atoms. The wavelength of X-rays are relatively short, in range from around 0.1-100Å, however, the commercial X-ray sources are generally confined to the region of 0.1Å to 25Å. X-ray sources, such as ultraviolet and visible emitters, can produce both continuum and line spectra. Continuum radiation is also called *white radiation* or *Bremsstrahlung*.[1] The continue radiation from an electron beam source on the cathode results from collisions with the anode materials, usually tungsten, molybdenum or copper.

X-ray line spectra are attributed to electronic transitions of involving inner atomic orbitals. When the energy of the accelerated electrons is higher than a certain threshold value, a vacancy will be created by removing the electrons from the specific orbital. The characteristic radiation is then formed as electrons from outer orbitals undergo transitions to the vacant inner orbitals.[2] As shown in Figure 2.1, the K series is the transition from outer orbital to the orbital nearest to the nucleus of an atom. The L series of lines results when an electron is lost from the second principal quantum level.[1]

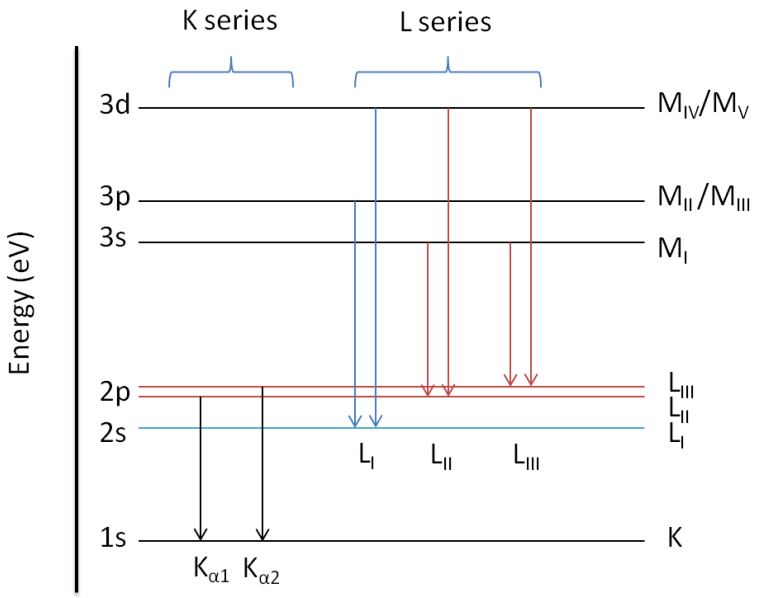

Figure 2.1 A schematic diagram represents a partial energy level diagram of common transitions producing X-rays.[1]

2.1.2 X-ray Diffraction (XRD)

X-ray diffraction (XRD) is a rapid and non-destructive technique used for analyzing phase identification of a crystalline material. It reveals the information on crystallographic structure and chemical composition of materials. When a monochromatic X-ray beam penetrates the ordered environment of a crystal at a certain angle, both constructive and destructive interferences occur among the scattered rays since the distance between the scattering centres are of the same order of magnitude as the wavelength of the radiation, resulting in diffraction.[3]

2.1.2.1 Bragg's Law

In 1912, W. L. Bragg found the diffraction of X-ray by crystals as shown in Figure 2.2.[4] When an X-ray beam is projected onto a material at an angle (θ), the difference in the

ray travelling distance between the top layer (i.e. stoke on the atom O) and the first inner layer (i.e. stroke on the atom P) in the crystal lattice is shown as AP + PC. Diffraction of radiation occurs when the difference in travelling distance is equal to an integer number *n* of wavelength, which can be expressed as

$$AP + PC = n\lambda \tag{2.1}$$

AP is also equal to d × sinθ, where d is the interplane distance. Therefore, equation 2.1 becomes

$$2d\sin\theta = n\lambda \tag{2.2}$$

Equation 2.2 is called the *Bragg's equation*.[3] Note, the constructive interference happens only if the angle of incident beam satisfies the condition of Bragg's law. At all other angle, destructive interference occurs.

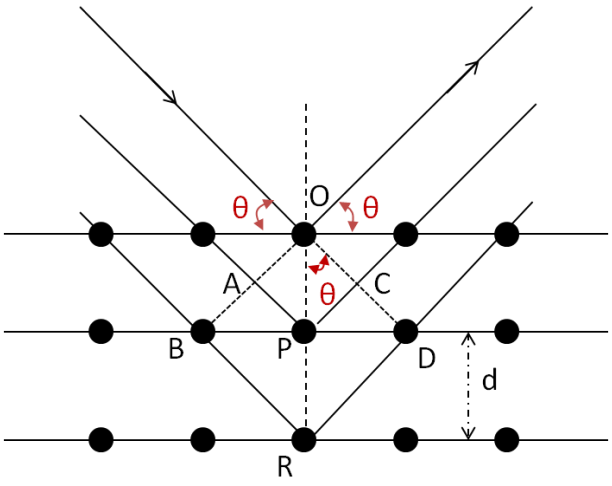

Figure 2.2 Diffraction of X-rays by a crystal. Incident radiation that comes from the left is reflected to the right.[4]

2.1.2.2 Powder Diffraction

Powder X-ray diffraction (XRD) is perhaps the most widely used technique for characterising materials. X-ray powder methods are based on the fact that each crystalline substance has unique diffraction pattern. As a result, if an exact match is observed between a sample and a known standard in the diffraction database, the sample can be assumed the same substance as the standard. For powder samples, the crystalline domains are randomly oriented. The identification of a material from its powder diffraction pattern is based upon the position of diffraction peaks (2θ) and intensity. Each diffraction angle is determined by the spacing between a particular set of planes. The spacing can be further derived from the known wavelength, diffraction angle and the Bragg's equation. Line intensity and line shape are affected by the number of oriented planes and the domain size. Domain size can be presented by the Scherrer equation as shown,[5]

$$d = \frac{K\lambda}{\beta \cos\theta} \tag{2.3}$$

where d is the domain size, K is a constant ($0.89 < K < 1$), λ is the wavelength of incident X-ray, β is the width of the peak at half maximum intensity of a specific phase, and θ is the diffraction angle. The determination for particle size is more accurate when the average particle size is below 20 nm because of the peak broadening effect.[5] Note that, the influence of particle size on the line shape will not be significant when the size exceeds 0.1 μm.[5]

The diffraction pattern of a powder sample is performed in automatic diffractometers using scintillation or CCD detectors to record the angle and the intensity of the reflected radiations. Either a transmission or a reflection method is used to produce diffraction data as shown in Figure 2.3.[4] The resulting diffraction patterns in these two methods are exactly the same as every possible crystalline orientation is represented equally in powder sample.

2.1.2.3 Thin Film Diffraction

The principle of thin film diffraction is not different to the powder diffraction. However, in terms of the unique performances of heterolayer structures in thin film, various diffraction measurements have been developed, including:[6] (1) Rocking curve measurements for the examination of the quality of thin film; (2) Superlattice measurements in multilayered heteroepitaxial structures; film thickness and its quality can be deduced from the data; (3) Precision lattice constants determination can provide the information on the lattice mismatch between the film and the substrate; (4) Glancing incidence X-ray reflectivity measurements reveal the thickness, roughness and density of a film; (5) Texture measurements are applied to determine the orientation distribution of crystalline grains in a film and thus whether it is a single crystal or a polycrystalline film. Application of synchrotron radiation as the X-rays source to thin film diffraction has become important as the consequences of the requirement of high angular resolution or hard X-ray source.

2.1.2.4 Instrumentation

X-ray diffraction measurements of powder and thin film samples were carried out with a PANalytical's X'Pert PRO Diffractometer as shown in Figure 2.4. The machine is equipped with an X-ray generator, Johansson monochromator containing cut Ge [111] crystal, and an X'Celerator detector assembled in a standard Bragg-Brentano geometry. The X-ray source is monochromated to transmit the Cu $K_{\alpha 1}$ radiation (λ = 0.15406 nm) only. The divergence slit is automatically adjusted to maintain a fixed sample irradiation area throughout the scan. Measurements were performed with a fixed X-ray source at a voltage of 45 kV and a current of 40 mA.

The ground powder samples were loaded onto a sample holder. The sample holder was placed on a spinner stage that was rotated at 1 rev/sec during the measurements. Thin film samples were placed on the same sample holder to avoid misplacement errors. Diffraction data were recorded with 2θ ranging from 20° to 75° at a scan speed of 0.0076°/sec.

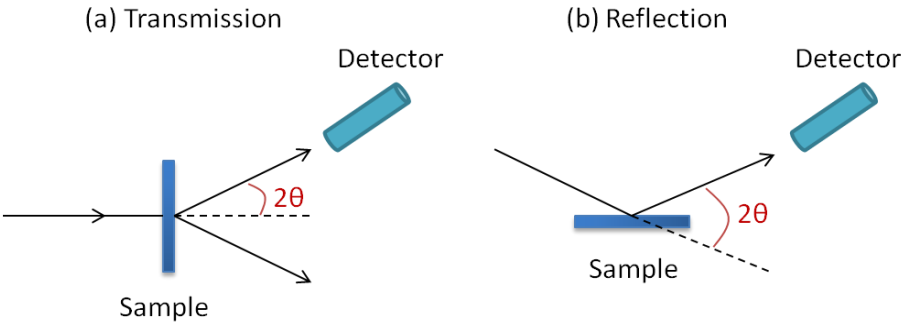

Figure 2.3 Schematic diagrams of (a) transmission mode and (b) reflection mode for powder X-ray diffraction.[4]

Figure 2.4 Snapshot for PANalytical's X'Pert PRO Diffractometer.

2.1.3 X-ray Photoelectron Spectroscopy (XPS)

Spectroscopy surface methods, distinguished by the type of primary beam (X-ray photons, UV photons, ions, electrons, and phonons), provide both qualitative and quantitative chemical information about the surface layer of a solid varying from a few angstrom units to a few tens of angstrom units. The most common type, which is based upon irradiation of sample surface with monochromatic X-rays, is called *X-ray photoelectron spectroscopy (XPS)* or *electron spectroscopy for chemical analysis (ESCA)*. XPS provides not only the information about atomic composition of a sample but also the information about oxidation state of the compounds being examined.

2.1.3.1 The Photoemission Process

The spectrometric measurements consist of the determination of the the incident X-ray power as a function of the energy of outgoing electrons. Figure 2.5 shows the schematic representation of the XPS physical process. When an atom or a molecule is irradiated with a monochromatic X-ray beam of known energy hν, an electron is removed from the inner orbital (for example K orbital in Figure 2.5) with a kinetic energy E_k that is measured with an electron spectrometer. Thus, the binding energy (E_b) of an electron in the specific orbital can be derived from the energy of incident beam and the kinetic energy of photoelectron expressed as

$$E_k = h\nu - E_b \tag{2.4}$$

The binding energy of electron is characteristic of the atom and orbital from which the electron was emitted.

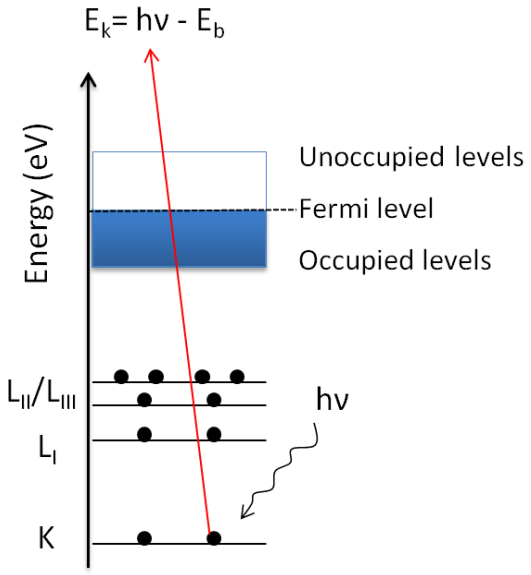

Figure 2.5 Schematic illustration of XPS physical process. Core level (K or L shell) electrons are solid circle. The Fermi level is located between the occupied levels (blue solid block) and unoccupied levels (hollow block).

2.1.3.2 Spin-Orbital Coupling

Spin-orbital coupling is defined as the coupling between the electron's spin and orbital angular momentum, which is seen as a splitting of p through f orbitals into two peaks.[3] The s orbitals do not split since they have no orbital angular momentum (l = 0). *j-j coupling* and *L-S coupling* (also called *Russell-Saunders coupling*) are the two main factors involving peak splitting. Within the j-j coupling scheme applicable to core electrons, the magnitude of total angular momentum for a given electron is the vector sum of its spin and orbital momenta, which can be expressed as $\hat{j} = \hat{l} + \hat{s}$. Since s orbitals have no angular momentum (l = 0), the only permitted value is j = 1/2 (i.e. no splitting peak in a XPS spectrum). For p orbitals with l = 1, j is either 3/2 or 1/2, showing two splitting peaks in a XPS scan. L-S coupling is arisen from the interaction between the total spin angular momentum (S) and the total orbital

angular momentum (L), where S is the sum of each electron spin (s_i) interacts to each other as well as the sum of orbital angular momentum (l_i) forms the total orbital angular momentum (L).

The magnitude of the coupling between electron spins and orbital angular momentum determines the width of the spin-orbital splitting. The coupling is proportional to $<1/r^3>$, where r is the radius of the orbital. Empirically, the level of coupling decreases with increasing principal quantum number or the angular momentum quantum number (i.e. 4p > 5p or 4p > 4f). Coupling increases with increasing atomic number due to an increase in nuclear charge, for example, Au (3.7 eV) > Pt (3.4 eV) > Ir (3.0 eV).

2.1.3.3 Inelastic Mean Free Path

Photoelectrons travelling within the solid may suffer inelastic scattering or other interactions and lose some of their energy before escaping from the solid. The energy loss leads to plasmon excitation, electron-hole pair formation or vibration excitation. The term of *inelastic mean free path, IMPF* (λ) is used to describe the probability that the photoelectron travels a distance (d) through the solid without being scattered,[1] which is given by

$$P(d) = \frac{I(d)}{I(0)} = \exp(-d/\lambda) \qquad (2.5)$$

where P(d) and I(d) are, respectively, the probability and the intensity of damped electrons as functions of travelling distance d within the solid, I(0) is the intensity of the primary electron beam. The inelastic mean free path increases sharply as the kinetic energy of the electron decreases because the quantum-mechanical wavelength of the electron increases, leading to the reduction of the inelastic scattering efficiency. Figure 2.6 demonstrates the variation of

the inelastic mean free path with the initial electron energy displayed as a universal curve for most metals.[7] The inelastic mean free path in metals is typically 20Å if the kinetic energy of the incident beam is between 10 eV and 1400 eV. Therefore, the XPS using Al K_α (1486 eV) or Mg K_α (1253 eV) as the X-ray source leads to photoelectron emission with the maximum kinetic energy of around 1480 eV or 1250 eV, respectively.

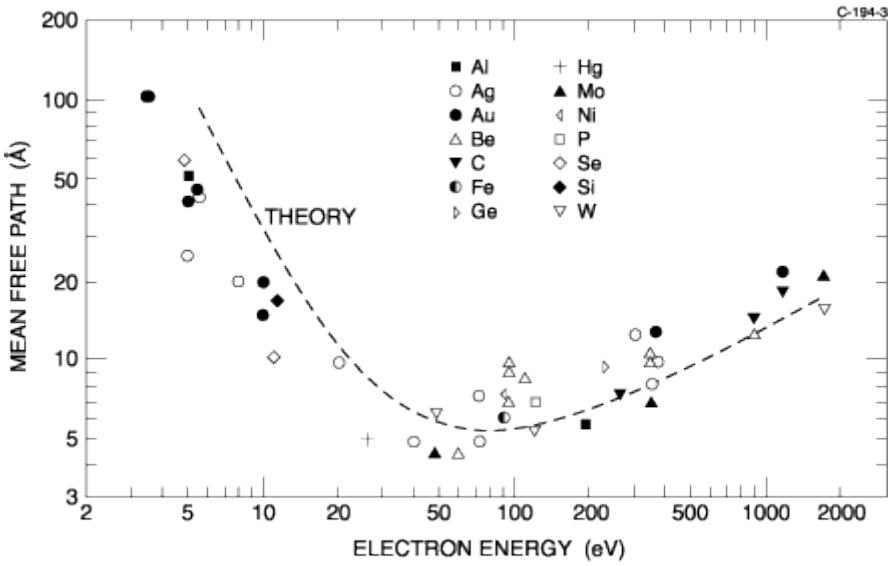

Figure 2.6 Variation of electron mean free path as a function of electron kinetic energy for metals.[7]

2.1.3.4 The Formation of Spectral Background

In theory, each peak in a XPS spectrum should be a sharp and straight line and the baseline over the scanning energy should be flat as shown at the topmost diagram of Figure 2.7. However, in addition to the limitation of the instrument, *finite lifetime broadening* and *inelastic collisions* account for a significant amount of the overall shape of a survey scan in the XPS spectrum, as seen in Figure 2.7. Finite lifetime is defined as the time needed for the excited electrons in XPS process relax back to their ground state. According to the Heisenberg's uncertainty principle,[3]

$$\Delta E_t \geq \frac{\hbar}{2\Delta t_l} \tag{2.6}$$

where ΔE_t is the expected broadening of the emission feature due to the lifetime uncertainty of Δt_l. Equation 2.6 demonstrates that a shorter life time leads to a wider spread of energy. Thus, the lifetimes for holes on the core and valence levels are of the order of 10^{-14} to 10^{-16} seconds, giving rise to lifetime broadening of the order of 0.05 eV to 5 eV at most. Generally speaking, lifetime broadening will be greater for photoemission emitted from the inner shell than that from the outer shell since the core hole has shorter relaxation time..

A photoelectron within the solid travelling toward surface will interact with surrounding atoms, leading to the loss of its energy in terms of scattering or plasmon oscillation. Although these electrons can escape from the solid and be detected, their kinetic energy is lower than at start, and will contribute to an increase in the background on the higher energy side of main photoemission peak and are not counted in part of the primary photoemission process. In the experimental aspect, electrons scatter with a few inelastic collisions will appear above a primary photoemission peak extending over a range as much as 500 eV in binding energy, depending on the materials and the initial energy of the photoelectron. Electrons encountering multiple inelastic scatterings will exhibit in higher binding energy side of background in an XPS spectrum, beginning to increase significantly as binding energy approaches within 100 eV of the source energy (hν).

The area of a photoemission peak is determined by subtracting an appropriate background and integrating under the resultant curve. The choice of background can have an impact on the resulting parameters. Three types of backgrounds are *Shirley*, *linear*, and *Tougaard*. The Shirley background is a convolution of the overlapping peak intensity and the inelastic background. The *Shirley background* is widely used for background subtraction as it

is most suitable for resolving the background intensity contributed from the inelastic scattering. The Shirley background is more accurate for the high binding energy area because the scattering intensity has a greater proportion at higher binding energy region. The Shirley background is not suitable for the peaks that have wide binding energy range or have increasing or decreasing intensity on either side of main peak, because the resulting complex background shape (Shirley) is a convolution of the overlapping peak intensity and the inelastic background.

The linear background is a straight continuous line removing the constant offset throughout the spectrum. This approximation is the most appropriate for the background intensities that are nearly identical on the both side of a photoemission peak.

The Taugaard background is derived from the first principle consideration of the intensity of the inelastically scattered electrons as a function of decreasing kinetic energy away from the primary photoelectron peak.

2.1.3.5 Line Shape and Position – Initial State and Final State Effects

In high resolution XPS spectra, the positions of peaks indentify the chemical elements, and the peak areas are proportional to the densities of states as well as used to quantify the elemental composition. This section will introduce the factors that have influence on the apparent binding energy of the photoelectrons before and after photoemission.

Initial state effect describes the influence on the binding energy of orbitals before the photoemission process takes place.[3] Three types of initial state effects are involved in the process, namely *chemical state shift*, *inhomogeneous matrix broadening*, and *charging shift*.

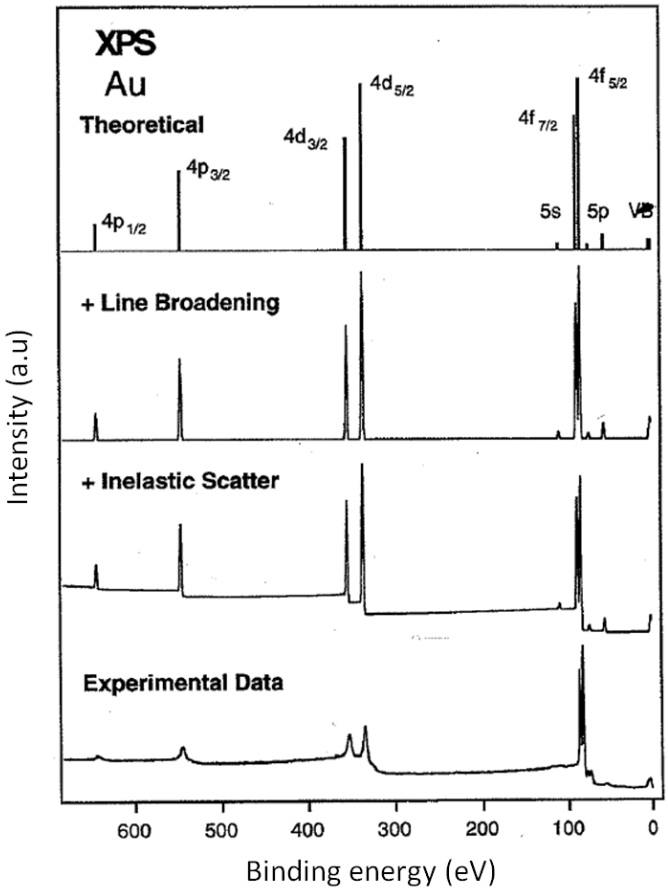

Figure 2.7 A series of XPS spectra demonstrated for Au from theoretical, plus line broadening and inelastic scatter factors, and a practical data from experiment.

(1) Chemical state shift: Chemical state is defined as the electronic, chemical or physical nature for an element as it exists in its elemental nature or in combination with a group of one or more other elements.[2] The chemical state of an atom depends on the types of bonding as it forms, including metallic, covalent, and ionic bonding. Although chemical bonding takes place through valence electrons, the binding energy of core electrons will unavoidably be affected. In the photoemission process, the energy required to emit an electron from the core level will be influenced proportionally by changes in the potentials on the valence shell. For example, for the core electrons, the attractive force from the nucleus will become weaker if the valence shell is negatively charged, and therefore less energy is needed to eject the

electrons from the inner shell, leading to a chemical shift toward the lower binding energy in XPS scan.

The chemical shift due to a change in valence charge can be expressed as[3]

$$\Delta E_b = k\Delta\left(\frac{q}{r}\right) + \sum_{j\neq i} kt_l \frac{\Delta q_i}{r_{ij}} \tag{2.7}$$

where ΔE_b is the chemical state shift, $k\Delta q$ is the change in valence charge on the atom, and r is the radius of the valence orbital. The summation for the second term is referred to the interactions of the charges from surrounding atoms. The value of Δq is positive if the negative charge increases. Note that, the radius of the valence orbital will change as the valence charge changes. However, we can replace the valence radius with the average value $<r_2>$ because the effect of this small change in charge can be neglected. The second term is negligible when Δq is small. Thus, equation 2.7 can be transformed into equation 2.8as[3]

$$\Delta E_b \approx k\Delta\left(\frac{q}{\langle r_2\rangle}\right) \tag{2.8}$$

Equation 2.8 implies that the charge shift effect at the same value of valence charge is greater for atoms of the smaller radius. In other words, this shift arisen from the chemical state is more distinguishable in light elements than that in heavy elements. In practical work, we often compare shifts in E_b values for an element in two different materials. As such, the equation 2.7 becomes[3]

$$E_{b1} - E_{b2} = k\left(\frac{\Delta q_2}{\langle r_2\rangle} - \frac{\Delta q_1}{\langle r_1\rangle}\right) + (V_2 - V_1) \tag{2.9}$$

where E_{b1} and E_{b2} are the binding energies of given orbitals in chemical state 1 and 2. The first difference term expression in the first brackets represents the differences in valence change between two atoms. The second term accounts for the differences in *Madelung*

potentials for the atom in two different states. In equation 2.9, the effect of valence potential and Madelung terms are competitive and may cancel each other. For instance, the binding energies for the Cu $2p_{3/2}$ in Cu (0), Cu_2O (+1) and CuO (+2) are 932.7 eV, 932.4 eV and 933.8 eV, respectively. The peak for Cu $2p_{3/2}$ shifts to low binding energy from Cu to Cu_2O which may be due to the differences in the Madelung potential term in equation 2.9.

(2) Inhomogeneous matrix broadening: This effect is due to the variation of bonding configurations for atoms in a material. The structure or elemental composition differs from atom to atom which leads to a change in the binding energy of orbital. However, owing to the limitation of photoelectron detector, the shift in binding energy attributed from inhomogeneities is hard to be distinguished from homogeneities. Therefore, this effect is expected to be represented as the Gaussian distribution peak broadening rather than a distinguishable distinctive peak shift.

(3) Charging shift: Charging shift is mainly characteristic of poor conductive materials. The charge accumulating on the surface is always positive, resulting in a shift of photoelectron toward higher binding energy. In addition to peak shifts, samples with rough surfaces may also have peak broadening as the extent of charging is not uniform across the sample areas.

Final state effects are those that occur after the photoemission process.[3] There are five types – *plasmon loss*, *Auger excitation*, *Relaxation*, *Shake-up or shake-off*, and *multiple splitting*.

(1) Plasmon loss effect: The plasmon loss process occurs when an outgoing electron interacts with the free electrons in the solid. Unlike inelastic scattering, the plasmon loss is quantized and does not extend over a broad energy range below the primary photoemission peak. The maximum loss energy can be defined by $\Delta E_{loss} = h\omega_p$, where ω_p is the plasmon frequency which can be derived from the free electron model. In practice, the peak caused by resulted from the plasmon loss effect is at higher binding energy than the main peak. Again, unlike

inelastic scattering process, the plasmon loss process is quantized so that its peak appears at integer multiple of the plasmon frequency.

(2) Auger excitation: Peaks arisen from Auger electrons can be seen in XPS spectrum. The Auger process (not described in this context) is usually accompanied by the formation of X-ray photoemission. After the formation of Auger electrons, the electron sites in the orbitals are left vacant, affecting the measured binding energy of photoelectrons.

(3) Relaxation: Relaxation is an instantaneous process that occurs after the photoemission process. This process is illustrated in Figure 2.8 (b), where the created hole vacant sites in an inner orbital is partially filled by as a result of atomic rehybridisation that can occur in the excited atom itself (intraatomic process) or between atoms (interatiomic process). The rehybridisation results in a shift of the orbital toward the Fermi level. Therefore, the resulting feature will appear in lower binding energy. The magnitude of the decrease in the binding energy due to relaxation process can be on the order of several electron volts. However, different to the charging effect, relaxation occurs to the same extend for all atoms that are in the same chemical environment in a material. As a result, this process does not produce a new peak in an XPS spectrum.

(4) Shake-up or shake-off: This process describe that an electron is excited from the valence band to conduction band above the Fermi level throughout the rehybridisation of ion, represented in Figure 2.8 (c). Both shake up and share off process shift the main photoelectron peak to higher binding energy region due to an upward shift of the Fermi level (i.e. the creation of a localised, occupied state above the initial Fermi level results in an upward shift of the Fermi level). The shake up or shake off process generate a satellite peak that appears up to a few electron volts above the primary photoelectron peak.

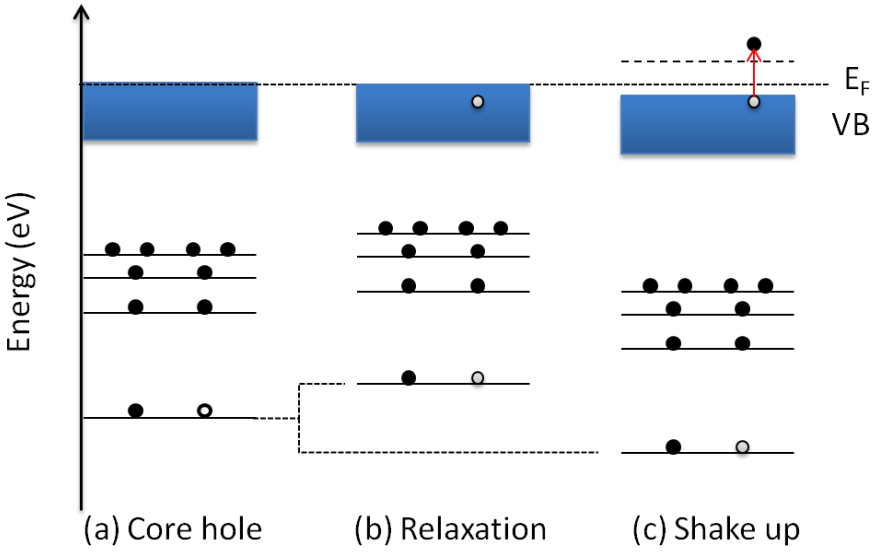

Figure 2.8 Schematic illustrations for the processes of (a) core hole, (b) relaxation, (c) shake-up. E_f is the Fermi level, VB is the valence band.[3]

(5) Multiple splitting: Multiple splitting occurs when a core hole is created by photoemission process and leaves behind an unpaired electron. The unpaired electron can couple with the nuclear or remaining electron spins as either a spin-up or spin-down, similar to the principle of spin-coupling discussed in Chapter 2.1.3.2. This process has a greater influence on the filled s orbital. The magnitude of multiple splitting can be on the order of a few electron volts below or above the main photoelectron peak, depending on the resulting spin-up or spin down states.

2.1.3.6 Elemental Compositions

To characterise the concentration of each element, we have to consider two factors. One factor is the flux of photoelectron ejected from a given orbital, and the other is the instrument. The former can be expressed as[3]

$$J_i^e = F\sigma\lambda_i C_i \tag{2.10}$$

where J_i^e is the flux of electrons emitted from a given orbital for a given element (i) in a sample (electrons / m^2·sec), F is the flux of the incident X-ray beam (photons / m^2·sec), σ is the cross-section (m^2), λ is the inelastic mean free path (m) and a in the homogeneous composition C_i (atoms / m^3) of an element throughout the material. Equation 2.10 describes the total flux of photoelectron generated from an orbital i in a homogeneous sample.

The second consideration for the integral photoelectron of an element is the instrument. Only when photoelectrons arrive the detector contributes to the count of signal. Thus, the relationship between the emitted electrons flux and the measured intensity I_i^m (number per unit time) is shown as[3]

$$I_i^m = f_s f_n \theta_s ATDJ_i^e \tag{2.11}$$

where f_s is the response function for the system electronics, and f_n is the response function for the lens, analyser, and detector. θ_s is the collection efficiency factor for the frontmost lens of the spectrometer, A is the sampling area on the surface, D is the transmission coefficient of the detector, T is the transmission coefficient of the lens and analyser. In general, the five coefficients except for A depend on the kinetic energy of the incident X-ray. Introducing equation 2.10 into equation 2.11, it becomes[3]

$$I_i^m = F\sigma f_a AT\lambda_i C_i = FS_i C_i \tag{2.12}$$

where f_a is the abbreviation for the f_s, f_n, θ_s and D. These variables are combined into the instrument-dependent sensitivity factor S_i for a particular orbital i in an element. Equation 2.12 is particularly useful for the elementary analysis as it can determine the *absolute atomic fraction*, *relative atomic concentrations*, and *unknown composition of a sample by*

comparison with a sample of a known composition. The formula for the absolute atomic fraction (x_i) for an element in a homogeneous composition sample is shown as[3]

$$x_i = \frac{I_i^m / S_i}{\sum I_i^m / S_i} \tag{2.13}$$

The absolute atomic fraction derived from XPS can be accurate to better than ± 10% if an instrument is calibrated precisely. The equation for the Relative atomic concentrations is[3]

$$\frac{x_i}{x_j} = \frac{I_i^m / S_i}{I_j^m / S_j} = \frac{S_j}{S_i}\left(\frac{I_i^m}{I_j^m}\right) = R_{ji}\left(\frac{I_i^m}{I_j^m}\right) \tag{2.14}$$

where R_{ji} is the relative sensitivity factor of element j to element i. Because the variations, such as an instrument configuration or a sample composition, can cancel each other in taking the ratio, relative atomic concentrations determined from XPS are more reliable compared to absolute atomic concentrations. The last determination is to compare a sample of known atomic composition as standard with a sample of unknown atomic composition. The expression for this determination is shown as[3]

$$\frac{x_i}{x_{i0}} = \left(\frac{S_{i0}}{S_i}\right)\left(\frac{I_i^m}{I_{i0}^m}\right) \tag{2.15}$$

where the "0" subscript indicates a sample with known composition. To make a precise determination of this method, a homogeneous atomic distribution over the whole surface area of a sample is necessary. It should be noted that atomic concentrations can vary significantly across the analysis and they also differ across the sample depth even over the same spot area. A key parameter is the average sampling depth in comparison to the depth over which the composition varies. The average depth depends on the mean free path of the electron.

2.1.3.7 Instrumentation

High-resolution X-ray photoelectron spectra were obtained using a Scienta ESCA300 spectrometer located in the National Centre for Electron Spectroscopy and Surface Analysis (NCESS) at Daresbury Laboratory. The machine is equipped with a rotating anode Al K_α ($h\nu$ = 1486.6eV) X-ray source, a 7-crystal monochromator and a 300 mm mean radius spherical sector electron energy analyzer. These components are housed in an ultra-high vacuum (UHV) system incorporating an analysis chamber, a preparation chamber and a fast entry lock. The analysis chamber is equipped with a VSW electron flood gun which can deliver electrons at energies up to 10 eV. This enables stabilization of surface charge on insulating samples. For all the measurements in this thesis, the X-ray source was run with 100 mA emission current and 14 kV anode biases, while the analyzer was operated at 150 eV pass energy with 0.8 mm slits. The Gaussian convolution of the analyzer resolution with a linewidth of 260 meV for the X-ray source gives an effective instrument resolution of 0.45 eV. The instrument was calibrated with the silver reference, aligning the Fermi level position at 0 eV.[8]

For the thin film samples in this study, the samples were amounted on a metal sample holder. In order not for the surface charging, a carbon tape was used a ground wire to contact with the edge of sample and sample holder.

Powdered samples were amounted on the sample holder with a double-side tape. A metal mask was placed on the top of sample to reduce the surface charging. There was a hole in the centre of mask to allow X-rays shine on the sample. A flood gun was used to stabilise the surface charge. Use of a flood gun shifts all spectral features to high kinetic energy. Photoelectron spectra were therefore charge calibrated using the weak C 1s contaminant peak which was assigned a binding energy of 285.0 eV.

2.1.4 X-Ray Absorption Spectroscopy (XAS)

2.1.4.1 Principle of X-Ray Absorption Process

In contrast to XPS process that the excited electrons are emitted from absorbed atom, the electrons in XAS process are remained within the atom, jumping from inner orbitals to unoccupied states.[9] According to *Beer's law*, when an X-ray beam is passed though a thin layer of matter, its intensity is diminished due to absorption and scattering. The relationship for the absorption mode is expressed as $\ln(I/I_0) = -\mu(E) \cdot d$, where I_0 is the intensity of incident radiation, I is the reduced intensity after passing through a sample, and d is the thickness of a sample, μ(E) is the linear absorption coefficient, depending on the incident X-ray energy (E), atomic mass (A) and atomic number (Z) and density (ρ), shown as $\mu \sim \frac{\rho Z^4}{AE^3}$.[9]

Absorption occurs when the energy of incident photons is just sufficient to excite a core electron to continuum states in the absorbing atom, giving rise to a sharp absorption edge in an X-ray absorption spectrum as can be seen in Figure 2.9. The absorption edge labelled as L_3-edge indicates the excitation of a photoelectron from $2P_{2/3}$ orbital. Oscillation after absorption edge is formed when the ejected photoelectron from the absorbing atom is scattered by the neighbouring atom and then return back to interfere with itself to produce constructive and destructive interferences.

An X-ray absorption spectrum can be classified into *X-ray absorption near-edge structure (XANES)* and *extended X-ray absorption fine structure (EXAFS)*. XANES can provide the information on the density of electronic states, oxidation state, electronic structure and the coordination symmetry of the absorber. The scan range in XANES spectrum is from -200 eV to 30 eV with respect to the absorption energy (E_0) of absorbing atom. XANES can be carefully viewed in three sectors: (1) *pre-edge* (from -200 eV to -30 eV; E <

E_0), (2) *absorption edge* (E_0), and (3) XANES (-30 eV < E_0 < 20 eV). The feature in pre-edge is due to the electron transition across from core levels to higher unoccupied or half-occupied orbitals and the electron transition must obey the dipole selection rule (e.g. s → p for K and L_1 edges; p → d for L_2 and L_3 edges). This feature can be used to determine the local geometry around the absorbing atom. The absorption edge defines the ionization threshold to continuum states, which is sensitive to oxidation states (i.e. main edge shifts toward higher energy when the oxidation state increases). XANES features a multiple scattering resonance of photoelectron emitted with low kinetic energy, reflecting interatomic distance and bond angles.

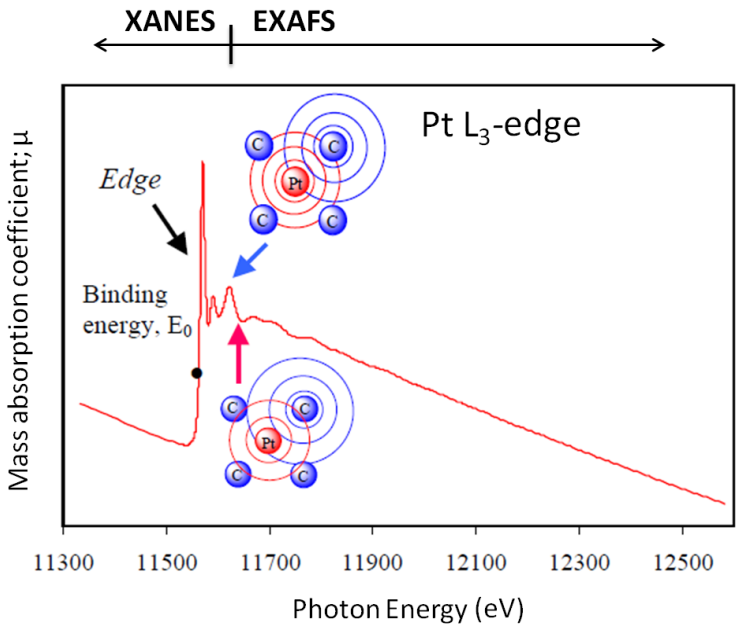

Figure 2.9 An X-ray absorption spectroscopy spectrum of Pt L3-edge. The energy of absorption edge (E_0) defines ionization threshold to continuum states.[9]

EXAFS is recorded from the photon energy greater than the absorption edge by 50 eV to 800 eV. This probe can provide the information on the local structure within the range of 10Å, coordination number, the type of neighbouring atom, and atomic distance. Compared to

XANES, the photoelectron in the EXAFS region has a higher kinetic energy and involves a single scattering by the nearest surrounding atoms rather than the multiple scattering in XANES.

2.1.4.2 Instrumentation

The Zn K-edge and Zn L_3-edge XAS were recorded at BL01C1 and the O K-edge XAS was measured at BL20A at the National Synchrotron Radiation Research Centre (NSRRC) in Hsinchu, Taiwan, operated at 1.5 GeV with a current of 360 mA. Figure 2.10 shows a schematic diagram for XAS facilities. A Si(111) double-crystal monochromator was used for the selection of photons with a specific energy, ranging from 6 keV to 33 keV at BL01C1 and from 60 eV to 1250 eV at BL20A, respectively. For BL01C1, the average resolution ($\Delta E/E$) and the photon flux at the sample position can achieve 1.6×10^{-4} and 3×10^{10} photons/sec, respectively. The focused beam size is about 0.9 mm (H) × 0.2 mm (V). For BL20A, the resolving power ($\Delta E/E$) and the photon flux can reach 8000 and 2.5×10^{10} photons/sec, respectively. The focused beam size is about 0.12 mm (H) × 0.055 mm (V). The absorption edges were determined from the peaks in the first derivative XANES after the subtraction of the post-edge baseline and the normalisation to the edge jump. All spectra were normalised to unit step height in the absorption coefficient from well below to well above the edges and yielded the information of the unoccupied states with p orbitals.

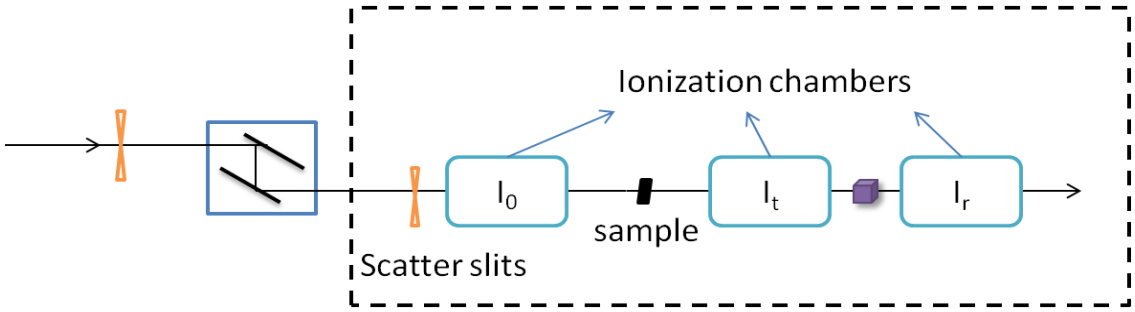

Figure 2.10 Schematic illustration of typical X-ray absorption spectroscopic experiment. The dashed line encloses the hutch.

2.2 Hall Effect Measurement

The effect was discovered in 1879 by Edwin H. Hall and named after him.[10] This technique is widely used to measure the transport properties of semiconducting materials: the type of carriers, their densities, mobility and the material electrical resistivity. These measurements can provide the quantitative information on impurities, imperfections, uniformity, and scattering mechanism over a wide range of temperature (4.2–300 K).

2.2.1 The Principle of Hall Effect

The basic physical principle underlying the Hall effect is the *Lorentz force* that occurs when a point charge moves in the electric and magnetic fields, and is given as,[11]

$$F_L = q\left[E + (v \times B)\right] \tag{2.16}$$

where F is the Lorentz force (Newton), q is the elementary charge (coulombs), E is the electric field (V/m), v is the velocity of the charged particle (in m/sec), B is the magnetic field (Tesla), and × is the vector cross product operator.

The model of the Hall effect system is shown in Figure 2.11. A current, which is passed parallel to the x axis through the semiconductor block in a fixed magnetic field B (y axis) perpendicular to the charged current, experiences a +z-directed magnetic force that deflects the moving carriers to the top side of the conducting materials. An electric field (E) along z axis is established due to the asymmetric distribution of charge density (i.e. the top is positive charge and the bottom is negative charge). The direction of the resulting electric force (F_e) is opposite to the magnetic force (F_B). The magnitude of the electric force is proportional to the magnitude of electric field. With increasing the electric field till the net force is null (i.e. $F_e = F_B$), the potential difference across the two sides of sample in the balanced situation is known as the Hall voltage (V_H), which is given as

$$v_d B = E = \frac{|V_H|}{d} \tag{2.17}$$

where V_H is the Hall voltage and d is the thickness of the sample. The velocity is related to the current density (J) and carrier density (n) as

$$v_d = \frac{J}{qn} = \frac{I}{qnd^2} \tag{2.18}$$

Thus, equation 2.19 can be re-written as

$$\frac{I}{qnd^2} B = \frac{|V_H|}{d} \tag{2.19}$$

$$n = \frac{IB}{qd|V_H|} \tag{2.20}$$

where n is the charged carrier density. In practice, the bulk carrier density can be calculated with the known values of I, B and q and the measured Hall voltage. Note that, the Hall voltage is negative for n-type semiconductor (i.e. the majority of the charged carriers are electrons) and positive for p-type semiconductor (i.e. the majority of the charged carriers are holes).

The Hall coefficient (R_H) is defined as the ratio of the perpendicular electric field (E) to the product of current density (J) and the applied magnetic field (B).

$$R_H = \frac{E}{JB} = \frac{dV_H}{IB} = -\frac{1}{qn} \tag{2.21}$$

Equation 2.21 clearly reveals that the Hall effect is an useful tool to determine either the carrier density or the magnetic field. It can characterise the type of semiconductor as R_H is negative for n-type and positive for p-type semiconductor. Taking the scattering mechanism in semiconductor into consideration, the Hall coefficient is written as

$$R_H = -\frac{r_H}{qn} \tag{2.22}$$

where r_H is the Hall scattering factor dependent on the details of the scattering mechanism. It is worth noting that the carriers undergo various scattering mechanisms that govern the carrier mobility in the electronic system when they travel through semiconductor. The carrier mobility (μ) can be calculated from the electrical resistivity (ρ) and Hall coefficient, expressed as

$$\mu = \frac{R_H}{\rho} \tag{2.23}$$

where the resistivity of the semiconductor can be obtained by using the van der Pauw technique.

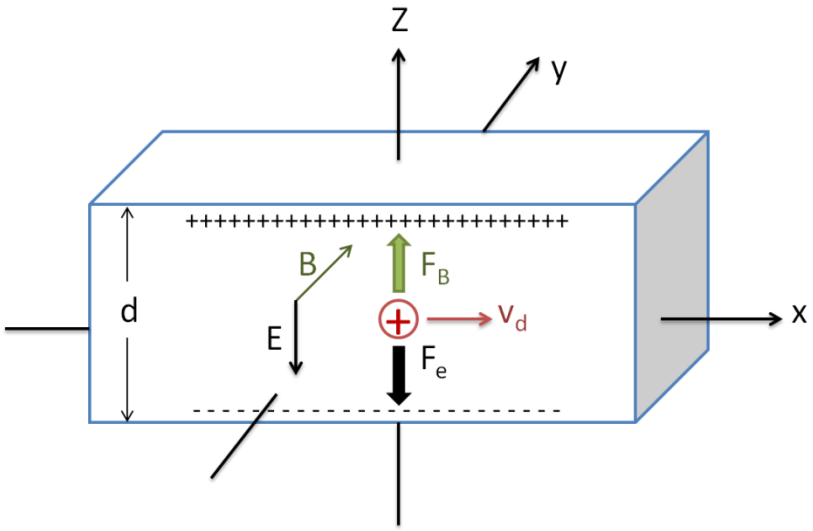

Figure 2.11 Schematic diagram of the Hall effect system. A positive point charge travels with the velocity (v_d) from left to right, and a fixed magnetic field is applied along y axis. The resulting Lorentz force applied to the point charge produces a magnetic force (F_B) in +z direction and an electric force (F_e) in -z direction. d is the thickness of a semiconductor.

2.2.2 Van Der Pauw Method

The van der Pauw method is coupled with the Hall effect system to determine the carrier mobility (μ) and the sheet carrier density (n_S). The van der Pauw method was first established by Leo J. van der Pauw in 1958.[12] It is a technique used to measure the electrical resistivity and the Hall coefficient on semiconductor samples of arbitrary shape. The basic conditions for performing the van der Pauw method are, (1) a flat sample of uniform thickness, (2) no isolated holes, (3) a homogenous and isotropic sample, (4) the resistance at any contact should be at least one order of magnitude smaller than that in the sample, and (5) all four contacts must be located at the edges of the sample, as shown in Figure 2.12. The error of the

Ohmic contacts is given as error = D / L, where D is the average diameter of contact and L is the distance between contacts. From the expression, it is known that the error of Ohmic contacts can be minimised by reducing the contact area or increasing the distances between contacts. .

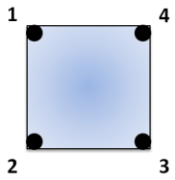

Figure 2.12 An illustration for Ohmic contacts.

To obtain the vertical sheet resistance ($R_{12,34}$), the measurement is performed by passing a DC current through the contact 1 towards the contact 2 (I_{12}) and measuring the DC voltage between the contact 3 and contact 4 (V_{34}). Next, the same procedure is repeated to obtain the horizontal sheet resistance ($R_{14,\,23}$) by probing the I_{14} and $V_{23.}$ According to the Ohm's law, the vertical and horizontal sheet resistance are derived as

$$R_{12,34} = V_{12}/I_{34}\,,$$
$$R_{14,23} = V_{14}/I_{23} \tag{2.24}$$

The average sheet resistance (R_s) is calculated through the van der Pauw equation

$$e\wedge(\frac{-\pi\times R_{12,34}}{R_s}) + e\wedge(\frac{-\pi\times R_{14,23}}{R_s}) = 1 \tag{2.25}$$

The bulk resistivity can then be calculated using multiplying the film thickness (d)

$$\rho = R_s \times d \tag{2.26}$$

The Hall effect measurement in conjunction with the van der Pauw technique can obtain the sheet carrier density (n_s) by measuring the Hall voltage (V_H). The determination of Hall voltage involves in a series of voltage measurements with a constant current flow (I) and applied magnetic field (B) perpendicular to the sample plane. Similar to the equation 2.20, the sheet carrier density can then be derived with the known values of I, B and q.

In the present work, the room temperature measurements of resistivity and Hall coefficient were performed by the van der Pauw method using a commercial Ecopia HMS - 3000 Hall measurement system (Figure 2.13(a)). Contacts were applied to the thin film and the ceramic samples using indium solder. Samples were amounted on the printed circuit boards (Figure 2.13 (b)) designed for the use in Ecopia HMS-3000 Hall measurement system. Before transferring the sample board into the measuring system, the resistivity of the contacts was checked with multimeter. Measurements were made in the fixed 0.5 Tesla magnetic field and the input current in the range between 5 mA and 10 µA for thin films and ceramic samples. The thickness of thin film was determined from the UV-Vis transmittance spectroscopy.

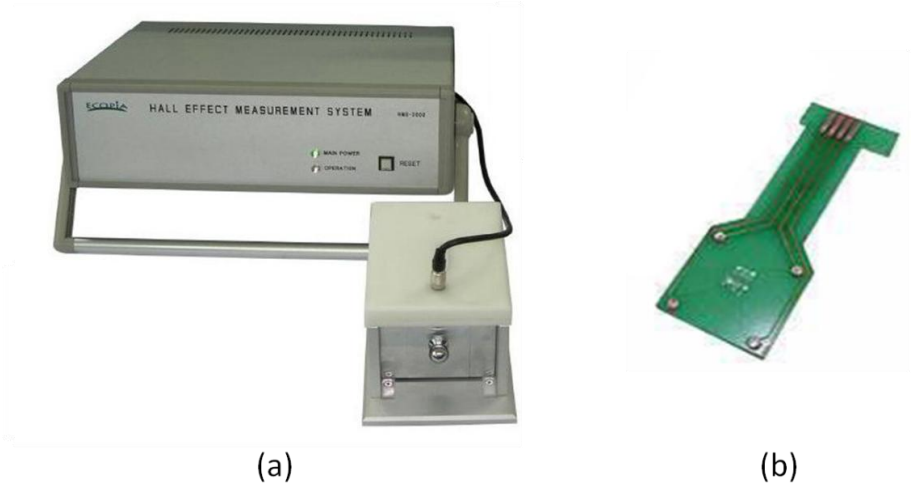

Figure 2.13 Photos of (a) a commercial system of Ecopia HMS -3000 Hall measurement system, and (b) a printed circuit sample board.

2.3 *Molecular Spectroscopy*

Molecular spectroscopy is the method that apples ultraviolet, visible, infrared and microwave radiations in the wavelength range from 10 nm to 3.75 mm as its source to irradiate matter.[1] There are three types of quantum transitions in a molecule, namely *bonding electrons*, *vibration* and *rotation*. The energy associated with these three motions is, $E = E_{elec} + E_{vib} + E_{rot}$, where E_{elec} implies the energy states of bonding electrons in a molecule, E_{vib} is the total energy of interatomic vibrations, and E_{rot} is the energy corresponding to several rotational modes. The first term E_{elec} is characterised by an ultraviolet-visible (UV-Vis) spectroscopy, and the last two terms, E_{vib} and E_{rot}, are determined with Raman spectroscopy, infrared (IR) spectroscopy or microwave spectroscopy. UV-Vis spectroscopy and Raman spectroscopy were used to characterise the samples in the present work, and those two techniques will be discussed below.

2.3.1 Ultraviolet Visible Absorption Spectroscopy

In semiconductor materials, the electron transition that is induced by optical photons involves between the top of the valence band and the bottom of the conduction bands, separated by the forbidden bandgap. Here, only the electronic transition occurred with just sufficient photon energy over the band gap will be considered. The electronic transition must obey the selection rules. First, the orbital angular momenta for the initial and final electron states must be different (i.e. $\Delta l = \pm 1$). Second, photon energy must be greater or equal to the band gap. That is,

$$E_f = E_i + h\nu \tag{2.27}$$

where hν is the photon energy, and E_f and E_i are the energies for final and initial states, respectively. Finally, in terms of an ideal crystalline material, crystal momentum also needs to be conserved in the transition, expressed as

$$k_f = k_i + k_{ph} \tag{2.28}$$

where k_{ph} is the photon wavevector, k_f and k_i are the wavevectors of an electron in the final and initial states, respectively. k_{ph} is negligible compared with a typical electron wavevector.[13] As it is shown in Figure 1.4, electron states as a function of wavevector form non-parabolic curves in the valence and conduction bands. *The fundamental bang gap* is defined as the transition between the valence band maximum (VBM) and the conduction band minimum (CBM) occurred at the same point in the Brillouin zone (i.e. $\Delta k = 0$). This transition between VBM and CBM at k = 0 (or the Γ point) is called *direct transition*. On the other hand, transitions between bands with different wavevectors are indirect (Figure 2.14). In the process of indirect transition, photon energy induces a vertical transition from VBM to a virtual state and the rest momentum is provided by phonon emission or absorption energies ($\hbar\omega_p$) to reach CBM. Then, equation 2.27 and equation 2.28 are changed to

$$E_f = E_i + h\nu \pm h_p \tag{2.29}$$

$$k_f = k_i + k_{ph} \pm q_p \tag{2.30}$$

In addition to the phonon emission or absorption energies, electron-electron or electron-impurities scatterings can also contribute to the required indirect transition energy in heavily doping semiconductors.

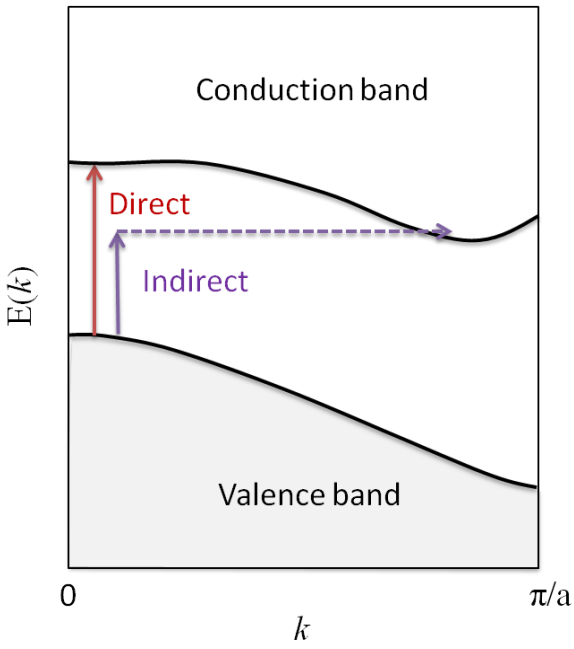

Figure 2.14 Optical absorptions with direct (red line) and indirect (purple line) transitions from the valence band to the conduction band in the band structure diagram.

UV-Vis absorption and transmittance data were measured in a Perkin-Elmer Lambda 750S instrument equipping with a 60 mm integrating sphere. UV-WinLab software was run to collect the spectra. Deuterium and tungsten halogen lamps as its light source are able to generate a broad range of wavelength from 200 nm to 2500 nm, with the resolution of 0.17 - 5 nm in UV-Vis region and of 0.2–20 nm in near IR. All measurements for thin film samples were performed at room temperature with a wavelength scan from 250 to 800 nm. Thin film thickness and the roughness of film samples were derived from the optical data by refining the observed transmission to a simulated transmission function using WVASE software package.

2.3.2 UV-Vis Diffuse Reflectance Spectroscopy (DRS)

UV-Vis diffuse reflectance spectroscopy (UV-Vis DRS) is suitable for measuring a solid sample with very week transmitted light. The detected signal is the sum of light via multiple reflection, refraction and scattering inside the solid sample, and is independent of the angle of the incident beam (Figure 2.15). Kubelka and Munk proposed an approximation for the diffuse reflectance on a rough surface solid in 1931,[14] which was shown as

$$\begin{aligned} -di &= -(S+K)\,i\,dx + S\,j\,dx \\ dj &= -(S+K)\,j\,dx + S\,i\,dx \end{aligned} \tag{2.31}$$

where i and j are the intensities of light travelling inside the sample towards its un-illuminated and illuminated surface, respectively, dx is the differential segment along the light path, K is the molar absorption coefficient, and S is the scattering coefficient. In a limited case of an infinite thick sample, the thickness has no influence on the value of reflectance (R). Thus, equation 2.31 becomes[15, 16]

$$R = \frac{S}{K + S\left[K\left(K+2S\right)\right]^{1/2}} \tag{2.32}$$

$$F(R) = \frac{(1-R)^2}{2R} = \frac{K}{S} \tag{2.33}$$

where F(R) is the remission of Kubelka-Munk function. If K is close to 0, then R is nearly equal to 1, implying that all incoming light are reflected, and vice versa.

Diffuse reflectance spectra were performed using a Cary 500 UV-visible-NIR spectrophotometer over wavelengths between 200 nm and 850 nm. Powder samples were analysed in air at room temperature. $BaSO_4$ was placed in the path of the reference beam during the measurements as a reference standard.

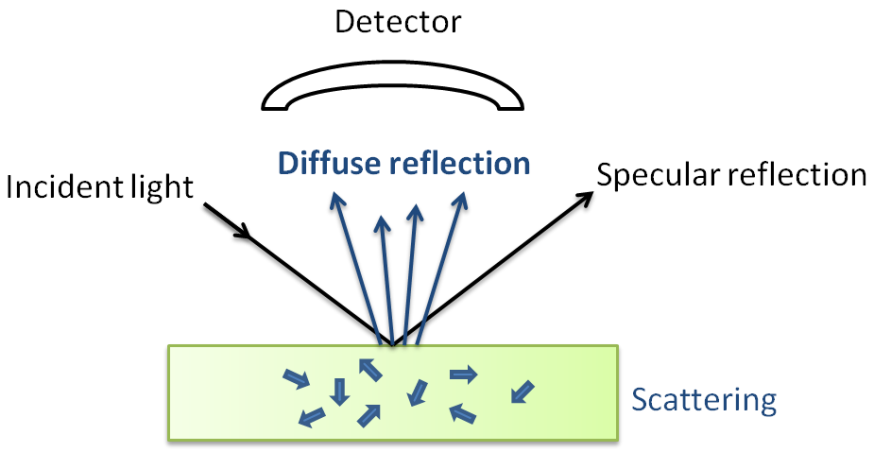

Figure 2.15A schematic representation for diffuse reflection relies upon the focused incident beam into a sample where the light is reflected and scattered inside the sample.[16]

2.3.3 Raman Spectroscopy

Raman spectroscopy requires a monochromatic laser source in the visible or near-infrared range to irradiate a sample. The Raman transition is attributed to molecular rotation or vibration. A typical Raman spectra records the intensity of phonons as a function of wavenumber shift ($\Delta\nu$; cm^{-1}) that is defined as the difference in a wavenumber between incident and scattered visible radiation.[1] Figure 2.16 shows an energy level diagram for Rayleigh scattering and Raman scattering (Stoke and anti-Stoke). The black arrow reflects an upward transition from ground states to virtual states when photons are absorbed by the molecule. Rayleigh scattering refers to an elastic collision (i.e. no energy loss) between photons and a molecule. The gain or loss of energy due to Raman scattering results in longer or shorter wavenumbers, which is called Stoke or anti-Stoke shifts. Note, the features for Stoke and anti-Stoke shifts are: (1) the shifts are independent of the wavelength of excitation. (2) The Stoke peaks and anti-Stoke peaks appear symmetrically on both sides of Rayleigh peak, and that the pattern of shifts on each side is identical. (3) Only Stoke peaks are used in

Raman spectra due to the fact that the intensity of Stoke peaks is greater than that of anti-Stoke peaks. Regarding the wave models in Rayleigh and Raman scatterings, when an electric field (E) of an incident photon interacts with the electron cloud of an analyte bond, an induced dipole momentum (m) in a bond is given by[1]

$$m = \alpha E = \alpha E_0 \cos\left(2\pi \nu_{ex} t\right) \tag{2.34}$$

where α is the polarisability constant, describing the deformability of the bond in an electric field, E_0 is the amplitude of the wave, and ν_{ex} is the frequency of incident radiation. Raman active should satisfy the condition that the polarisability of a bond varies with a function of the distance between nuclei, which can be expressed as

$$\alpha = \alpha_0 + \left(r - r_{eq}\right)\left(\partial\alpha / \partial r\right) \tag{2.35}$$

Where α_0 is the polarisability of the bond at the equilibrium internuclear distance r_{eq}, and r is the internuclear separation at any instant. Merging equation 2.34 and 2.35 produces

$$m = \alpha_0 E_0 \cos\left(2\pi \nu_{ex} t\right) + \frac{E_0}{2} r_m \left(\frac{\partial \alpha}{\partial r}\right) \cos\left[\left(2\pi\left(\nu_{ex} - \nu_v\right)t\right)\right] + \frac{E_0}{2} r_m \left(\frac{\partial \alpha}{\partial r}\right) \cos\left[\left(2\pi\left(\nu_{ex} + \nu_v\right)t\right)\right] \tag{2.36}$$

where r_m is the maximum internuclear separation relative to the equilibrium position. The first term in equation 2.41 implies Rayleigh scattering, which takes place at the excitation frequency ν_{ex}. The second and third terms are referred to the Stokes and anti-Stokes frequencies of $\nu_{ex} - \nu_v$ and $\nu_{ex} + \nu_v$, respectively. Therefore, it is known that Raman scattering only occurs when the term $\partial\alpha/\partial r$ (i.e. the polarisability of a bond varies as a function of distance) is greater than zero. Raman data were collected using a PerkinElmer RamanStation 400F Dispersive Raman Spectrometer equipped with a 350 mW near infrared

785 nm laser and a high sensitivity open electrode CCD detector. The spectral range is between 95 cm^{-1} - 3500 cm^{-1} Raman shift with peak resolution of 4 cm^{-1} in full width at half maximum. Powder sample was cooled down to -50˚C and each scan was measured from 95cm^{-1} to 3500 cm^{-1} in the air.

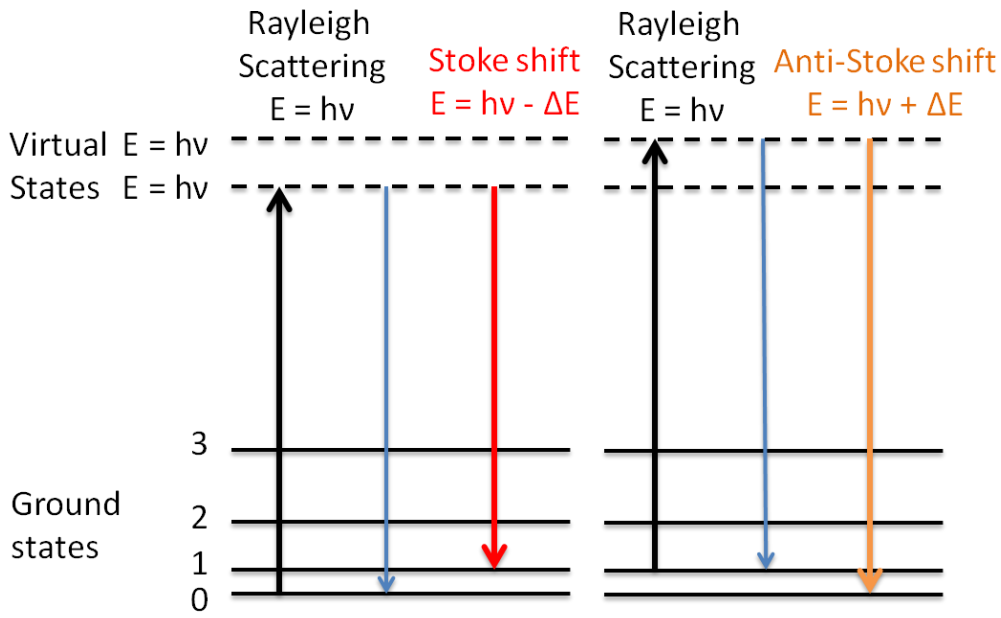

Figure 2.16 Energy level diagram represents for Rayleigh scatterings (blue arrow), Stoke shift (red arrow), and anti-Stoke shift (orange arrow).

2.4 Electron Microscopy

2.4.1 Scanning Electron Microscopy / Energy Dispersive Spectrometry

Scanning electron microscopy is an imaging technique to study surface morphology. Each image is obtained by scanning a sample in a raster pattern with an electron beam. Several types of signals are produced from a surface in this process, such as backscattered, secondary and Auger electron, or X-ray fluorescence photons. Among these signals from the

surface region, *backscattered* and *secondary electrons* are the basis of scanning electron microscopy.[17]

The interactions of an electron beam with a solid can be classified into two categories: elastic collision and inelastic collision. When an electron collides elastically with an atom, the kinetic energy of the electron remains unchanged, which is known as an elastic collision. On the other hand, it is called inelastic interaction if an electron loses its energy during collision. The energy of the electron beam in SEM is normally 20 keV and this enable the beam to penetrate a depth of 1.5 μm approximately. At such condition, the majority of the electrons undergo collisions, and finally leave the solid as backscattered electrons to detector. Secondary electrons are generated as a consequence of the interactions between the incident beam electrons and weakly bound conduction band electrons in the solid. Secondary electrons are produced from a depth of 50 - 500Å with a few electron volts of energy. This unwanted signal arisen from the secondary electrons can be excluded by applying a small negative bias to the transducer housing.

Energy-dispersive X-ray spectrometry (EDS) is a tool used to analyse elemental composition. The measured intensity is proportional to the mass or atomic concentrations for each analytical element.[3] In practical, all elements can be detected except for H, He and Li. The X-ray energy used in EDS is normally in the range from 100 eV to 100 keV to avoid spectral interference and to reduce the background processes to the peaks.

SEM-EDS data were obtained using Jeol JSM 5600 SEM at School of Chemistry, University of St. Andrews. The machine is equipped with a tungsten filament as an electron source and the accelerating voltage was between 0.5 kV and 30 kV.

2.4.2 Transmission Electron Microscopy (TEM)

Transmission electron microscopy (TEM) is a major tool to probe the microstructure with imaging or electron diffraction at atomic level. A TEM apparatus consist of a high voltage electron gun, focusing lenses, a sample stage and a display screen or a photographic plate (Figure 2.17). The accelerating electron beam is transmitted through a thin specimen and interacts with the specimen in three types, which are transmitted beam, elastic scattered electrons, and inelastic scattered electrons. The spatial variation from the specimen is then magnified by a series of magnetic lenses until it is focused on a fluorescent screen, producing a TEM image. The number of transmitted electrons depends on the thickness and quality of the specimen, (e.g. a thicker sample has less transmitted electrons, turning to a dark field in the image). An emitted electron that undergoes an elastic collision must be followed Bragg's law (equation 2.2) to form a diffraction pattern that is used to determine the atomic arrangement, orientation and phase. Inelastic scattered electrons is particularly useful for the analysis of elemental composition and atomic bonding, where electron energy loss spectroscopy (EELS) is performed by recording the inelastic scattered electrons..[18]

TEM images are arisen from the contrast caused by electron scattering of the incident beam with the specimen. The image contrast is given when the electron wave traverses the specimen and changes its amplitude and phase, which is known as *amplitude contrast* and *phase contrast*. The former results from the thickness or mass of a specimen, and diffraction contrast.[19]

TEM images were obtained using a Jeol JEM 2011 HRTEM apparatus at the School of Chemistry, University of St. Andrews. The machine is equipped with a LaB_6 filament as the electron source and the accelerating voltage is between 80 kV and 200 kV.

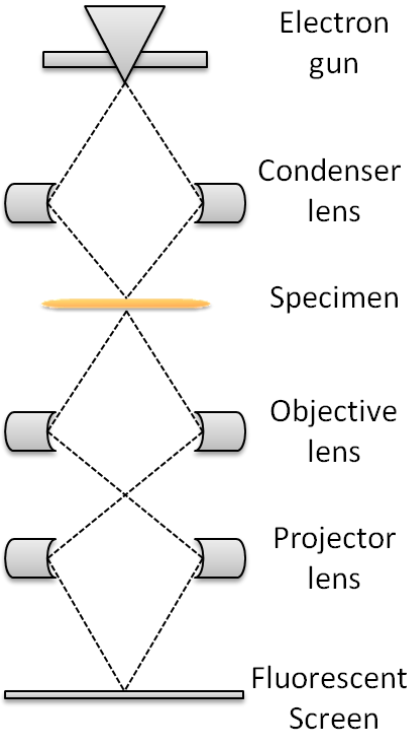

Figure 2.17 Layout of the components of transmission electron microscopy apparatus.[3]

2.5 Gravimetric Analysis

Gravimetric analysis is a quantitative determination of an analyte based on the mass of a solid. Thermal gravimetric analysis (TGA) is one of the gravimetric analysis techniques to measure the weight change of a material in relation to temperature. TGA is the act of heating a mixture to a high enough temperature to decompose one of the components into a gas. The technique can characterise materials that exhibit weight loss or gain due to decomposition, oxidation or dehydration with time and temperature. The thermogravimetric curves are given for the specific materials and chemical compounds due to the unique sequence from physical or chemical reaction occurring over the specific temperature ranges and heating rate. Based

on this, TGA can provide the information on the composition of a multicomponent system, thermal or oxidative stability, and the decomposition kinetics of materials. However, as many weight loss curves look similar, the data interpretation may be limited without combining other techniques.

Differential Scanning Calorimetry (DSC) is another thermoanalytical technique measuring temperatures and heat flows associated with thermal transition in a matter.[20] The subsequent heat may be reduced or increased depending on whether the transformation in the sample is exothermic or endothermic. Heat-flux DSC and power compensation DSC are the two most common systems that have been used in DSC apparatuses. In a heat-flux DSC only one furnace is employed in one enclosed system. A sample and reference are connected by a low resistance heat flow path in this system. Enthalpy or heat capacity changes in the sample cause a difference in its temperature relative to the reference. In power compensation DSC, two separate furnaces are used to heat the sample and the reference individually.

Assembling TGA and DSC (TGA-DSC) kits measure heat flow and weight changes in a material simultaneously which enhances the productivity and to simplifies the interpretation of the results. The TGA-DSC data in the work content were measured using a STA 6000 from PerkinElmer Company. Powder samples were measured run at a heating rate of 10˚C/min from 30˚C to 600˚C in Argon atmosphere.

2.6 Atomic Force Microscopy (AFM)

Atomic force microscopy (AFM) is a branch of microscopy that allows imaging of a surface by recording the interactive force between the AFM tip and the surface atoms. When

a tip is brought into the proximity of a sample surface, forces between the tip and the surface lead to the deflection of the cantilever according to Hooke's law. The deflection is measured using a laser spot reflected from the top surface of the cantilever into an array of photodiodes. AFM images were scanned using a NanoScope MultiMode AFM. This multimode allows both conductive and nonconductive samples to be analysed. Extender Electronic Module was applied in order to increase magnetic and electric filed imaging. The control system provides 16-bit resolution on all three axes (x, y, and z scanner drives with 220V range), with three independent 16-bit digital-to-analog converters (DACs) in x and y directions for control of the scan pattern, scaling, and offset. Digital Nanoscope software (version 5.12) was used to analyze the process the AFM topographic images. Measurements in this work were ex-situ in tapping mode which scanned a silicon probe (Nascatec GmbH Model NST-NCHFR), at resonant frequency of 3.2×10^5 Hz across the surface of samples. Tip velocities were chosen as 2, 5, and 10 μm/s for the scan size of 2, 5, 10 μm, respectively. All the images were treated with the "flatten" command and are presented using one of the standard colour palettes and the Nanoscope software.

2.7 Synthetic Techniques

2.7.1 Spray Pyrolysis

Spray pyrolysis was first developed in the 1940s for the preparation of transparent oxide films (TCO) and is regarded as an easy, safe and low cost route for thin film deposition [21]. In order to yield uniform films, a number of factors should be taken into consideration, including deposition temperature, the types and flow rate of carrier gas, precursor

concentration and composition, solution flow rate, and spray time. For example, deposition temperature affects the dynamic stabilization of films (bouncing and splitting of droplets) and the thermal stabilization of the films (evaporation rate and dragging of ionic species). Also, the deposition temperature cannot be too high as it may give rise to unwanted alloying and grading. Spray time should be selected properly in order to obtain the required transparency and thickness. Air flow rate can affect the size and the velocity distribution of droplets.[22] In the present work, the deposition of thin film samples was carried out by a locally made spray pyrolysis system (Figure 2.18). Deposition temperatures were controlled to within ± 5ºC (2216e Eurotherm Temperature Controller). The carrier gas (N_2) flow rate of 17 L/min and solution pump (Masterflex, Core-Parmer) setting "1.0" (approximate 0.33 mL/min) were used for the deposition of all films. Before deposition the substrate was cleaned in acetone and ethanol for 10 minutes using an ultrasonic bath (Ultrawave) and dried in compressed air. The substrate was secured on the heating stage and the spray pyrolysis compartment was sealed. The enclosed chamber was flushed with the carrier gas for 30 minutes while the substrate was heated to the required temperature at a rate of 25ºC/min. Once the temperature was stabilized, the solution pump was activated and deposition initiated. After the completion of deposition, the film was kept at the deposition temperature for 30 minutes. For experiments conducted at temperature above 200ºC, the system was cooled back to 200ºC manually at a rate of 15ºC/min to avoid the substrate cracking, after which the heater was turned off and the system was left to cool to room temperature.

In the chapter 3.1 of this thesis ZnO films were deposited onto glass substrates (Menzel-Gläser cover glass) at several temperatures in the range of 100ºC - 500ºC using 0.05M zinc acetate (Sigma-Aldrich, purity 99.99%) dissolved in a mixture comprising equal parts of distilled water and absolute ethanol Sigma-Aldrich) by volume, with the addition of a few drops of acetic acid to dissolve any precipitate.

In the chapter 3.2, 1 at.% $AlCl_3$ was added as doping into 0.05M zinc acetate precursor solution for the preparation of aluminium-doped ZnO (AZO) thin films. AZO films were deposited using 5, 10, 20 and 30 mL volumes of precursor solution, giving rise to 271 nm, 362 nm, 807 nm and 1281 nm film thickness, respectively. The deposition temperature was set up at 500C˚ for all AZO films. The epitaxial growth of ZnO films in the chapter 3.3 were prepared using sapphire(0001) as the substrates at 500˚C. The synthesis condition of spray pyrolysis is the same as description in the previous paragraph.

Cadmium nitrate tetrahydrate [$Cd(NO_3)_2 \cdot 4H_2O$] (Sigma-Aldrich, purity ≥ 99.0%) was used as cadmium impurity to be added into 0.05M zinc acetate precursor solution for the preparation of $Cd_xZn_{1-x}O$ thin films (chapter 4) and photoanodes (chapter 6). In the chapter 4, $Cd_xZn_{1-x}O$ layers were grown onto glass substrates at various Cd molar concentrations in 0.05M zinc precursor solution at 400ºC deposition temperature. For $Cd_xZn_{1-x}O$ photoanodes, all the synthesis conditions were the same that for making $Cd_xZn_{1-x}O$ thin films except for the substrate. The photoanode samples were used commercial indium tin oxide (surface resistivity: 8-12 Ω/cm^2; Sigma-Aldrich) as the substrates.

The prepared $ZnO_{1-x}S_x$ thin films in chapter 5 and the $ZnO_{1-x}S_x$ photoanodes in chapter 6 were used glass and commercial indium tin oxide (ITO) as substrates. All the samples were deposited at 500ºC with the supply of 0.05M zinc precursor solution mixed with thiourea at certain ratios.

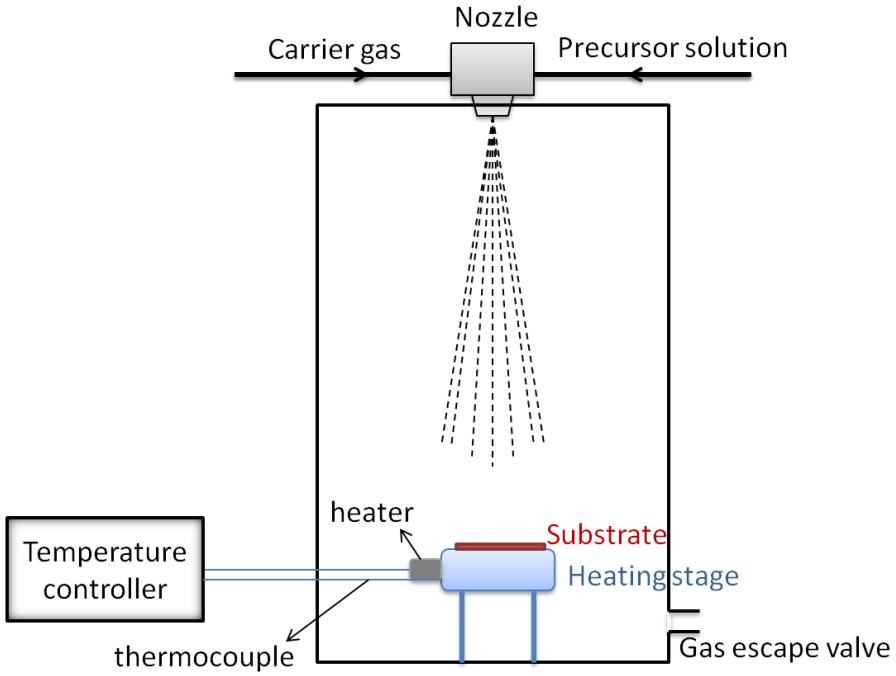

Figure 2.18A schematic diagram of spray pyrolysis apparatus.

2.7.2 Solid State Synthesis

Solid state synthesis involves the mixing and pressing into pellets of powdered reactants before sintering at an elevated temperature for prolonged periods.. The kinetics of solid state reactions are intrinsically slow because although reactants are dispersed on the particulate level (~ 1 μm), they are extremely inhomogeneous on the atomic level. The solid state reaction begins on the interface between reactant grains where the nucleation of small crystallites with the stoichiometry of the product occurs. The high temperature synthesis was carried out at 1000ºC in the air using a muffle furnace (Carbolite RHF 16/3 and RHF 14/3). In chapter 4, ternary $Cd_xZn_{1-x}O$ alloys were prepared by conventional solid state reaction.[23] A well-blended mixture of ZnO nanopowder (Sigma-Aldrich, purity 99.99%; particle size <100 nm) and CdO powder (Sigma-Aldrich, purity 99.99^{+}%) was ground, and pressed into pellets under uniaxial pressure (8 tons). To avoid the loss of volatile reactants during heating, the

pellets were embedded in a powder of identical stoichiometry, and were calcined at 1000ºC for 5 hours in air to form $Cd_xZn_{1-x}O$ ceramic samples. The above procedure was repeated to increase the sample's homogeneity.

2.8 Photocatalytic Degradation Reactions

The photocatalytic activity of $Cd_xZ_{1-x}O$ photocatalysts are evaluated by performing the degradation of methylene blue (MB) under simulated solar light irradiation. 0.2 g $Cd_xZ_{1-x}O$ photocatalysts and methylene blue (100 mL, 5 ppm) were placed in a 250 mL beaker. A magnetic stirrer was used continuously in the reaction so that $Cd_xZ_{1-x}O$ can be uniformly dispersed in the solution. Prior to irradiation, the reactant solution was stirred in the dark for 1 hour and then sucked for 4 mL as the pre-react sample. The reacting solution was extracted for around 4 mL in every 20 minutes at the first hour reaction time. Afterwards, the extraction procedure was repeated in every 30 minutes till the reaction finished. The extracted solution was centrifuged for 5 minutes to separate the powder and solution. The final solution was analysed by UV-Vis absorption spectroscopy.

2.9 Photoelectrochemical Cell Measurements

A potentiostat works with three electrodes immersed in a conductive electrolyte, including working electrode; WE (i.e. a sample of metal oxide being tested), reference electrode; RE (i.e. an electrode with a constant electrochemical potential) and a counter

electrode; CE (i.e. a current-carrying electrode that completes the cell circuit), as shown in Figure 2.19. The electrometer in the potentiostat measures the voltage difference between the WE and RE. The control amplifier compares the measured cell voltage with the desired voltage and drives current into the cell to force the voltages to be the same. The Current-to-Voltage (I/U) converter records the cell current, which forces the cell current to flow through a current measurement resistor (R_m).

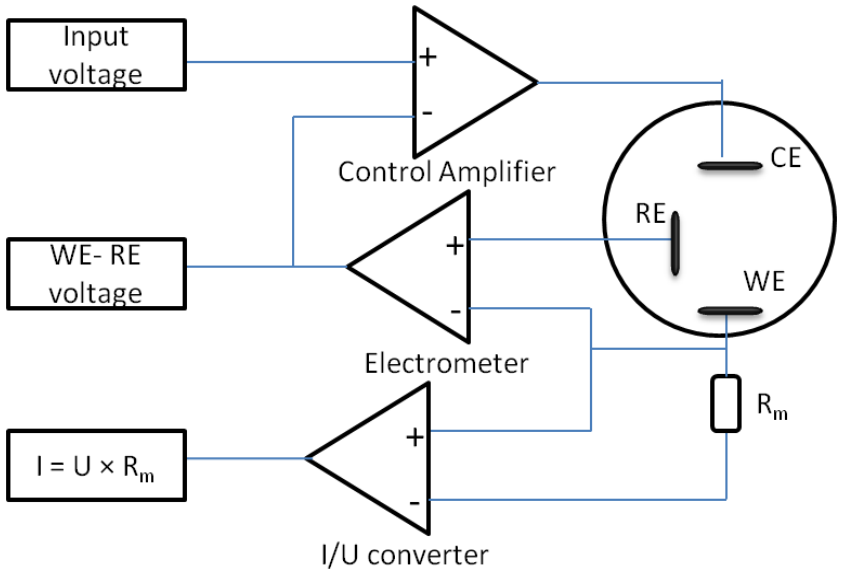

Figure 2.11A schematic representation of a three electrode potentiostat.[24]

Undoped ZnO, $ZnO_{1-x}S_x$ or $Cd_xZ_{1-x}O$ photoanodes was fashioned into a photoelectrochemical cell (PEC) test by placing a copper wire onto a bare portion of the conducting ITO substrate and securing with high purity silver conducting paint (RS 186-3593). Electrodes were sealed on all edges and around the active area of film with epoxy resin (Araldite) leaving exposed working electrode surface areas of 1.44 -1.96 cm^2.

A module of three-electrode cell was employed in the PEC measurements, as shown in Figure 2.20. A photoanode acts as a working electrode, a platinum wire was a counter

electrode, and an Ag/AgCl electrode was used as a reference electrode. All the photoelectrochemical cell tests were operated in a 0.5M Na_2SO_4 (Sigma-Aldrich, purity ≥ 99.99%) solution at pH = 6.8 as the electrolyte medium. The solar simulator was a 300W Xe lamp (Oriel research Arc lamp assembly and power supply) incorporating an air mass (AM) 1.5 global and a UV-cut filters to generate a simulated light (AM1.5) in the range from 390 nm to near IR. For the measurements of incident-photon-to-current-conversion efficiency (IPCE) a monochromator (Oriel Cornerstone 130, 1/8 m) was attached with the Arc lamp to emit the light of a specific wavelength. Photon intensity was recorded with a power meter (Newport, model 942-PE) coupled with a silicon assay detector. Potentiostat (Autolab PGSTAT128N) was used for electrochemistry measurements. Linear sweep voltammogram was employed to scan photocurrent signal at scan rate of 0.02 V/s from -0.5 V to 1.1 V with at the step potential of 0.1 V. Amperometric I-t curves were recorded for the undoped ZnO, cadmium and sulfur-doped ZnO photoanodes at an applied potential +0.8 V.

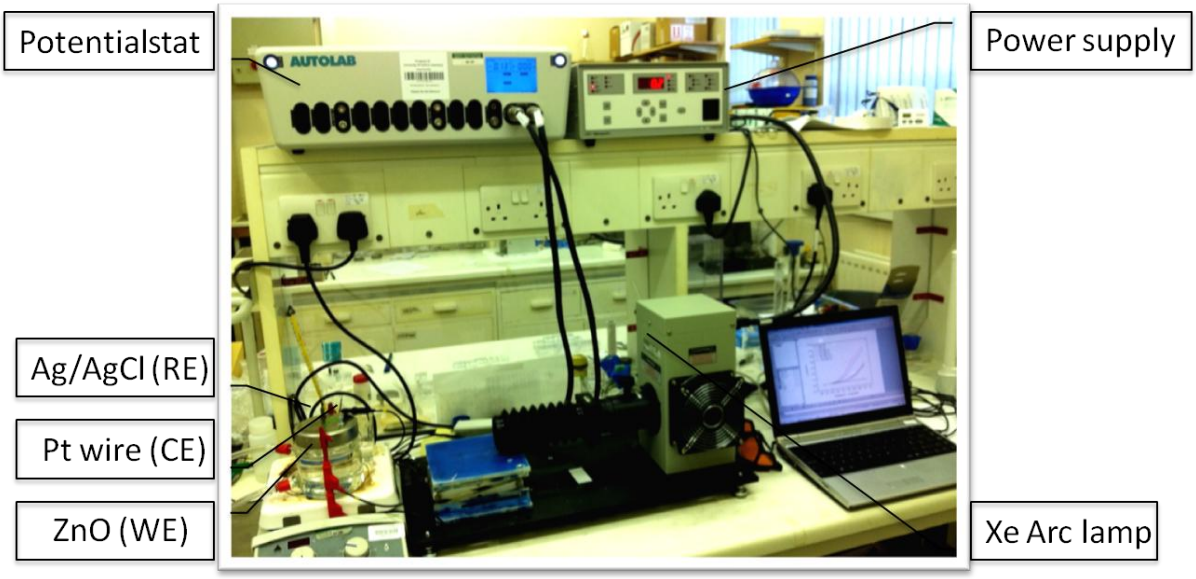

Figure 2.20A photo presented photoelectrochemical cell (PEC) station. The glassware in the left corner is a three electrode cell equipped with a working electrode (WE; ZnO), a counter electrode (CE; Pt wire), and a reference electrode (RE; Ag/AgCl).

2.10 References

1. D. A. Skoog, F. J. Holler and T. A. Nieman, *Principle of Instrumental Analysis*, 5 ed. (Harcourt Brace College, 1998).
2. P. Atkins, T. Overton, J. Rourke, M. Weller and F. Armstrong, *Inorganic Chemistry*, Fourth ed. (Oxford University Press, Oxford, 2006).
3. E. N. Kaufmann, *Characterization of Materials*. (Wiley, New Jersey, 2003).
4. B. D. Cullity and S. R. Stock, *Elements of X-ray Diffraction*, Third ed. (Addison-Wesley, Reading, 2001).
5. J. S. J. Hargreaves, Crystallography Reviews **11**, 21 (2005).
6. M. A. Moram and M. E. Vickers, Reports on Progress in Physics **72** (2009).
7. S. Hüfner, *Photoelectron Spectroscopy: principles and aplications*, Third ed. (Springer, Berlin, 2003).
8. D. H. O'Neil, A. Walsh, R. M. J. Jacobs, V. L. Kuznetsov, R. G. Egdell and P. P. Edwards, Physical Review B **81**, 085110 (2010).
9. B. K. Teo, *EXAFS: Basci Principles and Data Analysis*. (springer-Verlag, Berlin, 1986).
10. E. H. Hall, American Journal of Mathematics **2**, 287 (1879).
11. P. A. Cox, (Oxford University Press, Oxford, 1995).
12. L. J. v. d. Pauw, Philips Research Reports **13**, 1 (1958).
13. S. Elliott, *The Physics and Chemistry of Solids*. (John Wiley & Sons, West Sussex, 1998).
14. P. Kubelka and F. Munk, Zeitschrift fur technische Physik **12**, 593 (1931).
15. P. Kubelka, Journal of the Optical Society of America **38**, 448 (1948).
16. L. Yang and B. Kruse, Journal of the Optical Society of America a-Optics Image Science and Vision **21**, 1933 (2004).
17. B. Voutou and E.-C. Stefanaki, presented at the Physics of Advanced Materials Winter School, 2008 (unpublished).
18. D. B. Williams and C. B. Carter, in *A Text Book for Materials Science* (Springer, 1996), Vol. 2.
19. M. Vonheimendahl, G. Thomas and W. Bell, Journal of Applied Physics **35**, 3614 (1964).
20. E. S. W. Ridgefield and M. J. O'Neil, in *U.S. Patent* (1966), Vol. 3, pp. 484.
21. S. Oktik, Progress in Crystal Growth and Characterization of Materials **17**, 171 (1988).
22. J. Aranovich, A. Ortiz and R. H. Bube, Journal of Vacuum Science & Technology **16**, 994 (1979).
23. A. Mohanta and R. K. Thareja, Journal of Applied Physics **103**, 24901 (2008).
24. D. N. Staicopoulos, Review of Scientific Instruments **32**, 176 (1961).

CHAPTER 3

DEPOSITION AND CHARACTERISATION OF ZINC OXIDE THIN FILMS

The process of nucleation and growth in thin film materials occurs via several steps: (1) deposition, (2) diffusion on terraces, (3) nucleation on islands, (4) nucleation on second-layer islands, (5) diffusion to a lower terrace, (6) attachment to an island, (7) diffusion along a step edge, (8) detachment from an island, and (9) diffusion of dimmer.[1] Those steps in the growing process are driven by the *thermodynamic driving force* and the *lattice misfit between the substrate and the layer*. In terms of the spray pyrolysis method, essential parameters to represent the two driving forces are the *substrate deposition temperature* and the *type of substrate*. In addition, a variety of factors are also employed to optimise the quality of thin films, for instance, the film thickness, precursor (e.g. types, concentrations, and composition), and the flow rates of a carrier gas.

In this chapter, firstly, the effects of substrate deposition temperature and substrate will be studied for ZnO thin films. It is widely believed that substrate deposition temperature can dominate the structural phase and the preferential orientation of thin films via the variable precursor decomposition rates and resulting changes in atomic arrangement.

Secondly, aluminium (Al)-doped ZnO thin films will be produced using glass as a substrate. The sought-after electronic conduction in Al-doped ZnO films is due to free or itinerant electrons induced by substitution of Al for Zn in the host lattice, as well as carrier derived from oxygen vacancies. For carrier concentrations above the critical density n_c, the free electrons are able to occupy the ZnO (host) conduction band, and a subsequent widening

of the bandgap is observed, known as the Burstein-Moss (BM) effect.[2] At a higher doping concentration, an electronic bandgap shrinkage occurs and usually attributed to many-body effects.[2] Therefore, in highly doping AZO films, the observed optical bandgap is expected to reflect the combination of BM shift and bandgap shrinkage.

Lattice strain has also been shown to have an influence on the electronic bandgap. The strain has two main contributions: (1) The intrinsic strain caused by doping impurities or defects during the growth process, and (2) The extrinsic strain induced by lattice mismatch and the resulting difference in thermal expansion coefficients between the film and the substrate. Sharma *et al.*[3] showed that bandgap widening in 1-5% Al-doped ZnO films was due to lattice strain not the BM effect. The free carrier densities for these AZO films were smaller than the critical electron density, suggesting that the Fermi level was below the conduction band minimum (CBM) and the BM effect should not be involved in the variation in the bandgap. Recently, a blue shift in the electronic bandgap of ZnO was produced by increasing the biaxial strain via an annealing process.[4] *ab initio* calculations confirmed that the bandgap should increase with increasing biaxial tensile stress. These calculations further suggested that the offset in the valence band maximum (VBM) was larger than that in the CBM responding for the increase in the bandgap.[5] In contrast to the expected carrier density-dependent increase in bandgap, Mohanty *et al.*[6] observed that the optical bandgap in the AZO samples was narrowed by relaxing the in-plane stress by increasing the film thickness. According to these authors, the presence of in-plane stress in films is responsible for the anomalous changes in the bandgap.

The literature cited above point the lattice strain and not the BM effect as the dominant source of the shift of bandgap for AZO films. However, one could speculate that

the BM effect has a greater influence on AZO films as a consequence of the efficacy of the Al^{3+}-induced free electron carriers filling the CBM (with, in theory, 1 carriers per Al dopant ion). Although a number of papers ascribed the blueshift in the bandgap to the BM effect, the lattice strain-induced bandgap shift was not taken into account. This could lead to an inaccurate estimation for the relationship between the energy shift in the bandgap and the induced electron density. In this section, a series of AZO films were prepared with no lattice strain difference by controlling the film thickness. The strain effect, which was thought to be the major contributing factor, was excluded in the present work by examining the films with bandgap volume-deformation potentials and direct in-plain stress and out-plain strain measurements. As a result, the energy shift in the electronic bandgap can be accurate to account for the free electron density (BM effect).

The substrate plays an important role in the thin film growth. The lattice misfit at the substrate/film interface leads to the atomic arrangement at the initial nucleation step. A substrate can act as a template dominating the initial structure of thin layers if the lattice misfit is small. Heterogeneous substrates, such as *a*-, *c*- and *r*-plane sapphire, GaN, GaAs(001), Si(111) and $ScMgAlO_4$(0001) have been used to prepare ZnO epilayer.[1, 7-12] Among these substrates, *c*-plane sapphire(0001) (i.e. Al_2O_3(0001)) is one of the ideal substrates for growing ZnO epilayer due to the fact that it has the same lattice (hexagonal), assesses to grow a high quality ZnO film, and has a reasonable cost. Epitaxial growth of ZnO films on Al_2O_3(0001) has been demonstrated in the ultra-high vacuum (UHV) based techniques, such as molecular beam epitaxy (MBE), pulse laser deposition (PLD), and atomic layer deposition (ALD).[1, 7, 13, 14] The in-plane lattice mismatch (m) between ZnO and Al_2O_3(0001) is significant (31.7%), estimated by $m = (a_Z - a_A)/a_A$, where a_Z (0.324 nm) and a_A (0.475 nm) are the lattice constants of ZnO and Al_2O_3(0001), respectively. A large lattice

mismatch (31.7%) is not expected to yield epitaxial growth. However, it was found that the lattice mismatch at the ZnO/Al_2O_3(0001) interface is reduced to 18.1% through a 30˚ rotation of ZnO relative to sapphire in the c-plane.[1, 15] The subsequent mismatch is derived from the expression of m = $(\sqrt{3}a_Z - a_A)/a_A$. Based on this observation, the reduced lattice mismatch appears to give a reasonable explanation for growing a ZnO epilayer on Al_2O_3(0001). To the best of our best knowledge, the epitaxial growth of ZnO has been achieved by UHV-based techniques but not by any non-vacuum system method. Spray pyrolysis is a non-vacuum system with a large-scale film production at low cost. In this chapter, the epitaxial growth of ZnO films on Al_2O_3(0001) will be carried out using the spray pyrolysis technique and the relevant evidences will be presented by XRD and high resolution transmittance electron microscopy.

3.1 The Effect of Substrate Deposition Temperature

3.1.1 The Influence of Substrate Deposition Temperature on Film Texture

Zinc acetate (ZA) anhydrous [$Zn(CH_3COO)_2$ 99.99%, Sigma-Aldrich] was used as a precursor to prepare the ZnO thin films. Figure 3.1 shows the thermal properties of ZA precursors examined by the thermal gravimetric analysis (TGA) and the differential scanning calorimetry (DSC). DSC curve exhibits the decomposition of ZA as an endothermic reaction. The drops appeared at 70˚C in the TGA and DSC curves are attributed to the water evaporation and the formation of anhydrous ZA. The sublimation of ZA is observed at 193˚C, with a small tip in DSC curve.[16] As the temperature increases, a sharp endothermic peak at

250˚C appears and is referred to the melting of anhydrous ZA since there is no significant weight loss in the TGA curve. After the peak, a massive weight loss in the TGA curve and a significant endothermic drop in the DSC curve are found in the range of 230-330˚C. This downward plunge at 230-330˚C is ascribed to the releases of a variety of species, including acetic acid produced via deanation, acetone generated via ketonisation of acetic acid, water which may be produced via dehydrogenation of Zn-OH linkages, and carbon dioxide produced through the thermo-oxidation of organic species.[17, 18] This is followed by anhydrous ZA decomposition into ZnO at approximately 350˚C and the oxidation reaction at around 380˚C as shown in an exothermic peak. The pyrolysis process of ZA can be summarised as dehydration, vaporization, melting, decomposition, and oxidation.[16]

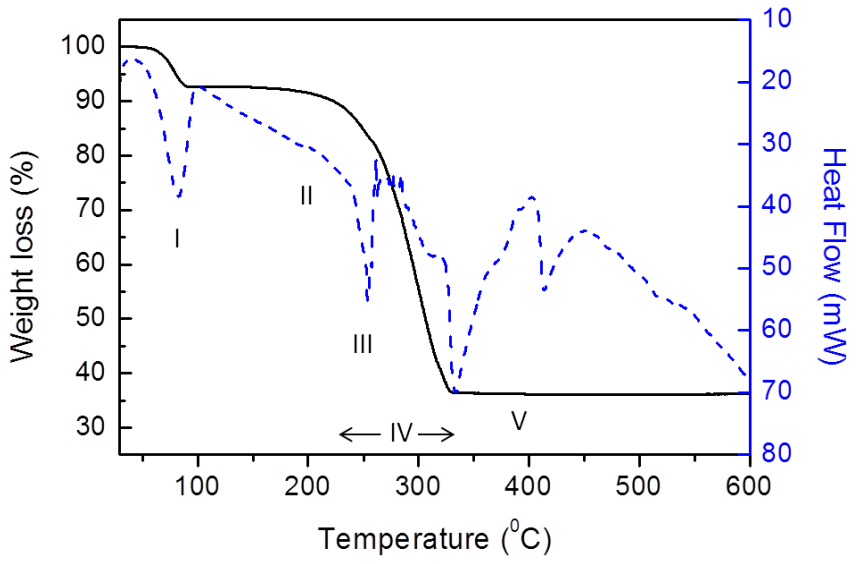

Figure 3. 1 Thermal gravimetric analysis (TGA) and differential scanning calorimetry (DSC) for Zinc acetate anhydrous, heating from 30˚C to 600˚C at heating rate of 5˚C/min with argon gas flow. The pyrolysis process of zinc acetate is listed as the following, I : dehydration, II : sublimation, III : melting, IV : decomposition and V : oxidation.

Figure 3.2 shows the X-ray diffraction patterns of ZA deposited on a glass substrate at various deposition temperatures (T_d). Consistent with the observation in Figure 3.1, the film at 100˚C still remains as ZA and starts to transform into ZnO at 200˚C. The weak ZnO peak and the high background intensity imply that a small number of crystallites are surrounded by a large portion of amorphous substances at this temperature. As T_d increases, the crystallinity is improved. The (100) and (110) planes are growing between 200°C and 350°C and diminishing at temperature above 350°C. In contrast, the (002) plane increasingly predominates when the T_d continues to rise, leading to a strong preferential orientation along the *c*-axis. The (002) plane becomes dominant at a higher temperature since the basal (001) plane has the lowest surface energy. The calculated surface energies for the wurtzite ZnO film follow the sequence $\gamma(001)$; 0.099 eV/Å^2 > $\gamma(110)$; 0.123 eV/Å^2 > $\gamma(101)$; 0.209 eV/Å^2.[19] On the film surface, the (001) plane can process lattice relaxing or reconstruction to minimum the surface energy but the (001) and (110) planes cannot act in the same way. The texture of the film tends to grow along [001] direction with the lowest surface energy under thermodynamic control conditions (i.e. a high thermal energy input). For example, the ZO500T film that grows at 500˚C, (i.e. ZO500T gains the highest thermal energy when compared to other films at lower temperatures) shows an absolutely strong orientation in (002).

Table 3. 1 The summary of the lattice constant, out-plane strain (δ), grain size and bandgap energy for ZnO thin films at different deposition temperatures. The grain size is derived from the XRD results via the Scherrer equation.

Samples	*c* (nm)	δ	grain size (nm)	Bandgap (eV)
ZO100T	-		-	3.95
ZO200T	-		-	3.33
ZO300T	0.5195	-0.0021	27.7	3.30
ZO350T	0.5184	-0.0042	56.3	3.30
ZO375T	0.5181	-0.0048	66.3	3.30
ZO400T	0.5181	-0.0048	81.6	3.31
ZO450T	0.5177	-0.0056	45.5	3.31
ZO500T	0.5177	-0.0056	56.3	3.30
ZnO single crystal	0.5206			

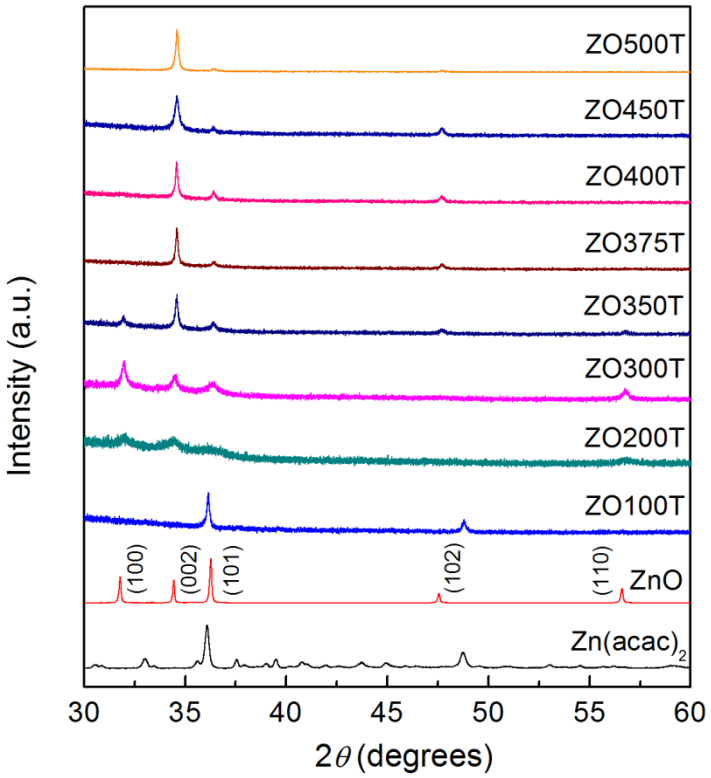

Figure 3. 2 Ex-situ X-ray diffraction measurements for ZnO films deposited at temperatures between 100˚C and 500˚C; reference spectra for zinc acetate salt and zinc oxide powders are included.

The derived lattice constant *c* for the deposited films is listed in Table 3.1. The out-plane strain (δ) is determined by the equation

$$\delta = \frac{(c - c_0)}{c_0} \tag{3.1}$$

where *c* and c_0 are the lattice constants for the films and a strain-free ZnO single crystal, respectively.[20] The negative δ shown in Table 3.1 indicates a compressive out-plane strain. In other words, the growing plane that is parallel to the substrate (i.e. in-plane) must be made tensile stress. It is found that the compressive stain increases with increasing T_d. Note that the lattice strains in these films are influenced by the different thermal expansion coefficients between the ZnO layer ($\alpha = 7 \times 10^{-6}$/°C) and the soda-lime glass substrate ($\alpha = 9 \times 10^{-6}$/°C). The extent of expansion in the glass is more significant than that in ZnO. As such, the faster expanding substrate enforces a tensile strain on the *ab* plane of ZnO. When the T_d is higher, the in-plain tensile stress will be larger.

Figure 3.3 presents the morphologies of ZnO films grown at (a) 400˚C (ZO400T), (b) 450˚C (ZO450T), and (c) 500˚C (ZO500T) deposition temperatures revealed by atomic force microscopy (AFM). ZO400T has the largest grains which have a rod-like shape. ZO450T had the smallest grain size among these three films. The observed grain sizes from the AFM are in consistence with the XRD results via the Scherrer equation (Table 3.1).

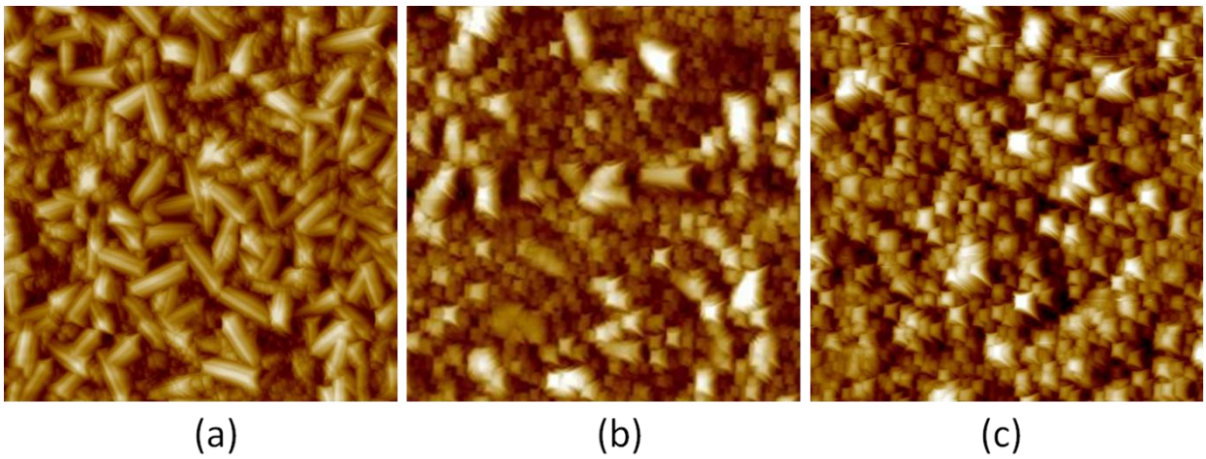

Figure 3. 3 Atomic force microscopy (AFM) images for (a) ZO400T, (b) ZO450T, and (c) ZO500T films. The dimension of each image is 5 x 5 µm.

3.1.2 Optical Properties

Figure 3.4 shows the UV-Vis transmittance spectra of ZnO films at various growing temperatures. All films are highly transparent (80-90%) in the region above 400 nm. The feature of ZO100T is similar to the glass substrate, reflecting the fact that ZnO is not formed at 100˚C and ZA does not absorb ultraviolet (UV) and visible light. At 200˚C, ZO200T is partially transparent in the near UV region because ZA decomposes to form ZnO. The rest of the films that are grown at higher temperatures demonstrate a typical n-type ZnO film with a wide bandgap.

The dependence of the electronic bandgap of ZnO films on T_d was determined by optical absorption measurements (Figure 3.5). Interband transitions in ZnO involve excitation from the states of dominant O 2p character at the top of the valence band to the states of dominant Zn 4s character at the bottom of the conduction band.[21] The lowest interband transitions are direct and the optical bandgap can be derived from the Tauc equation,[22]

$$(\alpha hv)^2 = c(hv - E_g) \tag{3.2}$$

where α is the absorption coefficient, hv is the incident photon energy, c is a constant and E_g is the optical bandgap energy. The determined bandgap values are approximately in the range of 3.0-3.1 eV except for ZO100T and ZO200T (Table 3.1). The value in ZO100T reflects the value of the glass substrate.

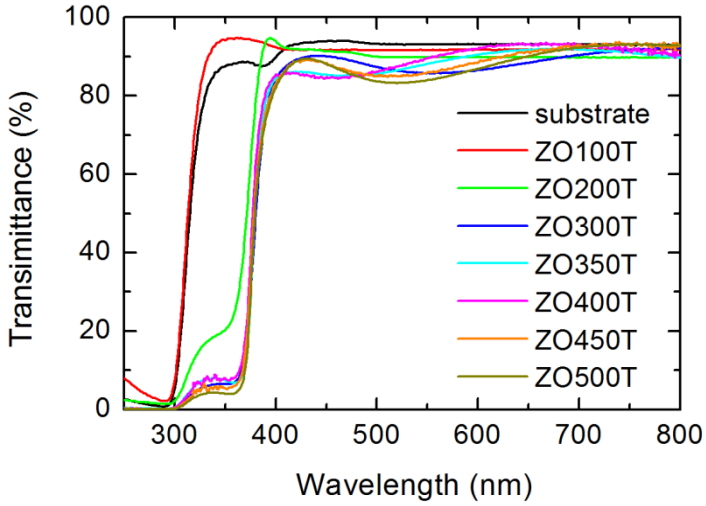

Figure 3. 4 The measured UV-Vis Transmittance spectra of ZnO films at the deposition temperatures from 100˚C to 500˚C. The substrate is a sode-lime glass.

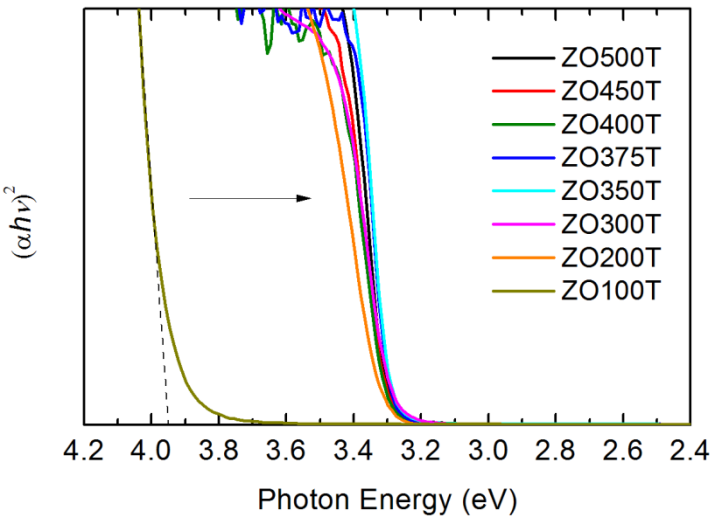

Figure 3. 5 Bandgap determination from the plots of $(\alpha h\nu)^2$ versus photon energy for ZnO films at the deposition temperatures from 100˚C to 500˚C.

3.1.3 Electrical Transport Properties

Electronic transport properties, including electron carrier density, electron mobility and conductivity depend on many factors, such as grain boundary, crystallinity, crystal structure, and lattice defects. A polycrystalline material is composed of differently orientated crystallites joined together by grain boundaries. Grain boundaries are the interfaces where crystals of different orientations meet. There are a significant number of defects formed by incomplete atomic bonding at the interface between the grains. However, each crystallite can be regarded as a single crystal due to a periodical atomic arrangement. Therefore, it is widely accepted that a crystal with larger grains has fewer grain boundaries and a higher degree of crystallinity.

Figure 3.5 shows the relationships between the grain size, electron density, and conductivity as a function of substrate deposition temperature in the prepared ZnO thin films.

The variations in the electron density and conductivity are consistent with the variations in grain size. Films deposited at 100˚C and 200˚C are not conductive due to the rough surface, porous texture and the presence of ZA material. The electron density and conductivity rise from ZO320T to ZO375T, followed by a dramatic increase in the electron density and conductivity in ZO400T film. Then the electron density and conductivity drop sharply in ZO450T and recover in ZO500T. Among these samples, ZO400T displays the best performance in terms of electron density and conductivity, which is due to the largest grain size. Moreover, in the Seto's model, the grain boundaries are capable of trapping electrons to create potential charged barriers. These barriers are likely to reduce the numbers of free carriers available for electrical conductivity.[23] Therefore, in terms of the effect of crystallinity and the established Seto's model, the grain size is assumed to affect the conductivity and electronic density in this case.

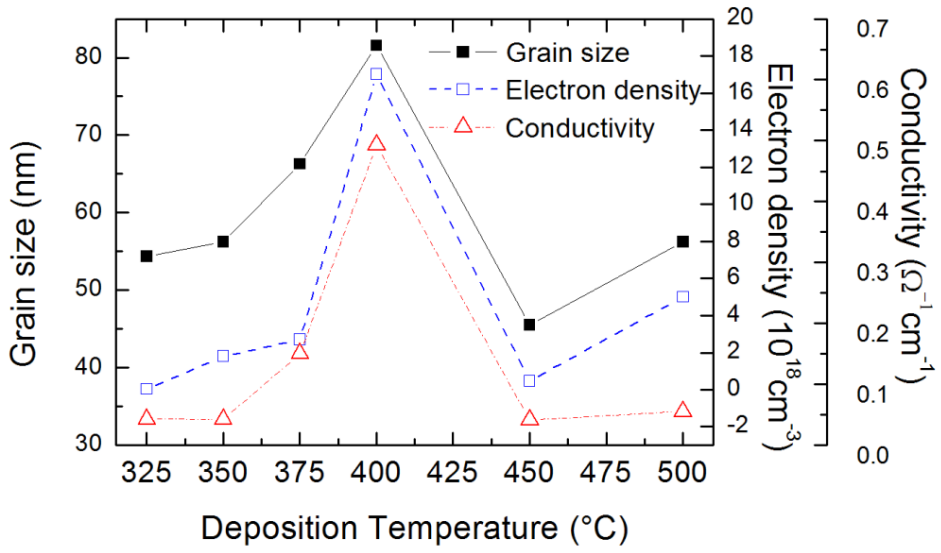

Figure 3. 6 Room-temperature electron density, conductivity and grain size versus the substrate deposition temperature of ZnO thin films.

3.2 Aluminium Electron-Induced or Strain-Induced Bandgap Blueshift

3.2.1 The Preparation of Aluminium Doped ZnO Thin Films

All films were deposited onto glass substrates (Menzel-Gläser cover glass) using a custom-built spray pyrolysis system with a substrate temperature of 500°C using nitrogen as carrier gas. 1 mol. % of $AlCl_3$ was added as a doping precursor to 0.5 M zinc acetate acid solution. The AZO films thickness was to be 271 nm, 362 nm, 807 nm and 1281 nm. There films are hereafter designed as AZO-271, AZO-362, AZO-807 and AZO-1281 in the present work, respectively. For comparison, an undoped ZnO film was deposited from 10 mL precursor solution (190 nm in film thickness). The thickness of these films (Table 3.2) was extracted from the optical data by fitting the observed transmission to a simulated transmission function using WVASE software package.

3.2.2 Aluminium Electron-Induced Bandgap Shift

Figure 3.6 shows a plot of the $(\alpha h\nu)^2$ versus photon energy $h\nu$ for ZnO and AZO films (all doped at 1% Al) with different thickness, where α is the optical absorption. The interband transitions of ZnO involve excitation from states of dominant O 2p character at the top of the valence band to states of dominant Zn 4s character at the bottom of the conduction band.[21] The direct bandgap can be derived from the Tauc equation. The results are presented in Table 3.2.[22] All AZO samples have larger optical bandgaps than ZnO. The bandgap increases from AZO-271 to AZO-807, then decreases in the thickest film, AZO-1281. The bandgap increase up to AZO-807 film can be viewed in terms of the BM effect. The subsequent decrease for the thickest film will be discussed in Chapter 3.2.3.

Table 3. 2 Optical and electronic measurements for the undoped ZnO and Al-doped ZnO films. Film thickness is extracted from the UV-Vis transmittance data. Electron density is measured by Hall effect measurement.

Sample	Film thickness (nm)	Bandgap (eV)	Electron density[(a)] (10^{19} cm^{-3})	BM shift (eV)	Mobility (cm^2/ Vs)	Roughness (nm)	Resistivity (Ωcm)
ZnO	190(4)	3.29(4)	0.18(6)	0.020	0.16(5)	48	16.3
AZO-271	271(7)	3.33(3)	2.35(5)	0.115	1.01(8)	4.75	0.132
AZO-362	362(9)	3.36(2)	3.61(9)	0.153	1.14(3)	7.23	0.153
AZO-807	807(1)	3.37(4)	3.84(7)	0.160	1.82(3)	15.21	0.089
AZO-1281	1281(4)	3.31(3)	0.99(1)	0.065	0.66(4)	80.52	0.943

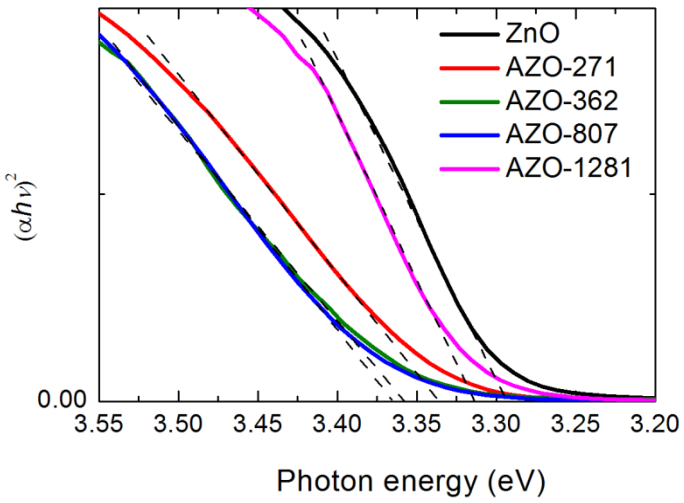

Figure 3. 7 The Squared optical absorption coefficient *v.s.* photon energy for the undoped ZnO and Al-doped ZnO films of different thickness (thickness shown as the number behind AZO-). Bandgap values were determined by a linear extrapolation along the leading edge curve to the background.

The magnitude of the BM energy shift, i.e. the position of Fermi level, with respect to the bottom of conduction band, can be obtained from the free-electron approximation:[2]

$$\Delta E_{BM} = E_f - E_c = \hbar^2 / 2m^* \left(3\pi^2 n\right)^{2/3} \quad (3.4)$$

where $\hbar$ is the Planck constant, m^* is the electron effective mass and n is the electron density determined from Hall effect measurements (Table 3.2). We use $m^* = 0.26\ m_0$ here, assuming that the electron effective mass remains unchanged within the occupied part of the conduction band.[2, 24] The results of the calculations are listed in Table 3.2.

The Fermi levels lie above the CBM by between 0.065 eV and 0.160 eV for the films investigated. The value for the undoped ZnO is relatively low, and (reassuringly) reflects the fact that the Fermi level should be near the bottom of conduction band. Carrier densities derived from the Hall effect data confirm that the blue shift in the optical bandgap is dominated by the BM effect. Moreover, the Mott-Edwards-Sienko criterion was adopted here to identify the critical density for the onset of degeneracy at which it is presumed that the position of the Al^{3+} donor states merges with the CB:[25, 26]

$$n_c^{1/3} a^* \geq 0.26 \quad (3.5)$$

where a^* is the Bohr radius of the isolated donor state, here taken as 1.4 nm for n-type donors in ZnO.[27] The critical electron concentration is then calculated to be 6.41×10^{18} cm^{-3}. When the free carrier concentration is greater than the critical carrier concentration ($n > n_c$), then the Fermi level lies above the CBM. In contrast, the Fermi level lies within the bandgap when $n < n_c$.

The bulk electron densities derived from the Hall effect measurements are listed in Table 3.2. In all cases carrier densities are above the critical value. This observation is

consistent with the results of the BM shift energy. The reduction in the thickest film is probably due to an increasing number of defects that act as compensating carrier traps,[20] which will be subsequently discussed in Chapter 3.2.3.

The valence band (VB)-XPS of the ZnO and the AZO-362 film are shown in Figure 3.8. High resolution VB-XPS probes the cross section weighted density of states in the valence band. The two spectra are aligned with the Fermi level at 0 eV. The peak at the binding energy of 10.9 eV is attributed to Zn 3d states. In the VB region, peak A (7.8 eV) correspond mainly to the hybridised of Zn 3d, Zn 4s, and O 2p orbitals. Peak B (4.9 eV) is O 2p states mixed with Zn 3d and a small amount of Zn 4p states.[6, 21, 28] The position (ξ) of the valence band maximum (VBM) relative to the Fermi level (E_f) can be determined from the linear extrapolation of the band edge. ξ is 3.30 ± 0.05 eV for the ZnO, indicating that the VBM is below the Fermi level by 3.30 ± 0.05 eV. It is worth noticing that the ξ value for the ZnO is within experimental error the same as the optical bandgap value of 3.29 ± 0.04 eV. This implies that the Fermi level is located near the CBM. The ξ for the AZO film (362 nm) is 3.41 eV ± 0.05 eV, indicating that the Fermi level lies above the conduction band minimum. These results confirm the determinations of BM shift energy and also our analysis based on the Mott-Edwards-Sienko criterion.

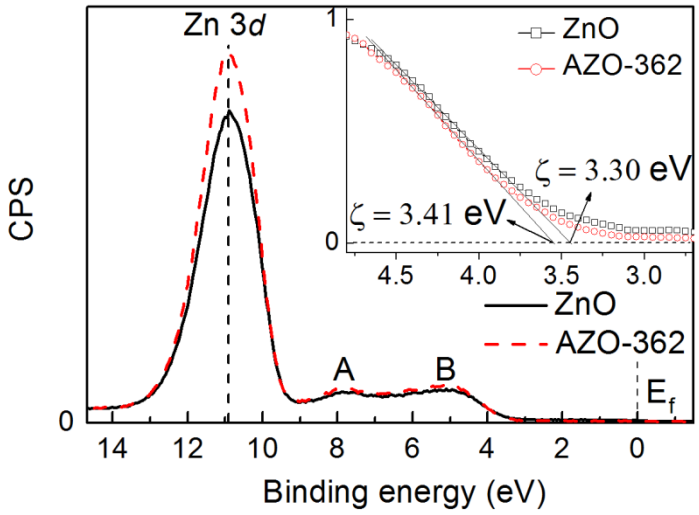

Figure 3. 8 Valence band (VB) X-ray photoelectron spectra of ZnO and the 362 nm thick Al-doped ZnO films are displayed in the region of VB and Zn 3d. The position (ξ) of the valence band maximum (VBM) relative to the Fermi level is obtained from the linear extrapolation of the band edge - see insert.

Figure 3.9 shows XRD patterns for a range of ZnO and AZO films deposited at 500°C normalised to the (002) peak. Only ZnO peaks are apparent in the XRD patterns. Not surprisingly the signal to noise ratio is the poorest for the thinnest film AZO-271. The (002) peak becomes more intense and sharper as the thickness increases. The intensity of (101) reflection is enhanced relative to (002) as the film thickness increases. The (002) peak for the AZO films is shifted to lower 2θ values relative to the ZnO thin film sample, yet to higher values compared to a ZnO bulk reference. A decrease in the angle for the (002) diffraction peak with Al^{3+} doping is attributed to the difference in ionic sizes between Zn^{2+} (72pm) and Al^{3+} (53pm).[29-31] The literature contains reports of shifts toward both high and low angle, depending on film preparation techniques and experimental conditions.[29-31] In agreement with previous work we infer from the peak narrowing that the grain size increases slightly as the film thickness increases.[32] The grain size increases slightly as the film thickness increases,

because the deeper layers of atoms are subjected to stronger interatomic forces thus rearranging into larger crystals.[32, 33]

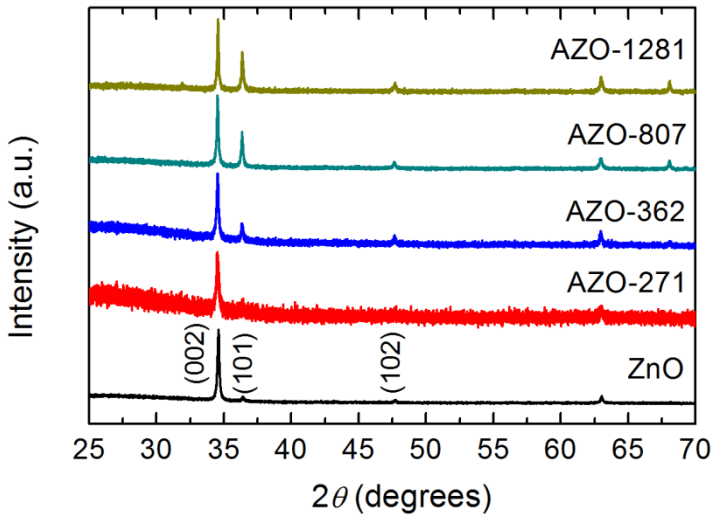

Figure 3. 9 Powder X-ray diffraction spectra for the undoped ZnO and Al-doped ZnO films deposited at 500°C from 5, 10, 20 and 30 mL of precursor solutions, which resulted in films of different thicknesses.

3.2.3 Examination of Strain

Strain is another essential factor which influences changes in the electronic bandgap. In order to explore the influence of strain on the bandgap, two factors had to be considered. First of all, the bandgap volume-deformation potential (α_v) describes the relationship between strain and the magnitude of bandgap change. In the case of hydrostatic stress application, the energy shifts in the conduction and valence bands are related to the magnitude of the fractional unit cell volume change, which is expressed as $\alpha_v = \partial E_g / \partial \ln V$, where ∂E_g is the electronic bandgap offset and V is the unit cell volume.[34] Based on this equation, the variation of bandgap with pressure can be therefore derived in terms of the relative volume change: $\Delta E = \alpha_v \times (V - V_0)/V_0$, where V_0 is the reference volume.[35] For hexagonal wurtzite ZnO α_v

value is -1.7 eV.[36] The fractional changes in cell volume derived from the diffraction date are 0.38%, 0.48%, and 0.42% for the 362 nm, 807 nm, and 1281 nm thick AZO films with respect to 271 nm one. These volume changes are expected to produce corresponding changes to the bandgap of -6.46 meV, -8.20 meV, and -7.14 meV, respectively. The values are much too small to be counted in the optical bandgap shift. For instance, the bandgap increases by 40 meV from the 271 nm to the 807 nm thick film, compared with the value of the volume-induced bandgap shift of only 8.2 meV.

The second approach to examine the effect of strain is to estimate the out-plane and the associated in-plane stress in ZnO and AZO films. The out-plane strain (δ) is defined as,

$$\delta = (c - c_0)/c_0 \tag{3.6}$$

where c and c_0 are the lattice constants for the samples and the strain-free bulk ZnO, respectively.[20] The negative value of δ shown in Table 3.3 indicates a compressive strain. The ZnO film reveals an effective compressive strain of -0.00012 along the c-axis.

With regard to AZO films, due to the lack of information for a strain-free 1% Al-doped ZnO lattice as the c_0 reference, the strain-free bulk ZnO is adapted as the reference for all AZO films instead. The out-plane strains for the AZO films are almost the same, which implies that there is nearly no out-plane strains difference between the AZO films.

In-plane stress (σ), i.e. parallel to the substrate surface, can be derived via the biaxial stress model:[6, 20]

$$\sigma = \left[2C_{13} - C_{32} \times \frac{C_{11} + C_{12}}{C_{13}} \right] \times \frac{c - c_0}{c_0} \tag{3.7}$$

where C_{ii} is the elastic stiffness constant (C_{13} = 1.05×10^{11} Nm^{-2}, C_{33} = 2.1×10^{11} Nm^{-2}, C_{11} = 2.1×10^{11} Nm^{-2}, and C_{12} = 1.2×10^{11} Nm^{-2}).[3] This yields a numerical relation between in-plane stress and out-plane strain values: σ = - 450 × 10^9 δ. Table 3.3 shows that σ is a tensile stress

with values ranging between 13.8×10^7 and 25.9×10^7 Nm^{-2} for the studied AZO films. It should be mentioned that both the out-plane strain and in-plane stress in the AZO samples are almost the same for all samples as the differences between the σ and δ values are negligible. Therefore, the bandgap shift is not related to the strain. Be aware that the growth temperature and doping concentration for all the films were controlled to be the same. Therefore, the magnitudes of strain induced by thermal expansion and impurity dopants are expected to be the same.

Table 3. 3 Lattice parameters (a and c), grain size, out-plane strain (δ), and in-plane stress (σ) for the undoped ZnO film, Al-doped ZnO films, and ZnO bulk reference. Grain size was derived from the XRD patterns through the Scherrer equation. ZnO bulk reference data adapted from database (JCPDF number: 00-003-0888).

Sample	*a* (nm)	*c* (nm)	V (nm^3)	Grain size (nm)	δ	σ (10^7 N/m^2)
ZO bulk ref.	0.32480	0.52069	-	-	-	-
ZnO	0.32500(9)	0.52064(1)	0.04765(1)	56	-0.00012	4.32
AZO-271	0.32450(7)	0.52040(1)	0.04740(8)	53	-0.00058	25.1
AZO-362	0.32490(4)	0.52041(7)	0.04758(8)	53	-0.00056	24.2
AZO-807	0.32505(6)	0.52050(1)	0.04763(2)	61	-0.00037	16.4
AZO-1281	0.32500(1)	0.52040(3)	0.04760(4)	70	-0.00058	24.2

The increasing bandgap for the AZO films of 271 nm, 362 nm and 807 nm thickness is related to the BM effect and drops to 3.31 eV in 1281 nm. The out-plane strain for these films is constant.

A red shift in the optical bandgap for the AZO 1281 nm thick film is as compared to other samples likely attributed to the decrease in free carrier density. The bandgap reduces as well as the BM shift energy as the result of fewer free electrons filling in the CB. Interestingly, a thicker film with a larger grain size normally has a higher carrier mobility and density and lower resistivity. However, the thickest film in the present work exhibits the

opposite trend, exhibiting lower carrier density, lower mobility, and higher resistivity. A polycrystalline material model was proposed to explain this phenomenon with the considerations of grain boundary and potential energy barrier.[23] A polycrystalline material is of course characterised by grain boundaries between and within different small crystallites. The atoms or ions at the grain boundaries can be viewed as defects due to the incomplete bonding. The defects act as carrier traps to block the free carriers and thereby immobilise them, in which a potential energy barrier is formed and the barrier inhibits the motion of carriers from one crystallite to another. Therefore, we propose that the observed reductions in the mobility, free electron density and conductivity for the thickest film probably arise from the above factors. The electronic properties for all films are listed in Table 3.2.

3.3 The Effect of Substrate

3.3.1 The Orientation Relationship between Film and Substrate

The X-ray diffraction pattern of the ZnO (0002) epilayer grown on Al_2O_3(0001) substrate is shown in Figure 3.10. The substrate deposition temperature for preparing the epitaxial film is controlled at 500˚C. The ZnO (0002) diffraction peak demonstrates a highly orientated growth perpendicular to the substrate surface. The full width at half maximum (FWHM) of (0002) peak is 0.069^{o}, indicating an excellent crystallinity of ZnO epitaxial film.

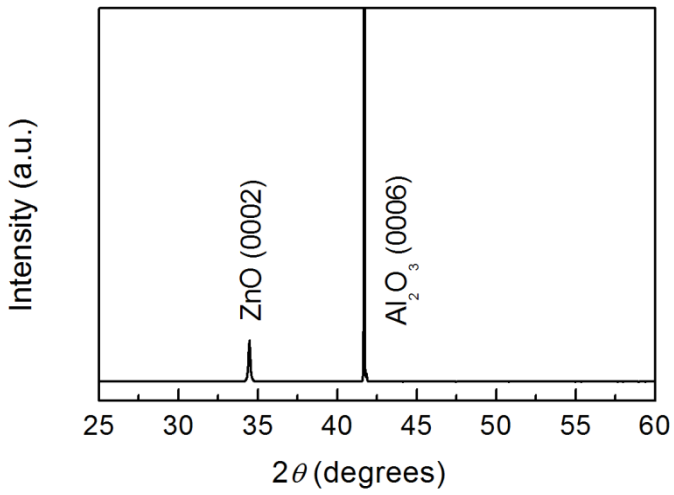

Figure 3. 10 High resolution X-ray diffraction 2 ϑ scan for ZnO grown on Al_2O_3(0001) substrate.

To investigate the orientation relationship at the interface of ZnO and Al_2O_3(0001), the cross-sectional image obtained using the high resolution transmittance electron microscopy (HRTEM) is shown in Figure 3.11. The ZnO layer is on the bottom left while Al_2O_3(0001) is on the top right. The electron beam penetrates along $[2\bar{1}\bar{1}0]$ axis of ZnO. The image shows a highly crystalline ZnO with a large single-crystal domain. The measured d spacings of d_Z and d_A are 0.52 nm and 0.43 nm, corresponding to the ZnO (0002) and Al_2O_3 (0003), respectively. This indicates that the two *c*-axis of ZnO and Al_2O_3(0001) are parallel, expressed as ZnO (0001) ‖ Al_2O_3 (0001).

Figure 3.12 shows a selected area electron diffraction pattern of the heteroepitaxial ZnO on Al_2O_3(0001) film. The electron beam is directed along the $[2\bar{1}\bar{1}0]$ axis of ZnO. The small spots reflect the diffractions by ZnO and the larger points are made by Al_2O_3(0001). This pattern presents the orientation relationship between the film and the substrate: ZnO $(0001)[21\bar{1}0]$ ‖ Al_2O_3 $(0001)[2\bar{1}\bar{1}0]$. Therefore, a 30˚ rotation the main domain is observed

in the ZnO (0001) lattice in reference to Al_2O_3(0001) substrate. A schematic illustration of the orientation relationship is exhibited in Figure 3.13.

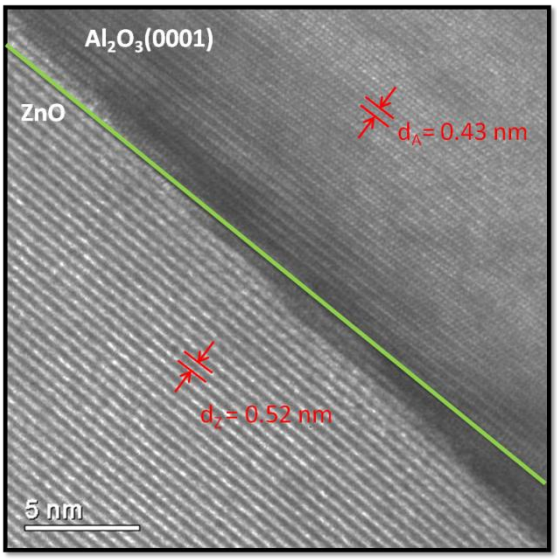

Figure 3. 11 Cross-sectional high resolution transmission electron microscopy (HRTEM) image displays the ZnO epitaxial layer (bottom left) deposited on the Al_2O_3(0001) substrate (top right). The green diagonal line is the interface. d_Z and d_A are referred to d spacings for ZnO and Al_2O_3(0001), respectively.

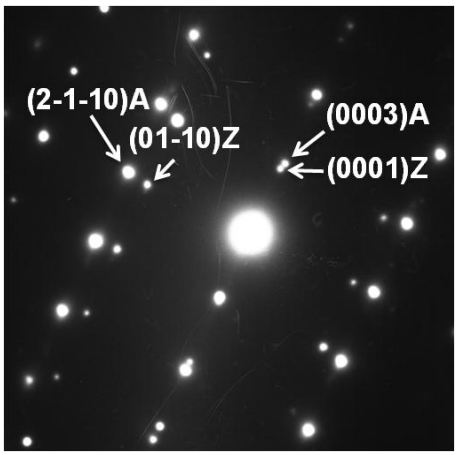

Figure 3. 12 The selected area electron diffraction pattern of the ZnO epitaxial film. The electron beam is directed along the $[2\bar{1}\bar{1}0]$ zone axis of ZnO. The Z and A are referred to ZnO and Al_2O_3(0001), respectively.

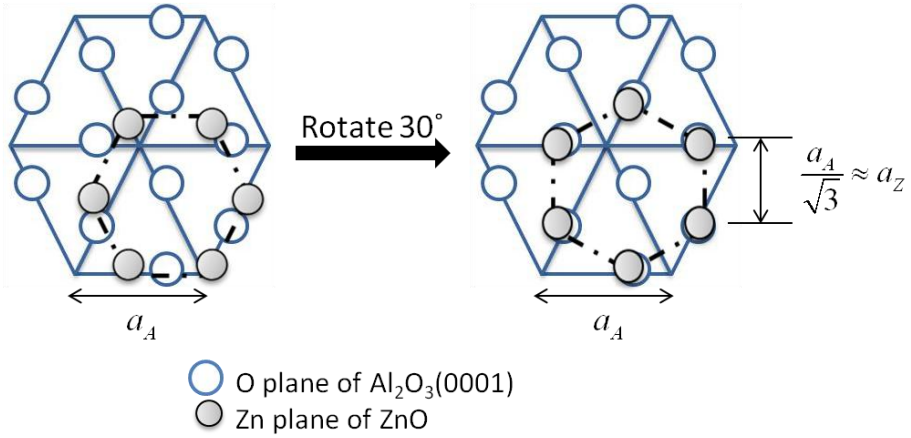

Figure 3. 13 Illustration of orientation relationship between ZnO and Al_2O_3(0001) substrate with a 30˚ rotation of the main domain.

3.3.2 Lattice Matching Epitaxy versus Domain Matching Epitaxy

According to conventional models for lattice matching epitaxy (LME), the critical lattice misfit should be less than 7-8% in order to promote epitaxial growth of a thin film. Films tend to grow textured or polycrystalline morphology if the values of LME is larger than 7%.[37, 38] However, the lattice mismatches are often larger than 7% in many heteroepitaxial films, for instance TiN/Si(100) and AlN(0001)/Si(111).[38] The LME describes that film layers grow by one-to-one matching of lattice constants across the film/substrate interface.[38] Based on this, the LME value for our film is 18.1% with the consideration of lattice rotation. On the other hand, domain matching epitaxy (DME), where integral multiples of planes match across the interface, is able to interpret the epitaxial growth of a thin film with a large lattice mismatch (> 8% by LME).[38, 39] The equation of DME is expressed as

$$m_d(\%) = \frac{ma_f - na_s}{na_s} \times 100\% \qquad (3.8)$$

where m and n are the integral numbers of the lattice planes for the film and substrate in the domain, and a_f and a_s are the lattice constants for the film and substrate, respectively. The domain match plane numbers are 5/6 for ZnO/Al_2O_3(0001).[38] Therefore, the equation 3.8 becomes $m_d = (5\times\sqrt{3}\times a_Z - 6\times a_A) / 6\times a_A$, and gives the DME values at approximately -1.5%. Based on the small values obtained with the DME expression, it is concluded that Al_2O_3(0001) can be used as the substrate for growing ZnO epilayer.

3.3.3 Al_2O_3(0001) Substrate versus Glass Substrate

As mentioned at the beginning of this chapter, the thin film growth process is determined by the thermodynamic driving force and the misfit between the substrate and the layer. The influence of those two driving forces can be seen in Figure 3.14. This figure shows the XRD patterns of ZnO deposited on Al_2O_3(0001) and glass substrates at the deposition temperatures of 400-500˚C.

The effects of the substrate deposition temperature on ZnO deposited on glass films have been discussed in chapter 3.1, where a film is favourably growing along *c*-axis at high temperature since (0002) plane has the lowest surface energy (i.e. thermodynamic control). This effect is also seen in the ZnO deposited on Al_2O_3(0001) film. The films grown at 400˚C and 450˚C demonstrate a polycrystalline structure, which is the same as for the films grown on glass substrate. Interestingly, the critical temperature is 500˚C at which ZnO epilayer can be produced by using a Al_2O_3(0001) substrate but not a glass substrate. ZnO films grown on a glass substrate at temperatures of 400˚C, 450˚C, and 500˚C are polycrystalline.

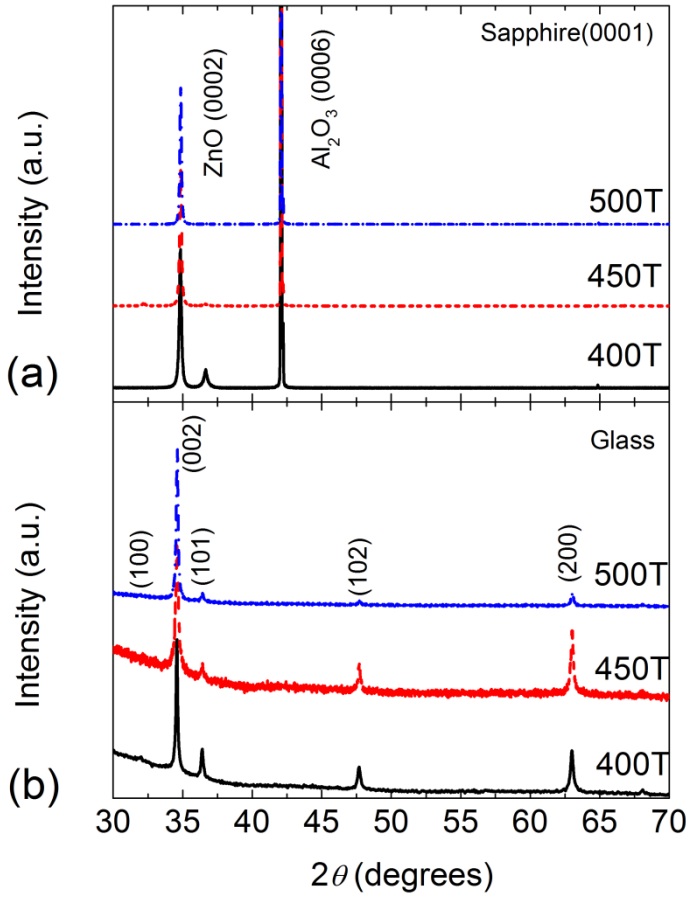

Figure 3. 14 XRD plots of ZnO film deposited on (a) Al_2O_3(0001) and (b) glass substrates at 400^{0}C, 450^{0}C and 500^{0}C.

3.4 Summary

The thermodynamic driving force (e.g. substrate deposition temperature) has been recognised to affect the film texture, optical properties, and electronic transport properties. At a lower deposition temperature, the film growth intends to a kinetic control, showing the non-polar (100) plane as the fastest growing plane. In contrast, as the substrate deposition temperature increases, thermodynamic control dominates the thin film growth. The (002)

phase that has the minimum surface energy shows the strongest diffraction peak in XRD. The grain size determines the electron density and the conductivity due to the grain boundaries.

The film thickness influence on the optical bandgap of the carefully-prepared series of Al-doped ZnO films (1% Al doping level throughout), apart from the behaviour of the thickest film (1281 nm), can be solely attributed to the Burstein Moss (BM) effect; that is, arising from the presence of free electrons occupying the bottom of the conduction band. This was further confirmed by the free-electron approximation to explore the magnitude of Fermi level upwards shift. For the reported thickest film, the conduction electrons from the substitutional Al^{3+} ions were most likely to be trapped by defects in the growing film which resulted in poor electronic properties and a bandgap similar to the undoped ZnO film. Importantly, for these thin films prepared by the spray pyrolysis technique, we find that the influence of strain-induced bandgap shift in the AZO films was negligible and the differences in out-plane/in-plane strains remained nearly constant for the films of 271 nm to 1281 nm thick.

Epitaxial growth of ZnO thin films was carried out using *c*-Al_2O_3(0001) as the substrate at 500˚C deposition temperature. Only one peak (0002) was displayed in the X-ray diffraction (XRD). High resolution transmittance electron microscopy (HRTEM) and the selected area electron diffraction (SAD) confirmed that the ZnO layer was a large single-crystal domain and its orientation relationship with the *c*-Al_2O_3(0001) substrate. During growth, ZnO lattice rotated 30˚ to reduce the lattice mismatch from 31.7% to 18.1% which is in line with the conventional model of lattice matching epitaxy (LME). The use of the domain matching epitaxy (DME) model gives the lattice mismatch of -1.5%, which proves that Al_2O_3(0001) can be used successfully as the substrate for ZnO epitaxial growth.

3.5 References

1. R. Triboulet and J. Perriere, Progress in Crystal Growth and Characterization of Materials **47**, 65 (2003).
2. B. E. Sernelius, K. F. Berggren, Z. C. Jin, I. Hamberg and C. G. Granqvist, Physical Review B **37**, 10244 (1988).
3. B. K. Sharma and N. Khare, Journal of Physics D-Applied Physics **43**, 465402 (2010).
4. Y. F. Li, B. Yao, Y. M. Lu, C. X. Cong, Z. Z. Zhang, Y. Q. Gai, C. J. Zheng, B. H. Li, Z. P. Wei, D. Z. Shen, X. W. Fan, L. Xiao, S. C. Xu and Y. Liu, Applied Physics Letters **91**, 21915 (2007).
5. Y. F. Li, B. Yao, Y. M. Lu, Y. Q. Gai, C. X. Cong, Z. Z. Zhang, D. X. Zhao, J. Y. Zhang, B. H. Li, D. Z. Shen, X. W. Fan and Z. K. Tang, Journal of Applied Physics **104**, 83516 (2008).
6. B. C. Mohanty, Y. H. Jo, D. H. Yeon, I. J. Choi and Y. S. Cho, Applied Physics Letters **95**, 62103 (2009).
7. S. M. Yang, S. K. Han, J. W. Lee, J. H. Kim, J. G. Kim, S. K. Hong, J. Y. Lee, J. H. Song, S. I. Hong, J. S. Park and T. Yao, Journal of Crystal Growth **312**, 1557 (2010).
8. P. Kuppusami, G. Vollweiler, D. Rafaja and K. Ellmer, Applied Physics a-Materials Science & Processing **80**, 183 (2005).
9. A. Nahhas, H. K. Kim and J. Blachere, Applied Physics Letters **78**, 1511 (2001).
10. I. Levin, A. Davydov, B. Nikoobakht, N. Sanford and P. Mogilevsky, Applied Physics Letters **87**, 103110 (2005).
11. A. B. M. A. Ashrafi, A. Ueta, A. Avramescu, H. Kumano, I. Suemune, Y. W. Ok and T. Y. Seong, Applied Physics Letters **76**, 550 (2000).
12. A. Ohtomo, K. Tamura, K. Saikusa, K. Takahashi, T. Makino, Y. Segawa, H. Koinuma and M. Kawasaki, Applied Physics Letters **75**, 2635 (1999).
13. S. Yang, B. H. Lin, W. R. Liu, J. H. Lin, C. S. Chang, C. H. Hsu and W. F. Hsieh, Crystal Growth & Design **9**, 5184 (2009).
14. X. W. Sun and H. S. Kwok, Journal of Applied Physics **86**, 408 (1999).
15. H. P. Sun, X. Q. Pan, X. L. Du, Z. X. Mei, Z. Q. Zeng and Q. K. Xue, Applied Physics Letters **85**, 4385 (2004).
16. H. W. Suh, G. Y. Kim, Y. S. Jung, W. K. Choi and D. Byun, Journal of Applied Physics **97** (2005).
17. G. Adamopoulos, A. Bashir, W. P. Gillin, S. Georgakopoulos, M. Shkunov, M. A. Baklar, N. Stingelin, D. D. C. Bradley and T. D. Anthopoulos, Advanced Functional Materials **21**, 525 (2011).

18. G. A. H. Mekhemer, S. A. Halawy, M. A. Mohamed and M. I. Zaki, Journal of Catalysis **230**, 109 (2005).
19. N. Fujimura, T. Nishihara, S. Goto, J. F. Xu and T. Ito, Journal of Crystal Growth **130**, 269 (1993).
20. C. Koidis, S. Logothetidis, S. Kassavetis, A. Laskarakis, N. A. Hastas and O. Valassiades, Physica Status Solidi a-Applications and Materials Science **207**, 1581 (2010).
21. P. D. C. King, T. D. Veal, A. Schleife, J. Zuniga-Perez, B. Martel, P. H. Jefferson, F. Fuchs, V. Munoz-Sanjose, F. Bechstedt and C. F. McConville, Physical Review B **79**, 205205 (2009).
22. S. Locmelis, C. Brunig, M. Binnewies, A. Borger, K. D. Becker, T. Homann and T. Bredow, Journal of Materials Science **42**, 1965 (2007).
23. J. Y. W. Seto, Journal of Applied Physics **46**, 5247 (1975).
24. X. P. Li, B. L. Zhang, H. C. Zhu, X. Dong, X. C. Xia, Y. G. Cui, Y. Ma and G. T. Du, Journal of Physics D-Applied Physics **41**, 35101 (2008).
25. P. P. Edwards and M. J. Sienko, Physical Review B **17**, 2575 (1978).
26. A. P. Roth, J. B. Webb and D. F. Williams, Physical Review B **25**, 7836 (1982).
27. Y. Danhara, T. Hirai, Y. Harada and N. Ohno, Physica Status Solidi C **3**, 3565 (2006).
28. R. T. Girard, O. Tjernberg, G. Chiaia, S. Soderholm, U. O. Karlsson, C. Wigren, H. Nylen and I. Lindau, Surface Science **373**, 409 (1997).
29. C. M. Muiva, T. S. Sathiaraj and K. Maabong, Ceramics International **37**, 555 (2011).
30. Z. Q. Xu, H. Deng, Y. Li and H. Cheng, Materials Science in Semiconductor Processing **9**, 132 (2006).
31. J. Mass, P. Bhattacharya and R. S. Katiyar, Materials Science and Engineering B-Solid State Materials for Advanced Technology **103**, 9 (2003).
32. L. G. Parratt, Physical Review **95**, 359 (1954).
33. A. A. Hashim, M. T. Mohammad and M. H. Al-Maamory, Materials Chemistry and Physics **99**, 382 (2006).
34. A. Janotti and C. G. Van de Walle, Physical Review B **75**, 121201 (2007).
35. W. Shan, W. Walukiewicz, J. W. Ager, K. M. Yu, Y. Zhang, S. S. Mao, R. Kling, C. Kirchner and A. Waag, Applied Physics Letters **86**, 153117 (2005).
36. Y. Z. Zhu, G. D. Chen, H. G. Ye, A. Walsh, C. Y. Moon and S. H. Wei, Physical Review B **77**, 245209 (2008).
37. J. W. Matthews and A. E. Blakeslee, Journal of Crystal Growth **27**, 118 (1974).
38. J. Narayan and B. C. Larson, Journal of Applied Physics **93**, 278 (2003).

39. C. J. Sun, P. Kung, A. Saxler, H. Ohsato, K. Haritos and M. Razeghi, Journal of Applied Physics **75**, 3964 (1994).

CHAPTER 4

CADMIUM DOPED ZINC OXIDE

The narrowing of the electronic bandgap of ZnO by doping with cadmium oxide opens up further potential uses of the material for photocatalytic applications. Cadmium is recognised as a promising candidate for allowing this particular bandgap engineering in ZnO. CdO itself adopts the cubic rocksalt structure with an indirect lowest bandgap.[1] Although a value of 0.55 eV is widely quoted for this indirect gap, more recent work suggests that values between 1.1 eV and 1.2 eV have been obersved.[2] The direct bandgap of CdO is about 2.2 eV. The solubility limits and phase stability for $Cd_xZn_{1-x}O$ solid solution depend sensitively on the preparation conditions and are different for thin films and powdered samples. In general, the range of solubility for CdO in ZnO is wider in thin films than that in powders. Sadofev et al. reported that a single phase of $Cd_{0.32}Zn_{0.68}O$ epilayer could be grown on a *a*-plane sapphire by molecular beam epitaxy.[3] Other techniques such as plasma-enhanced molecular-organic chemical vapour deposition and magnetron sputtering, have been used to produce single phase ZnO films with the maximum Cd content up to x = 0.69 and 0.66, respectively.[4, 5] The structural and optical properties of $Cd_xZn_{1-x}O$ films and powders have been studied previously[3, 4, 6] However, there has been no photoemission studies on $Cd_xZn_{1-x}O$ alloys to directly probe the effect of Cd doping on the electronic structure of ZnO. To date, the mechanism of this important bandgap modification by Cd dopant is still unclear. This chapter will demonstrate the relationship between the crystal and electronic structures at various doping concentrations.

4.1 Electronic Structure of Ternary $Cd_xZn_{1-x}O$ ($0 \leq x \leq 0.075$)

4.1.1 Crystal Structure Analysis

The diffraction patterns of the $Cd_xZn_{1-x}O$ ceramic samples prepared in the present work by solid state synthesis are shown in Figure 4.1. ZnO pattern exhibits a hexagonal wurtzite structure with lattice constant, a = 3.2397Å and c = 5.1889Å, while CdO displays a cubic structure with a = 4.6767Å. Samples with x = 0.039 and 0.075 have a single phase composition and exhibit peaks of ZnO wurtzite structure only. A rocksalt phase (CdO) appears when the Cd concentration is in excess of x = 0.139. The lattice constant a increases from 3.2397Å to 3.2673Å for x = 0 and x = 0.075, respectively, while c rises from 5.1889Å to 5.222Å for x = 0 and x = 0.075, respectively. The increasing values in constants a and c reflect a lattice expansion in ZnO, as a consequence from smaller ionic radius of Zn^{2+} ions substituted by larger ionic radius of Cd^{2+} ions (i.e. Zn^{2+}: 0.88Å *versus* Cd^{2+}: 1.09Å).

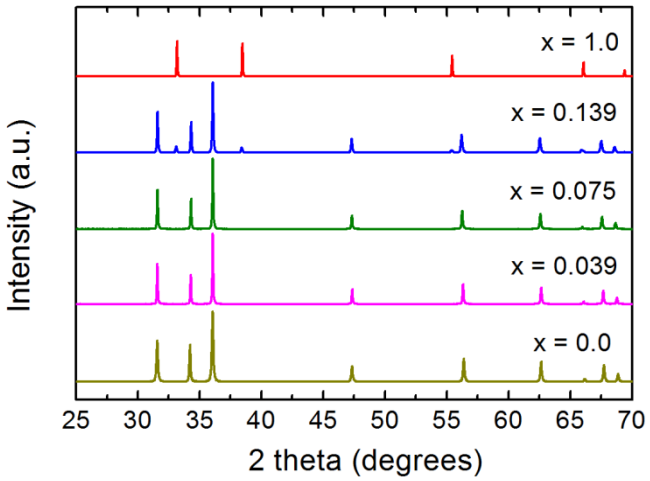

Figure 4. 1 X-ray diffraction patterns of ternary $Cd_xZn_{1-x}O$ ($0 \leq x \leq 1$) alloys.

Another approach to examine the impurity substitution was elemental analysis by X-ray photoelectron spectroscopy (XPS). Figure 4.2 (a) shows XPS O 1s core level scans for $Cd_xZn_{1-x}O$ alloys with x = 0, 0.039, 0.075, and 1.0. Z reflects the oxygen in the ZnO environment while C is in the CdO lattice. To compare the atomic ratio of Z to C, the areas of oxygen components were integrated and compared in Figure 4.2 (b). The decreasing ratio of Z opposite to the increase in C indicates that Zn sites have been replaced by Cd atoms with increasing in Cd concentration. Note that an observed broad peak at around 532 eV and 534.5 eV in x = 0.0 is ascribed to hydroxyl molecule (i.e. $Zn(OH)_2$) and absorbed water on the ZnO surface, repectively.[7] The contribution from hydroxyl molecule to O2 intensity is expected to be similar in all our samples. Therefore, the measured relative intensity of Z/C is reliable used as an indication to describe the relative amounts of Cd incorporated in the ZnO lattice. The broad peak at 534 eV in x = 1.0 is associated with $CdCO_3$ or hydroxyl species.[8]

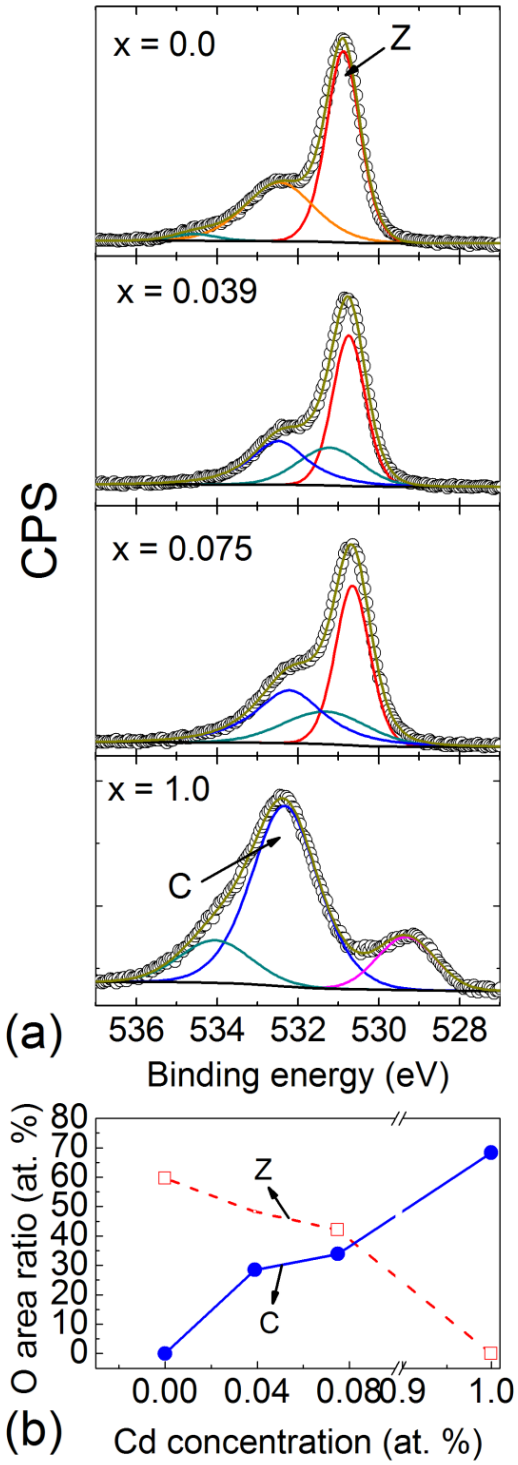

Figure 4. 2 (a) XPS spectra fitting for the O 1s core lines of $Cd_xZn_{1-x}O$ with x = 0, 0.039, 0.075, and 1.0. (b) The ratios of Z and C components vary as a function of Cd concentration.

The host materials can be perturbed by impure atoms that change the mass matrices of the lattice vibrations. Raman spectrum is commonly used to investigate the effect of Cd^{2+} incorporation, structural disorder and phase segregation in the ZnO host lattice through their local vibration modes.[9, 10]

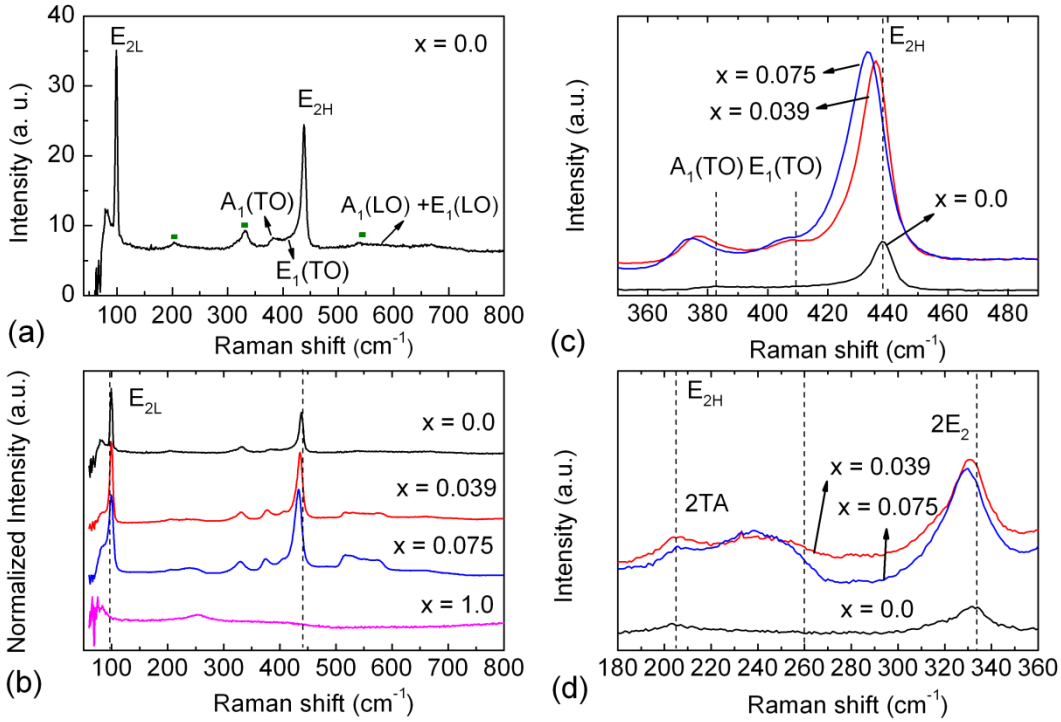

Figure 4. 3 (a) Nonresonant Raman features for polycrystalline ZnO. (b) Normalised Raman spectra for $Cd_xZn_{1-x}O$ ($0 \le x \le 1$). (c) A narrow Raman shift range between 350 cm^{-1} and 490 cm^{-1} for $Cd_xZn_{1-x}O$ ($0 \le x \le 1$). (d) The features of multiphonon process and E_{2H} are demonstrated in 180-360 cm^{-1} for $Cd_xZn_{1-x}O$ ($0 \le x \le 1$).

Figure 4.3 (a) exhibits nonresonant Raman spectra for polycrystalline ZnO, where the active modes are following: E_{2L} = 99 cm^{-1}, A_1 (TO) = 380 cm^{-1}, E_1 (TO) = 408 cm^{-1}, E_{2H} = 438 cm^{-1}, A_1 (LO) + E_1 (LO) = 574-583 cm^{-1}, and the mulitiphonon processes arisen from zone-boundary are at 203 cm^{-1} (2TA), 331 cm^{-1} ($2E_2$) and 540 cm^{-1} (2LA).[11] E_{2L} and E_{2H} are attributed to the vibrations of heavy Zn sublattice and oxygen.

E_{2L} feature is also an indication for the high lifetime by determining its intensity and FWHM according to the uncertainty principle.[10] A_1 and E_1 correspond to the atomic vibrations parallel and normal to the *c*-axis, respectively (Figure 1.11). The two symmetries of A_1 (LO) and E_1 (LO) in powder are expected to interact and thus create a single mode which is known as the quasi-LO mode.[12]

In Figure 4.3 (b) we demonstrate the normalised Raman spectra for $Cd_xZn_{1-x}O$ powdered samples. The all features corresponding to Raman shift are summarised in Table 4.1. The overall spectral intensity increases significantly from x = 0.0 to x = 0.075, and diminishes at x = 1.0. The sudden rise in the intensity from x = 0.0 to x = 0.039 confirms that an increasing lattice constant (Table 4.1) is due to the replacement of Zn^{2+} ions with Cd^{2+} ions. The broadening ZnO peaks that reflects the structural deterioration in ZnO is due to the distortion of the local atomic arrangement around the Cd^{2+} impurity. In addition, the increasing ratio of E_{2L} to E_{2H} from 0.76 (x = 0.0) to 1.06 (x = 0.075) reveals that a greater influence on Zn sublattice than O sublattice with the addition of CdO. The line shapes of E_{2H} and E_{2L} tend to asymmetry at higher Cd concentration, ascribed to the structure disorder and anharmonic phonon-phonon interactions.[10] In other words, the observed line broadenings in E_{2H} and E_{2L} are the consequence of lattice disorder induced by Cd atoms incorporation.

Table 4. 1 The summary of lattice constants and Raman features of $Cd_xZn_{1-x}O$ samples.

$Cd_xZn_{1-x}O$	*a* (nm)	*c* (nm)	Intensity ratio (I_{E2h} / I_{E2l})	E_{2L} (cm^{-1})	E_{2H} (cm^{-1})	E_{2L}, FWHM (cm^{-1})	A_1(TO) (cm^{-1})	E_1(TO) (cm^{-1})
x = 0.0	0.3240	0.5189	0.73	99	438	4.7	382	409
x = 0.039	0.3262	0.5217	0.87	99	436	6.03	377	408
x = 0.075	0.2267	0.5222	1.06	99	434	10.16	375	408

A narrow scan between 350 cm^{-1} and 480 cm^{-1} is shown in Figure 4.3 (c). A shift towards the lower frequency with an increasing Cd concentration is caused by the atomic weight difference and the lattice volume change arisen from the difference in cationic radius uniformly distributed over all the atoms of the crystal.[13] The calculated differences for the atomic mass defect and the cationic radius are 47.02Å and 0.23Å, respectively. It is known that positive values for the of mass defect and the volume change both imply that Cd^{2+} cation is heavier in mass and larger in volume than Zn^{2+}. Hence, the incorporation of Cd^{2+} into ZnO lattice gives a rise to a lattice expansion, which causes a shift towards the lower frequency in E_{2H}. This result is in a good agreement with XRD data. Furthermore, the E_{2H} mode, originating from the oxygen vibration in ZnO lattice, shift from 438 to 434 cm^{-1} with Cd doping. In contrast, the E_{2L} peak, ascribed to zinc sublattice, does not move with increasing Cd amount. This indicates that the E_{2H} mode is more affected by Cd doping than the E_{2L} mode, suggesting that the oxygen defects probably dominate in the formation $Cd_xZn_{1-x}O$ alloys.[11]

A_1 (TO) pattern at 380 cm^{-1} in Figure 4.3 (c) is also ascribed to oxygen vacancies.[11] For example, the feature at 380 cm^{-1} in the sample with x = 0.075 has a higher intensity and a red shift, which suggests the presence of oxygen deficiency.[11] Figure 4.3 (d) focuses on the multiphonon region in the range of 180-360 cm^{-1}. The multiphonon feature in ZnO reflects the activation or the formation of structural defects in-doped ZnO.[14] The multiphonon processes presented at 208 cm^{-1} (2TA) and 332 cm^{-1} ($2E_2$) become broader and greater as Cd concentration increases, which suggests that the number of structural defects is increasing. Finally, a broad peak at 240-260 cm^{-1} is observed in x = 0.039 and 0.075 but x = 0.0.

4.1.2 Electronic Structure of $Cd_xZn_{1-x}O$ ($0 \leq x \leq 0.075$) Alloys

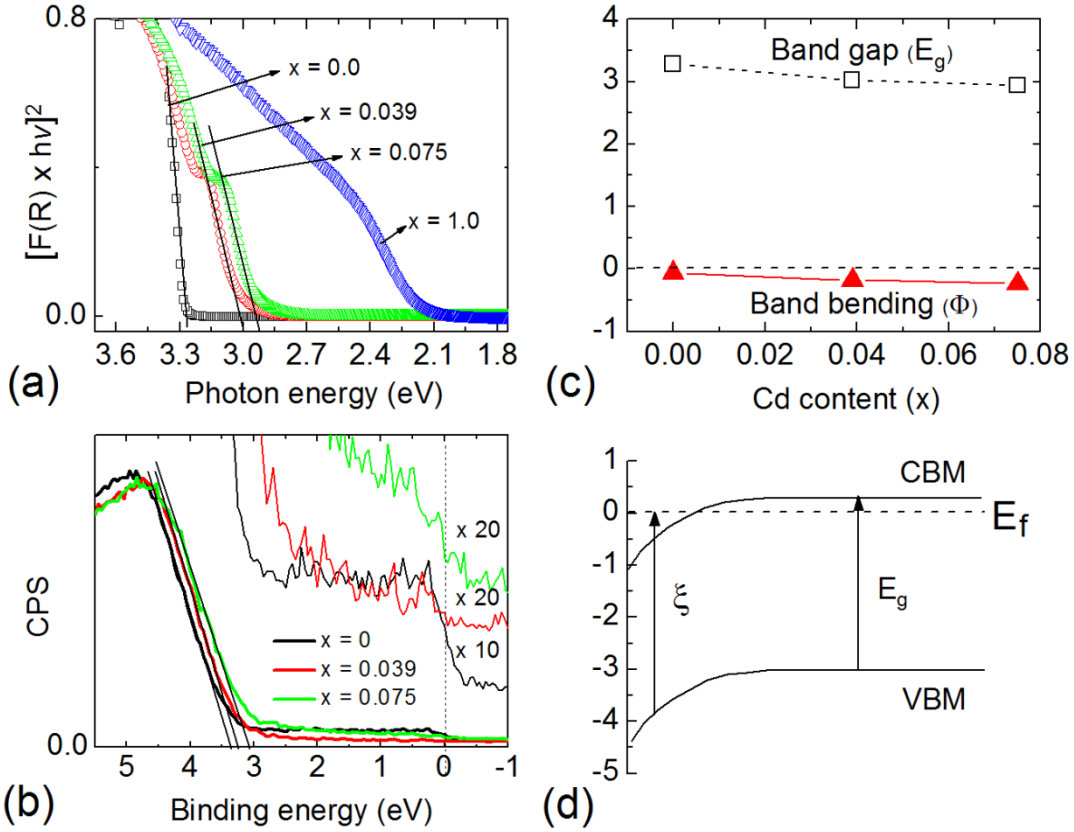

Figure 4. 4 (a) Square of Kubelka-Monk scattering F(R) as a function of photon energy for ternary $Cd_xZn_{1-x}O$ alloys. (b) Valence band XPS of $Cd_xZn_{1-x}O$ alloys. (c) Electronic bandgaps (open squares) and band bending (closed triangles) as a function of Cd concentration in $Cd_xZn_{1-x}O$ ceramic samples. (d) A downward band bending due to an electron accumulation at the near surface.

The UV-Vis DRS spectra of $Cd_xZn_{1-x}O$ are shown in Figure 4.4 (a) as a plot of the square of the Kubelka-Munk function F(R) versus photon energy. The bulk bandgap was determined from the linear extrapolations of the experimental data and summarised in Table 4.2. The absorption edge shifts to lower photon energy with an increasing Cd concentration. The undoped ZnO has an absorption edge at 3.28 eV, while samples with

x = 0.039 and x = 0.075 display a strong absorption in the range of 3.02 eV - 2.94 eV. The powder colour is also observed to change from white (ZnO), to yellow ($Cd_xZn_{1-x}O$; x = 0.039 and x = 0.075), and to brown/red (CdO).

Table 4. 2 The summary of experimental data for $Cd_xZn_{1-x}O$. n_b and n_s are the electron densities in the bulk and on the surface. ξ is the energy gap between the VBM and Fermi level ε_∞ = 5.3 and m* = 0.24 were used for calculating the n_s of CdO.[15]

$Cd_xZn_{1-x}O$	n_b (cm^{-3})	Bulk bandgap (eV)	ξ (eV)	Plasmon energy (eV)	n_s (cm^{-3})	BM shift (eV)
x = 0	3.11×10^{14}	3.28	3.35	0.33	8.06×10^{19}	0.26
x = 0.039	3.46×10^{18}	3.02	3.25	0.45	1.45×10^{20}	0.39
x = 0.075	1.01×10^{18}	2.94	3.10	0.48	1.68×10^{20}	0.43
x = 1	6.20×10^{19}	2.18	0.93	0.59	3.20×10^{20}	0.71

Figure 4.4 (b) demonstrates the valence band XPS for all samples. It should be mentioned that the spectra have been carefully aligned the Fermi edge with the binding energy at 0 eV. The Fermi edges for x = 0, x = 0.039 and x = 0.075 are enlarged by 10 times, 20 times and 20 times and shown as the insert in Figure 4.4 (b). As mentioned in Chapter 2.1.3.7, each sample exhibited different levels of shift due to surface charging and the use of flood gun. Binding energies in photoelectron spectroscopy are measured with respect to the Fermi level. Therefore, the shifts can be calibrated with the alignment of the Fermi edge at 0 eV. The position (ξ) of the valence band maximum (VBM) relative to the Fermi level (E_f) can be determined from a linear extrapolation of the band edge in XPS. Table 4.2 displays the ξ values for $Cd_xZn_{1-x}O$ samples and shows a low energy shift in ξ with increasing Cd concentration, in agreement with bulk bandgap shifting.

An examination of critical carrier density for a metal-semiconductor transition at which Fermi level merges into conduction band is performed via Edwards-Siernko and Mott's criterion,[16, 17]

$$n_c^{1/3} a^* \geq 0.26 \quad (4.1)$$

where a^* is the Bohr radius of 1.4 nm for ZnO.[18] The critical electron concentration (n_c) is then calculated to be 6.41×10^{18} cm^{-3}. The measured bulk carrier concentrations (n_b) for x = 0.039 and 0.075 in Table 4.2 are smaller than n_c, which implies that the bulk Fermi level is below the CBM. Hence, the optical bandgap determined by UV-Vis DRS can be regarded as the fundamental direct bandgap due to the examination of Edwards-Siernko and Mott's criterion. Interestingly, the fundamental bandgap is however smaller than the ξ measured by XPS. This difference can be attributed to band bending. Figure 4.4 (c) shows the composition dependence of the electronic bandgap and band bending in $Cd_xZn_{1-x}O$ alloys. The band bending (Φ) is calculated by subtracting ξ from the fundamental bandgap (E_g), $\Phi = E_g - \xi$. The negative Φ implies that surface Fermi level is further above the conduction band. This also reflects a downward band bending of conduction and valence bands at the surface, resulting in a surface electron accumulation, as shown in Figure 4.4 (d).[19]

The XPS spectral profiles of the Zn $2p_{3/2}$ core line of powders with x = 0, 0.039 and 0.075 are presented in Figure 4.5 (a). The Zn $2p_{3/2}$ level shifts to a lower binding energy with an increase in the Cd concentration. All spectra exhibit a degree of asymmetry, which was also found in impurity-doped metal oxides, such as Sn-doped In_2O_3 and Sb-doped SnO_2.[20, 21] Providing that the multiple plasmon excitation or the contributions from chemical shift in the topmost ionic layer are ignored, the asymmetric

peak broadening can arise as a result of superposition of an unscreened plasmon satellite positioned at high binding energy and a screened main peak at lower binding energy.[20] The results of fitting of XPS experimental data to a Shirley background with two Voigt components are presented in Table 4.3.[20] The area of the screened peak increases with increasing surface carrier concentration. The plasmon energy, determined as a binding energy difference between screened and unscreened peaks, is 0.33 eV for ZnO and higher for the x = 0.039 and 0.075 samples; the calculation results are displayed in Table 4.2. The surface free carrier concentration can be then derived from the relationship,

$$\hbar\omega_p = \hbar\left(\frac{ne^2}{m^*\varepsilon_0\varepsilon_\infty}\right)^{1/2} \qquad (4.2)$$

where ω_p is the plasmon frequency, n is the carrier density, ε_0 is the permittivity of free space, and ε_∞ is the high frequency dielectric constant, equal to 3.85 for ZnO.[22] We use $m^* = 0.26m_0$, assuming that the CBM remains located at the centre of Brillouin zone and that the effective mass is unchanged in $Cd_xZn_{1-x}O$ alloys.[22, 23] The calculation results are presented in Table 4.2, revealing a significant increase in surface carrier density between pure ZnO and $Cd_xZn_{1-x}O$.

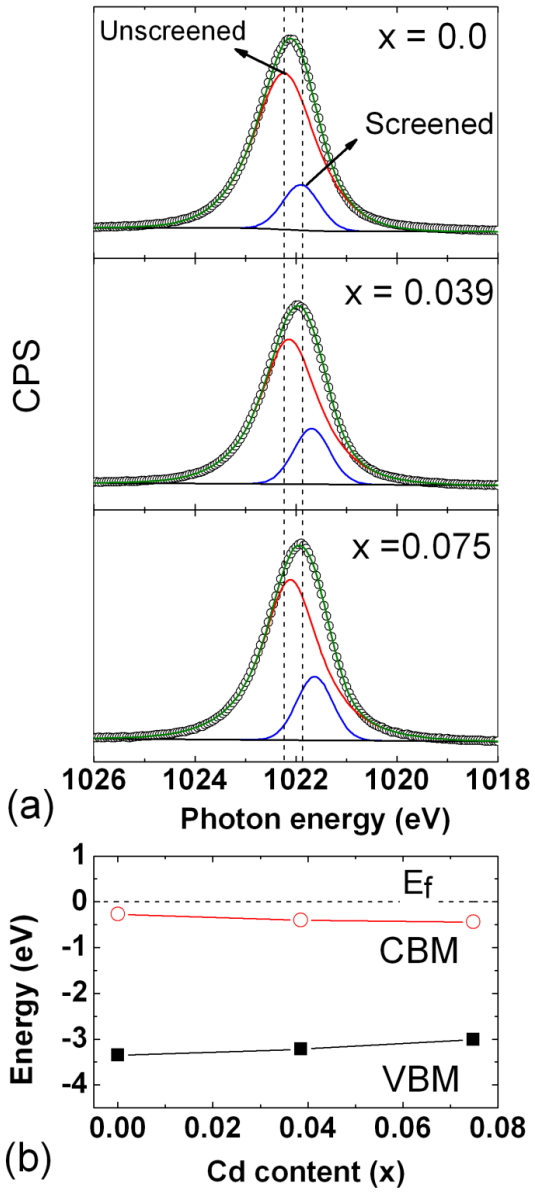

Figure 4. 5 (a) XPS spectra fitting with two Voigt components for the Zn $2p_{3/2}$ core line of $Cd_xZn_{1-x}O$ with x = 0, 0.039 and 0.075. (b) The movement of surface band positions of CBM (open circles) and VBM (closed squares) with respect to the Fermi level (dash line) at 0.0 eV.

Table 4. 3 The summary of XPS spectra fitting with two Voigt components for the Zn $2p_{3/2}$ core line of $Cd_xZn_{1-x}O$ with x = 0, 0.039 and 0.075.

$Cd_xZn_{1-x}O$		B.E. (eV)	FWHM (eV)	Lorentzian conc. (%)	Area (%)	Plasmon energy (eV)
x = 0	screened	1021.90	0.8551	20	13.59	0.33
	unscreened	1022.24	1.4526	75	86.41	
x = 0.039	screened	1021.69	0.8444	20	17.26	0.45
	unscreened	1022.14	1.3712	85	82.74	
x = 0.075	screened	1021.63	0.8365	13	17.35	0.48
	unscreened	1022.11	1.3401	90	82.65	
x = 1	screened	404.04	1.1321	60	9.32	0.59
	unscreened	404.63	1.0240	70	7.51	

The surface carrier densities (n_s) in all samples are approximately one order of magnitude higher than the critical carrier density (n_c), explaining why the surface Fermi level lies above the CBM and the conduction band is partially occupied by free electrons. This is consistent with the downward band bending revealed by the valence-band XPS result shown above. Moreover, the surface carrier concentration is consistently higher than the bulk values obtained from Hall effect data. Even the surface region of ZnO exhibits a high carrier concentration, although it is not as high as that observed for $Cd_xZn_{1-x}O$ alloys. It is important that the mechanism of increasing carrier concentration in the isovalently substituted $Cd_xZn_{1-x}O$ solid solution is different from that of Al-doped ZnO, where Zn^{2+} ions are replaced with Al^{3+} ions so as to release one additional electron to the ZnO lattice. The increasing carrier concentration by incorporating Cd^{2+} into ZnO is likely attributed to the downward movement of conduction band and gaining electrons from crystallographic defects. It is well known that the conduction band of ZnO consists of Zn 4s states hybridised with O 2p and O 2s states.[24] The introduction of Cd 5s impurity states, which are located below the conduction band of ZnO, perturbs the CBM of ZnO. The host conduction band of ZnO

is therefore re-normalised by alloying with CdO and the edge of conduction band moves closer to the valence band. In addition, the intrinsic defects in n-type ZnO, such as oxygen vacancies or zinc interstitials, induce donor states below the CBM.[17, 25] When the conduction band is pulled down, free electrons associated with donor states can occupy the bottom of the re-hybridized conduction band. Therefore, a significant downward shift in the CBM causes a higher concentration of free electrons in the conduction band.

The position of surface Fermi level with respect to CBM can be described in terms of the Burstein-Moss (BM) effect,[17]

$$\Delta E_{BM} = E_f - E_c = \frac{\hbar^2}{2m^*}\left(3\pi^2 n\right)^{2/3} \quad (4.3)$$

The calculated BM shift energy is listed in Table 4.2. The magnitude of BM shifts increases from 0.26 eV to 0.39 eV when 3.9 mol.% of CdO is added to pure ZnO and continues to increase up to 0.43 eV at x = 0.075. The resulting band positions on the surface of $Cd_xZn_{1-x}O$ alloys are shown in Figure 4.5 (b). The Fermi level is pinned at 0 eV and the valence band was plotted according to the values of ξ. The CBM is then drawn in terms of the BM energy shift. Figure 4.5 (b) demonstrates that the bandgap narrowing in $Cd_xZn_{1-x}O$ alloys not only lowers the conduction band but also increases the level of the valence band. The ratio of conduction band offset to valence band offset is approximately 1:1, which is somewhat different from the work of Chen *et al.*[26] where $Cd_{0.05}Zn_{0.95}O$ thin film showed the ΔE_c to ΔE_v ratio of 1:2. Chen's and our experimental works have established that the narrowing of electronic bandgap occurs with the offsets of conduction and valence bands, in contrast to the first-principle studies, which suggested that the narrowing is only due to a downward shift of the CBM.[27]

4.1.3 Conduction Band Feature of $Cd_xZn_{1-x}O$ ($0 \leq x \leq 0.075$) Alloys

The analysis of X-ray absorption near-edge structure (XANES) provides the information on the lowest unoccupied states, which is particularly useful for the investigation of the electronic band structure of semiconductor materials. A XANES spectrum of O K-edge spectra for $Cd_xZn_{1-x}O$ alloys is shown in Figure 4.6 (a). For the undoped ZnO, the pre-edge region of 525-532 eV arises from the electronic transition from O 1s to O 2p - Zn 3d hybridised states in the bandgap.[28] Owing to the fully occupied d^{10} configuration in Zn^{2+} atom, the O K-edge of undoped ZnO does not show any feature related to the O 2p-Zn 3d hybridised orbitals.[29] The photon energy region of 530-539 eV corresponds to electronic transitions from O 1s states into conduction band states of dominant Zn 4s characters which acquire O 2p character through covalent mixing. Absorption between 539 and 550 eV is assigned to O 2p states hybridised with Zn 4p states. Above 550 eV, absorption is a result of O 2p states mixed with Zn 4d states.[30] The overall spectral intensity in x = 0.039 and x = 0.075 increases with respect to the undoped ZnO, suggesting that the number of unoccupied states increases by the incorporation of Cd^{2+} atoms. The introduction of impurity levels into ZnO electronic structure leads to an increase in the net number of unoccupied states, resulting in a higher transition probability and a higher spectral intensity. The insert diagram in Figure 4.6 clearly exhibits a significant growing intensity in the region of 532-537.5 eV, indicating that the Cd^{2+} 5s states are shallow donors in the ZnO electronic structure, laying near the Zn 4s-O 2p hybridising levels.

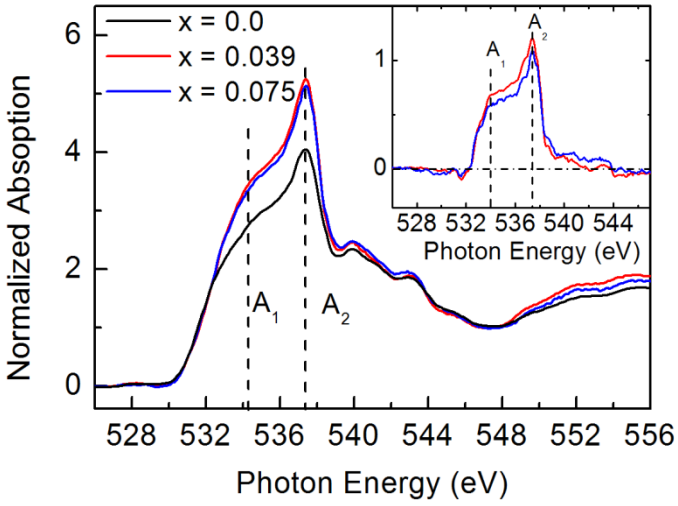

Figure 4.6 O K-edge XANES spectra of the $Cd_xZn_{1-x}O$ samples with x = 0, x = 0.039, and x = 0.075. The insert shows the differences between undoped ZnO and Cd-doped ZnO samples.

The XANES spectra of Zn L_3-edge and Zn K-edge for $Cd_xZn_{1-x}O$ samples are displayed in Figure 4.7. It is known that the pre-edge feature in XANES reflects the local geometry around the absorbing atom arisen from 1s → 3d transition. The pre-edge feature here is considered as impurity-induced local interference effect instead of bound state transition.[31] For the undoped ZnO with fully filled 3 d orbitals, there is no transition in pre-edge region as there is no peak seen at B_1 in Figure 4.7 (a). In contrast to x = 0.0, x = 0.039 and x = 0.075 samples demonstrate a broad pre-edge peak (B_1), which indicates an impurity-induced local lattice distortion. This observation confirms our finding in the XRD and Raman data.

Zn K-edge XANES is commonly used to examine the conduction band of ZnO with or without dopant addition, since the conduction band is derived from unoccupied Zn 4p and O 2p orbitals. Feature B_2 (white line) exhibits the dipole transition from Zn 1s to $4p_\pi$ (along *c*-axis) states.[32] The observed reductions in B_2 in the x = 0.039 and x =

0.075 samples are possibly contributed from two reasons: (1) Cd dopants induce additional free carriers to occupy the unfilled Zn 4p density of states in ZnO lattice.[33] The increasing free carrier density has been shown by the Hall effect measurements in Table 4.2. (2) The density of overall Zn 4p states decreases due to the replacement of Zn atoms with Cd atoms.

The features C_1, C_2 and C_3 consist of the electronic transitions from Zn $2p_{2/3}$ to Zn 4s and antibonding $3d_{3/2}$ and $3d_{5/2}$ states.[28] In Figure 4.7 (b) the intensities of C_2 and C_3 decrease dramatically when forming $Cd_xZn_{1-x}O$ alloys but less influence on C_1. The p-d transition dominates Zn L_3-edge spectrum because the unoccupied Zn 3d orbital is more localised than the unfilled 4s orbital (i.e. the transitional probability of Zn $2p_{2/3} \rightarrow$ 3d is greater than that of Zn $2p_{2/3} \rightarrow$ 4s).[28] The decrease in the magnitude of overall intensity in x = 0.039 and x = 0.075 samples explains the reduction in the number of Zn 3d unoccupied states by the substitution of Cd^{2+} for Zn^{2+} ions, which is in consistent with Zn K-edge XANES as well as the increase in ZnO lattice interspacing in XRD.[28]

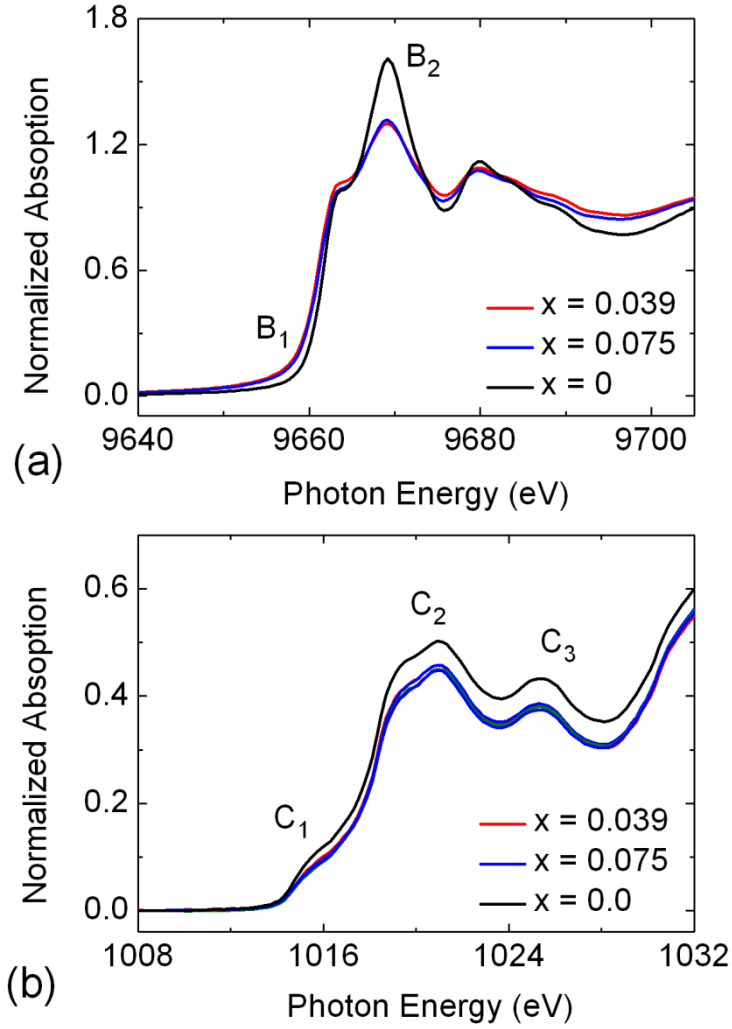

Figure 4. 6 (a) Zn K-edge XANES spectra of the $Cd_xZn_{1-x}O$ samples with x = 0, x = 0.039, and x = 0.075. B_1 represents the pre-edge feature while B_2 shows the white line. (b) Zn L_3-edge XANES spectra of the $Cd_xZn_{1-x}O$ samples with x = 0, x = 0.039, and x = 0.075.

4.2 Bang Gap Bowing Effect of Ternary $Cd_xZn_{1-x}O$ Alloys

To determine the bandgap bowing of ternary $Cd_xZn_{1-x}O$ alloys, a series of samples with different atomic ratios of Cd to Zn were synthesised in chapter 4.2. (Note:

the powdered samples here were re-produced, different to those samples in chapter 4.1) Figure 4.8 shows a photograph of powdered $Cd_xZn_{1-x}O$ samples. Starting from left hand side, the colour changes from white (undoped ZnO) to yellow (dilute CdO in ZnO), then to dark tallow, brown, navy (dilute ZnO in CdO), and brown red (undoped CdO) on the right. The Cd concentrations in $Cd_xZn_{1-x}O$ alloys were confirmed with energy-dispersive X-ray spectroscopy (EDX).

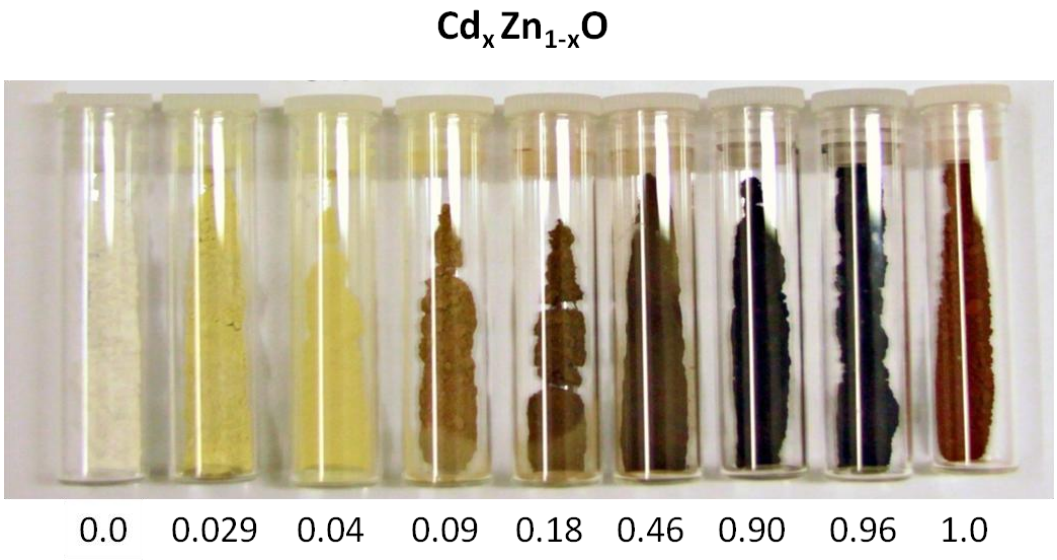

Figure 4. 7 A photograph of powdered $Cd_xZn_{1-x}O$ samples. The values marked underneath the bottles are the x values in $Cd_xZn_{1-x}O$.

The determination of optical bandgap for $Cd_xZn_{1-x}O$ is shown in Figure 4.9 (a) through the UV-Vis DRS measurements and the derivations of Kubelka-Monk scattering. As anticipated, the bandgap reduces with increasing in CdO amount from the undoped ZnO at 3.29 eV to $Cd_{0.46}Zn_{0.54}O$ at 1.72 eV, and to CdO at 2.07 eV. Additionally, the optical bandgaps across the whole Cd concentrations display a bowing curve rather than a linear dependence. Figure 4.9 (b) presents the bandgap bowing curve

for the $Cd_xZn_{1-x}O$ alloys, where the lowest bandgap is at x = 0.78. The compositional variations of bandgap energy in II-VI isovalent semiconductor alloys $Cd_xZn_{1-x}O$ can be described as:[34]

$$E_g = (1-x)\cdot E_g(ZnO) + x\cdot E_g(CdO) - bx\cdot(1-x) \quad (4.4)$$

where E_g(ZnO) and E_g(CdO) are the bandgaps for ZnO and CdO, respectively. b is the bowing coefficient, which describes the deviation from a linear interpretation and indicates the degree of wave-function localisation in the band edge states. Optical bowing effect in semiconductor alloys is caused by the difference between the volume deformation potentials of the constituents and coupling of folded states through a perturbation potential.[35-37] The perturbation potential is defined as the difference between the alloy potential and the average potential of the constituents. The perturbation potential is influenced by the differences of electronegativity or atomic size between constituents A and B. For instance, the greater the difference of atom size, the larger optical bowing is expected. Moreover, when the perturbation potential couples states within the valence band (conduction band), it leads to rising (lowering) the valence band maximum (conduction band minimum), and therefore results in a narrowing of the bandgap. This explains our observations in chapter 4.1.2, in which an introduction of Cd^{2+} atoms in ZnO lattice narrows the host bandgap with an upward shift in VBM and a simultaneous downward movement in CBM.

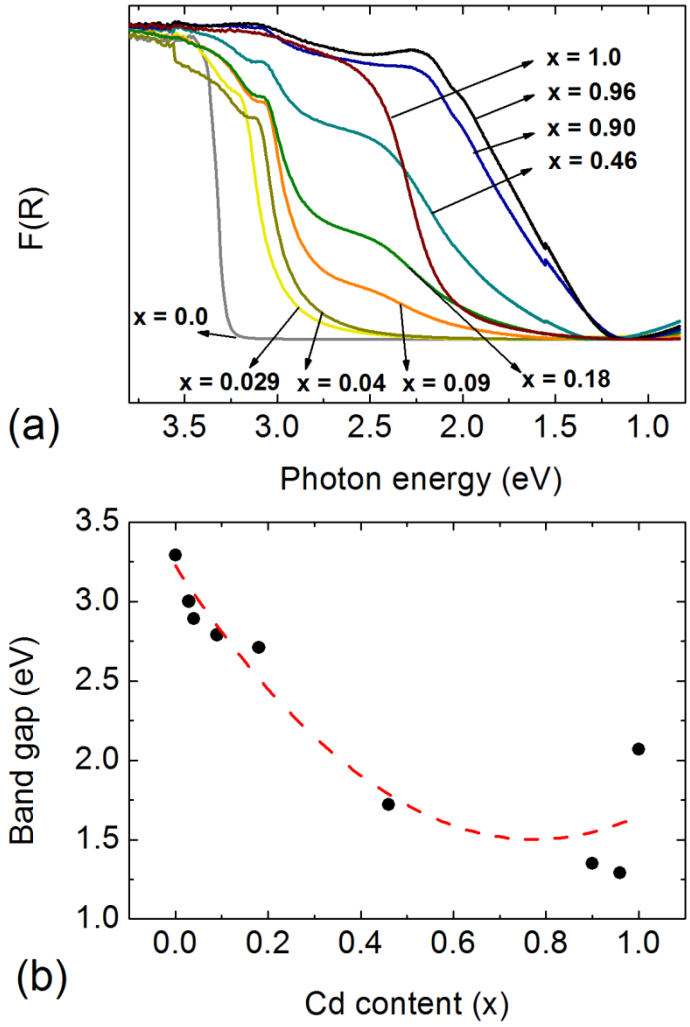

Figure 4. 8 (a) Square of Kubelka-Monk scattering F(R) as a function of photon energy for ternary $Cd_xZn_{1-x}O$ alloys with various Cd doping concentrations. (b) Optical bandgap bowing curve is displayed via polynomial curve fit based on equation 4.4. The R square for this fitting is 0.916.

The derived bowing coefficients are listed in Table 4.4 showing that: (1) The bowing coefficient depends on the component's composition. (2) Bowing coefficient increases significantly at the dilute impurity limits but minor changes at intermediate Cd content. (3) The bowing curve shows asymmetry at the two sides. The formation of bandgap bowing can be explained by their relative band edge positions. According to

the relative band positions of ZnO and CdO (Figure 4.10), the incorporation of Cd^{2+} into ZnO creates the impurity levels below CBM of ZnO, whereas the diffusion of Zn^{2+} in CdO produces the impurity levels above CBM of CdO. In the dilute doping alloys, the defect levels are strictly localised at the band edge, giving rise to a larger bowing coefficient. On the other hand, in the middle range of mixed Cd content, the resulting defect levels become more delocalised than in the dilute-doped alloys. Hence, the bowing coefficient is smaller and relatively constant.

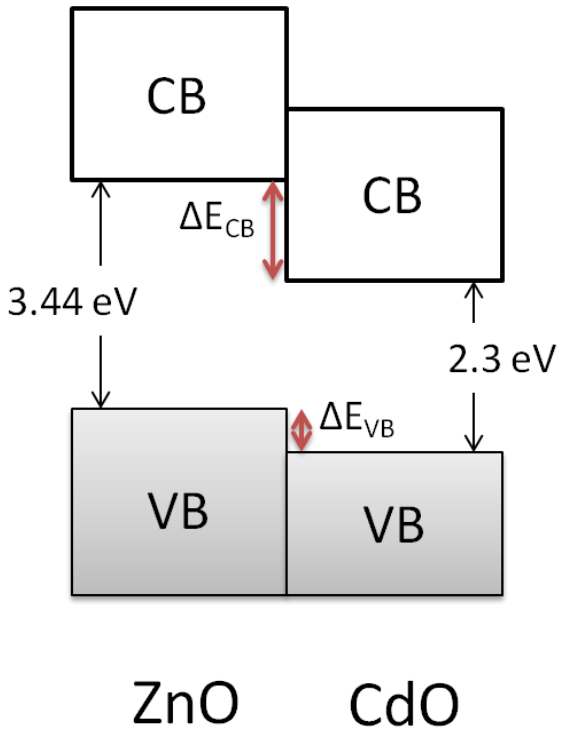

Figure 4. 9 Electronic band position in wurtzite ZnO and rocksalt CdO semiconductors. The direct bandgaps for ZnO and CdO are 3.44 eV and 2.3 eV, respectively. ΔE_{CB} and ΔE_{VB} are the conduction band offset energy and valence band offset energy for 1.6 eV and 0.46 eV, respectively.

Table 4. 4 The summary of measured bandgap values by UV-Vis DRS and bowing coefficients for $Cd_xZn_{1-x}O$ alloys.

$Cd_xZn_{1-x}O$	Bandgap (eV)	b
x = 0.0	3.29	-
x = 0.029	3.0	10.6462
x = 0.04	2.89	7.1368
x = 0.09	2.79	4.2
x = 0.18	2.71	2.1
x = 0.46	1.72	3.84
x = 0.90	1.35	9.3556
x = 0.96	1.29	17.7053
x = 1.0	2.07	-

The fully occupied cation d orbitals around 7-11 eV below VBM have been shown to have a great influence on the formation of valence band in II-VI semiconductors.[38, 39] The d-p repulsion reduces the direct bandgap by repelling Γ_{15}^* upwards without affecting the CBM. It should be noticed that this direct d-p mixing states occur only in T_d symmetry (e.g wurtzite or zincblende), and are forbidden in O_h symmetry (e.g. rocksalt) due to the crystal field theory.[40] A schematic molecular orbital diagram with or without d orbitals coupling is shown in Figure 4.11.[38] Figure 4.11 (a) demonstrates p-p orbitals coupling to form one bonding (Γ_{15}) orbital in the valence band and one antibonding (Γ_{15}^*) orbital in the conduction band. IIA-VI compound, such as MgO, is an example for this model. By contrast, in Figure 4.11 (b), metal d (t_2) and anion p (t_2) states generate a d-p bonding, Γ_{15} (d-p) underneath Γ_{12} (d), and an Γ_{15}^* (d-p) antibonding state. As a consequence, Γ_{15}^* (d-p) is viewed as an upward shift with respect to Γ_{15} level in Figure 4.11 (a). The magnitude of p-d repulsion is given by[39]

$$\Delta E_{pd} \approx \frac{V_{pd}^2}{\varepsilon_p^a - \varepsilon_d^c} \tag{4.5}$$

where ΔE_{pd} is the magnitude of d-p repulsion, V_{pd}^2 is a matrix element, ε_p^a is the energy of anionic p orbital, and ε_d^c is the energy of cationic d orbital. Equation 4.5 indicates that the repulsion is inversely proportional to the energy difference between the cation d and anion p states. In other words, the cation with shallower d states repels the anion p band upwards more significant than the cation with deeper cationic d states since the shallower d orbitals are closer to anionic p orbital.

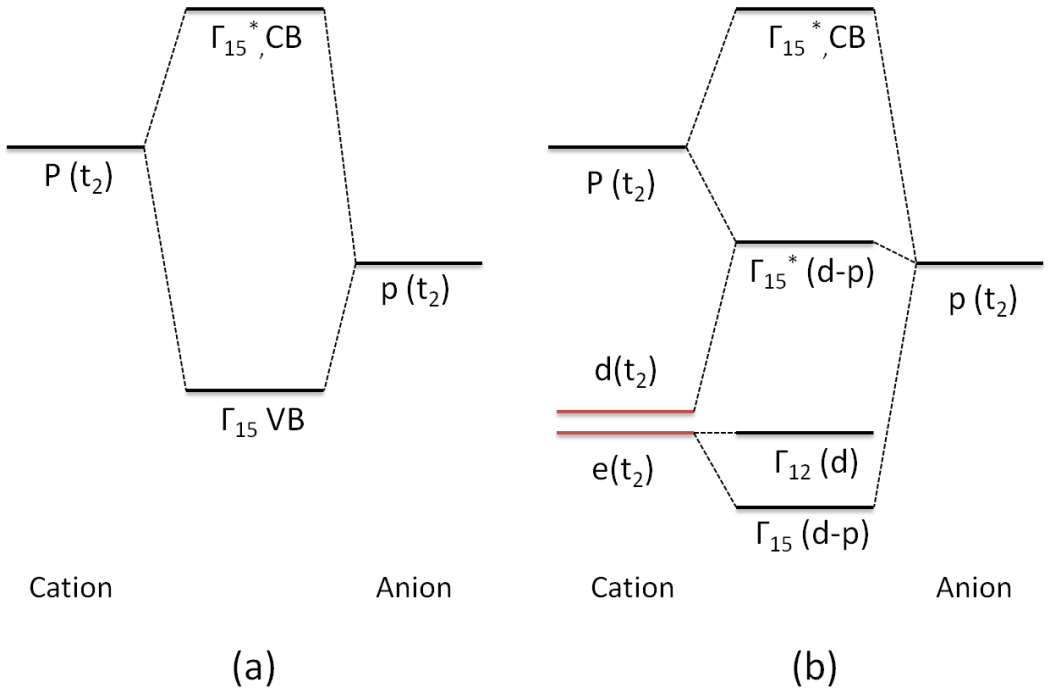

Figure 4. 10 (a) Schematic diagram of molecular orbitals of a IIA-VI compound. p-p orbitals coupling forms bonding and antibonding levels. (b) Schematic diagram of molecular orbitals of an IIB-VI compound with d-p orbitals coupling and p-p orbitals coupling.

It is know that the amount of CdO incorporated into ZnO is very restricted due to the different crystal structures. Figure 4.12 shows a single phase solid solution with

ZnO wurtzite structure at x = 0.0, 0.029 and 0.04, and another single phase solid solution with CdO rocksalt structure at x = 1.0, 0.96 and 0.90. When x is between 0.09 and 0.46, $Cd_xZn_{1-x}O$ alloys encounter two phases. The XRD refinements are shown in Figure 4.13 and their lattice parameters are summarised in Table 4.5. The lattice constants (i.e. a_z and c_z) and cell volume (V_z) of ZnO phase increases from the sample of x = 0.0 to x = 0.04, implying a lattice expansion in $Cd_xZn_{1-x}O$ single phase solid solution. Above x = 0.04, the lattice parameters are barely changed, implying that the solubility of CdO in ZnO is saturated, and then CdO begins to precipitated. On the other hand, in terms of ZnO-doped CdO, the lattice constant and cell volume of CdO decrease from x = 1.0 to x = 0.9 and then increases when the second phase (ZnO) takes place. This reveals the lattice shrinkage in the host structure when Zn^{2+} ions are being incorporated. The mixture of two phases has more impact on CdO lattice than on ZnO lattice as the lattice parameters vary more significantly in CdO.

Table 4. 5 XRD refinement data for ZnO lattice parameters (a_Z, c_Z, and cell volume; V_Z) and CdO lattice parameters (a_C, c_C, and cell volume; V_C).

$Cd_xZn_{1-x}O$	a_Z (nm)	c_Z (nm)	V_Z (nm^3)	a_C (nm)	V_C (nm^3)
x = 0.0	0.3250(2)	0.5207(3)	0.0476	-	-
x = 0.029	0.3259(6)	0.5213(4)	0.0480	-	-
x = 0.04	0.3268(2)	0.5224(7)	0.0483	-	-
x = 0.09	0.3273(1)	0.5231(0)	0.0485	0.4692(4)	0.1033
x = 0.18	0.3272(4)	0.5228(5)	0.0485	0.4689(1)	0.1031
x = 0.46	0.3272(8)	0.5231(6)	0.0485	0.4681(5)	0.1026
x = 0.90	0.3273(3)	0.5234(8)	0.0486	0.4690(9)	0.1032
x = 0.96	-	-	-	0.4695(3)	0.1035
x = 1.0	-	-	-	0.4697(6)	0.1037

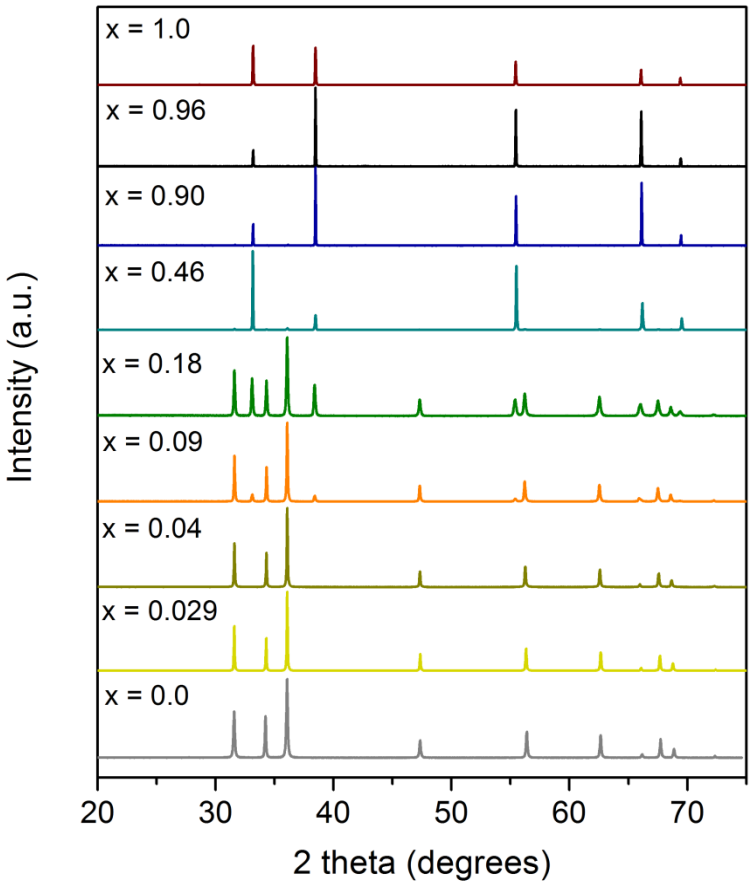

Figure 4. 11 Powder X-ray diffraction patterns of ternary $Cd_xZn_{1-x}O$ ($0 \leq x \leq 1$) alloys.

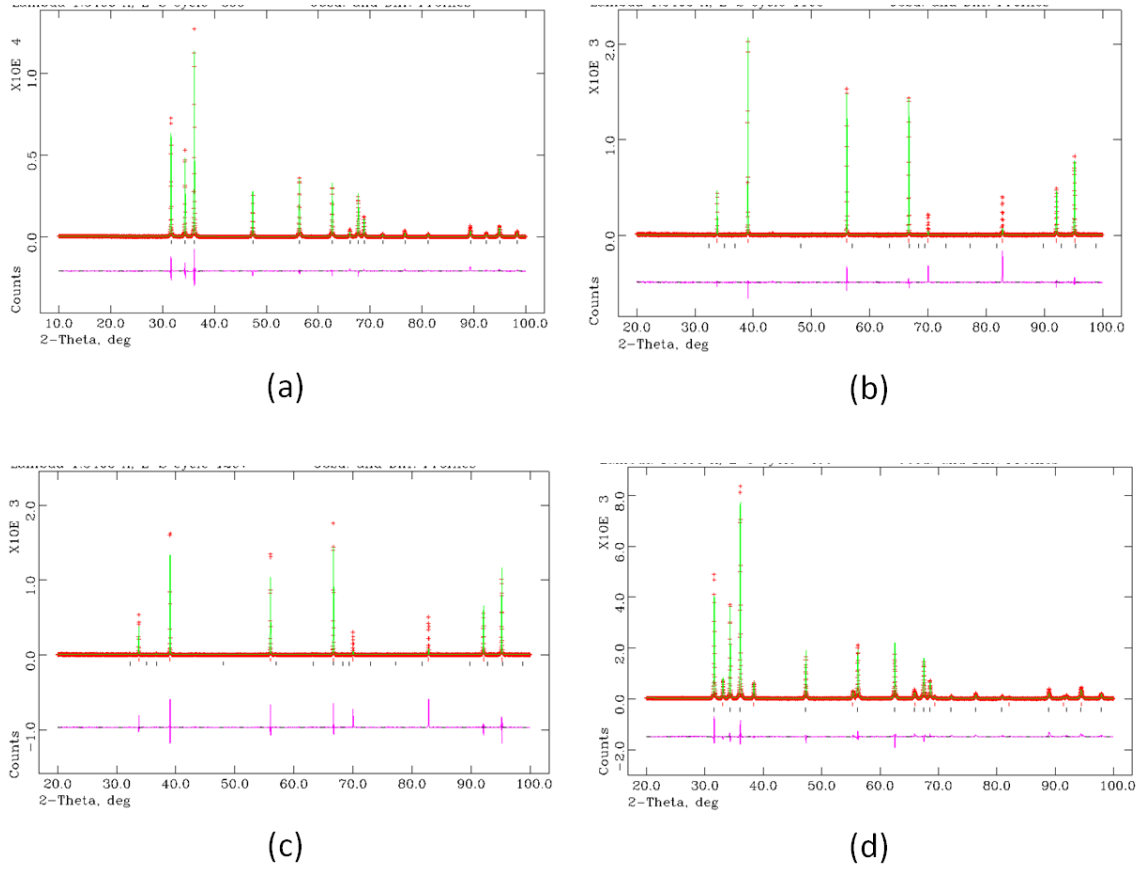

Figure 4. 12 XRD refinements of $Cd_xZn_{1-x}O$ powdered samples of (a) x = 0.04, (b) x = 0.09, (c) x = 0.9, and (d) x= 0.96.

The room temperature nonresonant Raman spectrum is presented for $Cd_xZn_{1-x}O$ alloys (Figure 4.14). As mentioned in chapter 4.1.2, the pattern for the undoped ZnO is E_{2L}, E_{2H}, A_1 (TO), E_1 (TO), A_1 (LO)-E_1 (LO) at 99 cm^{-1}, 438 cm^{-1}, 382 cm^{-1}, 408 cm^{-1}, and 580 cm^{-1}, respectively. The observed red shifts in E_{2H} and E_1 (TO) from x = 0.0 to x = 0.09 indicate a lattice distortion due to the effect of alloying. In the higher Cd concentrations, E_{2H} and E_1 (TO) are extinguished. Interestingly, the spectral intensities increases from x = 0.0 to x = 0.04 significantly when forming a single phase solid solution of $Cd_xZn_{1-x}O$ but decreases sharply when CdO exists. There is no Raman peak except for the TO mode at 262 cm^{-1} for CdO due to O_h space group symmetry.[41]

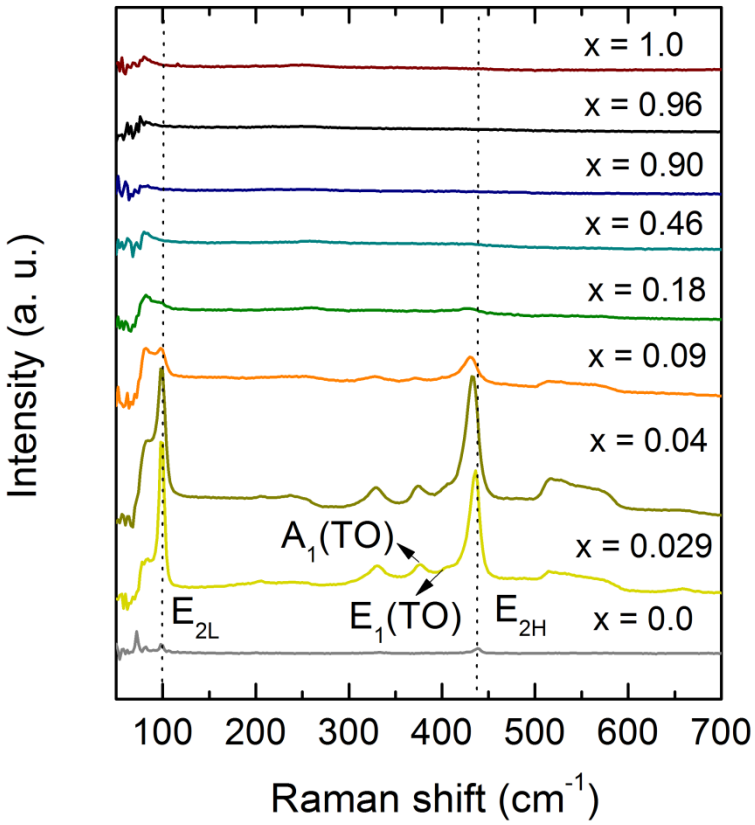

Figure 4. 13 The room temperature nonresonant Raman spectra of $Cd_xZn_{1-x}O$ alloys.

Figure 4.15 shows the morphologies of (a) x = 0.0, (b) x = 0.04, (c) x = 0.90, and (d) x = 1.0 samples performed by scanning electron microscopy (SEM). Commercial ZnO and CdO powders display hexagonal and cubic particles, respectively. The single-phase and two-phase solid solution $Cd_xZn_{1-x}O$ ceramic samples obtained through a calcine process demonstrate the particles were aggregated as dense lumps.

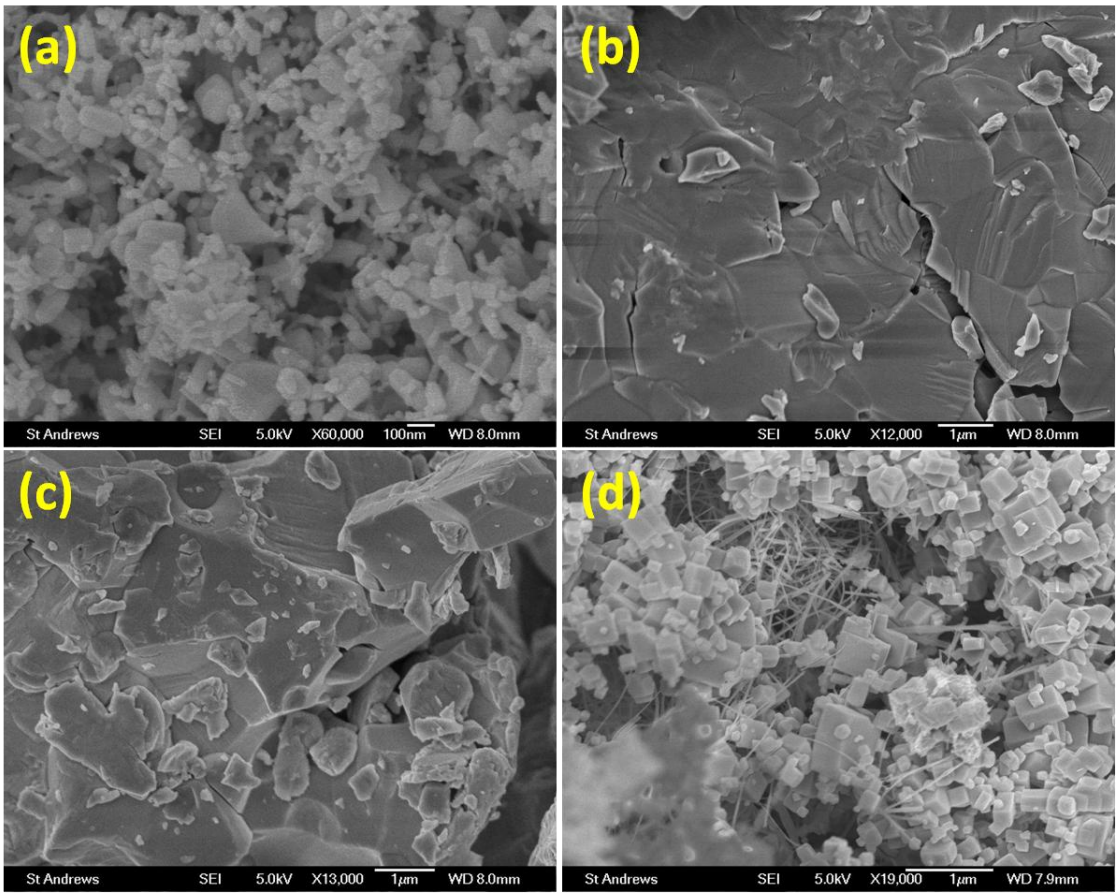

Figure 4. 14 Scanning electron microscopy (SEM) images of $Cd_xZn_{1-x}O$ of (a) x = 0.0, (b) x = 0.04, (c) x = 0.90, and (d) x = 1.0.

4.3 Photocatalytic Degradation of Methylene Blue

The textile industry produces a huge amount of toxic and coloured effluents with organic dyes. These dyes are hardly decomposed by biological treatments and become serious pollutants to the environment. Methylene blue is the one of the organic dyes that resistant to biodegradation and yields potentially carcinogenic aromatic amines. Oxide semiconducting materials have been considered to enhance the decomposition process

of dyes by UV light irradiation. The general scheme of photocatalytic destruction of an organic dye begins with absorption of light, generation of electrons and holes, transportation of charge carriers, and a redox reaction between free charge carriers and organic dyes. Various oxides, such as ZnO has been tested as a photocatalyst for a dye decomposition reaction. In this work, we will examine the photocatalytic degradation of methylene blue with our prepared $Cd_xZn_{1-x}O$ samples.

Figure 4.16 (a)-(g) represents the results of photocatalytic degradation experiments of methylene blue with $Cd_xZn_{1-x}O$ alloys upon irradiation, equipped with a UV cut-off filter. Methylene blue exhibits the strongest absorption peak at 664 nm. It is seen that the reactants of methylene blue (100 mL; 5 ppm) with present samples were decomposed down to nearly 100% during a 4-hour exposing time, demonstrating that $Cd_xZn_{1-x}O$ alloys are capable of photodegradating methylene blue. The presented decomposition rates of methylene blue as a function of degradation time for all $Cd_xZn_{1-x}O$ samples is shown in Figure 4.16 (h). The undoped ZnO nanoparticle (ca. 80-100 nm) has the best performance relative to CdO and the others prepared $Cd_xZn_{1-x}O$, even though it has the largest bandgap. This suggests that particle size dominates the decomposition rate. It is generally believed that the surface specific active areas increases when the particle size become small. Among $Cd_xZn_{1-x}O$ alloys, x = 0.18 and x = 0.09 samples with two-phase solid solution have the highest photodegrading rate, x = 0.04 sample has a comparatively slower degrading rate, and x = 0.029 and x = 0.96 samples have the slowest rate, of similar value to the rate of CdO. These results indicate the mixed phase that may be regarded as a heterojunction structure benefits to the photocatalytic degradation reaction. The interface between CdO and ZnO may enhance the diffusion of free charge carriers due to the difference in their band positions.

Therefore, the free charge carriers in x = 0.18 and 0.09 can reach the surface rapidly and react with methylene blue. Their decomposition rates of methylene blue are faster at the beginning of the reaction, giving rise to an exponential curve. On the other hand, the free charge carriers in x = 0.029, x = 0.04 and x = 0.96 samples transport slowly and thus the degradation curves display in a straight line. In single phase solid solution, the degradation efficiency in x = 0.04 is higher than in x = 0.029 since x = 0.04 has a smaller bandgap, beneficial to the absorption of incident photons. CdO powder is not promising in photocatalytic degradation of methylene blue. The majority component in x = 0.96 is CdO which is expected to have a poor degradation rate for methylene blue.

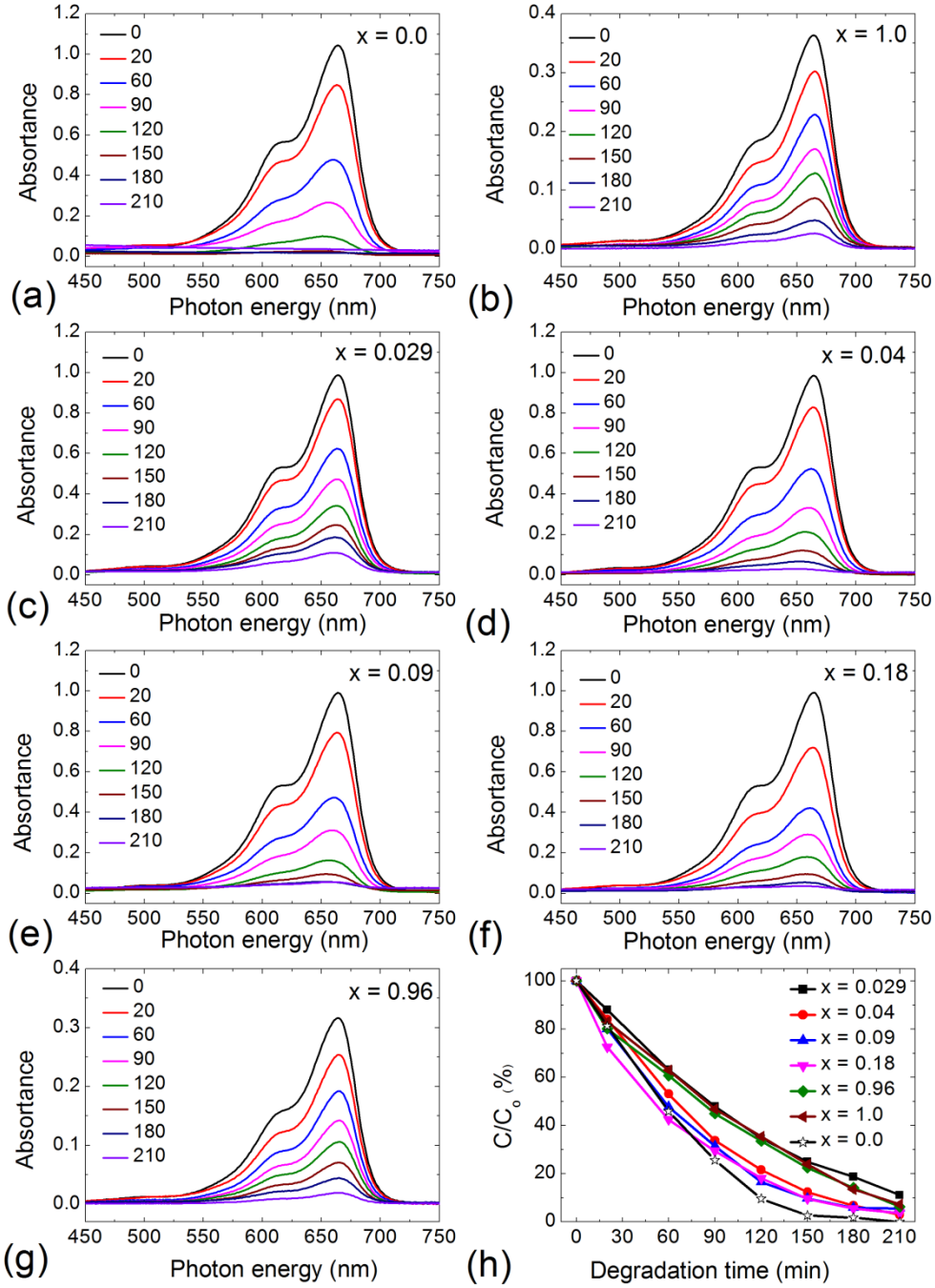

Figure 4. 15 (a)-(g) Variation of UV-Vis absorption spectra of methylene blue photocatalytised by various Cd concentrations of $Cd_xZn_{1-x}O$ alloys upon the illumination of simulated solar light from 0 min to 210 minutes. (h) Evolution of the relative concentration of methylene blue solution as a function of degradation time for $Cd_xZn_{1-x}O$ alloys. C is the concentration at t minute and C_0 is the initial concentration before irritation.

4.4 $Cd_xZn_{1-x}O$ Thin Film Properties

For some catalytic reactions, a thin layer of materials has advantage in terms of less raw material consumption. The performances in thin films are equal or even better in catalytic reaction than those in bulk materials. This section will present the physical and chemical properties of $Cd_xZn_{1-x}O$ thin films and illustrate the differences of these properties in $Cd_xZn_{1-x}O$ films comparing to powdered $Cd_xZn_{1-x}O$ samples.

All $Cd_xZn_{1-x}O$ films were deposited on glass substrates in nitrogen atmosphere at 400˚C. Cadmium nitrate tetrahydrate [$Cd(NO_3)_2{\cdot}4H_2O$] (Sigma-Aldrich, purity ≥ 99.0%) was used as the Cd source added in the 0.05 M zinc acetate precursor solution. Figure 4.17 (a) shows the 2 theta X-ray diffraction scans for $Cd_xZn_{1-x}O$ thin films ($0 \leq x \leq 1$). All $Cd_xZn_{1-x}O$ films have polycrystalline structure grown on amorphous glass substrates. No other reflections except for the host ZnO pattern are seen in the films with x = 0.02 and x = 0.04. As the Cd concentration increases to x = 0.10, a second phase of CdO precipitates out. In Figure 4.17 (a) the (002) peak shifts to a higher Bragg angle. The XRD data shows that the unit cell volume and the FHWM of (002) increase with increasing Cd amount, as shown in Figure 4.17 (b) and Table 4.6. The increasing cell volume implies a lattice expansion due to the substitution of larger ionic size of Cd^{2+} (0.97Å) for Zn^{2+} (0.74Å).[42] In contrast to ZnO powder, the undoped ZnO and $Cd_xZn_{1-x}O$ thin films exhibit a strong crystal orientation along *c*-axis. The greatest intensity peak in ZnO films is (002) instead of (101) in ZnO powder. This is attributed to the ability of the polar (0001) and $(000\bar{1})$ planes in thin films to rearrange the ions and to minimise the surface energy during growth.[43]

Table 4. 6 The summary of lattice constants, unit cell volume (V), crystalline size (d) and out-plain strain (δ) and in-plain strain (σ) of $Cd_xZn_{1-x}O$ films ($0 \le x \le 1$). ZnO bulk is a defect free single crystal.

$Cd_xZn_{1-x}O$ thin films	(002)	a (nm)	c (nm)	V (nm^3)	d (nm)	δ (10^{-3})	σ (10^7 N/m^2)
ZnO bulk		0.3248(1)	0.5206(9)	0.04711		-	-
x = 0	34.5375	0.3241(1)	0.5189(7)	0.04721	41.83	-3.296	141
x = 0.02	34.5407	0.3242(3)	0.5189(3)	0.04723	41.62	-3.384	145
x = 0.04	34.5443	0.3244(7)	0.5188(8)	0.04731	37.84	-3.484	149
x = 0.10	34.5455	0.3245(4)	0.5188(6)	0.04733	34.68	-3.518	151
x = 0.25	34.5377	0.3247(3)	0.5189(7)	0.04739	31.18	-3.299	141

The increasing FWHM as well as the decreasing crystalline size (d) with higher Cd concentration reflect a deteriorating crystallinity. This suggests that an increasing amount of Cd^{2+} in ZnO lattice results in a more serious lattice distortion. Furthermore, it is known that the lattice stress can be affected by an introduction of impurity. The formula for the determination of the out-plane strain (δ), i.e. perpendicular to the substrate surface, is expressed as:

$$\delta = (c - c_0)/c_0 \tag{4.6}$$

where c and c_0 are the lattice constant for our prepared $Cd_xZn_{1-x}O$ thin films and a stress-free bulk ZnO, respectively.[44] The negative value of δ shown in Table 4.6 indicates a compressive stress. In-plane stress (σ), i.e. parallel to the substrate surface, can be derived via the biaxial stress model:[44, 45]

$$\sigma = \left[2C_{13} - C_{32} \times \frac{C_{11} + C_{12}}{C_{13}} \right] \times \frac{d - d_0}{d_0} \tag{4.7}$$

where C_{ii} is the elastic stiffness constant (C_{13} = 1.05 × 10^{11} Nm^{-2}, C_{33} = 2.1 × 10^{11} Nm^{-2}, C_{11} = 2.1 × 10^{11} Nm^{-2}, C_{12} = 1.2 × 10^{11} Nm^{-2}), and d is the lattice spacing in (002) phase.[46] The positive σ value shows a tensile stress with the values ranging between 141 × 10^{7} Nm^{-2} and 151 × 10^{7} Nm^{-2} among $Cd_xZn_{1-x}O$ films.

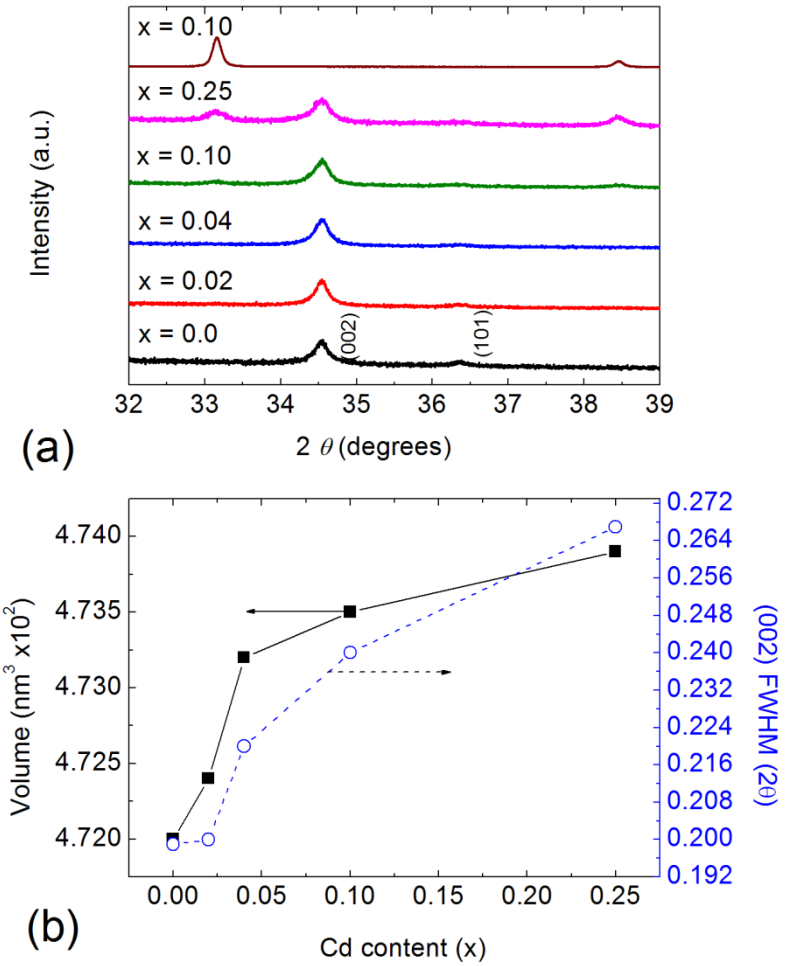

Figure 4. 16 (a) XRD 2 theta scans for $Cd_xZn_{1-x}O$ (0 ≤ x ≤ 1) films. (b) The illustration of the relationship between CdO concentration, cell volume and (002) FWHM.

Bandgap determinations conducted from UV-Vis absorption spectra of $Cd_xZn_{1-x}O$ films are shown in Figure 4.18. The bandgap values are shifted to lower binding

energy when x increases. The spectra of x = 0.1 and x = 0.25 samples that encompass a broad shoulder on the lower energy side reveals the formation of a cadmium-rich phase. The broad feature at a low energy is also likely to be due to a higher concentration of defects because two mixing phases can create more grain boundaries. The insert in Figure 4.18 shows the bandgap values as a function of CdO concentration. A polynomial fit is employed and expressed as $y = 0.361x^2 – 0.612x + 3.296$. The bandgap is reduced to 3.27 eV at x = 0.04 in a single phase solid solution and further down to 3.16 eV at x = 0.25 in a two-phase solid solution. The bandgap narrowing from single phase to two phases is also found in $Cd_xZn_{1-x}O$ powders.

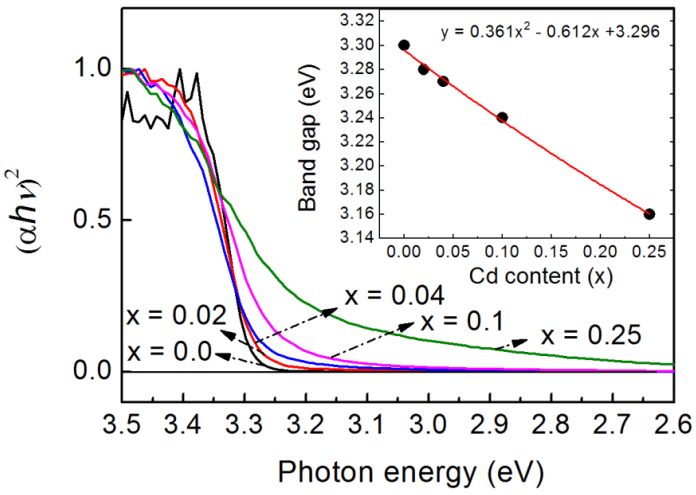

Figure 4. 17 The square of optical absorption coefficient versus photon energy of $Cd_xZn_{1-x}O$ ($0 \le x \le 1$) films. The insert displays a polynomial fit for the bandgap values as a function of CdO content.

The valence band XPS spectra for $Cd_xZn_{1-x}O$ films are displayed in Figure 4.19. Since samples were electrically connected to the sample holder, the Fermi level is at a constant energy, which is calibrated with a silver reference. In Figure 4.19 the XPS

measurements were scanned from the Fermi level (0 eV) to the Zn 3d and Cd 4d photoemission peaks. For the undoped ZnO, a symmetrical Zn 3d peak appears at 10.5 eV. As Cd concentration increases, the shoulder extends to the higher energy side of the Zn 3d peak. This increasing peak at 12.5 eV is assigned to Cd 4d photoemission, which was approved by the first-principle calculation.[27] The position (ξ) of VBM relative to the Fermi level (E_f) was determined by the intersection linear fits to the leading edge of the valence band photoemission and the background (Table 4.7).

Table 4. 7 A summary of optical bandgap values and the results of X-ray photoemission spectra of $Cd_xZn_{1-x}O$ ($0 \leq x \leq 1$) films.

$Cd_xZn_{1-x}O$ thin films	Optical bandgap (eV)	Zn $2p_3$ (eV)	ξ (eV)
x = 0	3.30	1022.05	3.32
x = 0.02	3.28	1022.05	3.27
x = 0.04	3.27	1022	3.21
x = 0.10	3.24	1021.95	3.19
x = 0.25	3.17	1021.8	3.11

The ξ values are smaller than the energies of optical bandgap except for the undoped ZnO, revealing that the position of Fermi level lies within the gap. This finding is different to the powdered samples, for which their Fermi levels lie above CBM. The explanation for the difference of Fermi level position between the films and powers is the surface area ratio. In general, a sphere particle (0.01-1.0 μm) has a larger surface area than a random packing film.[47] For n-type semiconductors with a highly dispersive conduction band, larger surface area would create more intrinsic surface electronic states via the process of surface reconstruction or extrinsic surface electronic states. For an n-type semiconductor, positively (negatively) charged surface states are balanced by

a negative (positive) space charge region to maintain the charge neutrality. This compensating process is achieved by a downward (upward) bending on electronic bands to increase (decrease) the electron density at the surface, leading to accumulation (depletion) of electrons on the surface region.[48] Therefore, surface electron accumulation can be possible found in $Cd_xZn_{1-x}O$ powders with a larger surface area rather than in $Cd_xZn_{1-x}O$ films.

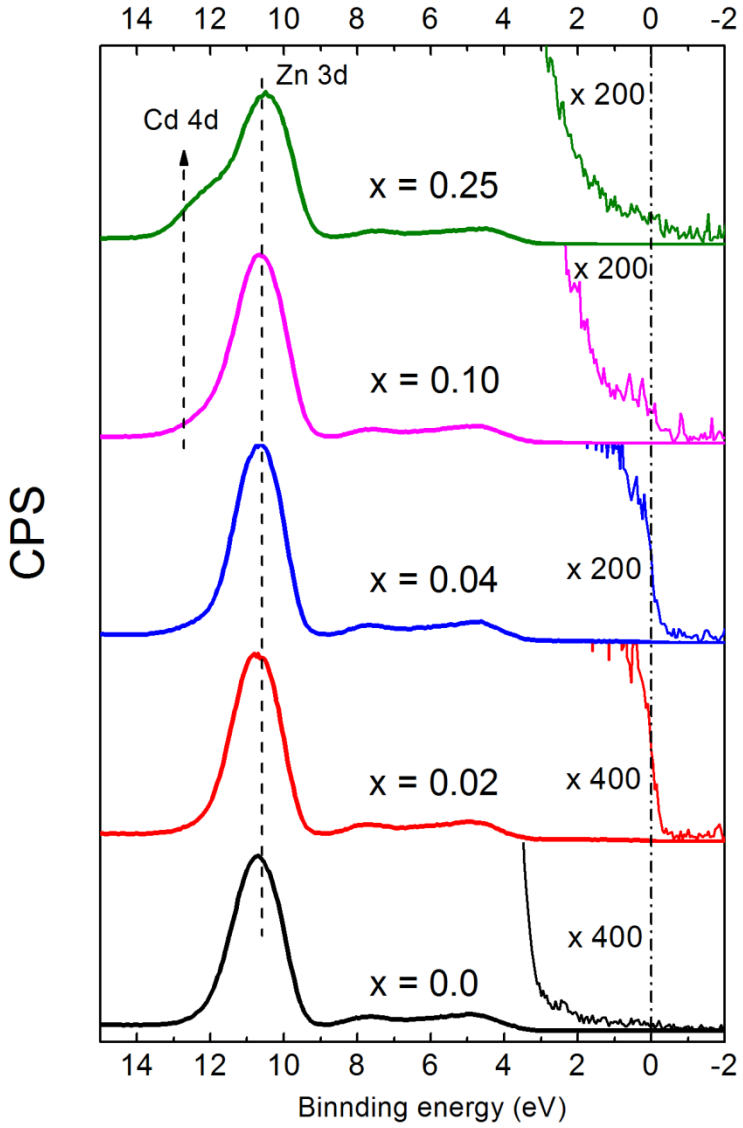

Figure 4. 18 Valence band (VB) X-ray photoelectron spectra of $Cd_xZn_{1-x}O$ ($0 \le x \le 1$) films are displayed in the region of VB, Zn 3d and Cd 4d core levels. The Fermi edges are enlarged by 200-400 times.

4.5 Summary

Ternary $Cd_xZn_{1-x}O$ ceramic samples and thin films were prepared by conventional solid-state reaction and spray pyrolysis in various compositions. The

addition of Cd element into ZnO lattice effectively decreases the electronic bandgap in the $Cd_xZn_{1-x}O$ solid solution, both in powder or in thin film.

The electronic bandgap in powders was effectively reduced from 3.28 eV (undoped ZnO) to 2.94 eV ($Cd_{0.075}Zn_{0.925}O$). The Fermi level in the bulk area resides within the bandgap confirmed by Edwards-Siernko-Mott criterion. On contrast, owing to a surface electron accumulation and a downward band bending, the Fermi level at the surface is above the conduction band edge. The electronic band bending (valence and conduction bands) in the surface region of $Cd_xZn_{1-x}O$ (x = 0.039 and 0.075) alloys were established from a combination of UV-Vis DRS and high resolution XPS. The features of the conduction band were determined with XANES measurements, suggesting that the CBM was pulled down and the induced free carriers were pumped into the conduction band with increasing CdO concentration.

$Cd_xZn_{1-x}O$ thin films also exhibited an bandgap reduction with increasing Cd doping. However, surface band bending and electron accumulation were not found in these films.

Photocatalytic degradation of methylene blue were tested with $Cd_xZn_{1-x}O$ powders. Nanoparticle ZnO powder showed the best performance because it has the highest surface areas when compared to the other $Cd_xZn_{1-x}O$ powders in micron scale. The samples of x = 0.09 and x = 0.18 with two-phase solid solution dominated the degradation reaction could be due to a formation of heterojunction band.

4.6 References

1. L. F. J. Piper, L. Colakerol, P. D. C. King, A. Schleife, J. Zuniga-Perez, P. A. Glans, T. Learmonth, A. Federov, T. D. Veal, F. Fuchs, V. Munoz-Sanjose, F. Bechstedt, C. F. McConville and K. E. Smith, Physical Review B **78**, 165127 (2008).
2. C. McGuinness, C. B. Stagarescu, P. J. Ryan, J. E. Downes, D. Fu, K. E. Smith and R. G. Egdell, Physical Review B **68**, 165104 (2003).
3. S. Sadofev, S. Blumstengel, J. Cui, J. Puls, S. Rogaschewski, P. Schafer and F. Henneberger, Applied Physics Letters **89**, 201907 (2006).
4. J. Ishihara, A. Nakamura, S. Shigemori, T. Aoki and J. Temmyo, Applied Physics Letters **89**, 91914 (2006).
5. X. Y. Ma, P. L. Chen, R. J. Zhang and D. R. Yang, Journal of Alloys and Compounds **509**, 6599 (2011).
6. T. Gruber, C. Kirchner, R. Kling, F. Reuss, A. Waag, F. Bertram, D. Forster, J. Christen and M. Schreck, Applied Physics Letters **83**, 3290 (2003).
7. L. G. Mar, P. Y. Timbrell and R. N. Lamb, Thin Solid Films **223**, 341 (1993).
8. L. F. J. Piper, P. H. Jefferson, T. D. Veal, C. F. McConville, J. Zuniga-Perez and V. Munoz-Sanjose, Superlattices and Microstructures **42**, 197 (2007).
9. T. C. Damen, S. P. S. Porto and B. Tell, Physical Review **142**, 570 (1966).
10. R. Cuscó, E. Alarcón-Lladó, J. Ibáñez, L. Artús, J. Jiménez, B. Wang and M. J. Callahan, Physical Review B **75**, 165202 (2007).
11. M. Scepanovic, M. Grujic-Brojcin, K. Vojisavljevic, S. Bernik and T. Sreckovic, Journal of Raman Spectroscopy **41**, 914 (2010).
12. L. Bergman, J. L. Morrison, X. B. Chen, J. Huso and H. Hoeck, Applied Physics Letters **88**, 23103 (2006).
13. M. Ghosh, N. Dilawar, A. K. Bandyopadhyay and A. K. Raychaudhuri, Journal of Applied Physics **106**, 84306 (2009).
14. X. F. Wang, J. B. Xu, B. Zhang, H. G. Yu, J. Wang, X. X. Zhang, J. G. Yu and Q. Li, Advanced Materials **18**, 2476 (2006).
15. P. H. Jefferson, S. A. Hatfield, T. D. Veal, P. D. C. King, C. F. McConville, J. Zuniga-Perez and V. Munoz-Sanjose, Applied Physics Letters **92**, 22101 (2008).
16. P. P. Edwards and M. J. Sienko, Physical Review B **17**, 2575 (1978).
17. A. P. Roth, J. B. Webb and D. F. Williams, Physical Review B **25**, 7836 (1982).
18. Y. Danhara, T. Hirai, Y. Harada and N. Ohno, Physica Status Solidi C **3**, 3565 (2006).

19. M. W. Allen, C. H. Swartz, T. H. Myers, T. D. Veal, C. F. McConville and S. M. Durbin, Physical Review B **81**, 75211 (2010).
20. C. Korber, V. Krishnakumar, A. Klein, G. Panaccione, P. Torelli, A. Walsh, J. L. F. Da Silva, S. H. Wei, R. G. Egdell and D. J. Payne, Physical Review B **81**, 165207 (2010).
21. R. G. Egdell, T. J. Walker and G. Beamson, Journal of Electron Spectroscopy and Related Phenomena **128**, 59 (2003).
22. B. E. Sernelius, K. F. Berggren, Z. C. Jin, I. Hamberg and C. G. Granqvist, Physical Review B **37**, 10244 (1988).
23. X. P. Li, B. L. Zhang, H. C. Zhu, X. Dong, X. C. Xia, Y. G. Cui, Y. Ma and G. T. Du, Journal of Physics D-Applied Physics **41**, 35101 (2008).
24. P. D. C. King, T. D. Veal, A. Schleife, J. Zuniga-Perez, B. Martel, P. H. Jefferson, F. Fuchs, V. Munoz-Sanjose, F. Bechstedt and C. F. McConville, Physical Review B **79**, 205205 (2009).
25. A. Janotti and C. G. Van de Walle, Reports on Progress in Physics **72**, 126501 (2009).
26. J. J. Chen, F. Ren, Y. J. Li, D. P. Norton, S. J. Pearton, A. Osinsky, J. W. Dong, P. P. Chow and J. F. Weaver, Applied Physics Letters **87**, 192106 (2005).
27. X. D. Zhang, M. L. Guo, W. X. Li and C. L. Liu, Journal of Applied Physics **103**, 63721 (2008).
28. J. W. Chiou, K. P. K. Kumar, J. C. Jan, H. M. Tsai, C. W. Bao, W. F. Pong, F. Z. Chien, M. H. Tsai, I. H. Hong, R. Klauser, J. F. Lee, J. J. Wu and S. C. Liu, Applied Physics Letters **85**, 3220 (2004).
29. T. Yao, W. S. Yan, Z. H. Sun, Z. Y. Pan, Y. Xie, Y. Jiang, J. Ye, F. C. Hu and S. Q. Wei, Journal of Physical Chemistry C **113**, 14114 (2009).
30. J. H. Guo, L. Vayssieres, C. Persson, R. Ahuja, B. Johansson and J. Nordgren, Journal of Physics-Condensed Matter **14**, 6969 (2002).
31. D. A. McKeown, Physical Review B **45**, 2648 (1992).
32. H. M. Chen, C. K. Chen, C. C. Lin, R. S. Liu, H. Yang, W. S. Chang, K. H. Chen, T. S. Chan, J. F. Lee and D. P. Tsai, Journal of Physical Chemistry C **115**, 21971 (2011).
33. H. S. Hsu, J. C. A. Huang, Y. H. Huang, Y. F. Liao, M. Z. Lin, C. H. Lee, J. F. Lee, S. F. Chen, L. Y. Lai and C. P. Liu, Applied Physics Letters **88** (2006).
34. S. Locmelis, C. Brunig, M. Binnewies, A. Borger, K. D. Becker, T. Homann and T. Bredow, Journal of Materials Science **42**, 1965 (2007).
35. S. H. Wei and A. Zunger, Journal of Applied Physics **78**, 3846 (1995).
36. S. H. Wei and A. Zunger, Physical Review B **43**, 1662 (1991).

37. S. H. Wei, L. G. Ferreira, J. E. Bernard and A. Zunger, Physical Review B **42**, 9622 (1990).
38. S. H. Wei and A. Zunger, Physical Review B **37**, 8958 (1988).
39. S. H. Wei and A. Zunger, Applied Physics Letters **72**, 2011 (1998).
40. P. Atkins, T. Overton, J. Rourke, M. Weller and F. Armstrong, *Inorganic Chemistry*, Fourth ed. (Oxford University Press, Oxford, 2006).
41. Z. V. Popovic, G. Stanisic, D. Stojanovic and R. Kostic, Physica Status Solidi B-Basic Research **165**, K109 (1991).
42. R. D. Shannon, Acta Crystallographica Section A **32**, 751 (1976).
43. K. Ellmer, A. Klein and B. Rech, edited by R. Hull, J. Parisi, R. Osgood and H. Warlimont (Springer, New York, 2008), pp. 443.
44. C. Koidis, S. Logothetidis, S. Kassavetis, A. Laskarakis, N. A. Hastas and O. Valassiades, Physica Status Solidi a-Applications and Materials Science **207**, 1581 (2010).
45. B. C. Mohanty, Y. H. Jo, D. H. Yeon, I. J. Choi and Y. S. Cho, Applied Physics Letters **95**, 62103 (2009).
46. B. K. Sharma and N. Khare, Journal of Physics D-Applied Physics **43**, 465402 (2010).
47. D. M. Smith and N. E. Olague, Journal of Physical Chemistry **91**, 4066 (1987).
48. H. Lüth, *Solid Surfaces, Interface and Thin Films*. (Springer, Berlin, 2001).

CHAPTER 5

SULPHUR DOPED ZINC OXIDE

ZnO is an II-VI group semiconductor with a wide direct bandgap of 3.37 eV and a large exciton binding energy of 60 meV. It has a high transparency in the visible region (85%-95%) and high electron mobility when substantially doping.[1-3] It is well established that bandgap engineering by alloying dopants enables one to tune the basic materials performance required for application in diverse areas such as the photocatalytic splitting of water or use as a transparent electrode. Isovalent anionic substitution provides another means of tuning the bandgap in $ZnO_{1-x}A_x$ (A = S, Se and Te) solid solutions.[4-6] In general bandgaps do not change monotonically as a function of anion substitution level due to so-called band bowing effects.[4, 6-8] Sulphur is of particular interest as a substitutional anion. It possesses a smaller electronegativity (2.58) than that of oxygen (3.44) and a larger anionic radius (i.e. S^{2-}: 1.7Å *versus* O^{2-}: 1.26Å). However, in contrast to the usual trend found in III-V materials the electronic bandgap does not decrease monotonically with decreasing electronegativity of the anion; the bandgap of ZnS (3.80 eV) is actually larger than that of ZnO. Yoo *et al.*[9] studied the changes in the optical and electrical properties of $ZnO_{1-x}S_x$ films prepared by pulsed laser deposition with increasing sulphur concentration. Later Meyer *et al.*[10] showed that optical spectra of films prepared by reactive sputtering over the whole composition range showed a red shift in the interband absorption edge with increasing S concentration at low doping levels, and a monotonic increase in bandgap for $x > 0.45$. Locmelis et al.[11] used chemical transport techniques to prepare single-crystal $ZnO_{1-x}S_x$ with a wurtzite structure in the range 0

$\leq x \leq 0.05$ and a cubic zincblende structure in the range $0.96 \leq x \leq 1$. In addition, Bae et. al. [12] used chemical vapour deposition techniques to prepare $ZnO_{1-x}S_x$ nanorod arrays on silicon.

In contrast to the mentioned above vacuum-based physical deposition techniques, spray pyrolysis is a non-vacuum system employed to prepare $ZnO_{1-x}S_x$ films in our study. The technique of spray pyrolysis is a simple and inexpensive deposition technique which in principle can produce a large-scale thin film at low cost.[13, 14] There have been several reports of preparing partially *c*-axis textured polycrystalline ZnO films by spray pyrolysis. However, none of them have achieved epitaxial growth of highly crystalline ZnO thin films. Moreover, although $ZnO_{1-x}S_x$ alloys have been treated by density-functional theory and related methods in recent years, there have been no comparable experimental studies on the importance of valence band structure with photoemission electronic techniques.[6, 8, 15, 16] In the present chapter we demonstrate the growth of highly crystalline $ZnO_{1-x}S_x$ thin films on $Al_2O_3(0001)$ substrates by spray pyrolysis of a zinc acetate precursor in an acidic solution. The electronic structure of these films has been characterised by optical spectroscopy in conjunction with high resolution X-ray photoemission spectroscopy, which provide complementary methods for the investigation of the influence of S doping on the electronic structure and the bandgap.

5.1 Bandgap Narrowing in $ZnO_{1-x}S_x$ Thin Films ($0 \leq x \leq 0.023$)

5.1.1 Structural and Morphological Characterisation

In Figure 5.1 (a), we show the x-ray diffraction (XRD) pattern of an undoped ZnO film deposited on an $Al_2O_3(0001)$ single crystal substrate. A single epilayer diffraction

feature in range between 33.8˚ and 34.8˚ attributable to the film is the wurtzite-(0002) reflection, which confirms a highly oriented growth with the epilayer *c*-axis perpendicular to the substrate surface. The full width at half maximum (FWHM) of the (0002) peak is only 0.072˚, which indicates the high quality of the ZnO film.

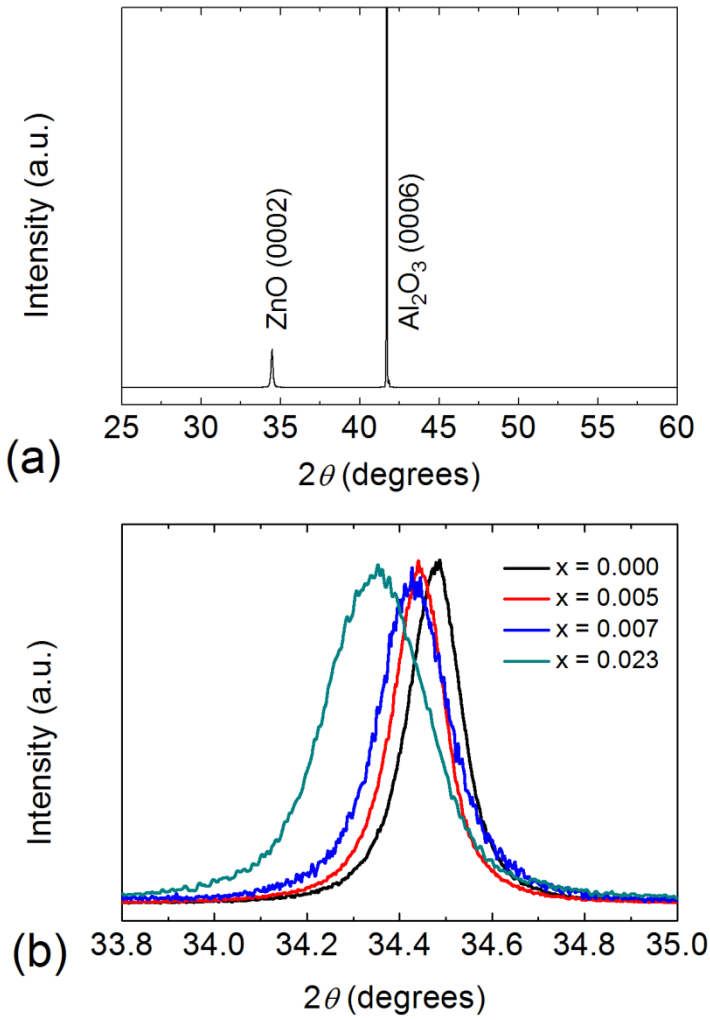

Figure 5. 1 (a) X-ray diffraction profile of an undoped ZnO film deposited on single crystal Al_2O_3(0001) substrate. (b) Detail of the (0002) diffraction peak between 33.8 and 34.9 degree for $ZnO_{1-x}S_x$ for x = 0.000, x = 0.005, x = 0.007 and x = 0.023.

The expanded XRD scans over the (0002) reflection are shown in Figure 5.1(b). The (0002) peak shifts toward lower angle with increasing sulphur concentration as presented in Table 5.1. Furthermore, the examination of the lattice parameter revealed that the lattice constant *c* increases with increasing sulphur content. This indicates that the lattice spacing has expanded along the *c*-axis due to the partial replacement of the oxygen anion with the larger sulphur anion.[9, 10] The FHWM of the (0002) peak broadens compared to the undoped ZnO film, increasing from 0.072˚ in the ZnO to 0.230˚ in the film for x = 0.023. Instrument broadening can be excluded because all the measurements were performed in the same XRD machine with the same slit width and sample size. It is known that crystalline size and strain have a great influence on the width of peak profile. Crystalline size can be derived from the Scherrer's equation,

$$d = \frac{K\lambda}{\beta \cos\theta} \tag{5.1}$$

where d is the domain particle size, K is a constant ($0.89 < K < 1$), λ is the wavelength of incident X-ray, β is the width of the peak at half maximum intensity of a specific phase, and θ is the diffraction angle. The calculated results in Table 5.1 reveal that the crystalline size decreases as the sulphur content increases. Moreover, the out-plain strain along the *c*-axis for $ZnO_{1-x}S_x$ films was measured with values and presented in Table 5.1. Interestingly, the out-plain strain at x = 0.0 and x = 0.005 shows a compressive force along *c*-axis whereas it turns to an elastic strain at higher sulphur incorporation. The peak within a single phase may be explained by strain inhomogeneities due to the larger size of the sulphur anions surrounding the oxygen anions in the lattice.[12] Therefore, the increasing level of size mismatch with increasing S content transforms a compressive strain to an elastic strain. Thereby it explains

why the peak width increases significantly from x = 0.005 to x = 0.007 and further to x = 0.023.

Table 5. 1 The lattice parameters, crystalline size (d) and out-plain strain (δ) of $ZnO_{1-x}S_x$ films are obtained from XRD measurements, and roughness is determined by AFM experiments. ZnO bulk is referred to a defect-free single crystal ZnO (JCPDF number: 00-003-0888).

$ZnO_{1-x}S_x$ thin films	2θ (002)	c (nm)	d (nm)	δ (10^{-3})	FWHM (θ)	Roughness (nm)
ZnO bulk		0.5207(2)		-	-	
x = 0.0	34.47	0.51996(3)	57.80	-1.421	0.072	19.21
x = 0.005	34.42	0.52063(2)	54.18	-0.134	0.077	8.38
x = 0.007	34.41	0.52079(3)	36.12	0.173	0.115	8.52
x = 0.023	34.34	0.52187(5)	18.06	2.247	0.230	2.68

The morphologies of $ZnO_{1-x}S_x$ films are presented in Figure 5.2 and were obtained by performing an ex-situ scan with atomic force microscopy (AFM) to confirm that the particle size decreases as the S amount increases, which is consistent with the observation in XRD. The roughness values presented in Table 5.1 are 19.21 nm, 8.38 nm, 8.52 nm, and 2.68 nm for x = 0.0, x = 0.005, x = 0.007, and x = 0.023, respectively. In general, a smaller particle has a smoother surface.

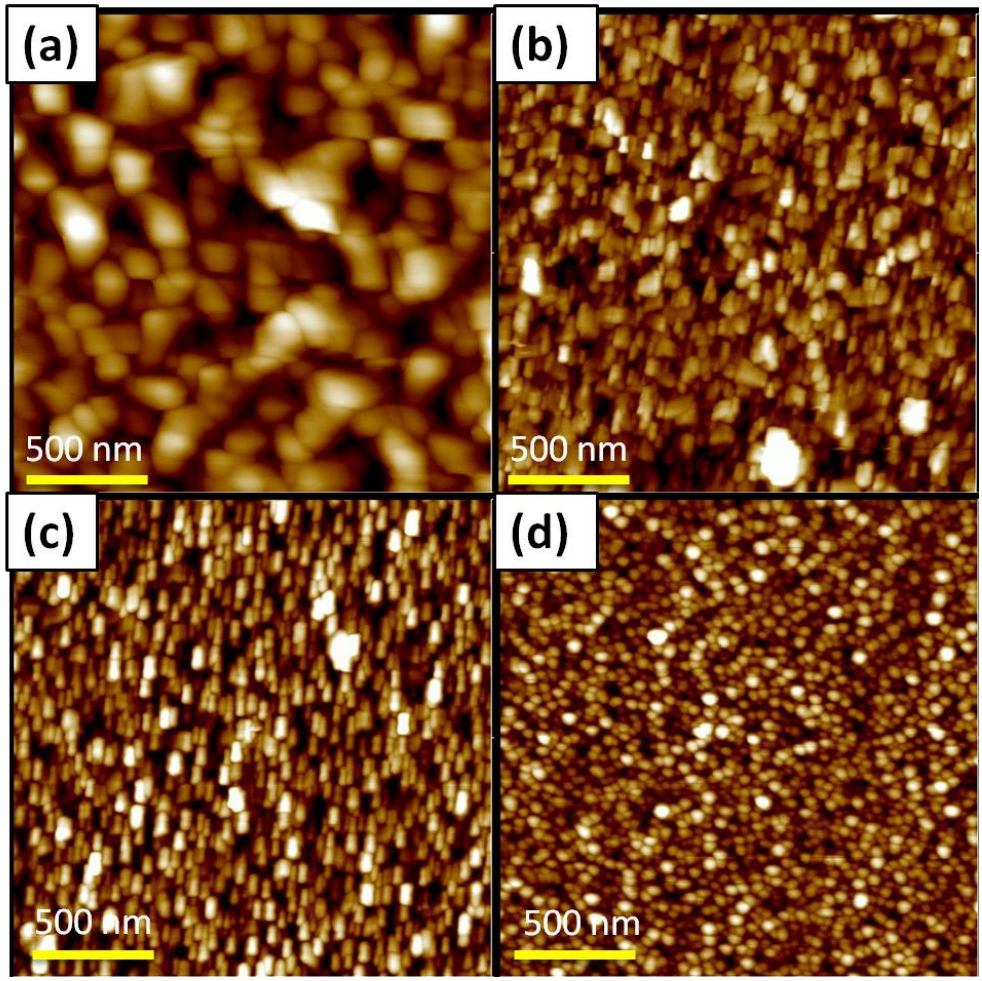

Figure 5. 2 Atomic force microscopy (AFM) images of $ZnO_{1-x}S_x$ films with (a) x = 0.0, (b) x = 0.005, (c) x = 0.007, and (d) x = 0.023.

5.1.2 Electronic Structure of $ZnO_{1-x}S_x$ Thin Films

The dependence of the electronic bandgap on the sulphur concentration in $ZnO_{1-x}S_x$ films was determined by optical absorption measurements and presented in Figure 5.3. The interband transitions of ZnO involve excitation from states of dominant O 2p character at the top of the valence band to states of dominant Zn 4s character at the bottom of the conduction band.[15] The lowest interband transitions are direct and the bandgap may be derived from the Tauc relation:[11]

$$(\alpha h\nu)^2 = c(h\nu - E_g) \quad (5.2)$$

where α is the absorption coefficient, $h\nu$ is the incident photon energy, c is a constant and E_g is the energy of optical bandgap. The bandgap estimated as 3.30 eV for the undoped ZnO is in a good agreement with the literature value of 3.37 eV.[2] The bandgap decreases to 3.28 eV and 3.20 eV for samples with x = 0.007 and x = 0.023, respectively. As mentioned above, the bandgap for pure ZnS is around 3.80 eV.[17] Nevertheless, the values of optical bandgap in $ZnO_{1-x}S_x$ solid solution display a bowing effect rather than a linear dependence with either dilute S doping into ZnO or dilute O doping into ZnS, so that S doping leads to a narrowing of the bulk bandgap. The compositional variations of the bandgap energy in II-VI isovalent semiconductor alloys $ZnO_{1-x}S_x$ has been approximated as:[11]

$$E_g(x) = (1-x)\cdot E_{g,(ZnO)} + x\cdot E_{g,(ZnS)} - b\cdot x\cdot(1-x) \quad (5.3)$$

where b is a bandgap bowing coefficient, which describes the deviation from a linear interpolation. The value of b is composition-dependent, indicating the degree of localisation of the wave-function of the band edge states. The b values for x = 0.007 and x = 0.023 S-doped ZnO obtained in the current work are 3.02 and 4.96 respectively. In principle, optical bowing can result from either the difference of volume deformation potentials of the constituents or the coupling of folded states through a perturbation potential.[7, 18, 19] In our scenario, the perturbation potential is the difference between the alloy potential and the average potential of the constituents. The perturbation is affected by the electronegativity difference and the size mismatch between the constituent O and S anions. When the electronegativity of the isovalent impurity is smaller than that of the host atom (i.e. S → ZnO), the isovalent impurity levels with a_1 symmetry will lie near the VBM whereas when the electronegativity of the isovalent impurity is larger than that of the host atom (i.e. O →

ZnS), the isovalent impurity levels with t_2 symmetry will appear near the CBM therefore resulting in a narrowing of the bandgap.

In Figure 5.3, the film with the highest S doping has puzzling band edge absorption. One may speculate that the absorption may be due to indirect transitions or defects. The energy required for indirect transition is 8.5 eV from $\Gamma^5_v \rightarrow M^2_c$ for the undoped ZnO,[20] and is unlikely to be relevant. Therefore, the feature of an extended tail in the highest doping sample is attributed to the imperfect crystallinity in $ZnO_{1-x}S_x$. The higher S concentration incorporated in ZnO leads to a higher defect concentration or lattice dislocation and thus a lower slope of the tail.

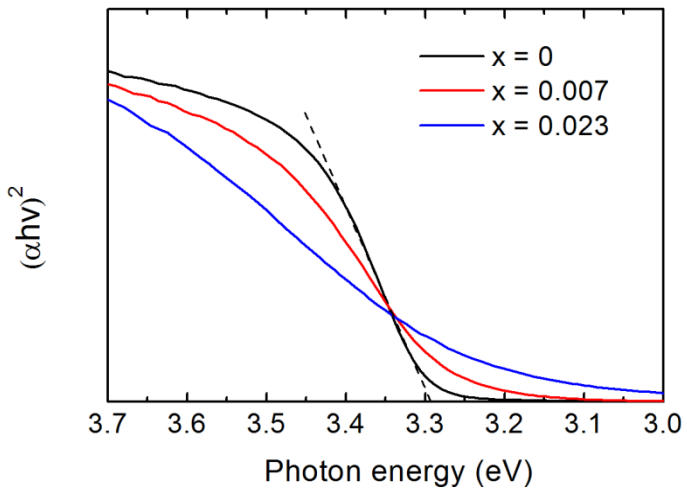

Figure 5. 3 Plots of $(\alpha h\nu)^2$ *versus* photon energy for $ZnO_{1-x}S_x$ films with x = 0.0, x = 0.007 and x = 0.023. A typical linear extrapolation used to determine the bandgap is shown for the undoped film.

The valence band (VB) X-ray photoemission spectra of $ZnO_{1-x}S_x$ films with x = 0.0, x = 0.007 and x = 0.023 are shown in Figure 5.4. The spectra are normalised to the Zn 3d photoemission peak at 11 eV since the atomic ratio of Zn remains unchanged. These three

spectra were aligned with the Fermi level at 0 eV. Since samples were electrically connected to the sample holder, the Fermi level is at a constant energy, which is calibrated with a silver reference. The VB spectrum of the undoped ZnO film has onset energy of 3.30 ± 0.05 eV as defined by a linear extrapolation of the valence band edge. In S-doped ZnO films, the VB onset energies are shifted to 3.27 eV and 3.18 eV for x = 0.007 and x = 0.023, respectively. The shift of the valence band onset energy is consistent with the results obtained from the optical measurements: the difference of 0.01 eV between the optical bandgap and the valence band onset is barely significant yet may possibly arise from the pinning of the Fermi level marginally below the conduction band minimum. The valence band onset also broadens in a fashion reminiscent of broadening of the optical onset. The results suggest that the incorporation of S into ZnO leads to a formation of isovalent defect levels above the VBM.[7, 8] In ZnO itself the position of the valence band maximum is determined by hybridisation between O 2p, Zn 3d and Zn 4s states: the defect-induced S states will be involved in similar hybridisation.[7] However, S 3p orbital is more delocalised than O 2p orbital and its energy level position is slightly higher than that of O 2p. Consequently, the mixing of O 2p and S 3p orbitals moves the valence band maximum upward. It is finally worth noting that the intensity of the valence band peaks A (~4.75 eV) and B (~7.60 eV) labeled in Figure 5.4 (a) and associated with states of dominant O 2p character show a small decrease in intensity because the electron density is transferred out of O 2p states into S 3p states as O is replaced with S.[15] According to Persson's study of S-doped ZnO using density functional theory (DFT), S 3p states were laid at about 1 eV higher than the uppermost O 2p states and there was no shift in the position of the CBM with S doping.[8]

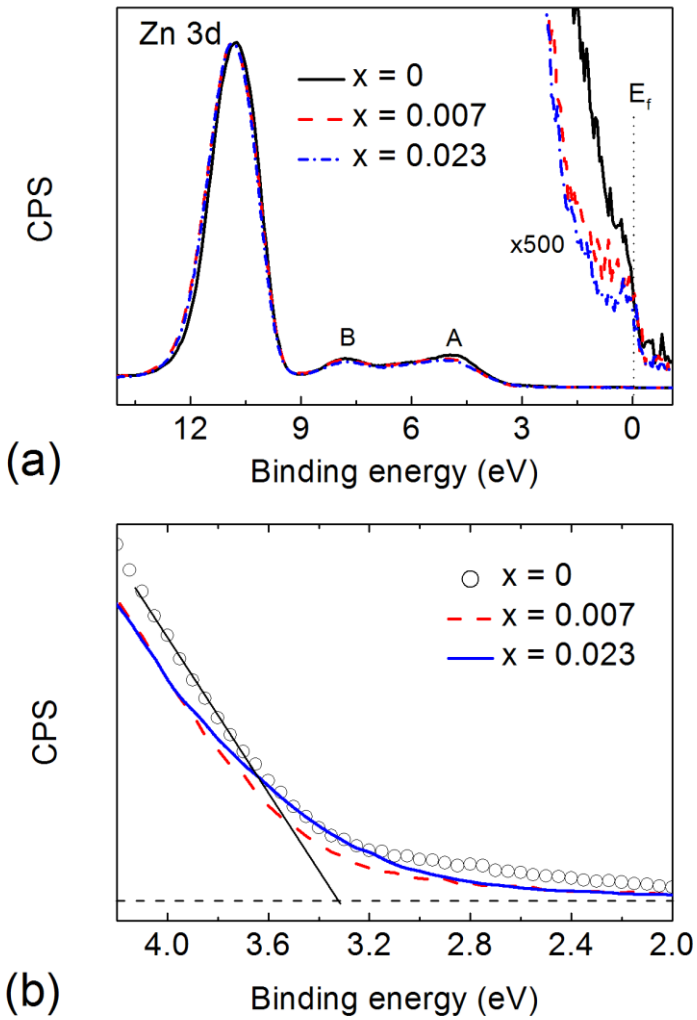

Figure 5. 4 (a) X-ray photoelectron spectra of $ZnO_{1-x}S_x$ thin films with x = 0.000, x = 0. 007 and x = 0.023 encompassing the Zn 3d shallow core level and the valence band. The intensities have all been normalised with respect to the Zn 3d peak at around 10 eV binding energy. Three curves on the right hand side multiple by 500times to display that all spectra are aligned the Fermi level at 0.0 eV. (b) Zoom in to the onset of valence band maximum spectra. Fundamental bandgaps are obtained by plotting a linear extrapolation, where x = 0.

Figure 5.5 presents the normalised O K-edge XANES spectra of ZnO and S-doped ZnO thin films. The photon energy region of 530-539 eV corresponds to electronic transitions from O 1s states into the conduction band of dominant Zn 4s characters which acquire O 2p

character through covalent mixing. Absorption between 539 eV and 550 eV is assigned to O 2p states hybridised with Zn 4p states. Above 550 eV, absorption is a result of O 2p states mixed with Zn 4d states.[21] In Figure 5.5, the absorption edge at 532-533 eV does not shift in these samples, reflecting the fact that the CBM does not change significantly with S doping. This result is in agreement with Persson's DFT study.[8]

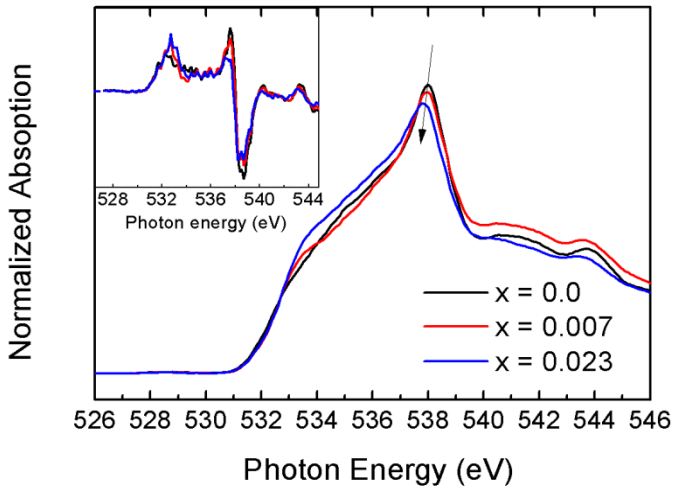

Figure 5. 5 O K-edge XANES spectra of the $ZnO_{1-x}S_x$ ($0 \leq x \leq 0.023$) samples. The insert in the top left corner shows the 1st differential for the absorption region.

The sample with x = 0.023 displays the lowest intensity of white line at around 538 eV and the broadest feature between 532 eV and 545 eV. The insert diagram demonstrates the 1st differential for the O K-edge XANES spectra in the region from 526 eV to 544 eV. It demonstrates that the three curves in Figure 5.5 are approximately identical except for the peaks at 533 eV and 537-539 eV. Be aware that the region after the absorption edge contains multiple scattering (i.e. multiple bounces of the photoelectron from surrounding ions or atoms), which provides the information on the positions of neighbouring atoms. For x = 0.023, the spectral features above the absorption edge are different compared to other

samples. This could be due to structural distortion in the samples with the highest S concentration. This observation is consistent with XRD data that x = 0.023 has the broadest FWHM in (002). The XANES spectra of Zn K-edge and Zn L_3-edge for $ZnO_{1-x}S_x$ samples are shown in Figure 5.6 (a) and (b). The Zn K-edge corresponds to the electron transition from Zn 1s states to unoccupied Zn $4p_\pi$ states (along *c*-axis), and Zn L_3-edge XANES illustrates the electron transition from Zn $2p_{2/3}$ states to Zn 4s, Zn $3d_{3/2}$, and Zn $3d_{5/2}$ states.[22] Overall, the three samples with different sulphur compositions show nearly an identical feature in the Zn K-edge and Zn L_3-edge XANES spectra. The sample x = 0.023 exhibits a slightly weaker intensity in the white line (at 9630 eV) of Zn K-edge XANES attributed to the fact that the ZnO (host) energy levels are perturbed by the introduction of sulphur atoms.

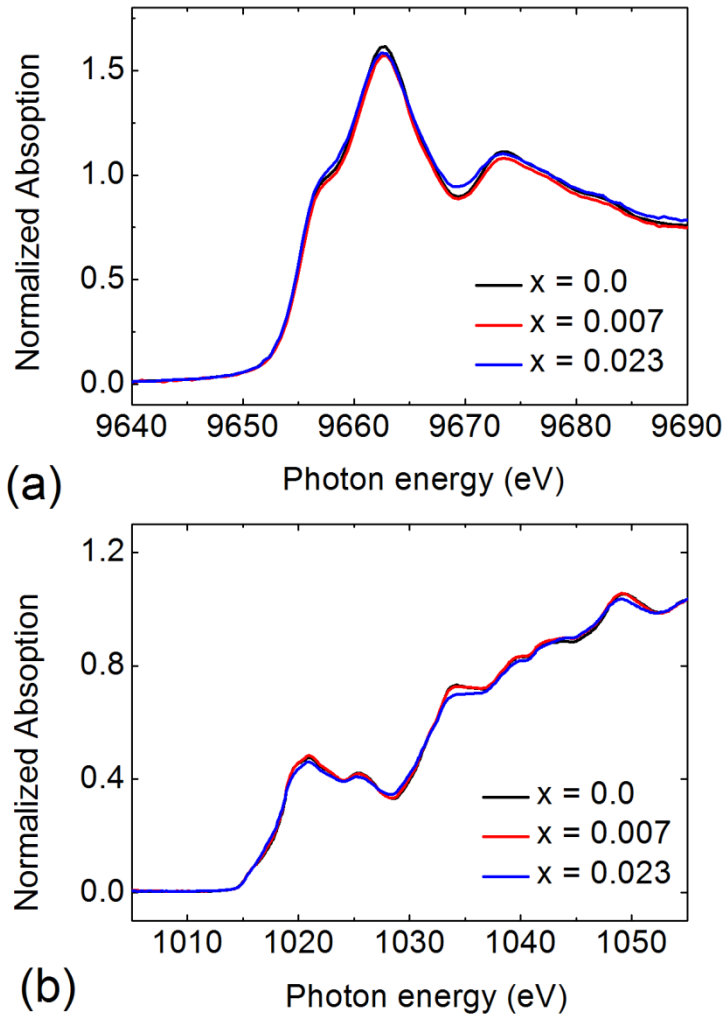

Figure 5. 6 (a) Zn K-edge and (b) Zn L_3-edge XANES spectra of the $ZnO_{1-x}S_x$ ($0 \leq x \leq 0.023$) samples.

A schematic energy level diagram summarising the current results is shown in Figure 5.7. The energies of the optical bandgap were obtained by UV-Vis measurements. It is assumed that the position of the Fermi level relative to the vacuum level does not change with S doping. The positions of the Fermi level were examined by VBM spectra. For the undoped ZnO film in our study, the position of the Fermi level is approximately 0.1 eV below the bottom of conduction band. The hybridisation of S 3p and O 2p energy states shortens the

electronic transition between VB and CB, i.e. an electron transits from hybridised S 3p to the lowest part of conduction band. However, in order to establish the veracity of this assumption, further experimental work is necessary to measure the work functions of S-doped samples as a function of S doping level.

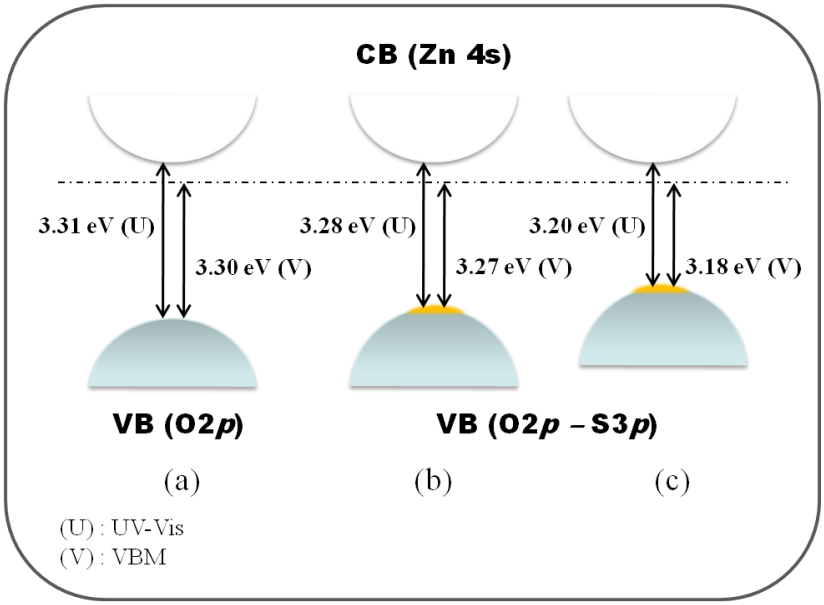

Figure 5. 7 Schematic energy level diagrams for $ZnO_{1-x}S_x$ films of (a) x = 0.0, (b) x = 0.007, and (c) x = 0.023. The energies of bandgap were obtained by UV-Vis measurements. The positions of the Fermi level were examined by VBM spectra.

5.1.3 Electrical Transport Properties

The carrier concentration, electron mobility and electrical conductivity of $ZnO_{1-x}S_x$ ($0 \leq x \leq 0.007$) versus temperature in the range of 80-330 K are shown in Figure 5.8. In our samples, the addition of sulphur atoms leads to a poor performance in electrical transport properties because of a significant decrease in crystalline size. The decreased crystalline size with S doping can be found in AFM images (Figure 5.2) and XRD measurements through Scherrer's equation (Table 5.1). The level of grain boundary scattering increases due to the

reduction in crystallite size, leading to a lower electron mobility in S-doped ZnO thin films as prepared in this work.[23] Furthermore, the XRD data also showed that the S incorporated into ZnO produces lattice imperfection (e.g. dislocations or grain boundaries) as the result of atomic size mismatch. These imperfections could act as electron traps to inhibit the electron movement, leading to lower electron mobility in S-doped ZnO thin films.

The fact that the electron trapping by grain boundaries significantly affecting the electron mobility and electrical conductivity is well established in transparent conducting oxide (TCO) materials.[24] In our case the electrical transport properties in S-doped ZnO thin films are similar to the TCO model that a higher level of grain boundaries (i.e. smaller crystalline size) results in lower conductivity and electron mobility. The undoped ZnO film with the largest crystalline size shows the best performances in electron mobility, carrier concentration and electrical conductivity. The relationship between these electrical transport properties is shown as

$$\sigma = ne\mu \tag{5.4}$$

where σ is the electrical conductivity (Ω^{-1} cm^{-1}), n is the carrier concentration (cm^{-3}), e is the electronic charge, μ is the electron mobility (cm^2/Vs).[25] Therefore, as for the undoped ZnO the greatest electron mobility and carrier concentration dominate the highest conductivity.

The carrier concentrations measured for these $ZnO_{1-x}S_x$ films are nearly constant over a range of temperature from 80 K to 350K, reflecting that no free electrons were populated into conduction band with S doping. In other words, the incorporation of S does not neither generates free carriers in the conduction band nor creates impurity states below the conduction band. This confirms that the conduction band in ZnO is not affected by

incorporating S, as investigated in XAS. The S doping would produces impurity levels above the valence band only.

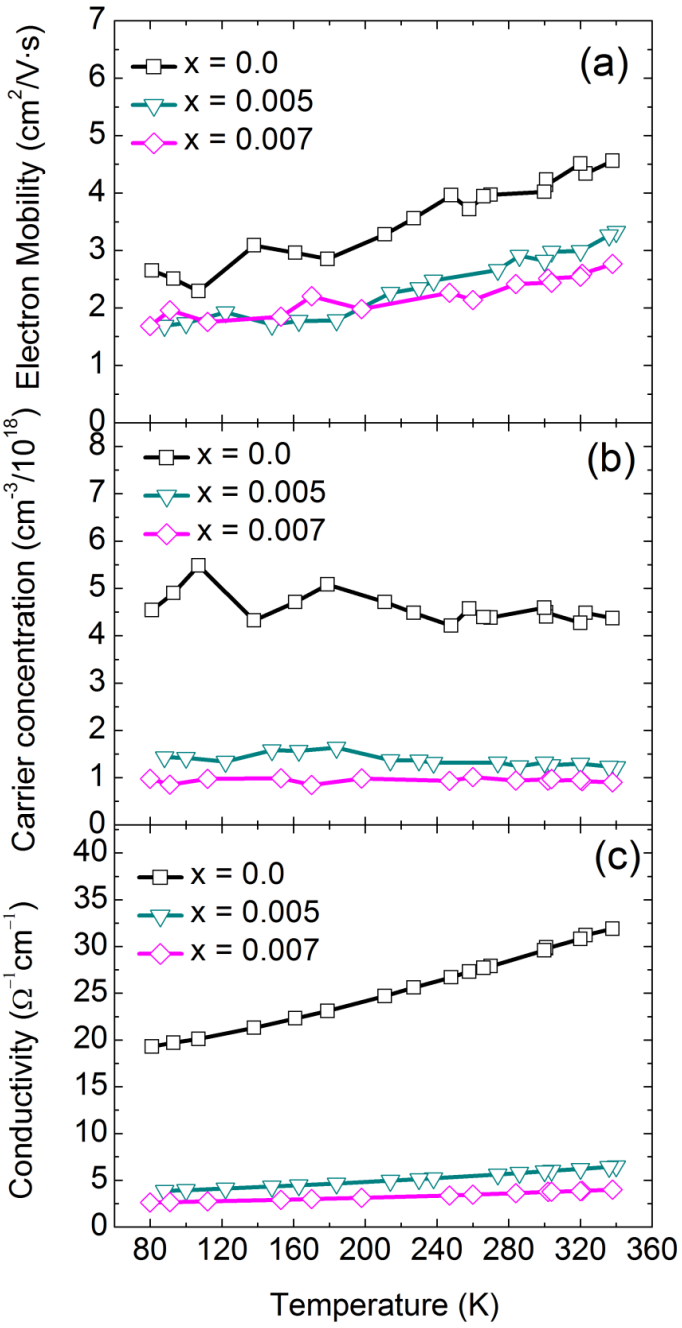

Figure 5. 8 Electrical transport properties (a) electron mobility, (b) carrier concentration, and (c) conductivity of $ZnO_{1-x}S_x$ thin films with x = 0, 0.005 and 0.007 obtained by variable temperature Hall effect measurements.

5.2 Summary

In conclusion, we have synthesised highly crystalline $ZnO_{1-x}S_x$ thin films by a simple spray pyrolysis technique. All films exhibit strongly oriented growth with the *c*-axis of the hexagonal wurtzite phase of the epilayer normal to the surface of the Al_2O_3(0001) substrate. S doping leads to a shift in the epilayer (0002) reflection to low angles and the narrowing of the bulk bandgap, as evident from both optical and photoemission measurements. The incorporation of sulphur in ZnO shifts the valence band maximum towards the conduction band due to the rehybridisation of S 3p with O 2p states but did not affect the conduction band minimum. The electrical transport properties did not benefit from the sulphur incorporation due to the creation of imperfections, such as dislocations and grain boundaries.

5.3 References

1. J. V. Foreman, J. Y. Li, H. Y. Peng, S. J. Choi, H. O. Everitt and J. Liu, Nano Letters **6**, 1126 (2006).
2. C. Klingshirn, Physica Status Solidi B-Basic Solid State Physics **244**, 3027 (2007).
3. U. Ozgur, Y. I. Alivov, C. Liu, A. Teke, M. A. Reshchikov, S. Dogan, V. Avrutin, S. J. Cho and H. Morkoc, Journal of Applied Physics **98**, 41301 (2005).
4. M. A. Mayer, D. T. Speaks, K. M. Yu, S. S. Mao, E. E. Haller and W. Walukiewicz, Applied Physics Letters **97**, 22104 (2010).
5. W. Walukiewicz, Physics of Semiconductors 2002, Proceedings **171**, 109 (2003).
6. C. Y. Moon, S. H. Wei, Y. Z. Zhu and G. D. Chen, Physical Review B **74**, 233202 (2006).
7. S. H. Wei and A. Zunger, Journal of Applied Physics **78**, 3846 (1995).
8. C. Persson, C. Platzer-Bjorkman, J. Malmstrom, T. Torndahl and M. Edoff, Physical Review Letters **97**, 146403 (2006).
9. Y. Z. Yoo, Z. W. Jin, T. Chikyow, T. Fukumura, M. Kawasaki and H. Koinuma, Applied Physics Letters **81**, 3798 (2002).
10. B. K. Meyer, A. Polity, B. Farangis, Y. He, D. Hasselkamp, T. Kramer and C. Wang, Applied Physics Letters **85**, 4929 (2004).
11. S. Locmelis, C. Brunig, M. Binnewies, A. Borger, K. D. Becker, T. Homann and T. Bredow, Journal of Materials Science **42**, 1965 (2007).
12. S. Y. Bae, H. W. Seo and J. H. Park, Journal of Physical Chemistry B **108**, 5206 (2004).
13. M. R. Islam and J. Podder, Crystal Research and Technology **44**, 286 (2009).
14. F. Paraguay, W. Estrada, D. R. Acosta, E. Andrade and M. Miki-Yoshida, Thin Solid Films **350**, 192 (1999).
15. P. D. C. King, T. D. Veal, A. Schleife, J. Zuniga-Perez, B. Martel, P. H. Jefferson, F. Fuchs, V. Munoz-Sanjose, F. Bechstedt and C. F. McConville, Physical Review B **79**, 205205 (2009).
16. K. M. Yu, J. Wu, W. Walukiewicz, J. W. Beeman, J. W. Ager, E. E. Haller, I. Miotkowski and A. Ramdas, Journal of Electronic Materials **31**, 754 (2002).
17. R. Chen, D. H. Li, B. Liu, Z. P. Peng, G. G. Gurzadyan, Q. H. Xiong and H. D. Sun, Nano Letters **10**, 4956 (2010).
18. S. H. Wei and A. Zunger, Physical Review B **43**, 1662 (1991).
19. S. H. Wei, L. G. Ferreira, J. E. Bernard and A. Zunger, Physical Review B **42**, 9622 (1990).
20. K. Ellmer, A. Klein and B. Rech, edited by R. Hull, J. Parisi, R. Osgood and H. Warlimont (Springer, New York, 2008), pp. 443.

21. J. H. Guo, L. Vayssieres, C. Persson, R. Ahuja, B. Johansson and J. Nordgren, Journal of Physics-Condensed Matter **14**, 6969 (2002).
22. J. W. Chiou, K. P. K. Kumar, J. C. Jan, H. M. Tsai, C. W. Bao, W. F. Pong, F. Z. Chien, M. H. Tsai, I. H. Hong, R. Klauser, J. F. Lee, J. J. Wu and S. C. Liu, Applied Physics Letters **85**, 3220 (2004).
23. B. Z. Dong, G. J. Fang, J. F. Wang, W. J. Guan and X. Z. Zhao, Journal of Applied Physics **101** (2007).
24. J. Y. W. Seto, Journal of Applied Physics **46**, 5247 (1975).
25. P. P. Edwards, A. Porch, M. O. Jones, D. V. Morgan and R. M. Perks, Dalton Transactions, 2995 (2004).

CHAPTER 6

PHOTOELECTROCHEMICAL CELL

Photoelectrochemical (PEC) cells have the potential to generate hydrogen and oxygen by utilising solar energy without producing carbon based pollutants. The main challenge is to find a suitable photoelectrode to solve the problem of low energy conversion efficiency. ZnO is one of the promising candidates for use as a photoelectrode due to its favourable band edge positions (i.e. the conduction band edge is higher than the hydrogen reduction potential and the valence band edge is lower than the oxygen reduction potential), and its stability during photoelectrochemistry process. However, its large bandgap value leads to lower energy conversion efficiency using solar radiation. In order to solve this problem, several strategies are being developed to increase visible light absorption. These include the narrowing bandgap by forming a solid-state solution or by doping with impurities, the incorporation of organic dyes or quantum dots in the host, and the inhibition of electron-hole pair recombination by either modifying the surface or developing nanoarchitecture.[1-5]

Nanostructured photoanodes can be used to improvement in the transport of charged carriers and the separation of photogenerated electrons and holes. One-dimensional (1D) nanostructures, such as nanorods and nanowires, exhibit higher electron mobility than 0 dimensional (0D) nanostructures (i.e. spherical particle). The first demonstration of using 1D concept to prepare PEC electrode was the hematite nanorod arrays.[6]

Other metal oxide semiconductors, such as ZnO, TiO_2, WO_3, have been extensively studied in recent years.[7-9] ZnO has received considerable attention as a photoelectrode

because high quality of nanostructures (e.g. 0D, 1D and 2D) that can be grown by various methods, including hydrothermal, vapour-liquid-solid process, and metal organic chemical vapour deposition.[10, 11] In addition to the synthesis of nanostructure sensitizers, such as organic dyes or quantum dots (e.g. CdSe or CdS) were added in ZnO to enhance the photoelectrochemical water splitting reaction.[3] These sensitizers generally have smaller bandgap in visible light and the range of absorption is tuneable according to the sizes of molecules and nanoparticles.

To the best of our knowledge, thin film structures have rarely been investigated in the PEC water splitting reaction. The advantages of using thin films as photoelectrodes include fast synthesis process and easy modification in composition and doping. Furthermore, there has seen no work to check on the influence of bandgap reduction on PEC performance using cadmium or sulphur-doped ZnO thin films as the photoanode. In this chapter, the performance of ZnO thin films at various film thicknesses will be examined in PEC experiments in section 6.1. Chapter 6.2 and Chapter 6.3 report tests of the efficiencies of the PEC using ternary $Cd_xZn_{1-x}O$ and $ZnO_{1-y}S_y$ photoanodes. All PEC measurements here were performed using 0.5 M Na_2SO_4 solution as the electrolyte (pH = 6.8) against a saturated Ag/AgCl reference electrode (+0.198 V versus NHE). A 300 W Xenon ozone-free lamp equipped with an airmass 1.5 (AM1.5) filter and a 400 nm cut-off filter was used to simulate solar light.

6.1 The Effect of Thickness of ZnO Photoanode on Photoelectrochemical Performances

When an n-type semiconductor is immersed into an electrolyte, a positive space charged layer is usually created near the surface of semiconductor. The thickness of the charged layer is typically range between 100Å and a few microns, depending on the conductivity of the semiconductor and the level of band bending in the electrolyte/electrode interface.[12] It is known that the width of the space charge layer can influence on the efficiency of photoelectrochemical water splitting. Thus, the investigation of the ideal thickness for ZnO photoanodes is essential in this work.

Figure 6.1 (a) shows the UV-Vis transmittance spectra for the four different thicknesses of the undoped ZnO layers deposited on an indium tin oxide (ITO)-coated glass substrate. The thickness of films was obtained from the optical data by fitting the observed transmission to a simulated transmission function using the variable angle spectroscopic ellipsometry from Woollam (WVASE) analysis software. The films represent a typical transparent feature of ZnO in the visible range of 380-800 nm. The optical transmittance data were used to derive to the square of optical absorption coefficient as shown in Figure 6.1 (b). The bandgaps of these films are approximate 3.30 eV except for the thickest one which is 3.32 eV. As film thickness increases, the strain is released and optical properties approximate to those of the bulk.[13] The bandgap for the thickest film is close to bulk ZnO crystal value (3.2-3.3 eV).

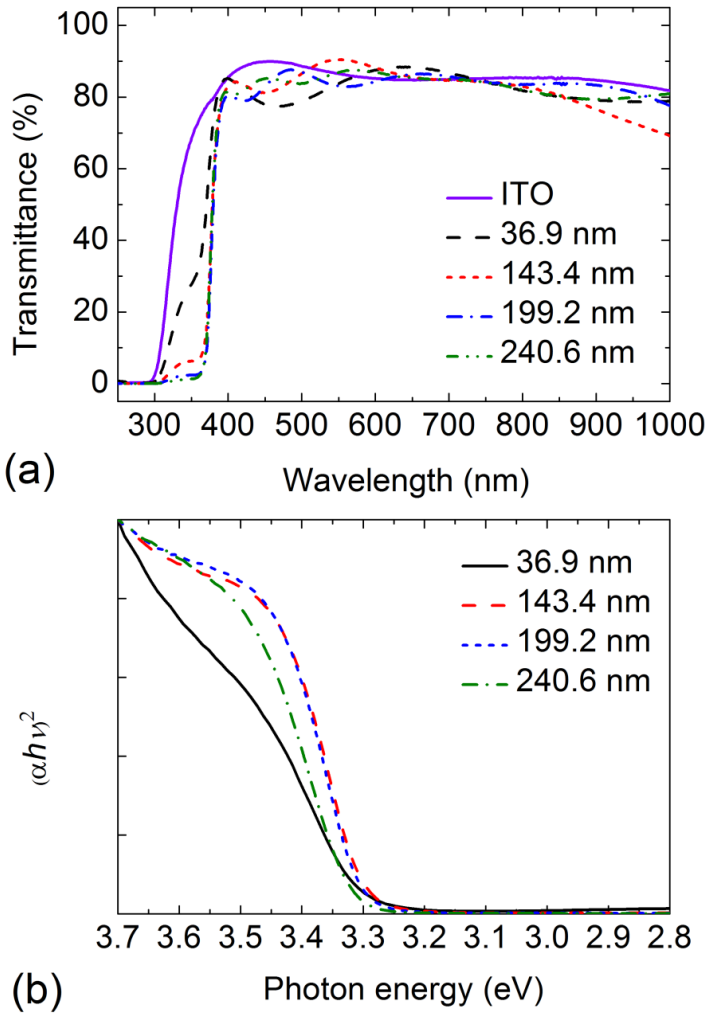

Figure 6. 1 (a) Optical transmittance spectra of ZnO layers deposited on an indium tin oxide (ITO)-coated glass substrate with the thicknesses of 36.9 nm, 143.4 nm, 199.2 nm, and 240.6 nm. (b) Plots of $(\alpha h\nu)^2$ versus photon energy of undoped ZnO photoanodes at various thicknesses. A typical linear extrapolation along a leading edge is used to determine the bandgap.

Figure 6.2 shows linear sweep voltammetry measurements for undoped ZnO films of various thicknesses. Dark scans correspond to a scan without irradiation. Figure 6.2 demonstrates a typical photocurrent-potential curve for an n-type semiconductor material, which reveals three main regions: (1) In region I (below -0.4 V against Ag/AgCl reference electrode) an electron accumulation layer is generated at the interface of the semiconductor

electrode. The electrode acts as a cathode generating cathodic current both in the dark and under irradiation. (2) In region II (from -0.4 V to -0.2 V) the conduction and valence band edges at the surface are equal with those of the bulk. This is the so-called flatband potential (V_{fb}) region.[14] At this potential, there is no net electric field internal to the ZnO (i.e. no photocurrent in the dark and upon irradiation). The flatband potential can be determined by measuring the onset potential of anodic current onset in the I-V curve.[15, 16] (3) In region III (above -0.2 V): a depletion layer is created and there is no oxidative current in the dark. However, upon irradiation, a photocurrent is generated since the conduction band level is more negative than the H_2/H_2O redox potential.

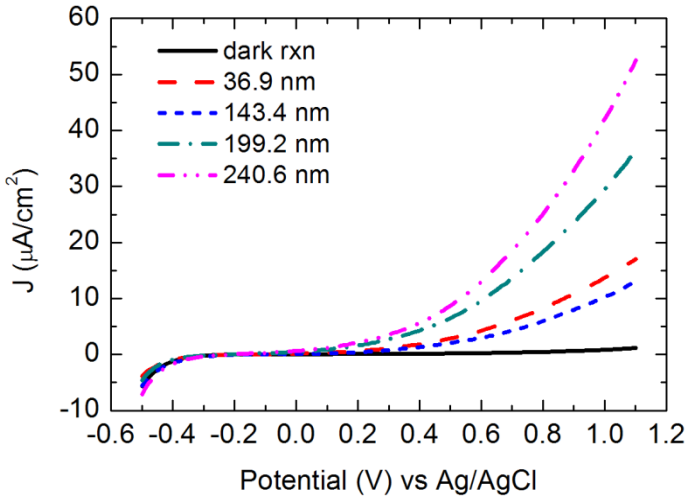

Figure 6. 2 Photocurrent – applied potential curves of undoped ZnO photoanodes for various film thicknesses. The measurements were performed using a 0.5 M Na_2SO_4 solution as the electrolyte at pH = 6.8 against a saturated Ag/AgCl reference electrode. The simulated light is using a 300 W Xenon ozone-free lamp equipping with an airmass 1.5 (AM1.5) filter and a 400 nm cut-off filter.

The thickest film (240.6 nm) exhibits the highest photocurrent efficiency and reaches 45 μA/cm^2 at 1.0 V. The lower photocurrent generated in films with thickness of 36.9 nm and 143.4 nm is likely due to the higher level of strain in the thinner films. It is believed that the strain strongly depends on the film thickness. The stress will be relaxed when the film grows thicker over the critical thickness.[13] In addition, a large strain leads to a higher lattice imperfection (e.g. dislocation or defects).[17] Those imperfections trap mobile electrons to create a potential charged barrier, resulting in a lower mobility, a lower free electron density and a higher resistivity.[18, 19] Therefore, the thickest film with the improved electrical transport properties produces the highest performance among these films.

As mentioned earlier in this chapter, a positive depletion layer (i.e. an upward band bending) will be obtained when an n-type semiconductor is placed into aqueous electrolyte. In Figure 6.2, there is no saturation of the photocurrent even at the limiting potential of +1.1 V. This suggests that not only the film thickness is greater than the width of the positive depletion layer, but also that there is an efficient charge separation in the film upon illumination.[3] Furthermore, the degree of band bending is associated with the difference between the Fermi level of the semiconductor and the redox level of the electrolyte. These films have nearly the same onset potential (i.e. flatband potential = -0.02 V), which indicates that the levels of band bending among the films are almost equal.

6.2 *Cadmium Doped Zinc Oxide Photoanode*

6.2.1 Characterisation of $Cd_xZn_{1-x}O$ Photoanodes

Cd-doped ZnO photoanodes were prepared by spray pyrolysis and the surface elemental compositions were determined by XPS.

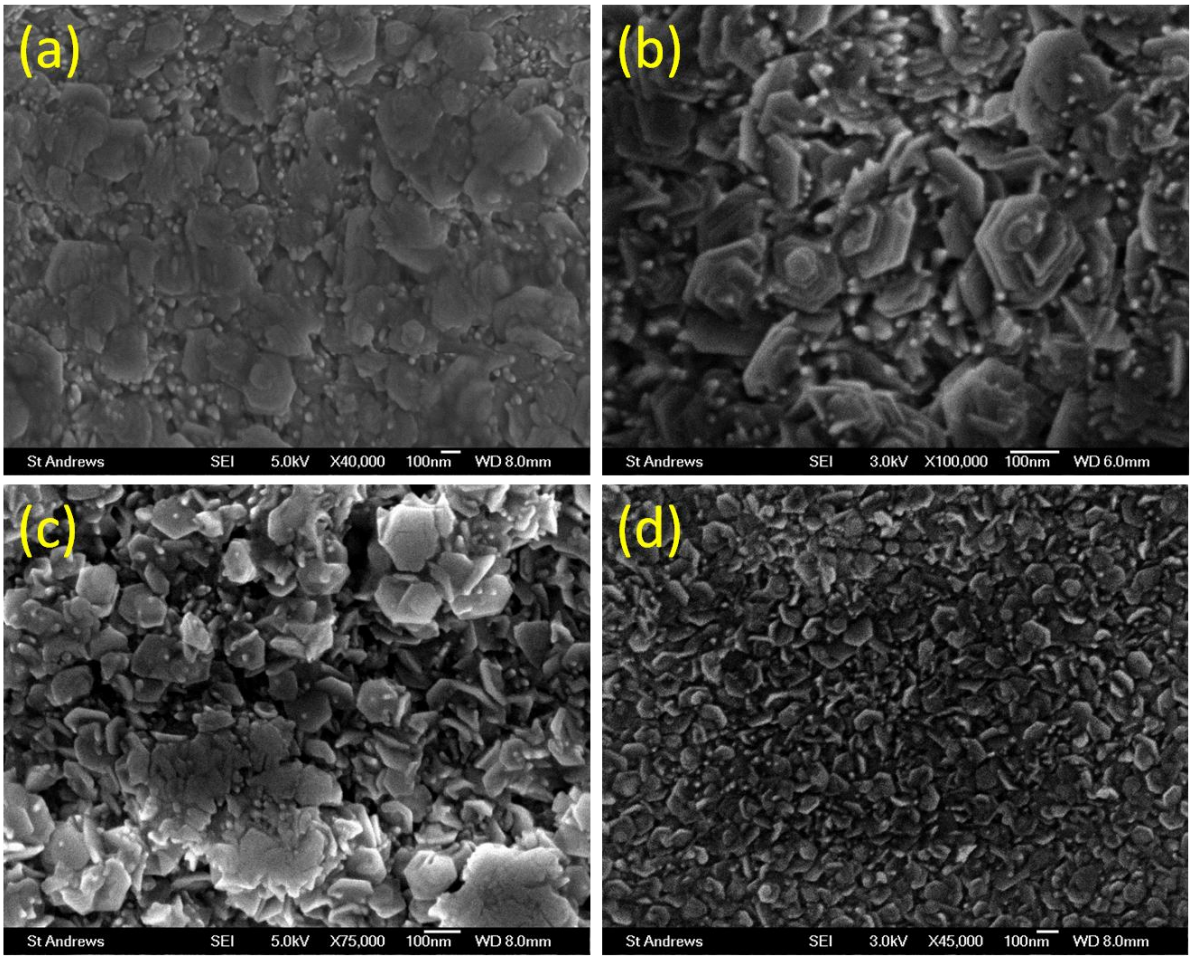

Figure 6. 3 Scanning electron microscopy (SEM) top-view images of $Cd_xZn_{1-x}O$ photoanodes with (a) x = 0.0, (b) x = 0.026 (c) x = 0.038, and (d) x = 0.065.

Figure 6.3 shows scanning electron microsocpy (SEM) images of $Cd_xZn_{1-x}O$ of (a) x = 0, (b) x= 0.026, (c) x = 0.038, and (d) x= 0.065 layers grown on conducting ITO substrates

at the deposition temperature of 400˚C. The thickness for these films is around 200-250 nm. Note that the scale bars in each image are different. The morphology for x = 0.0 shown in Figure 6.3 (a) exhibits a dense packing structure. The image shows that the film consists of plate-like grains around 30-50 nm diameter along with a number of smaller particles which may have seeded growth. Those plates stack together and form a larger island-like crystallites with a dimension of several hundred micrometers. A general tendences toward hexagonal morphology in the smaller size of flakes may be discerned. Figure 6.3 (b) - (c) display that as the Cd amount increases, the average diamension of hexagonal flakes reduces. The diameters of hexagonal plates in the samples with x = 0.026, x = 0.038, and x = 0.065 are around 125 nm, 100 nm, and 80 nm, respectively.

X-ray diffraction of $Cd_xZn_{1-x}O$ photoanodes are shown in Figure 6.4. Films with x = 0.0 and x = 0.026 contain a single phase of hexagonal ZnO phase. On the other hand, x = 0.038 and x = 0.065 films contain a second cubic rocksalt phase in addition to the hexagonal phase. The dominant reflection is ZnO (002) in all samples except for the x = 0.065 where the (111) phase dominates in the rocksalt structure.

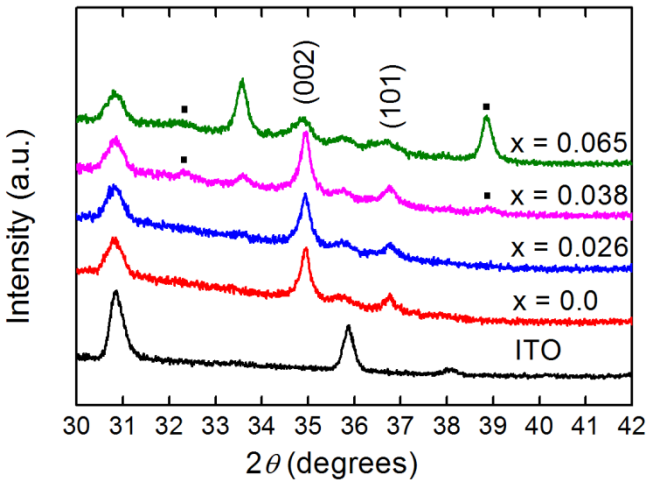

Figure 6. 4 XRD patterns of $Cd_xZn_{1-x}O$ layers deposited on an ITO substrate with x = 0, 0.023, 0.038, and 0.065. The black square blocks at 2θ = 32.3˚ and 38.8˚ are the CdO (111) and CdO (200) phases, respectively.

The absorption coefficient is plotted in Figure 6.5 as a function of photon energy. The optical bandgap can be obtained by a linear extrapolation along the leading edge curve to the background. The bandgap values for x = 0.0, x = 0.026, x = 0.038 and x = 0.065 films are 3.32 eV, 3.28 eV, 3.27 eV and 3.17 eV, respectively. The dilute doping of Cd impurity slightly reduces the ZnO bandgap while the highest Cd concentration exhibits the greatest bandgap reduction.

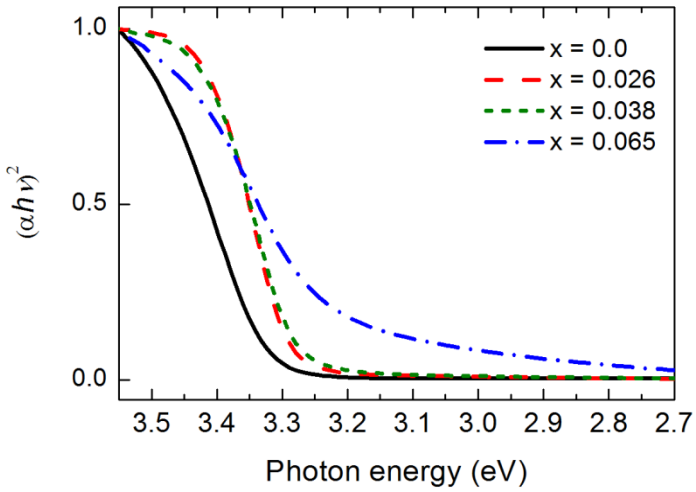

Figure 6. 5 Plots of $(\alpha h\nu)^2$ *versus* photon energy of $Cd_xZn_{1-x}O$ photoanodes with x = 0.0, 0.026, 0.038, and 0.065. A typical linear extrapolation along the leading edge curve to the background is used to determine the bandgap.

6.2.2 Photon Energy Conversion Efficiency of $Cd_xZn_{1-x}O$ Photoanodes

Systematic electrochemical measurements were performed to evaluate the photoelectrochemical cell properties of the fabricated $Cd_xZn_{1-x}O$ photoanodes. Linear sweep voltammograms in the dark conditions and under illumination (67 mW/cm^2) were undertaken to measure the generated photocurrent (Figure 6.6). I-V curves show a typical n-type semiconductor behaviour that gives anodic current under irradiation but no current is generated under dark condition (light off) when the applied potential is positive. On the other hand, at the negative applied potential, the n-type photoelectrode generates cathodic current both under illumination and dark scan.

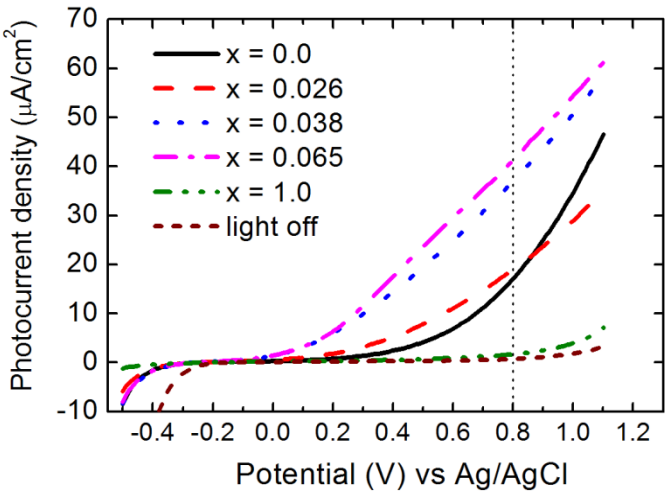

Figure 6. 6 Linear sweep voltammograms in the dark and under the irradiation (67 mW/cm^2; AM1.5) were performed for $Cd_xZn_{1-x}O$ ($0 \leq x \leq 1$) photoanodes in a 0.5 M Na_2SO_4 electrolyte.

A weak dark current is observed above +1.0 V due to minor defects in the dense film.[5] Upon irradiation with a solar simulator, the initial photocurrent in x = 0.0 is generated at -0.05 V and continues to increase to 17 μA/cm^2 at +0.8 V. The photocurrent densities in Cd-doped ZnO photoanodes are all higher than that in the undoped ZnO. The photocurrent densities at +0.8 V are 19, 37 and 41 μA/cm^2 for the samples of x = 0.026, x = 0.038 and x = 0.065, respectively (Table 6.1). For x = 0.065 sample, the photocurrent density increases by 240% compared to the undoped ZnO electrode. The increasing photocurrent reveals that the bandgap narrowing with Cd doping can effectively improve the performance of photoanodes.

Interestingly, the photoanodes (x = 0.038 and x = 0.065) with a mixture of two solid phases produce a higher photocurrent than that with a single solid phase (e.g. x = 0.026). This suggests that a heterojunction structure ($ZnO/Cd_xZn_{1-x}O/CdO$) is beneficial to free carrier transport, resulting in a higher photocurrent density. There is no saturation in the photocurrent before the appearance of the dark current (+1.0 V) for all photoelectrodes,

indicating that an efficient charge separation is achieved upon illumination and the width of space charged layer at the near surface of anode is smaller than the film thickness.[3, 20]

Table 6. 1 Measured photoelectrochemical properties of $Cd_xZn_{1-x}O$ ($0 \leq x \leq 1$) photoanodes in three-electrode cell.

$Cd_xZn_{1-x}O$	V_{fb} (V)[a]	j ($\mu A/cm^2$) at +0.8 V	Photon-to-hydrogen efficiency (%)
x = 0.0	-0.05	17	0.18
x = 0.026	-0.13	19	0.24
x = 0.038	-0.23	37	0.40
x = 0.065	-0.24	41	0.40
x = 1.0	+0.80	1.5	

[a] The V_{fb} is measured in reference to the Ag/AgCl (+0.197 V) electrode

The onset potential of the photocurrent (V_i) reflects a flatband potential (V_{fb}), where the levels of conduction and valence band edges are flat both in the interior and the interface of the semiconductor (i.e. no band bending).[5, 12] Table 6.1 reveals that the onset potential (or flatband potential) is shifted toward negative potential with increasing Cd concentration.

The maximum open-circuit potential in a PEC is the value of band bending (E_B). E_B is generally short of 1.23 eV and needs external energy input, such as applied voltage (V_{app}) or photons to produce a photoelectron. In other word, if a photoanode has a larger band bending, the PEC reaction occurs at the more negative potential.

This suggests that the sample with higher Cd doping requires less external energy (i.e. applied potential) and is more efficient to achieve a given photocurrent. It should be mentioned that band bending is larger if the flatband potential is more negative. Thus, a smaller potential is needed to obtain a flow of photocurrent. The value of band bending is taken as the difference between the Fermi level (E_f) in the electrode and the O_2/H_2O redox potential (E_{redox}) in the electrolyte, is given by

$$E_B = E_f - E_{redox} \quad (6.1)$$

For an n-type semiconductor, the Fermi level is generally higher (or more negative) than the O_2/H_2O redox potential. According to equation 6.1, the more higher the Fermi level (i.e. the more negative the flatband potential), the greater value of the E_B. As the result of a larger value of E_B, less external energy is required to generate a photoelectron. Furthermore, a large E_B is able to boost electrons into the conduction band and therefore reduces the recombination with holes, in which the photocurrent generation will be more efficient.[21]

Another reason for the benefit of large band bending in generating a greater photocurrent is the concept of *overvoltage*. The magnitude of current flow is related to the overvoltage of photoanodes. The overvoltage is determined by the difference between the sum of applied potential (E_{app}), band bending (E_B), and the energy required to decompose water (E = 1.23 eV). Hence, the equation for the overvoltage is shown as $V_o = E_{app} + E_B - 1.23$. From equation above, it is known that a larger band bending (i.e. more negative flatband potential) results in a larger overvoltage. Therefore, the photocurrent can be produced with less applied potential input.

The CdO (x = 1.0) photoanode shows a smaller photocurrent and more positive of onset of photocurrent than any of the other $Cd_xZn_{1-x}O$ photoelectrodes. The lowest photocurrent density is ascribed to inappropriate band position that its conduction band edge is lower than the H_2 reduction potential.

During the steady-state operation of a PEC device, the induced photocurrent is directly related to the performance of hydrogen generation. The efficiency of photon-to-hydrogen generation (η) is then expressed as[3, 22]

$$\eta(\%) = \frac{j(1.23 - V_{appl})}{P_0} \times 100\% \quad (6.2)$$

where j is the induced photocurrent density ($\mu A/cm^2$), 1.23 is the theoretical potential required to split water into hydrogen, V_{appl} is the applied potential, P_0 is the power of incident light ($\mu W/cm^2$). P_0 needs to be calibrated according to the effective photon response region in each material. For example, the photoanodes with x = 0.0 and x = 0.026 mainly absorb UV light. The integrated spectral response to UV is approximately 5%, estimated from the individual irradiance measurements through the UV-Vis spectrum at various wavelengths. Therefore, the corrected P_0 is around 5% of the original incident light (67000 $\mu W/cm^2$). Likewise, the power of the incident light for x = 0.038 and x = 0.065 are corrected by 6% and 7%, respectively, in reference to UV-Vis absorption spectra. The plot of efficiency versus the applied potential (Figure 6.7) shows that the η value in x = 0.0 (0.18%) is twice as high as that in x = 0.065 (0.40%) at an applied potential of +0.8 V against a Ag/AgCl reference electrode. Importantly, the bandgap narrowing by incorporating Cd into ZnO is seen as greatly enhance the efficiency of photon-to-hydrogen conversion. Moreover, the heterojunction structure in biphase $Cd_xZn_{1-x}O$ samples (x = 0.038 and x = 0.065) photoanodes demonstrates the highest energy conversion efficiency, consistent with the observation in the I-V curves. The equality of efficiency in the x = 0.038 and x = 0.065 samples indicates that the energy conversion of photon-to-hydrogen is saturated.

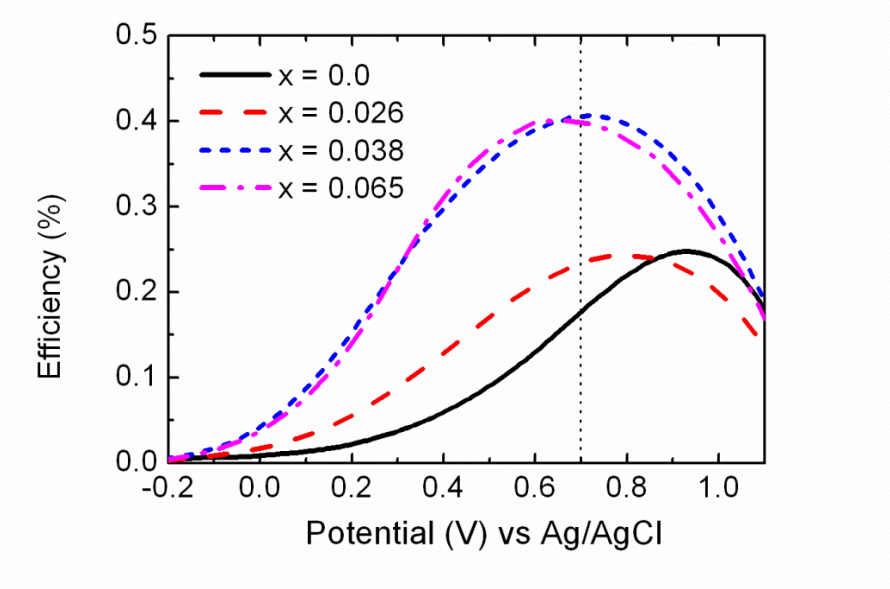

Figure 6. 7 Photon-to-hydrogen conversion efficiency of the photoelectrochemical cell with $Cd_xZn_{1-x}O$ ($0 \leq x \leq 0.065$) photoanodes as a function of applied potential.

To examine the evolution of photoresponse of the films as a function of exposure time, an amperometric I-t curve collected from $Cd_xZn_{1-x}O$ photoanodes during light on/off cycles at +0.8 V is shown in Figure 6.8. When the light is on, a spike appears at the initial photoresponse due to the recombination of photogenerated electrons and holes.[20] A slight decay in photocurrent over the exposure time indicates that $Cd_xZn_{1-x}O$ photoanodes are stable in the photo-oxidation process in an aqueous 0.5 M Na_2SO_4 electrolyte. Moreover, the photocurrent vanishes when the light is switched off, reflecting an efficient charged carrier separation.[23] The order of performances for $Cd_xZn_{1-x}O$ photoelectrodes at +0.8 V is x = 0.065 (j = 32 $\mu W/cm^2$) > x = 0.026 (j = 18 $\mu W/cm^2$) > x = 0.0 (j = 16 $\mu W/cm^2$) > x = 1.0 (j = 1 $\mu W/cm^2$), the same trend seen in I-V measurements.

In order to quantify the PEC performance of $Cd_xZn_{1-x}O$ photoanodes, the incident-photon-to-current-conversion efficiency (IPCE) was measured as a function of photon energy, as shown in Figure 6.9. The IPCE is given[4, 24]

$$IPCE(\%) = \frac{1240 \times j_i}{\lambda_i \times P_i} \tag{6.3}$$

where j_i is the photocurrent density in mA/cm^2 , λ_i is the selected wavelength of incident light in nm, and P_i is the power density of incident light at the selected wavelength in mW/cm^2. The ZnO samples incorporating Cd show a higher photoresponse in the region between 360 nm and 410 nm. For the single phase solid solution with x = 0.026, although the substitution of Cd^{2+} for Zn^{2+} increases the capability of visible light absorption, it scarifies the absorption in the UV region. Thus, it gives the least energy conversion efficiency with the irradiation of a solar simulator. On the other hand, the smaller bandgap of $Cd_xZn_{1-x}O$ extends the onset of photoresponse from 370 nm to 420 nm compared to the undoped ZnO photoanode. The IPCE efficiencies for the samples with x = 0.0 and x = 0.026 are similar. These two samples that consist of two solid phases exhibit a stronger photoresponse in both UV and visible regions. Therefore, photoanodes with a two-phase solid solution have a superior performance in harvesting solar energy, the photon-to-hydrogen and the IPCE conversion efficiencies.

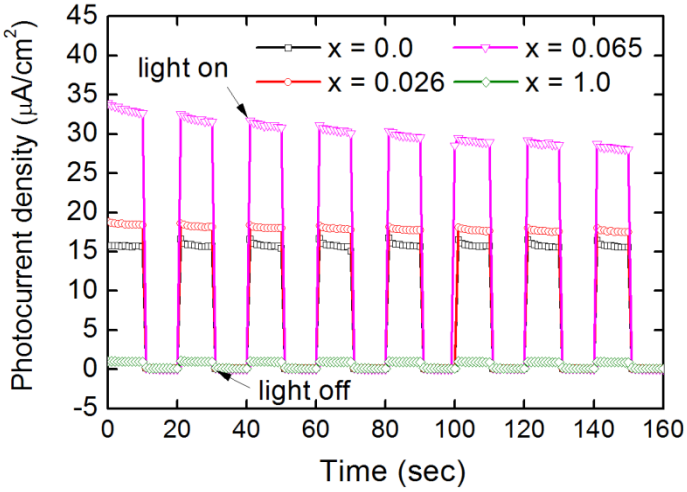

Figure 6. 8 Amperometric I-t curves of $Cd_xZn_{1-x}O$ ($0 \leq x \leq 0.065$) photoanodes at an applied potential of +0.8 V under 67 mW/cm^2 light on/off cycles.

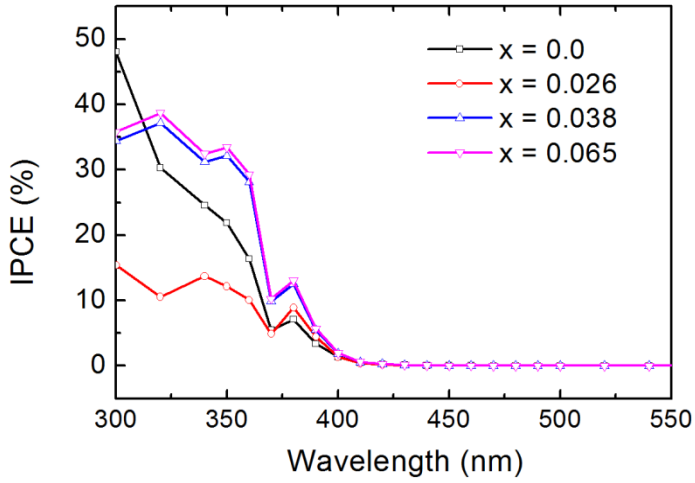

Figure 6. 9 Measured incident-photon-to-current conversion efficiency (IPCE) spectra of $Cd_xZn_{1-x}O$ ($0 \leq x \leq 0.065$) photoanodes in the region of 300-550 nm at a fixed applied potential +0.8 V against Ag/AgCl electrode.

6.3 *Sulphur Doped Zinc Oxide Photoanode*

6.3.1 Characterisation of $ZnO_{1-x}S_x$ Photoanodes

Sulphur-doped ZnO photoanodes were prepared using the spray pyrolysis method and the elemental surface composition analysis was performed by XPS.

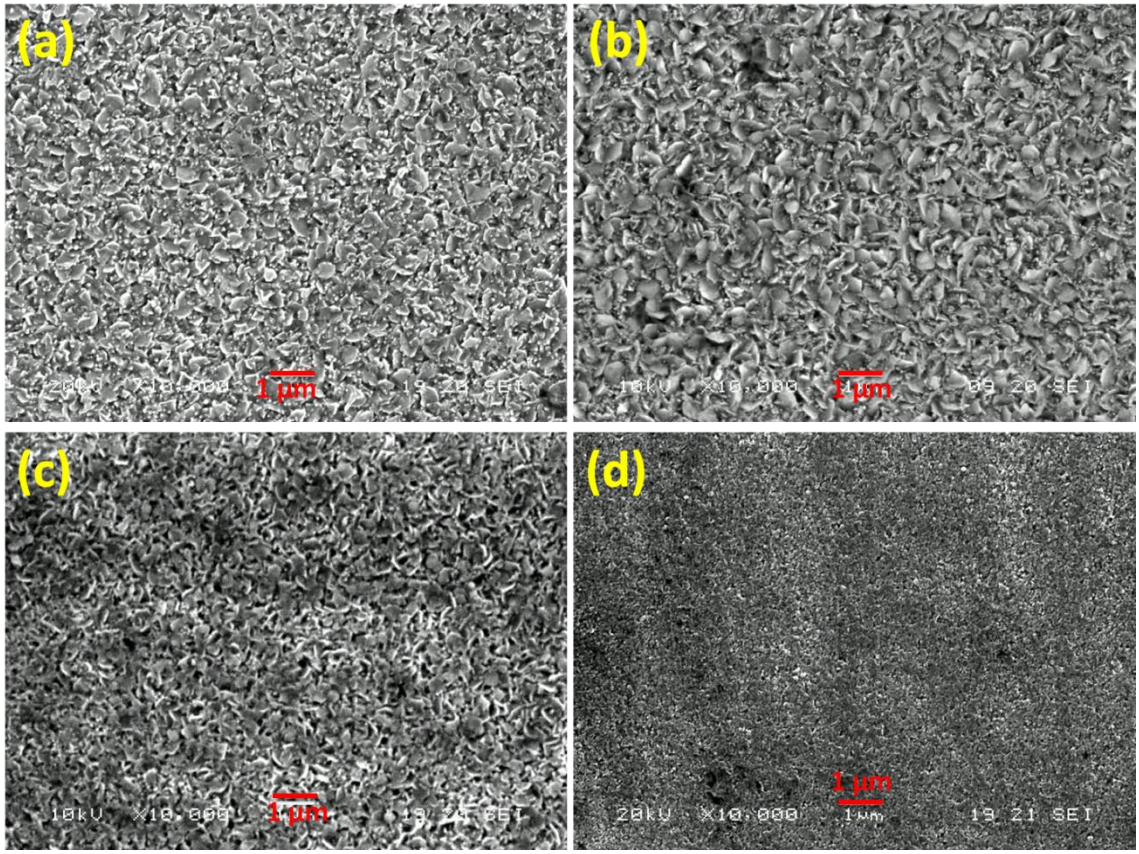

Figure 6. 10 Scanning electron microscope images of $ZnO_{1-x}S_x$ photoanodes of (a) x = 0.0, (b) x = 0.004, (c) x = 0.01, and (d) x = 0.028.

Figure 6.10 shows scanning electron microscopy images microscopy (SEM) of $ZnO_{1-x}S_x$ photoanodes. The morphology uncovers a random distribution of hexagonal plates distribute randomly on the film surface. The grain size decreases from estimate a micron to tens of nanometres with increasing sulphur content. The root mean square (RMS) roughness

measured by atomic force microscopy (AFM) are 44.11 nm, 21.68 nm, 18.89 nm, and 9.75 nm for x = 0.0, x = 0.004, x = 0.01, and x = 0.028, respectively,

X-ray diffraction patterns of $ZnO_{1-x}S_x$ photoanodes are shown in Figure 6.11. All peaks are attributed to a hexagonal ZnO phase and a ITO substrate are observed in the diffraction patterns. In the undoped ZnO sample, the preferentially orientation plane is (102), which switches to (002) when sulphur is incorporated. The shifts toward lower angles for the peaks (002), (101) and (102) indicate a lattice expansion when the oxygen atom in ZnO lattice is substituted by the larger sulphur atom.

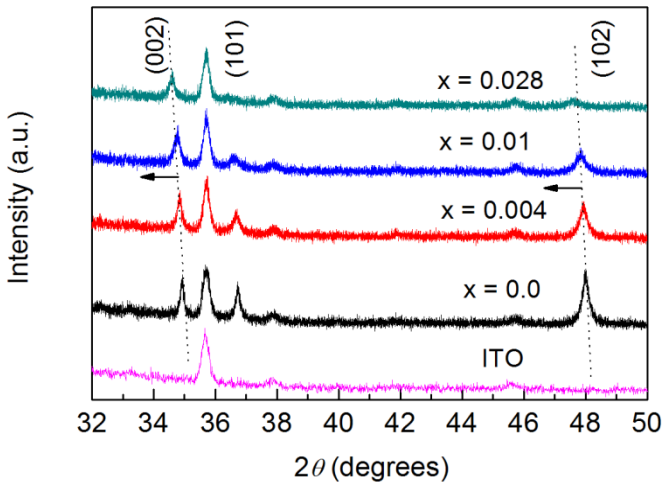

Figure 6. 11 2 theta X-ray diffraction patterns of $ZnO_{1-x}S_x$ photoanodes. Indium tin oxide (ITO) is used as the conducting substrate in the photoanodes.

The photoanode with x = 0.0 is around 80-85%transparent to visible light and it absorbs UV light completely below 370 nm (Figure 6.12 (a)). For S-doped ZnO samples, the transparencies remain between 80% and 85% in the mid visible region. However, the transmittance edges broaden significantly and the intersection of the transmittance edge to the

line of maximum transmittance moves towards higher wavelength with increasing sulphur doping level, which illustrates an increase in visible light absorption.

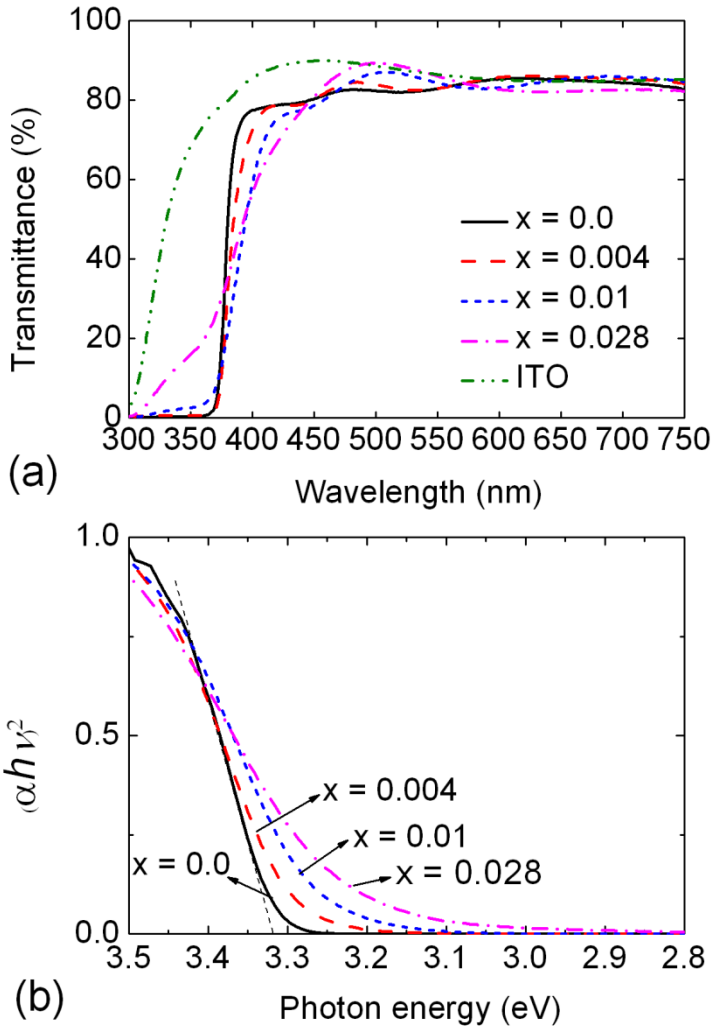

Figure 6. 12 (a) UV-Vis transmittance spectra of $ZnO_{1-x}S_x$ photoanodes with x = 0.0, 0.004, 0.01, and 0.028, and (b) plots of $(\alpha h\nu)^2$ versus photon energy for $ZnO_{1-x}S_x$ photoanodes.

Figure 6.12 (b) exhibits a plot of the square absorption coefficient versus photon energy. The absorption tails shift to the lower photon energy. The bandgap values, which are obtained by an extrapolation of leading edge to baseline, are 3.31 eV, 3.29 eV, 3.26 eV and 3.22 eV for x = 0.0, x = 0.004, x = 0.01, and x = 0.028, respectively. A bandgap reduction is seen with sulphur doping.

Valence band X-ray photoemission spectra were used to record the ZnO valence band features with and without the sulphur doping. Figure 6.13 shows that the valence band maximum (VBM) shifts to the lower binding energy with increasing sulphur doping, confirming that the sulphur 3p states hybridise with O 2p states in the valence band of ZnO. A repulsion interaction between O 2p and S 3p states occurs and results in an upward movement in the VBM, which account for the reduction in the optical bandgap.

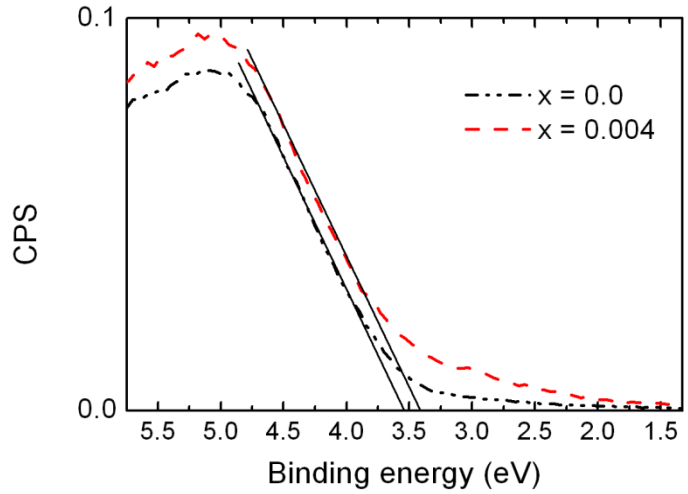

Figure 6. 13 Valence band X-ray photoemission spectra of $ZnO_{1-x}S_x$ (x = 0.0 and x = 0.004). The values from the valence band maximum to the Fermi level are determined by doing linear extrapolation of leading edge to background.

6.3.2 Photon Energy Conversion Efficiency of $ZnO_{1-x}S_x$ Photoanodes

The $ZnO_{1-x}S_x$ photoanodes were tested by performing amperometric I-t scans under light on/off cycles as shown in Figure 6.14. When applying a constant potential at + 0.8 V, the intensity of generated photocurrent densities in sequence is x = 0.004 (j = 49 $\mu W/cm^2$) > x = 0.01 (j = 32 $\mu W/cm^2$) > x = 0.0 (j = 18.5 $\mu W/cm^2$) > x = 0.028 (j = 9.8 $\mu W/cm^2$). The photocurrents in all photoanodes exhibit a sharp decay without a tail when the light is

switched off, suggesting that the charged carrier transport is efficient. Throughout the measurement time, there is no significant reduction in the photocurrent intensities among samples, implying that the $ZnO_{1-x}S_x$ films are stable and durable in neutral Na_2SO_4 electrolyte under PEC testing.

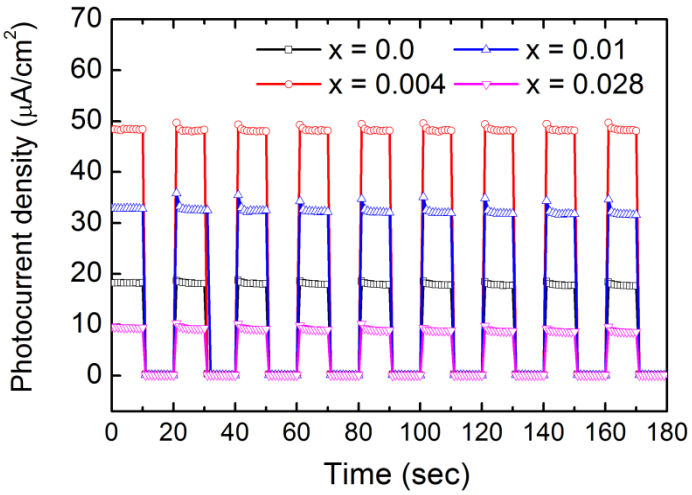

Figure 6. 14 Amperometric I-t curves of the $ZnO_{1-x}S_x$ as photoanodes at an applied potential of +0.8 V under 67 mW/cm^2 light on/off cycles.

Linear sweep voltammograms were used to record the photocurrent densities versus the applied potential for $ZnO_{1-x}S_x$ photoanodes in Figure 6.15. The ordering of photocurrent performance in the I-V curve is the same as that in the I-t curve (Figure 6.14). The highest photoresponse is x = 0.004 and the lowest one is x = 0.028, as listed in Table 6.2. The onset photocurrent potential (V_i) shifts to the more negative potential when sulphur concentration increases. In other words, the photoanodes of x = 0.028, x = 0.01, and x = 0.004 are superior to x = 0.0 in terms of the extra energy required (i.e. applied potential) to achieve a given photocurrent.

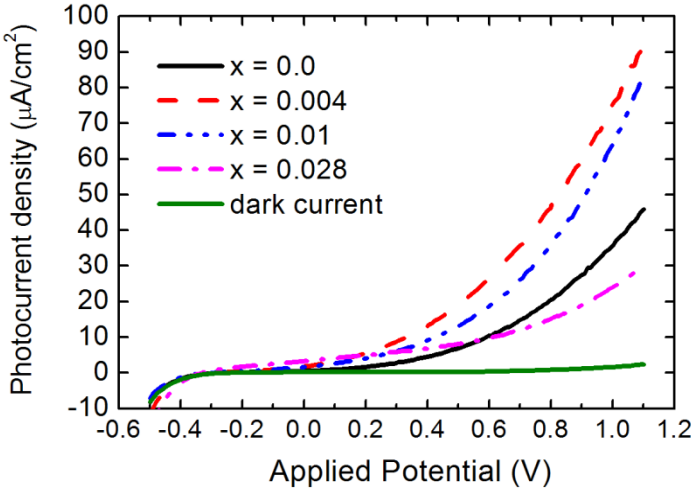

Figure 6. 15 Linear sweep voltammograms under dark and upon 67 mW/cm^2 illumination were performed for $ZnO_{1-x}S_x$ photoanodes.

Table 6. 2 The PEC Properties of $ZnO_{1-x}S_x$ photoanodes.

$ZnO_{1-x}S_x$	V_{fb} (V)	j (μA/cm^2) at +0.8 V	Photon-to-hydrogen efficiency (%)
x = 0.0	-0.08	18.3	0.18
x = 0.004	-0.22	48.4	0.60
x = 0.01	-0.25	33.1	0.47
x = 0.028	-0.32	9.8	0.18

Figure 6.16 demonstrates the photon-to-hydrogen conversion efficiency of $ZnO_{1-x}S_x$ photoanodes. The maximum energy conversion efficiency of $ZnO_{1-x}S_x$ photoanodes at +0.85 V are 0.18%, 0.60%, 0.47% and 0.18% for x = 0.0, x = 0.004, x = 0.01, and x = 0.028. The addition of S at low doping level (x = 0.004) in ZnO leads to the highest energy conversion efficiency. However, the efficiency decreases in the higher sulphur doping, even the samples of x = 0.01 and x = 0.028 have the smaller flatband potential. For example, the photon-to-

hydrogen efficiency in x = 0.028 is only 0.18% at +0.8 V but the required energy input to drive the photocurrent process is the smallest (i.e. the applied potential is the most negative).

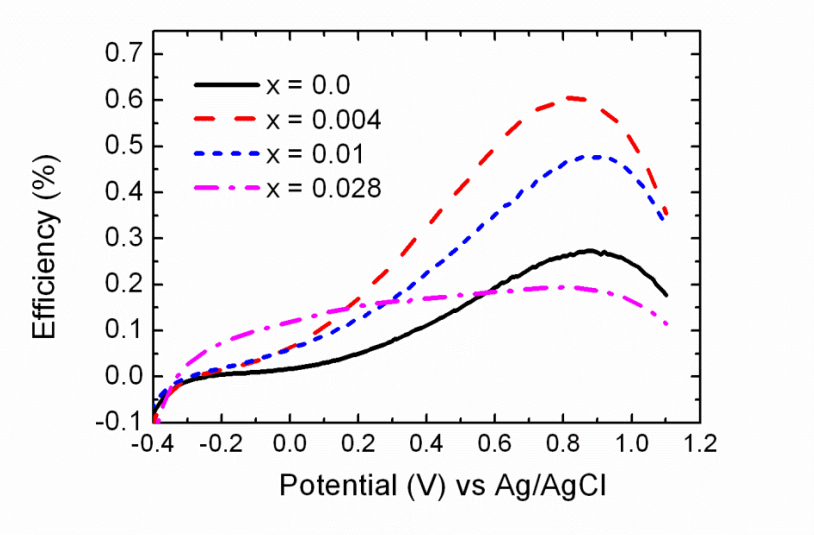

Figure 6. 16 Photon-to-hydrogen conversion efficiency of $ZnO_{1-x}S_x$ photoanodes upon irradiation AM1.5 (67 mW/cm^2).

To quantify the spectral dependence of the photoresponse, the incident-photon-to-current conversion efficiency (IPCE) as a function of wavelength was measured and the results are shown in Figure 6.17. The sample with x = 0.004 has the greatest light harvesting across the UV and visible regions, giving the best photoresponse in I-t and I-V measurements. Furthermore, the sample with x = 0.01 can absorb more visible light (i.e. above 400 nm) but less UV light when compared to x = 0.0. As a result, the overall light harvest in x = 0.01 is higher than that in x = 0.0, resulting in a higher energy conversion efficiency.

It is worth noticing that although the sample with x = 0.028 has the strongest absorption in the visible region, its visible region photocurrent response is no higher than that of undoped ZnO. In reviewing the SEM images (Figure 6.10), the crystallite size of x = 0.028 is significantly smaller than the other samples. As discussed in chapter 5.2, a small crystallite

size accompanies with a high level of grain boundary, leading to a lower mobility and a lower. The inefficient charge separation due to the poor electrical transport properties could dominate the photon-to-hydrogen efficiency instead of the bandgap.

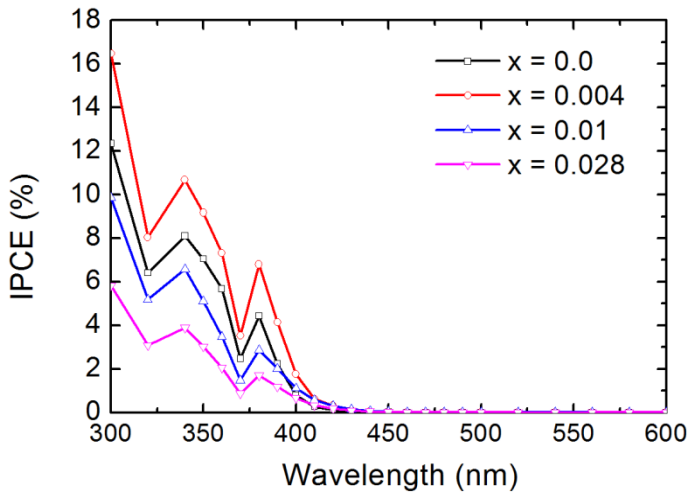

Figure 6. 17 Measured incident-photon-to-current conversion efficiency (IPCE) spectra of $ZnO_{1-x}S_x$ photoanodes in the region of 300-600 nm at a fixed applied potential +0.8 V with reference to Ag/AgCl electrode.

Figure 6.18 (a) shows the I-V curves of single-phase solid solution photoanodes of $Cd_{0.026}Zn_{0.974}O$, $ZnO_{0.972}S_{0.028}$ and Cd:S co-doped ZnO; $Cd_{0.026}Zn_{0.974}O_{0.972}S_{0.028}$. The onset potentials of photocurrent in these samples are -0.26 V, -0.29 V, and -0.33 V, respectively. The onset potential in S-doped ZnO is more negative than that in Cd-doped ZnO, showing that the Fermi level position in S-doped ZnO is higher (or more negative) than that in Cd-doped ZnO. As a consequence, the S-doped ZnO that is assumed to have a greater band bending needs less external energy to generate a photocurrent compared to Cd-doped ZnO.

Interestingly, the Cd:S co-doped ZnO photoanode displays the most negative onset potential, implying the Fermi level at the most negative potential and the largest band bending related to the reduction potentials in the Cd-doped ZnO and S-doped ZnO.

Moreover, the Cd:S co-doped ZnO also generates the highest photocurrent density below +0.8 V. The UV-Vis spectrum in Figure 6.18 (b) demonstrates that Cd:S co-doped ZnO has the superior photoresponse in the UV and visible regions, confirming the largest photocurrent density observed in I-V measurement.

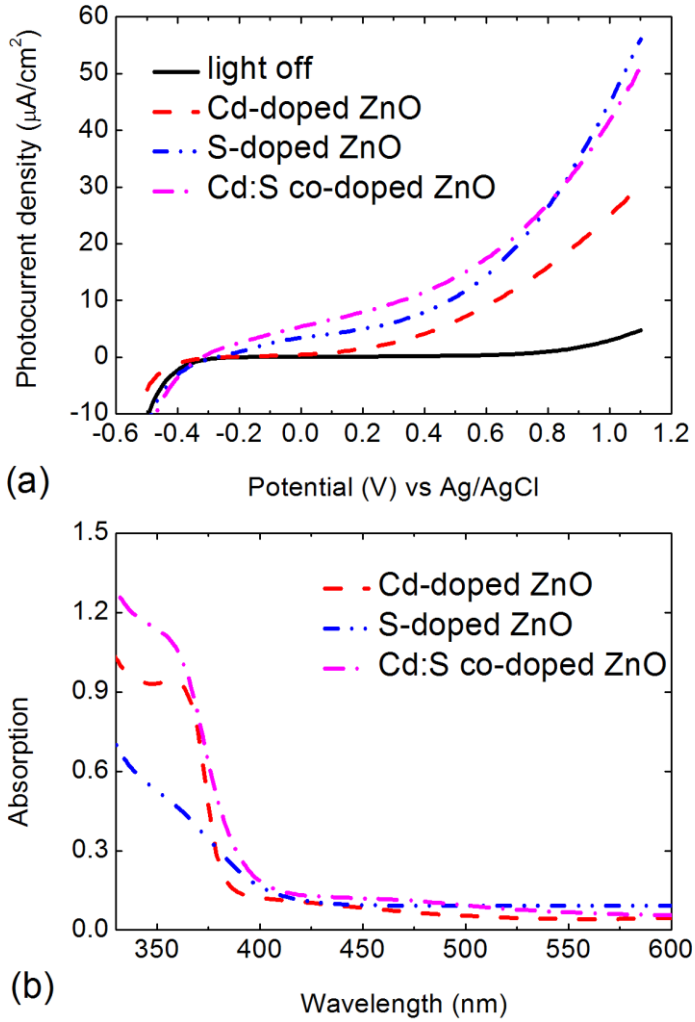

Figure 6. 18 (a) I-V measurements and (b) UV-Vis absorption spectra of $Cd_xZn_{1-x}O$, $ZnO_{1-y}S_y$, and Cd:S co-doped ZnO photoanodes.

6.4 *Summary*

In this chapter, we have report measurements of the photocurrent response and energy conversion efficiencies for the ZnO, $Cd_xZn_{1-x}O$ and $ZnO_{1-x}S_x$ photoanodes using linear sweep voltammogram (photocurrent versus applied potential measurement) and amperometric photocurrent-time measurements.

Examinations of the effects of film thickness for undoped ZnO samples showed that a 200nm thick film had a superior photocurrent response to that of thinner films. The thicker film is expected to have better electrical transport properties due to the lower level of strain-induced lattice imperfections.

For $Cd_xZn_{1-x}O$ photoanodes, the highest photon-to-hydrogen energy conversion efficiency in PEC tests is obtained for the sample with x = 0.065. The reduction in the bandgap effectively increases the solar energy harvest by absorbing more visible light. In addition, a heterojunction structure with a mixture of hexagonal and cubic phases in the samples with x = 0.065 and x = 0.038 samples could benefit to the electron transfer between semiconductors ($ZnO/Cd_xZn_{1-x}O/CdO$) and results in an enhancement in the photon energy conversion efficiency. When compared to the undoped ZnO photoanode, the $Cd_{0.065}Zn_{0.935}O$ sample enhanced by 240% in the photocurrent density at +0.8 V and increased by 220% in the photon-to-hydrogen efficiency.

The PEC performance in S-doped ZnO photoanodes is determined by the crystallite size, instead of bandgap reduction. The sample with x = 0.004 showed the greatest photocurrent density and the highest energy conversion efficiency. The photocurrent density and the photon-to-hydrogen efficiency in the x = 0.004 sample increased by 260% and 330% compared to the undoped ZnO. The x = 0.028 sample presented the lowest photon energy conversion efficiency due to the smallest grain size. The smallest grain size in x = 0.028 leads

to the lowest electrical transport properties due to the effect of grain boundary. The photogenerated electrons and holes were not able to separate efficiently, giving the lowest energy conversion efficiency.

With the similar amount of impurities doping, the onset potential of photocurrent was more negative in S-doped ZnO electrode than that in Cd-doped ZnO electrode. This suggested that the Fermi level in S-doped ZnO is more negative than that in Cd-doped ZnO. As a result, the S-doped ZnO electrode is expected to have a larger band bending and more efficient in photoresponse when compared to the Cd-doped ZnO electrode. For the Cd:S co-doped ZnO sample, the energy conversation efficiency was superior to Cd-doped ZnO and S-doped ZnO electrodes. This is because Cd:S co-doped ZnO has the smallest bandgap, the highest light harvesting ability, and it acquires the least extra energy to generate a photocurrent due to the most negative Fermi level position.

6.5 References

1. M. Gratzel, Nature **414**, 338 (2001).
2. F. Le Formal, M. Gratzel and K. Sivula, Advanced Functional Materials **20**, 1099 (2010).
3. X. Y. Yang, A. Wolcott, G. M. Wang, A. Sobo, R. C. Fitzmorris, F. Qian, J. Z. Zhang and Y. Li, Nano Letters **9**, 2331 (2009).
4. H. M. Chen, C. K. Chen, Y. C. Chang, C. W. Tsai, R. S. Liu, S. F. Hu, W. S. Chang and K. H. Chen, Angewandte Chemie-International Edition **49**, 5966 (2010).
5. A. Wolcott, W. A. Smith, T. R. Kuykendall, Y. P. Zhao and J. Z. Zhang, Advanced Functional Materials **19**, 1849 (2009).
6. N. Beermann, L. Vayssieres, S. E. Lindquist and A. Hagfeldt, Journal of the Electrochemical Society **147**, 2456 (2000).
7. J. Nowotny, T. Bak, M. K. Nowotny and L. R. Sheppard, International Journal of Hydrogen Energy **32**, 2609 (2007).
8. A. Kudo and Y. Miseki, Chemical Society Reviews **38**, 253 (2009).
9. D. W. Hwang, J. Kim, T. J. Park and J. S. Lee, Catalysis Letters **80**, 53 (2002).
10. C. Klingshirn, Physica Status Solidi B-Basic Solid State Physics **244**, 3027 (2007).
11. B. F. Yang, H. W. Yan, J. B. Hou, Z. P. Fu, P. H. Yang, K. P. Liu, M. W. Wen, Y. J. Chen, S. Q. Fu and F. Q. Li, Materials Research Bulletin **44**, 1954 (2009).
12. Y. Xu and M. A. A. Schoonen, American Mineralogist **85**, 543 (2000).
13. Y. F. Li, B. Yao, Y. M. Lu, Y. Q. Gai, C. X. Cong, Z. Z. Zhang, D. X. Zhao, J. Y. Zhang, B. H. Li, D. Z. Shen, X. W. Fan and Z. K. Tang, Journal of Applied Physics **104**, 83516 (2008).
14. L. A. Harris and R. H. Wilson, Annual Review of Materials Science **8**, 99 (1978).
15. J. M. Bolts and M. S. Wrighton, Journal of Physical Chemistry **80**, 2641 (1976).
16. A. J. Nozik and R. Memming, Journal of Physical Chemistry **100**, 13061 (1996).
17. K. H. L. Zhang, V. K. Lazarov, P. L. Galindo, F. E. Oropeza, D. J. Payne, H. H. C. Lai and R. G. Egdell, Crystal Growth & Design **12**, 1000 (2012).
18. A. Jain, P. Sagar and R. M. Mehra, Materials Science-Poland **25**, 233 (2007).
19. J. Y. W. Seto, Journal of Applied Physics **46**, 5247 (1975).
20. K. S. Ahn, Y. F. Yan, S. H. Lee, T. Deutsch, J. Turner, C. E. Tracy, C. L. Perkins and M. Al-Jassim, Journal of the Electrochemical Society **154**, B956 (2007).
21. D. E. Scaife, Solar Energy **25**, 41 (1980).
22. H. M. Chen, C. K. Chen, C. C. Lin, R. S. Liu, H. Yang, W. S. Chang, K. H. Chen, T. S. Chan, J. F. Lee and D. P. Tsai, Journal of Physical Chemistry C **115**, 21971 (2011).
23. K. S. Ahn, Y. Yan, S. Shet, K. Jones, T. Deutsch, J. Turner and M. Al-Jassim, Applied Physics Letters **93**, 163117 (2008).

24. H. M. Chen, C. K. Chen, R. S. Liu, C. C. Wu, W. S. Chang, K. H. Chen, T. S. Chan, J. F. Lee and D. P. Tsai, Advanced Energy Materials **1**, 742 (2011).

CHAPTER 7

CONCLUDING REMARKS & FUTURE WORK

This thesis has attempted to investigate the fundamental mechanisms of visible light absorption in anion and cation-doped ZnO semiconductors, and to explore the potential of these doped materials to modify the electrical properties of ZnO photoanodes for photocatalytic water splitting. Aluminium, cadmium, and sulphur-doped ZnO thin films and photoanodes were deposited on glass, single crystal Al_2O_3(0001) and indium tin oxide-coated glass substrates by the spray pyrolysis technique. Additionally, cadmium-doped ZnO powdered sample were produced by solid state synthesis. An overview of the results and comments for future work will be presented in this chapter.

7.1 Concluding Remarks

In *Chapter 3*, the essential parameters for growing high quality ZnO thin films, such as the thermodynamic driving force and the misfit between the substrate and film, were investigated. ZnO thin films deposited on glass and Al_2O_3(0001) by spray pyrolysis demonstrated a high orientation in the *c*-axis of crystallites at the deposition temperature of above 350˚C due to the atomic arrangement on the terminated plane. The Burstein Moss (BM) effect determined the energy shift in the bandgap of Al-doped ZnO (AZO) thin films. A strain-induced bandgap shift in AZO films has been ruled out because the magnitudes of strain between AZO films are almost equal.

Epitaxial growth of ZnO thin films were carried out successfully by the spray pyrolysis method. The vital conditions for growing a ZnO epilayer is a substrate with small lattice mismatch (e.g. single crystal $Al_2O_3(0001)$), and a deposition temperature of around 500˚C.

Chapter 4 focused on the effect of Cd doping on the electronic structures, electrical transport and optical properties in ZnO. It revealed that the conduction and valence bands shift simultaneously when Cd was incorporated in ZnO. The valence band offset was caused by the rehybridisation of Cd 4d and Zn 3d orbitals while the conduction band offset was a result of the perturbation by underlying Cd 5s impurity states. The electron accumulation and downward band bending were observed on the surface of $Cd_xZn_{1-x}O$ powders, not in the deposited thin films.

Chapter 5 illustrated the influence of S doping in ZnO on the grain size and electronic structure. In contrast to $Cd_xZn_{1-x}O$, substituting of S only affected the ZnO valence band. This was because high lying S 3p states compared to O 2p states in the valence band, which leads to an upward shift in the valence band maximum.

A photoelectrochemistry workstation with a three-electrode cell was constructed to evaluate the undoped ZnO, $Cd_xZn_{1-x}O$, and $ZnO_{1-x}S_x$ photoelectrodes and those results were presented in *Chapter 6*. Under illumination, the bandgap reduction as well as the heterojunction structure in $Cd_xZn_{1-x}O$ photoelectrodes significantly increased visible light harvesting. When compared to the undoped ZnO photoanode, the $Cd_{0.065}Zn_{0.935}O$ sample was enhanced by 240% in the photocurrent density at +0.8 V and increased by 220% in the corresponding photon-to-hydrogen efficiency.

With regard to $ZnO_{1-x}S_x$ photoanodes, the photocurrent density and the photon-to-hydrogen efficiency in the x = 0.004 sample increased by 260% and 330%

compared to the undoped ZnO. However, as the S content increases, the photocurrent density and efficiency decreased. Film crystallinity, such as grain size, grain boundary and dislocation determined the photocurrent generation and the energy conversion efficiency instead of bandgap in $ZnO_{1-x}S_x$ photoanodes. It is accepted that crystallinity is responsible for the recombination rate of electrons and holes. Thus, the x = 0.028 photoelectrode has the highest level of grain boundaries as a result of the smallest grain size, leading to an inefficient charge separation and the consequences of low energy conversion efficiency.

7.2 Future Work

The photoelectrolysis of water can be achieved with photoelectrochemical cells (PEC). An ideal semiconducting material used in PECs needs to accomplish a significant absorption of visible light, have a suitable band edge position such that the conduction band edge is more negative than the hydrogen redox potential and the valence band edge is more positive than the oxygen reduction potential, and an efficient separation of photogenerated electrons and holes. Additionally, materials must be inexpensive and stable when operating in an aqueous electrolyte. In future work, greater attentions on achieving the above requirements will further enhance the energy conversion efficiency. The possible solutions to accomplish our goals are through device designing, nanoarchitecture, solid state solution or a combination are proposed in following sections.

7.2.1 The Quest for Two-Step Water Splitting: Tandem Cell (Z-scheme)

A strategy to enhance the photoelectrochemical water splitting performance is by means of designing a specific device configuration. The so-called tandem cell, which consists of a dual bandgap absorber, is equipped with an n-type semiconductor electrode as the photoanode and a p-type semiconductor electrode as the photocathode. Figure 7.1 (a) illustrates such an idealised tandem cell. Incident blue and red light are absorbed by a larger and smaller bandgap semiconducting electrodes, respectively.[1] In the design of two electrodes deposited on the both sides of a transparent conducting oxide (TCO) substrate, the electrode can not only increase harvesting solar light but also reduce the material cost.

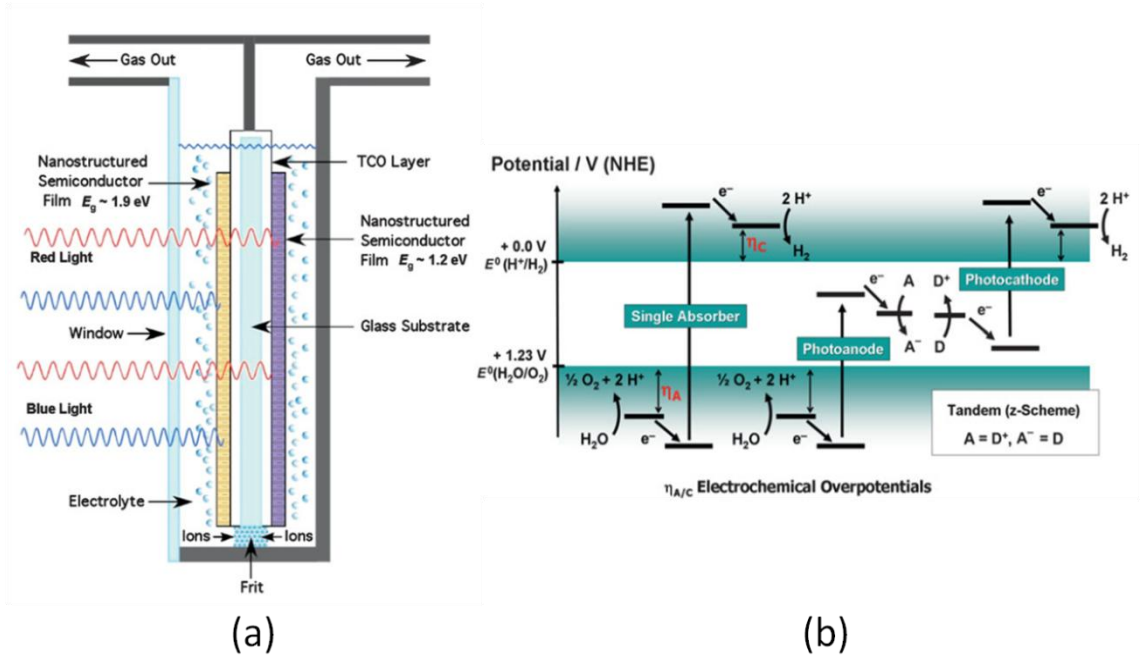

Figure 7. 1 (a) Photoelectrochemical cells with two visible absorbers deposited on the both side of a transparent conducting oxide (TCO) substrate. Blue rays are absorbed by a larger bandgap (E_g) semiconductor and red rays are harvested by a smaller bandgap semiconductor. (b) Schematic diagram of energy levels for single-absorber PECs, two-absorber PECs (tandem cell), hydrogen reduction potential, and oxygen reduction potential. A and D are electron mediators, representing as electron acceptors and electron donors, respectively.[1]

A schematic energy diagram for the photoelectrochemical water splitting is represented in Figure 7.1 (a). The single absorber diagram represents a single cell PEC device that associates with a photoanode and a metal cathode. On the other hand, the z-scheme tandem cell is composed of two visible light absorbers, one is H_2-evolving catalyst and the other is O_2-evolving catalyst, and electron mediators to achieve the whole water splitting process. This concept creates a flexibility of semiconducting electrode choices. Two smaller bandgap semiconductors that absorb visible light can be employed in the tandem cell.

7.2.2 The Quest for One-Step Water Splitting: Solid Solution Photocatalysts and Nanoarchitecture

In contrast to tandem cells, the one-step water splitting reaction (i.e. single electrode PECs) is a relatively simple process and does not require electron mediators. However, it is unusual to find a material that both absorbs significant amount of visible light and is stable under photoirradiation. Forming a solid state solution of metal oxide semiconductors is one of the most effective approaches in accomplishing the visible light absorption and to enhance the energy conversion efficiency. For example the isovalent substitution, oxynitride materials, which consist of hybridised O 2p and N 2p orbitals; $M_x(ON)_y$, are expected to harvest more visible light than the conventional metal oxide semiconductors. Figure 7.2 shows the band edge positions of a metal oxide (e.g. $NaTaO_3$) and a metal oxynitride ($BaTaO_2N$).[2, 3] When N atoms partially or entirely substitute the O sites, the valence band maximum can be moved towards the conduction band without affecting the conduction band, similar to the S-doped ZnO in chapter 5 in our study.

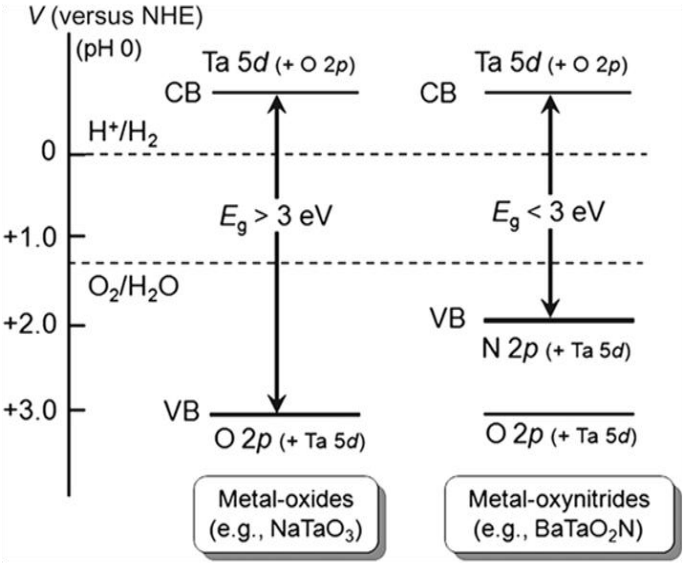

Figure 7. 2 Schematic diagram of band edge positions of a metal oxide ($NaTaO_3$) and a metal oxynitride ($BaTaO_2N$) related to hydrogen and oxygen reduction potentials versus the normal hydrogen electrode (NHE).[3]

Nano-scale materials have been considered as an efficient component of photoelectrochemical cell.[4] As shown in Figure 7.3 (a), electron transport via the hoping process in spherical α-Fe_2O_3 nanoparticles causes a significant electron-hole pair recombination, resulting in a lower photocurrent production. The orientation in the nanorods illustrated in Figure 7.3 (b) and (c) has affected the PEC efficiency as well. The performance in the vertical nanorods is better than that in the horizontal nonarods. The vertical nonarod film exhibits a higher PEC efficiency than the above two nanostructural films, which are ascribed to the less amount of ground boundaries in nanorods and the directed movement of electrons towards the back contact in the case of nanorods orientated normal to the substrate.[4] Nanotube structure (Figure 7.3(d)) can further enhance the PEC efficiency due to the larger surface area to volume ratio.[5]

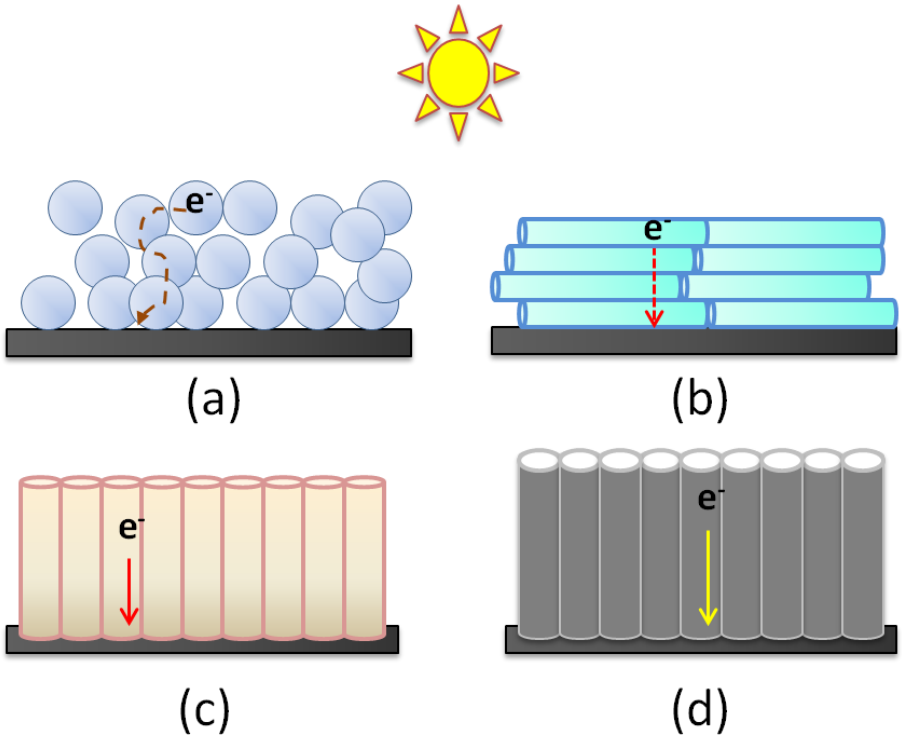

Figure 7. 3 Schematic illustrations of photogenerated electrons transport in the (a) spherical nanoparticlea, (b) horizontal orientated nanorods, (c) vertical orientated nanorods, and (d) vertical oriented nanotubes. [4, 5]

Another concept is core-shell or multi-layer nanowires to be made as a single electrode in PECs (Figure 7.4). The core-shell structure has been demonstrated for the high-brightness GaN light-emitting diode (LED) by combing an n-GaN nanowire (shell) and a p-Si (core) to achieve a p-n heterojunction diode.[6] In PEC devices, the core and shell materials can be replaced with two visible absorber semiconductors, which are similar to the idea of tandem cells. That is, each core-shell nanowire plays like a microtandem cell but does not need additional electron mediators in the electrolyte and two semiconducting electrodes in PECs. Furthermore, at the interface of core/shell, a solid state solution may be formed, which perhaps benefits to the light harvest and the charged carrier transport.

Figure 7.4 (b) is a schematic multi-layer $Cd_xZn_{1-x}O$ nanowire, of which each section represents a different Cd concentration incorporated in ZnO. In this design, each section with different bandgap values can absorb different wavelengths in the solar spectrum so as to increase light harvest. In addition to this, the charged carriers transport can be improved as well because the band edge levels decrease or increase one-by-one layers.

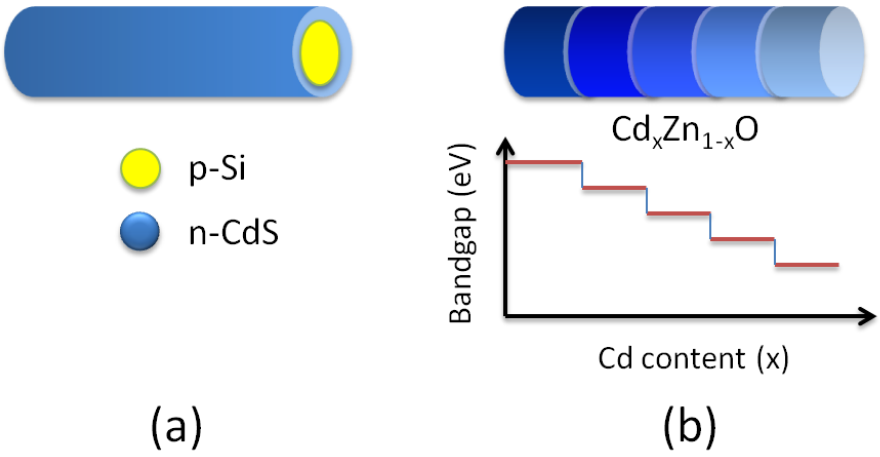

Figure 7. 4 Schematic representations of (a) a core-shell nanowire as a p-n heterojunction structure, and (b) a multi-layer alloying nanowire.[6]

7.3 Concluding Summary

This work has established key aspects of bandgap engineering control the conduction and valence band locations. I hope that these efficient advances highlighted here in tandem with the results obtained in this thesis can help providing a new generation of high efficient photoelectrochemical cells for water splitting reaction at a low cost.

7.4 References

1. F. E. Osterloh and B. A. Parkinson, Mrs Bulletin **36**, 17 (2011).
2. K. Maeda, K. Teramura, D. L. Lu, T. Takata, N. Saito, Y. Inoue and K. Domen, Nature **440**, 295 (2006).
3. K. Maeda and K. Domen, Mrs Bulletin **36**, 25 (2011).
4. N. Beermann, L. Vayssieres, S. E. Lindquist and A. Hagfeldt, Journal of the Electrochemical Society **147**, 2456 (2000).
5. N. Chouhan, C. L. Yeh, S. F. Hu, R. S. Liu, W. S. Chang and K. H. Chen, Chemical Communications **47**, 3493 (2011).
6. S. Chattopadhyay, L. C. Chen and K. H. Chen, Npg Asia Materials **3**, 74 (2011).